



**HAL**  
open science

# Robust control for manipulation inside a scanning electron microscope

Marcelo Gaudenzi de Faria

► **To cite this version:**

Marcelo Gaudenzi de Faria. Robust control for manipulation inside a scanning electron microscope. Micro and nanotechnologies/Microelectronics. Université de Franche-Comté, 2016. English. NNT : 2016BESA2068 . tel-01661447

**HAL Id: tel-01661447**

**<https://theses.hal.science/tel-01661447>**

Submitted on 12 Dec 2017

**HAL** is a multi-disciplinary open access archive for the deposit and dissemination of scientific research documents, whether they are published or not. The documents may come from teaching and research institutions in France or abroad, or from public or private research centers.

L'archive ouverte pluridisciplinaire **HAL**, est destinée au dépôt et à la diffusion de documents scientifiques de niveau recherche, publiés ou non, émanant des établissements d'enseignement et de recherche français ou étrangers, des laboratoires publics ou privés.



SPIM

Thèse de Doctorat



UFC

école doctorale sciences pour l'ingénieur et microtechniques  
UNIVERSITÉ DE FRANCHE-COMTÉ

# Robust control for manipulation inside a scanning electron microscope

■ MARCELO GAUDENZI DE FARIA



# SPIM

## Thèse de Doctorat

UFC

école doctorale sciences pour l'ingénieur et microtechniques  
UNIVERSITÉ DE FRANCHE-COMTÉ

THÈSE présentée par

MARCELO GAUDENZI DE FARIA

pour obtenir le

Grade de Docteur de  
l'Université de Franche-Comté

Spécialité : **Automatique**

## Robust control for manipulation inside a scanning electron microscope

Unité de Recherche :  
FEMTO-ST, UMR CNRS 6174

Soutenue publiquement le 17 Février 2016 devant le Jury composé de :

SERGEJ FATIKOW	Président	Professeur à l'Université d'Oldenburg - DE
FLORENCE MARCHI	Rapporteur	Maitre de conférences-HDR à l'Université Grenoble Alpes - FR
EDOUARD LAROCHE	Rapporteur	Professeur à l'Université de Strasbourg - FR
PHILIPPE LUTZ	Directeur de thèse	Professeur à l'Université de Franche-Comté - FR
YANN LE GORREC	Co-directeur de thèse	Professeur à l'École Nationale Supérieure de Mécanique et des Microtechniques - FR
YASSINE HADDAB	Co-directeur de thèse	Professeur à l'Université de Montpellier - FR



## ACKNOWLEDGEMENTS

The work presented here were developed in the Automation and Micro-Mecratic Systems (AS2M) department, at the FEMTO-ST Institute, which I would like to thank for receiving me during this period.

I would like to thank Prof. Philippe Lutz, director of the graduate school and my advisor, for the constant support and motivation, allowing me to complete this thesis within the best possible conditions.

My thanks also to my co-advisors: Prof. Yassine Haddab for the patience, friendship and the advices over several technical aspects for this work, which were essential, and Prof. Yann Le Gorrec for his constant support and guidance for my multiple questionings in the last years.

I can not forget all the FEMTO-ST team, specially Patrick Rougeot, Jean-Yves Rauch and Olivier Lehmann, for all the aid offered with the experiments and the operation of the scanning electron microscope.

My thanks to all my friends that, in the course of this thesis, contributed with extensive laughter and advice: Adrian, Ahmed, Alexandra, Amélie, Andrey, Arèf, Babs, Bassem, Benoit, Bilal, Didace, Elodie, Francisco 'Paco', Héctor, Haitem, Hussein, Iñigo, João Stotz, Kamran, Louise, Marco, Margot, Marina 'Tava', Marine, Martina, Max, Michelle, Mohamed, Mouloud, Nandish, Nathalie, Patricia, Racha, Sergio, Taha, Tristan, Valerian, Vincent, Viki, Vladimir, Wiem, Yannis, and many others.

Finally, I would also like to thank my family that, despite the distance, supported me and helped to make this work possible.

To you all, my most sincere thanks.



# CONTENTS

<b>General introduction</b>	<b>1</b>
<b>1 Challenges for robotics in nano-characterization and nano-manipulation</b>	<b>5</b>
1.1 The need for micro- and nano-objects characterization . . . . .	6
1.2 The NanoRobust project - a platform for nano-manipulation in SEMs . . . . .	9
1.2.1 Common tasks performed in SEMs . . . . .	9
1.2.2 Scope of the NanoRobust project . . . . .	11
1.3 Overview on nanorobotics system in SEM . . . . .	12
1.3.1 The scanning electron microscope . . . . .	12
1.3.1.1 Interaction between electron beam and matter . . . . .	13
1.3.1.2 SEM imaging characteristics . . . . .	14
1.3.2 Nanomanipulation systems . . . . .	16
1.3.3 End-effectors . . . . .	19
1.3.3.1 Needle tips . . . . .	19
1.3.3.2 Micro-grippers . . . . .	20
1.3.4 Sensors . . . . .	24
1.3.5 Examples of robotized tasks carried in SEMs . . . . .	26
1.3.5.1 Tele-operated manipulation and characterization in SEMs . . . . .	26
1.3.5.2 Development of autonomous tasks in SEM . . . . .	30
1.3.5.3 Improving performance and precision in SEM through the use of models . . . . .	32
1.4 Thesis context . . . . .	33
1.4.1 Review of the issues presented . . . . .	33
1.4.2 Thesis objectives . . . . .	35
<b>2 Characterization and analysis of disturbance on SEM</b>	<b>37</b>
2.1 Overview on sources of disturbances occurring in the SEM . . . . .	37
2.1.1 Mechanical and acoustic disturbances . . . . .	38
2.1.2 Electromagnetic disturbances . . . . .	39
2.1.3 Thermal disturbances . . . . .	41

2.1.3.1	Thermal noise . . . . .	41
2.1.3.2	Thermal effects on sensors and micro-structures . . . . .	41
2.1.3.3	Heating due to electron beam . . . . .	43
2.1.4	Conclusion . . . . .	45
2.2	Vibration measurement inside a SEM . . . . .	46
2.2.1	Vibrometer characterization . . . . .	47
2.2.2	SEM disturbances and noises identification . . . . .	49
2.2.2.1	System under regular operation condition . . . . .	50
2.2.2.2	System under external acoustic excitation . . . . .	54
2.2.3	Conclusion . . . . .	56
2.3	Conclusion . . . . .	57
<b>3</b>	<b>Micro-gripper dynamics identification in vacuum and at atmospheric pressure</b>	<b>59</b>
3.1	The FT-G30 micro-gripper . . . . .	59
3.2	Identification of actuated finger at atmospheric pressure . . . . .	62
3.2.1	Experimental identification for the gripper in air . . . . .	63
3.2.2	Effects of electronic input disturbance over the electrostatic comb-drive in air . . . . .	65
3.3	Identification of actuated finger in vacuum . . . . .	66
3.3.1	Nonlinear stiffness effects . . . . .	66
3.3.2	Experimental identification for the gripper in vacuum . . . . .	68
3.3.3	Effects of electronic input disturbances over the electrostatic comb-drive in vacuum . . . . .	70
3.4	Resume of differences between air and vacuum . . . . .	71
3.5	Conclusion . . . . .	74
<b>4</b>	<b>Position control in the micro-world</b>	<b>75</b>
4.1	Control strategies for nano-positioning . . . . .	75
4.1.1	Examples of positioning tasks inside the SEM . . . . .	78
4.1.2	Conclusion . . . . .	80
4.2	Robust position control strategies for a micro-gripper in vacuum . . . . .	80
4.2.1	Uncertain systems and the LFT representation . . . . .	82
4.2.2	$\mu$ analysis - a tool for robust stability and performance evaluation . . . . .	83
4.2.3	$H_\infty$ controller . . . . .	85
4.2.4	Extended state observer structure . . . . .	88
4.2.4.1	High-gain observer . . . . .	90

4.3	Controller design . . . . .	93
4.3.1	Controller synthesis using $H_\infty$ . . . . .	94
4.3.1.1	Selection of the weighting functions . . . . .	94
4.3.2	Controller synthesis using ESO . . . . .	97
4.3.3	Robustness analysis . . . . .	99
4.3.4	Conclusion . . . . .	103
4.4	Experimental validation and results . . . . .	104
4.4.1	Reference tracking and steady state error under environmental disturbances	106
4.4.2	Disturbance rejection for external mechanical and acoustic perturbations	108
4.4.3	Conclusion . . . . .	110
4.5	Conclusion . . . . .	111
<b>5</b>	<b>Conclusions and perspectives</b>	<b>113</b>
5.1	Conclusions . . . . .	113
5.2	Future perspectives . . . . .	114
	<b>Personal publications</b>	<b>117</b>
	<b>References</b>	<b>119</b>
	<b>List of Figures</b>	<b>133</b>
	<b>List of Tables</b>	<b>139</b>
	<b>List of Definitions</b>	<b>141</b>
<b>I</b>	<b>Appendix</b>	<b>143</b>
<b>A</b>	<b>Atohm SD28CR08F datasheet</b>	<b>145</b>
<b>B</b>	<b>The Linear Fraction Transformation</b>	<b>147</b>
<b>C</b>	<b>Noise impact on high-gain observer</b>	<b>149</b>



# LIST OF ACRONYMS AND ABBREVIATIONS

- AFM - Atomic force microscope
- CNT - Carbon nano-tube
- DO - Disturbance observer
- DoF - Degree of freedom
- EMI - Electromagnetic interference
- ESO - Extended state observer
- EHGO - Extended high-gain observer
- FIB - Focus ion beam
- FFT - Fast Fourier transform
- FT-G30 - FemtoTools Gripper 30, a model of micro-gripper
- G0, G1, G2 and G3 - Gains for the vibrometer's analog output
- LFT - Linear fraction transformation
- LMI - Linear matrix inequality
- LQG - Linear quadratic gaussian
- MEMS - Micro electro-mechanical system
- MINIMAN - Miniaturized Manipulation, a family of robots
- MPC - Model predictive control
- Nano-FET - Nanowire field-effect transistor
- NCA - Nanoparticle chain aggregates
- OL - Open loop
- P/PI/PID - Proportional (P), integral (I) and derivative (D) controllers
- PMN-PT - Lead (Pb) magnesium (Mg) niobate (Nb) - lead titanate (Ti), a ceramic piezoelectric material
- PSD - Power spectral density
- RMS - Root mean square
- SEM - Scanning electron microscope
- SM - Sliding mode
- SNOM - Scanning near-field optical microscope
- SSV - Structured singular value
- STEM - Scanning transmission electron microscope

STM - Scanning tunneling microscope

TEM - Transmission electron microscopes

UIO - Unknown input observer

# GENERAL INTRODUCTION

Advances in nanotechnology allowed the development of new materials and the production of micro and nano-components with complex structures and geometries in large scales. Nano-objects, structures with one or more dimensions under 100 nanometers, and nano-materials have gathered the attention of various research fields (i.e. biology and medicine, chemistry, physics, computer science, engineering, and others). Exploring the unique properties, effects, and phenomena only existing at these scales allowed to develop various devices, by improving existing ones or by exploring news designs. Despite the evident progress brought by the study and manipulation of matter at these minuscule scales on the past years, various obstacles hinder the advances in this field.

The characterization of various nano-structures (single walled carbon nanotubes, graphene membranes, nano-particles, ...) is an essential step towards improving our knowledge over fabricated nano-structures. It is usually performed only on a reduced amount of samples, with the assumption of consistent properties over a larger number of individual. This method presents various limitations in face of current demands. Current fabrication methods can produce micro- and nano-objects in large quantities, and individual characterization (mechanical, chemical and electrical) becomes necessary. This more extensive process can deepen our knowledge over sample's singular properties, improve fabrication methods and detect faults, and help in the selection of suitable individuals with uniform characteristics from a larger group.

The minuscule operation scale required for manipulation and characterization of these nano-objects motivated the development of various strategies. When operating at micro and nano-scales, visual feedback is essential and commonly obtained with the aid of microscopes. Among them, the scanning electron microscope (SEM) is a popular tool. This device offers a large magnification range and can present relatively fast image acquisition speeds (up to tens of Hertz in some cases). Electron microscopes work by bombarding samples with a focused electron beam and are therefore not limited to the wavelength of visible light. As result, resolutions close to 1 nanometer can be achieved. In addition, the 3D manipulation of objects possible and often explored in this device.

This microscope operates in high vacuum, necessary to reduce deviations of the focused electron beam during its path from source to sample, bringing some advantages and disadvantages. By performing various tasks in this environment, such as characterization and assembly of devices, the risk of contamination is reduced. At the same time, operating remotely with a restricted work volume brings up new challenges, linked to the limitations this imposes over the instrumentation, where compact yet accurate sensors are required and sensor placement can become an issue.

Inside a SEM, all tasks are carried out with the aid of robotic manipulators and stages, using information from image, sensors and computational models. These tasks can be fully tele-operated or present various degrees of automation. The manipulators are usually equipped with micro-grippers or needle-like end-effectors, allowing to grasp, characterize and assemble various structures. Despite the success obtained so far in these tasks, problems do exist when performing them, specially when high precisions are needed. When component dimensions are reduced, they become more fragile and prone to the effects of disturbances and interaction forces. Sensors can

present unfavorable signal-noise ratios and their acquisition frequencies may not be adequate to capture the fast dynamic events in this scale. To reduce the chances of damaging both samples and end-effectors, movements should be carefully planned and slowly executed. Even when these strategies are employed, various researchers point out achieving high-precision positioning is not an easy feat. This can be partially attributed to the lack of reliable real-time information about the end-effectors position, specially over its dynamic behavior.

The works described in this document were developed in the scope of the NanoRobust project. It aimed for the robust manipulation and characterization of micro/nano-components and structures inside a scanning electron microscope. The term “robust” here expresses the desire to reduce the occurrence of failures when performing these tasks. In the project framework, this thesis explored the dynamic characteristics of a micro-gripper, considering various factors that could contribute to the degradation of its precise positioning. Conjointly, an analysis of the pressure effects over the end-effector was performed, indicating a few particular consequences of operating in a vacuum environment.

The thesis goal was to develop a robust control strategy for precise positioning of an end-effector inside the SEM. To measure the dynamic response of components in real-time, methods based on SEM image analysis are not well suited. For this reason, a dedicated setup was proposed, and included a high-resolution vibrometer to provide real-time position data used for measuring the end-effector and disturbance dynamics inside the vacuum chamber. The capacity to perform *in situ* identification of these elements is a singular characteristic of this work. This often unavailable and overlooked information was employed in the development of control laws for the end-effector position, aiming to achieve improved performance characteristics in terms of response speed, precision, accuracy and disturbance attenuation.

This document is structured as follows:

Chapter 1 introduces the importance of handling and characterizing micro and nano-structures, and how currently employed strategies experience difficulties towards achieving the required precisions and accuracies to manipulate nano-structures. The project NanoRobust aims to improve various aspects of the nano-manipulation, including the precise positioning of end-effectors and sensors. A short literature review is presented, covering various applications of manipulation in SEMs, in order to identify the causes of the reduced precision experienced and to delimit the objectives for this work.

Chapter 2 describes the disturbance problem in a SEM through a survey on various perturbation sources affecting this system. Based on this review, an experimental setup was proposed to directly measure a structure displacement inside the vacuum chamber. The employed sensor, a laser vibrometer, was sufficiently fast to capture the most important dynamic effects in this environment. This setup studied the influence of external mechanical and acoustic disturbances inside the SEM. As consequence, a model for these disturbances considering its frequency spectrum and amplitudes was obtained.

Chapter 3 presents the end-effector taken as case-of study for this work: the FT-G30 micro-gripper. This device was dynamically characterized in air and vacuum, and various differences in behavior related to pressure variation are commented. This highlights one of the common neglected aspects of SEM operation, as the modeling of devices in the vacuum can easily become a complex task.

Chapter 4 covers the nano-positioning control problem, focusing on SEM applications. A short review over control strategies used for nano-positioning is presented. Based on this, and considering the desired performance requirements for this task, two control strategies were se-

lected:  $H_\infty$  control and Extended State Observer based control. These controllers were developed based on the performance requirements, the identified models and the information about disturbances collected previously. Their robustness was tested through simulation and experimentally validated.

Finally, Chapter 5 presents some final remarks about this work and summarizes its contributions. Also, a brief discussion over ideas and perspectives for future developments are proposed.



# CHALLENGES FOR ROBOTICS IN NANO-CHARACTERIZATION AND NANO-MANIPULATION

The importance of nano-technology, the capability of producing and handling micro and nano-sized objects and materials with novel unique properties, is undeniable. It has the potential to restructure current technologies applied for material science, manufacturing, computation, medicine and health, aeronautics, environment and energy, biotechnology, defense and security, as well as transportation and communication [Fukuda et al., 2013]. Miniaturization and nano-technology can impact the production of virtually every man-made object. Figure 1.1 exemplifies some objects that can be found in the nature or manufactured, and where they location in the dimensional scale.

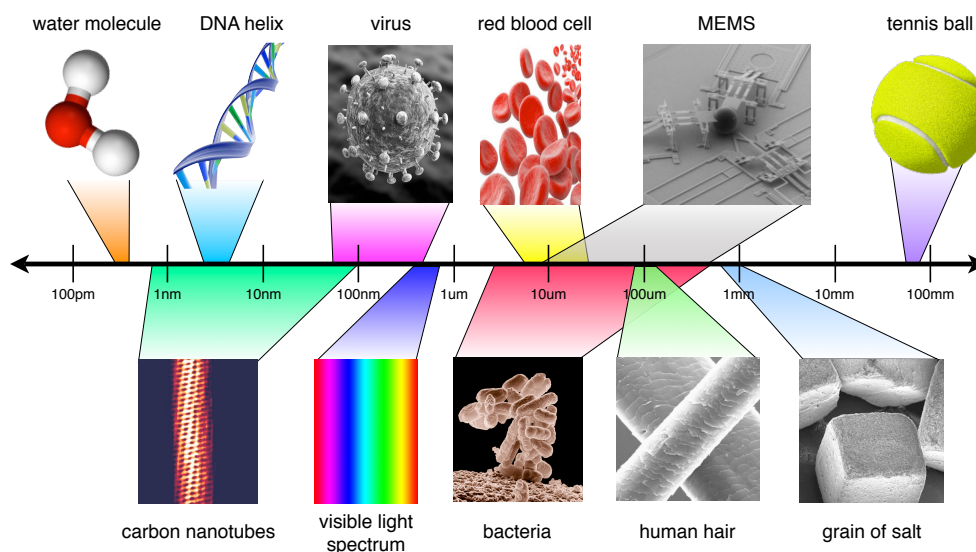


Figure 1.1: Size comparison for various objects, in logarithmic scale.

The International Organization for Standardizations (ISO) defines nano-objects as materials or structures which have at least one of its dimensions in the nano-scale, the range from approximately 1 nanometer to 100 nanometers. They can be classified as nano-plates, nano-fibers and nano-particles when one, two or its three dimensions are in this range, respectively. However, it is not rare to find in the literature the use of these terms for objects with dimensions up to a

few hundred nanometers. Similarly, the term micro-object includes structures with at least one dimension ranging from 0.1 to 100  $\mu\text{m}$ .

The properties of matter at nano-scales are not necessarily predictable compared to those observed at larger scales. The control over materials and the understanding of the phenomena taking place at these scales can lead to lighter, stronger materials and to the creation of devices exploring principles and architectures in ways not possible at macroscopic scales. Recent developments based on nano-technology include miniatures particle accelerators [Peralta et al., 2013], more efficient super-capacitors [Wu et al., 2013] and fuels cells, nanoparticles for recognition and marking of biological material [Otsuka et al., 2012], DNA injectors [Aten et al., 2014], quantum-dot solar cells [Semonin et al., 2011], smaller and more efficient transistors based on carbon nanotubes [Franklin et al., 2012], and various others. Through these technologies, miniaturized devices that integrate multiple functions for various application can be contemplated.

Yet, to achieve this stage, further developments in the study, assembly and handling of micro- and, more importantly, nano-objects is necessary. This chapter expresses the importance of accurate handling and characterization for micro- and nano-objects, and reveal some of the conditions limiting the advances on this domain. These issues are the field of interest for the NanoRobust project, a group effort between various research centers in France. This project aims to tackle some of the existing challenges on nano-manipulation, including the challenge in obtaining the high-accuracies required when positioning structures (samples, end-effectors, sensors), which forms the background for this thesis. Several practical examples of micro- and nano-manipulation from the literature were reviewed, searching for indications that could help identify and evaluate the causes for the presented degradation in these tasks. This information guides and assist in outlining the main objectives for this work.

## 1.1/ THE NEED FOR MICRO- AND NANO-OBJECTS CHARACTERIZATION

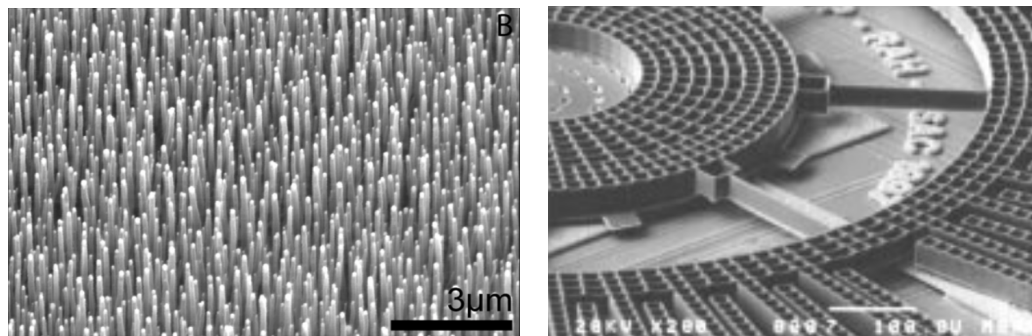
Micro- and nano-structures and materials have been objects of study for many decades. The advances brought by these studies led to breakthrough in miniaturization, the discovery and development of new materials and a better understanding of the phenomena at these scales. Yet, our knowledge over the produced objects and our domain over fabrication methods is far from perfect.

Multiple technologies currently employed in the fabrication of micro and nano-devices originated from existing ones developed for fabrications of macro-scale objects. Methods such as micro-machining and laser cutting were derived from their macroscopic counterparts, and can be traced back to the mid 1960's through the early 1970's. Fabrication methods were developed to follow the rapid growth of the micro electro-mechanical system (MEMS) industry. Today, several approaches can be used to produce a large variety of components and devices. These methods can be classified into two major groups: bottom-up and top-down.

The bottom-up approach is based on using simple building blocks, sometimes at the molecular or atomic levels, to create more ordered, complex, 2D or 3D structures. Chemists and biologists have pioneered these methods, and fabrication strategies include chemical synthesis and self-assembly, such as the DNA origami [Zadegan et al., 2012]. One of the most popular examples of bottom-up approach is the creation of carbon nanotubes, nano-structures which are grown in a controlled way, over a substrate. Figure 1.2(a) shows an example of grown CNTs. The challenge in this method is to control the synthesis and assembly of molecules into the desired structures. Methods based on self-assembly are still being studied and are not yet fully understood

[Cui, 2009].

The top-down approach is that which produces a desired object from a starting, larger one. This approach includes various types of lithographic techniques and nano-imprinting methods to cut, etch and grind a surface into smaller structures with a desired shape, or by adding material to a negative mold. These methods are generally applied in the fabrication of structures ranging from a few hundreds of micrometers to hundreds of nanometers. Figure 1.2(b) shows an example of an electrostatic angular actuator fabricated using top-down strategies, with a honeycomb structure and maximum diameter of 2.6 mm. Recent advances in the fabrication process allowed for the reduction of the minimum feature size to 32 nanometers for beam lithography, and up to 12 nm through dip-pen nano-lithography [Ziaie et al., 2007].



(a) Carbon nanotube forest, grown over a substrate [Gjerde et al., 2006].

(b) Angular electrostatic micro-motor, fabricated through a top-down approach [Horsley et al., 1998].

Figure 1.2: Examples of micro- and nano-objects produces with different fabrication methods.

Despite the current capacity to produce nano-structures in relative large quantities, in many cases their properties are not completely known. Furthermore, fabrication processes may produce unexpected results, a direct consequence of our limited knowledge and control over the various phenomena at this scale. The study and characterization of the produced objects allows to improve both aspects. The following motivation examples can be found in literature:

- Carbon nanotubes (CNT) demonstrate interesting properties for micro and nano-system. They can present one (single-walled CNTs, with diameters between 0.4 and 3 nm) or multiple layers (multi-walled CNT, diameters between 1.4 and 100 nm). The measured Young modulus for those presents a large variation across the literature and is attributed to differences in the measurement strategies, fabrication methods and measurement errors [Fukuda et al., 2003]. Also, single-walled CNTs can be either metallic or semiconductor, each one with different applications, requiring its identification before using them.
- A series of star-shaped structures produced by electron beam lithography, with sizes ranging from 1 to 4  $\mu\text{m}$  and under 50 nm thickness, is shown in Figure 1.3. In the center of the stars, other suspended structures were added (circles and other stars, 500 nm width) [Zhu et al., 2015]. This study considered different fabrication parameters for each individual structure, to observe its influence on various scales. As a result, thousands of relatively complex three-dimensional structures were produced, each one slightly different from each other.

Unfortunately, working with objects at these scales is not straightforward, as the difficulties in safely handling these structures increase with the reduction of their dimensions. Figure 1.4 demonstrates an example of how those samples can be easily damaged. In

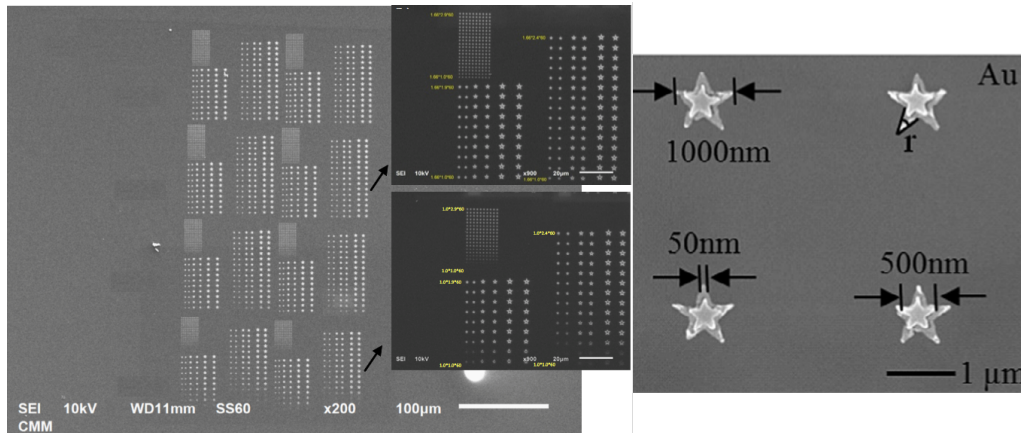


Figure 1.3: Structures produced by electron beam lithography. The smaller ones were 500 nm wide and 50 nm tall [Zhu et al., 2015].

[Abrahamians et al., 2014], the characterization of thin membrane-like structures, close to 200 nm in thickness, is described with the aid of a contact probe. For a successful measurement, the same structure should be inspected multiple times at different points. Despite the high-quality experimental setup available and the attention paid during tele-operated manipulation, early results presented a low success rate as one single failure in a measurement set could permanently damage the sample, preventing the completion of the task. Possible causes for these results included the electrical charging of the sample and the tip as well as difficulties in precise tip positioning, resulting in collisions.

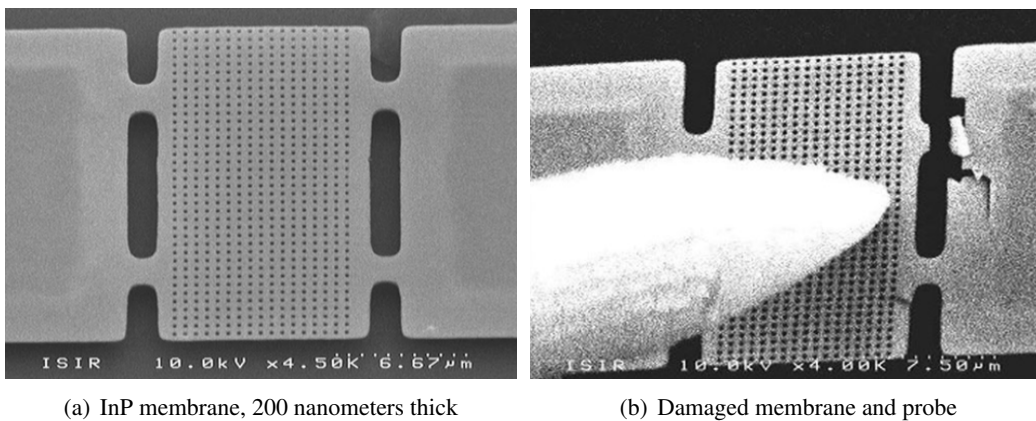


Figure 1.4: Characterization of a nano-structure in the SEM. (a) Sample before starting the measurements. (b) Membrane damaged by the measuring probe [Abrahamians et al., 2014].

There is a demand for more precise, repeatable handling, processing and characterization of nano-objects. As seen in the examples above, the difficulties imposed by scale result in an increased failure rate and a high variability in the obtained measurements. [Sitti, 2001] cites, as a rule of thumb, that the accuracy of actuators and end-effectors should be at least 10 to 100 times better than the size of the manipulated objects, depending on the task. This means that, in some cases, accuracies of a few nanometers or less are necessary. The precise handling of objects at these scales is difficult and involves multiple, complex domains. This is something the NanoRobust project, introduced in the next section, sets to investigate. It aims to improve various aspects of the nano-manipulation, searching to develop a robotic platform with increased

performance, robustness and reliability.

## 1.2/ THE NANOROBUST PROJECT - A PLATFORM FOR NANO-MANIPULATION IN SEMS

When working with nano-objects, the magnitudes of forces, displacements and other quantities often require the use of specialized robotic structures, actuators and sensors. Unfortunately, as seen earlier, some issues arise due to the scale, where various factors such as disturbances, interaction forces and other unknown effects can have major effects on the system, deteriorating its performance. These undesired, less known phenomena contribute to the challenges in studying and characterizing samples and processes at the micro- and nano-metric scales.

The NanoRobust Project consists of a partnership between four research centers in France, to develop and study a robotic platform for nano-manipulation and multi-physical characterization *in situ* inside the scanning electron microscope. The centers involved in this project are:

- Franche-Comté Electronique Mécanique Thermique et Optique - Sciences et Technologies (FEMTO-ST) Institute, in Besançon
- Institut des Systèmes Intelligents et de Robotique (ISIR), in Paris
- Institut de Recherche en Informatique et Systèmes Aléatoires (IRISA), in Rennes
- Laboratory for Photonics and Nanostructures (LPN), in Marcoussis

In this section, the scope and objectives of the NanoRobust project are introduced, aiming to improve the quality of nano-manipulation tasks inside the SEM. Next, a brief introduction about the works commonly performed in SEMs is made, highlighting the importance of precise control over position during nano-manipulation tasks.

### 1.2.1/ COMMON TASKS PERFORMED IN SEMS

Robotic systems are employed to remotely work nano-structures inside a SEM. These systems should be compact, so fitting all necessary components in the limited space of the vacuum chamber is possible without limiting their mobility. More important, the robotic system task is to provide a link between vastly different scales, where quantities in the micrometric, nanometric or even picometric scales should be translated into values more suitable for human interaction, and *vice versa*. With the SEM, large image amplification is possible, making a bridge between sub-nanometric scales and human vision. However, producing and measuring forces, displacements, voltages, and other physical quantities, and linking them to the macro-world, are tasks attributed to nano-robotic systems and their components. In the micro and, especially, the nano-world, the mentioned tasks can become real challenges, as interaction forces, uncertainties and disturbances have an increased influence while precision and accuracy requirements grow to be more strict.

When operating in a SEM closed environment, tasks need to be performed remotely. This usually involves the coordination of various elements (robots, platforms, end-effectors, ...) to achieve a complex goal. During manipulation and characterization inside SEMs, three main steps can be distinguished as illustrated in Figure 1.5:

- Preparation of nano-objects: This task includes identifying, isolating and holding the structure of interest.
- Transport and positioning: Once the sample is held, it may be necessary to move it to a different location, where it can be processed and tested. The precise positioning, not only of samples but also of the tools, is essential to minimize faults in the subsequent steps.
- Characterization/processing: Includes measurements of various properties of the sample, using a large variety of instruments, to obtain its mechanical, electrical and chemical properties. If the component is being processed, tasks such as adding or removing material, assembling components together, and others, can be performed.

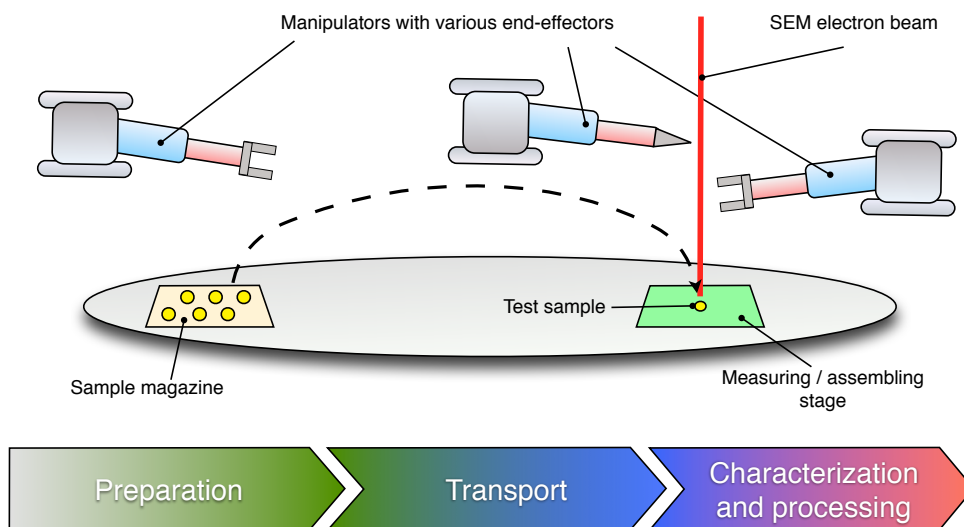


Figure 1.5: Representation of the characterization/assembly workflow of micro and nano-structures in SEM.

The preparation process depends largely on visual surveying in order to identify the working environment, samples and tools. Once a sample is selected, the manipulator should approach with sufficiently accuracy to only capture the target, separating it from the substrate without damage. Various methods can be used to hold the sample, such as grasping (through a gripper) or gluing (i.e. with focus ion beam soldering) the structure on a probe.

Once the sample is ready, the transport and positioning phase can start. The objective is to approach a target location without losing or damaging the sample. In this area, further tasks, such as inspection and assembly can be performed, also requiring precise positioning and orienting of the part. Strategies based on image processing and internal sensors are used to estimate the system position, orientation and forces during this task.

Finally, to characterize the samples, various measurement methods can be performed through probes, embedded sensors and others devices. In some cases, such as during electrical characterization, the contact should be sustained between the sample and probe. This apparently simple task is not trivial at the nano-scale, where contacts may be difficult to detect, and excess forces may damage both the sample and the probe. If the part is being further processed, a good control over its position and the forces is important to ensure the good quality of the task, and to avoid damaging or losing components.

### 1.2.2/ SCOPE OF THE NANOROBUST PROJECT

The manipulation *in situ* seeks to realize a larger portion of the tasks in a same environment, in this case the SEM vacuum chamber. Operations such as sample preparation (selection of a single structure, detachment from the fabrication substrate, thinning of thick layers, ...), its transportation, positioning and finally processing and characterization would be ideally realized entirely inside the microscope with the aid of robotic platforms, manipulators and other computational tools. The *in situ* approach can reduce the risks of contaminating and damaging samples during the transport and preparation phases between different machines. Furthermore, the project aims to expand the information available to operators, improving throughput, robustness and repeatability of tasks requiring extremely high accuracy and precision, such as those often found when dealing with nano-objects.

Commercially available platforms offer complete structures for manipulation and characterization, to be installed directly on SEMs. However, the success rate for these devices is often low, depending of the task complexity, and often present low flexibility, once tools for image, force or hybrid based control are not readily integrated. Robotic operation in SEMs, specially those dealing with samples with nanometric dimensions, often face the following obstacles:

- The attainable resolution and repeatability of sensors and actuators may be not sufficient for the tasks.
- Manipulation strategies containing integration of force/positioning control are rarely exploited.
- The automation of tasks in SEM is still in its early state, with only a few works dealing with image based tracking under this kind of microscope.

To achieve the project goals, the joint efforts of various expertise fields are required. Different strategies should be applied to manipulate, with sufficient dexterity, objects of different shapes and dimensions. Currently employed methods focus on studying particular cases. In addition, implemented systems present a reduced degree of automation and reliability, as most of the manipulation tasks inside a SEM are tele-operated. This project proposes the development of a more flexible approach through the fusion of different sensors to cover the multiple requirements imposed.

The following four main branches of study are encompassed by this project, each dealing with a different aspect:

- **Development of strategies for micro- and nano-manipulation and characterization:** Study of grasping strategies adapted to different objects in this scale and the interaction phenomena occurring (i.e. electrostatic, Van der Waals forces). Includes the development of collaborative manipulation with multiple end-effectors, and the use of different static and dynamic physical characterization techniques to study nano-objects.
- **Robust control for precise manipulation and characterization:** Aims to study the working conditions found in SEMs (noise levels, disturbances, uncertainties) limiting the attainable performance of actuators and sensors. At the micrometric and nanometric scales, systems are sensible to environmental conditions (temperature, humidity, ...) and to disturbances, which imposes addition difficulties when trying to achieve nanometric precision and accuracy. Furthermore, the signal-to-noise ratio can be unfavorable. Typical actuators used

for operations in the micro-world (piezoelectric, electrostatic, ...) can present strong non-linear effects to be considered when developing control laws for those systems. This branch also treats on the development of robust control laws for micro-robots and end-effectors inside the SEM environment, to improve their precision.

- **SEM imaging and vision:** The image processing is essential for the manipulation inside SEMs. This branch deals with some aspects related to the image acquisition process on the electron microscope (i.e. drift, distortion, projection effects). Some imaging parameters may change as function of the amplification. These effects requires a multi-scale calibration and real-time image compensation (accordingly to the image acquisition frequency) to ensure the correctness of the information extracted from it.
- **Visual servoing on SEM:** Intent to perform the manipulation of nano-objects, guiding the end-effectors through visual reference control while taking advantage of the tools developed in the other branches. It includes the selection of interest points to track in images. Objects of interest, such as samples and end-effectors, could be identified in the 3D environment based on a description of its geometry (CAD model of the components). Information from other sensors would help build a more precise representation of the events inside the vacuum chamber, improving the accuracy and reliability of such system.

This project aims to have a direct impact on works dealing with nano-objects, as they could largely benefit from improved reliability and speed during manipulation and characterization. From an industrial point of view, the integration of developed tools to commercially available solutions is possible and desired, contributing to the automation of various tasks in this environment.

The works developed in this thesis are part of the branch responsible for the robust control of manipulators and end-effectors in SEM, particularly their fine positioning to compensate for undesired behaviors. To better understand the uncertainties and disturbances in systems inside the SEM, it is important to know the components commonly used in robotic manipulations in this environment. Additionally, looking into research results in the domain help drawing a more accurate picture of the issues and how they deteriorate the quality of performed tasks. In the next section, the components of common nano-manipulation architectures are introduced, together with examples of their application found in the literature.

### 1.3/ OVERVIEW ON NANOROBOTICS SYSTEM IN SEM

When performing robotic tasks inside the SEM, various components are involved. To achieve the precisions aimed for in the NanoRobust project, all elements in the system possibly contributing to performance degradation should be analyzed. It is important to understand them and consider the advantages and limitations they bring into the system. In this section, the scanning electron microscope and the most commonly used components for manipulation and characterization of micro- and nano-structures are briefly summarized, together with some examples of its applications.

#### 1.3.1/ THE SCANNING ELECTRON MICROSCOPE

The electron microscopes are a popular tool among scientists due to its observation and characterization capabilities for samples ranging from nanometric to micrometric scales. The

family of electron microscopes include scanning, transmission and reflection electron microscope. SEMs are the most popular kind when manipulating micro and nano-structures. They can offer two-dimensional images with a large depth of field, over an amplification range between tens to hundred thousands times, and with relative short acquisition times. This section briefly introduces its working principle and main components, while a more detailed explanations can be found in [Newbury et al., 2003].

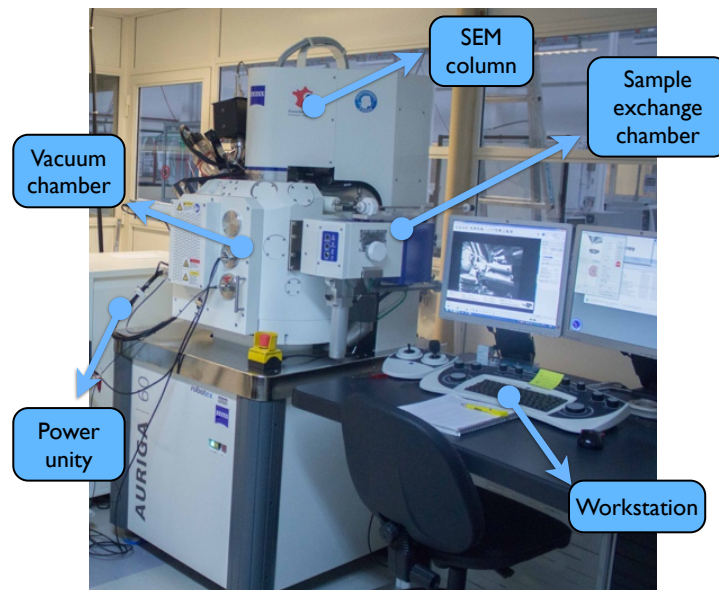


Figure 1.6: Carl Zeiss Auriga 60 scanning electron microscope, used during this work, and its main components.

The SEM is composed by a specimen (vacuum) chamber, a microscope column, a quick sample exchange chamber, a power unity, an operator workstation (shown in Figure 1.6) and vacuum pumps. The column contains a filament responsible for generating the electrons and a set of electromagnetic coils, responsible for accelerating and focusing them into a beam. The beam spot, usually less than 10 nanometers in diameter, is directly related to the image sharpness.

The electron microscopes, differently from its optical equivalents, captures the image point-by-point, by dividing the sample into micro-volumes and irradiating them sequentially with the focused electron beam. Electromagnetic scan coils are responsible for bending the beam, sweeping lines across the sample's surface and defining the scan path. During this operation, the microscope column and the specimen chamber sustain a high-vacuum, normally in the range of  $10^{-3}$ - $10^{-4}$  Pa. This is necessary to minimize beam deflections due to collisions with gas molecules in the air.

#### 1.3.1.1/ INTERACTION BETWEEN ELECTRON BEAM AND MATTER

The interaction between electron beam and matter produces back-scattered (primary) electrons, secondary electrons, x-rays and other particles that are captured by sensors, supplying information about the sample, such as topography and composition.

In an ideal scenario, a focused electron beam with infinitesimal spot area would interact with the first layer of atoms in the sample's surface, resulting in the best possible spatial resolution. In reality, the beam spot has a diameter of a few nanometers and penetrates multiple atom layers

into the sample, resulting in a complex interaction volume. This volume, varying in depth from hundreds of nanometers to a few micrometers, depends on several factors (i.e. sample composition, incident electron beam energy, ...). Figure 1.7 shows, in a simplified diagram, two of the possible interactions between the incident electron beam and the sample: backscattering and the production of secondary electrons.

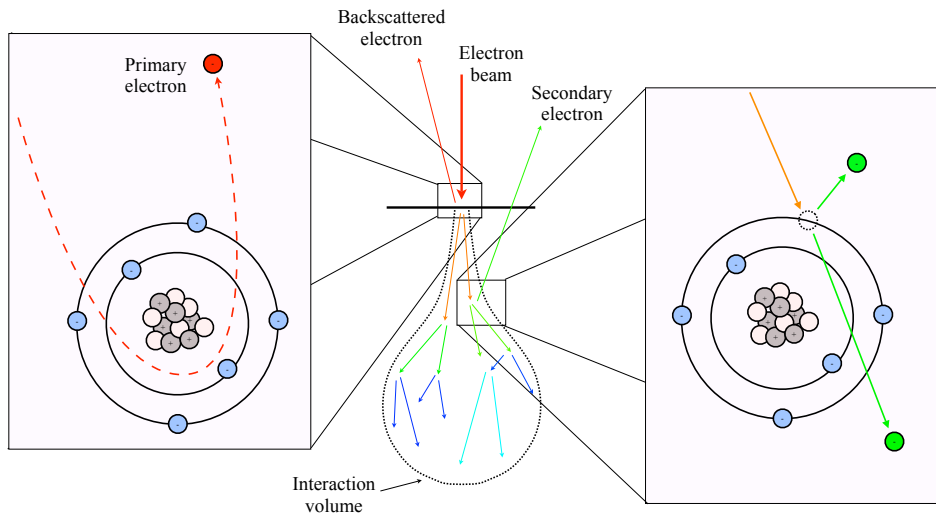


Figure 1.7: Interaction between the focused electron beam with the surface of a sample produces backscattered electrons and secondary electrons.

The scan speed defines the irradiation time for each one of the micro-volumes. Increasing its speed results in faster image acquisition times, ranging from less than 0.1 seconds up to tens of seconds, while producing more noisy images. When entering the sample surface, the negatively charged electrons in the beam interact with protons and electrons in the atom. Backscattered electrons are generated by elastic scattering produced by inter and intra-atomic forces. This process has, in theory, no kinetic energy loss and can, after a series of interactions, alter the electron path sufficiently to cause its ejection from the sample. The probability of backscattering increases with the atomic number  $Z$ , as heavier atoms have stronger positive charges, and decreases as the incident electron beam energy augments.

Simultaneously, inelastic collisions between the electron beam (primary electrons) and atoms occur in the volume, knocking electrons out of the atoms (secondary electrons), with loss of kinetic energy. These collisions propagate in the interaction volume, in a cascade effect, before losing all its energy. However, some electrons can be emitted from the surface before this happens.

The sensors capture these ejected electrons and convert the recovered signal in a numeric value, proportional to the number of recover particles. This process is repeated sequentially for all the surface, and the recovered information is transformed into a gray-scale image.

### 1.3.1.2/ SEM IMAGING CHARACTERISTICS

Through the operation station, it is possible to supervise and modify scanning parameters, i.e. beam energy and size, scan speed, sensors sensibility, and others. These parameters have a direct impact on the image characteristics (resolution, sharpness, contrast between features, ...)

and are selected accordingly to the sample composition and dimensions.

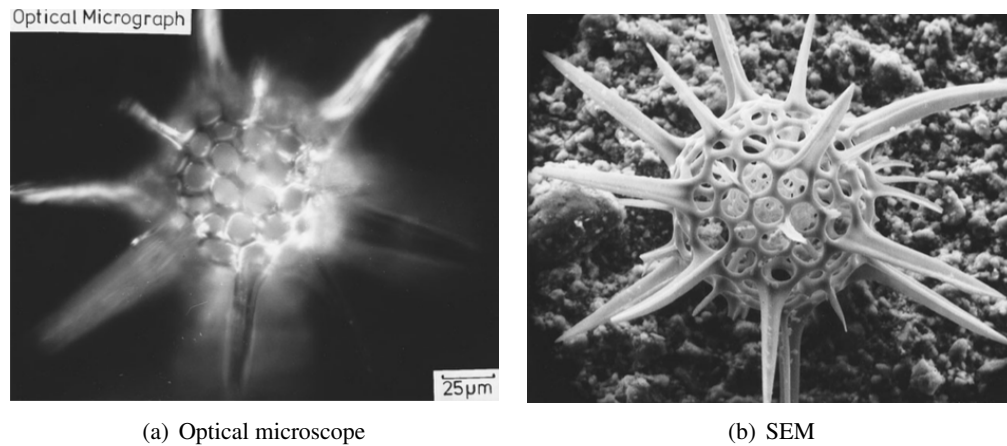


Figure 1.8: Image of the mineral skeleton of a Radiolarian protozoa, acquired with optical and scanning electron microscopes [Newbury et al., 2003].

One of the most used SEM features is the acquisition of high-resolution image. Nowadays, SEMs with resolutions close to 1 nanometer are commercially available. Furthermore, its large depth of field helps to provide more information about the sample. This property is useful for micro-manipulation tasks. Figure 1.8 compares two images, obtained with optical and scanning electron microscopes. The SEM image has a higher resolution and a much larger depth of field, allowing to observe with improved sharpness a greater portion of the structure. This property, combined with the shadows and highlights produced by the electron beam/sample interaction, results in a notion of depth attractive for various applications.

In addition, relative quick image acquisition can be obtained in SEMs, with sampling frequencies achieving tens of Hertz in modern devices. This allows operators to act on elements inside the vacuum chamber, (handling samples, assembling and characterizing components, ...) and obtain a visual feedback that is usually sufficiently quick for most of the desired tasks dealing with static and quasi-static phenomena.

It is important to stress the compromise between speed and image quality. Figure 1.9 helps exemplifying this aspect, where the extremity of a micro-gripper was captured under different conditions. Images A and B contrast the influence of the image acquisition speed considering a static gripper. When a slow scan is used (A), a less noisy image is obtained. An approach for the SEM compromise between image quality and acquisition speed was proposed in [Sievers, 2011]. It explored the idea of increasing the scan speed by reducing the electron beam irradiation time at each point, resulting in a more noisy image. Using algorithms robust to noise and the dynamic selection of the scan area, automatic tracking of objects could be achieved. Still, this method of image processing was limited by the SEM image acquisition capabilities, in this case close to 13 Hz.

Images C and D in Figure 1.9 compare, under fast acquisition speeds, the effects of movement. Image D indicates the fast dynamics of the studied object produces a blurred, incomplete photo of the gripper. The same effect can be observed at large magnifications, where small vibrations limit the accuracy on measurements performed directly by image analysis. The vibration of structures can be an issue when performing tasks requiring positioning precisions of a few nanometers. Methods based solely on image feedback encounter difficulties to achieve this level of accuracy, specially when fast dynamics are involved.

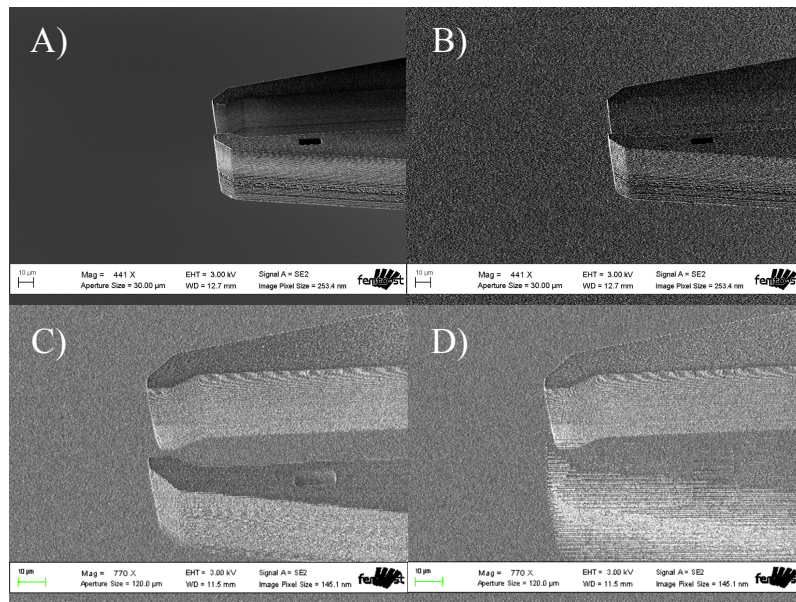


Figure 1.9: SEM images of a micro-gripper extremity.

### 1.3.2/ NANOMANIPULATION SYSTEMS

At the micro- and nanometric scales, robots are used to produce the desired precise displacements. Micro-manipulators are systems that can generate movements with at least micrometric precision. To improve their flexibility, manipulation and testing capabilities, stations can be composed of one or more robots, each with multiple degrees of freedom (DoF). A large working range (up to a few millimeters) is also desired for transporting materials. Nowadays, various structures are commercially available, although customized solutions are not rare to find in laboratories. Figure 1.10 illustrate some examples of nanomanipulation systems.

The Zyvex nProber system [zyv, ] is composed of 8 independent positioning arms and a positioning stage, each one capable of linear movements in the 3 directions. Each positioner is composed of a coarse and a fine positioning unit. By using separate actuating elements, this device can achieve a large fine motion range at the expense of a greater basis footprint [Zhang et al., 2013b]. In this device, the advertised movement resolutions for the positioning arms are under 1 μm in closed-loop, coarse mode and 2 nm when operating in open-loop, fine mode.

To reduce the robot's dimensions, it is common to only employ one piezomotor for both coarse and fine motions. The Kleindiek MM3A [kle, ] micro-manipulator is a 3 DoF arm (two rotations and one translation) actuated by piezomotors in open-loop configuration, with the nominal resolution close to 1 nanometer. To perform more complex tasks, multiple arms are often used. To overcome the lack of internal sensor in devices operating in open loop, methods such as modeling, characterization and visual servoing are often employed. This feedback suffers from shortcomings due to SEM imaging acquisition, discussed earlier, and the challenging of modeling and characterizing the device.

The company SmarAct develops various different robotic structures, ranging from systems with 1 DoF up to complex 16 DoF workstations. As example, a 15 DoF was taken, composed of four 3D manipulators and a 3D stage. This structure, advertised as possessing 1 nm movement resolution when operating in closed loop with an integrated position sensor [sma, ]. The enterprise Physik Instrumente also offers various solutions for nano-positioning problems. One example is

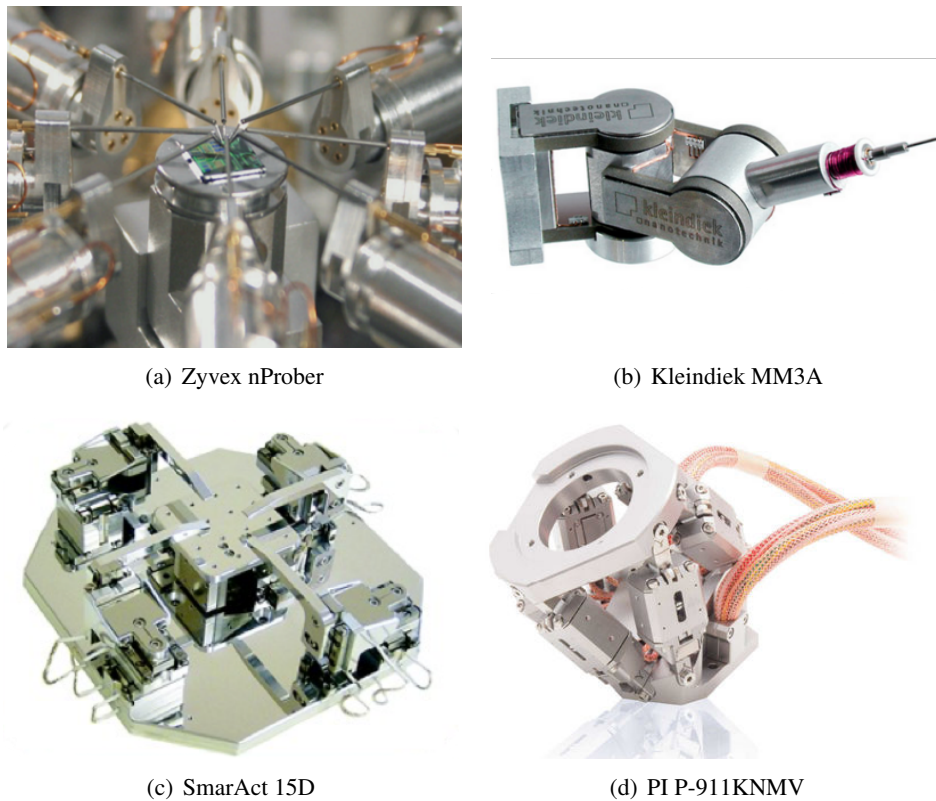


Figure 1.10: Examples of commercially available nano-manipulators.

the P-911KNMV [pi, ] station, a 6 DoF miniature parallel robot with large load capacity (1.5 kg) and a displacement resolution close to 100 nanometers.

When internal sensors are available, other issues may arise. Difficulties in integrating sensing capabilities into small actuators may prohibitively increase its dimensions, the often reduced signal/noise ratios present, drift and thermal influence, are some of the issues limiting its use and performance. The calibration of such sensors in a SEM environment can be challenging, usually resorting to imaging-based methods. Additionally, some internal sensors may not be sufficiently fast. Even though these sensors may achieve higher sampling frequencies than those obtained by SEM imaging, the dynamics of components in these structures not rarely surpass its measurement limits.

Figure 1.11 exemplifies the difficulty in obtaining precise positioning data, using a commercial micro-stage with three linear axis actuated by piezo-motors. The position data was acquired by the device's internal sensor (optical encoder). The stage is controlled in closed loop by its own software. Via a computer interface, users can send reference positions to be tracked and recover its measurements, via specific commands supplied by the manufacturer. To verify the correctness of this results, an external sensor (laser vibrometer) was used, capable of faster acquisition (tens of kHz against hundreds of Hz in the internal sensor) with resolution close to 1 nanometer. The graph highlights that, even at a relative fast acquisition speed, this internal sensor does not fully capture the displacement dynamics.

Various works also explore the design of custom made solutions [Yamamoto et al., 2003, Fukuda et al., 2003, Nakabayashi et al., 2007, Nakazato et al., 2009]. In addition, some researchers have moved towards the development of mobile manipulation systems

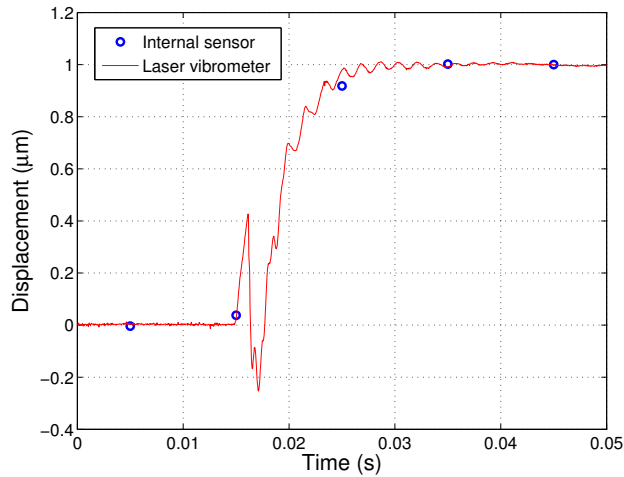
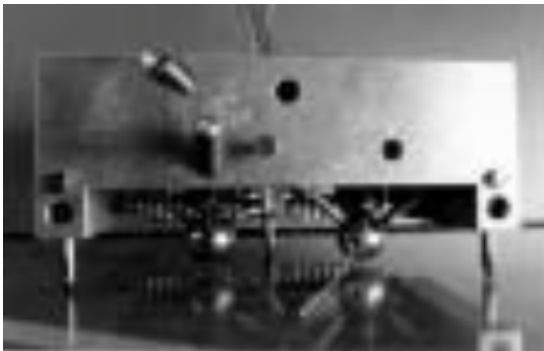


Figure 1.11: Comparison between position measurements given by the internal sensor and by an external laser vibrometer for a step in the desired reference position.

[Fatikow et al., 2000, Schmoeckel et al., 2001, Driesen et al., 2005]. These structures can present a large working range, interesting for real applications and an advantage over fixed designs. In addition, multiple robots can be used at the same time, each one with a specific task (manipulation, fixation, transport, ...). These systems could bring a large flexibility into nano-manipulation and fabrication. In [Fatikow et al., 2000], a flexible micro-assembly station is described to integrate different nano-components into hybrid micro-systems. The workstation was implemented using two robots from the MINIMAN (MINIaturized MANipulation robot) family (Figure 1.12). One of the employed robots (MINIMAN-II) was mobile, and could move freely over the platform by using the stick-slip principle to control its piezoelectric leg [Fahlbusch et al., 1999].



(a) MINIMAN-I



(b) MINIMAN-II

Figure 1.12: Piezoelectric nano-manipulators from the MINIMAN family. Multiple robots were used in [Fahlbusch et al., 1999] to increase the flexibility for this manipulation station. In addition, the MINIMAN-II robot is mobile and could move freely over the platform.

### 1.3.3/ END-EFFECTORS

Various different end-effectors can be coupled to the nano-robotic structures, accordingly to the sample characteristics and desired applications. When operating in SEM environment, additional restrictions are imposed, as these tools should be compatible with the requirements for operation in the vacuum. The most common end-effectors can be classified into two categories: grippers and needles.

#### 1.3.3.1/ NEEDLE TIPS

Needle tips consist of a single, thin element with a sharp point, that aims to reduce its contact area with the sample. Some of the most known example of this group are the AFM tips, although other specialized structures are not uncommon.

When using a single tip, 2D manipulation can be performed by pushing components across the surface. Various works report the use of a AFM tool to roll and slide CNT across surfaces. As results, translational displacement, bending, kinking and breaking were achieved [Hertel et al., 1998, Postma et al., 2000]. Figure 1.13 demonstrates a sequence of 2D manipulation tasks performed over a CNT in a surface using an AFM tip. The red marker indicates a reference point in the substrate. By deforming the tubes, it was also possible to investigate their behavior under large strain and bending [Wong et al., 1997, Falvo et al., 1997].

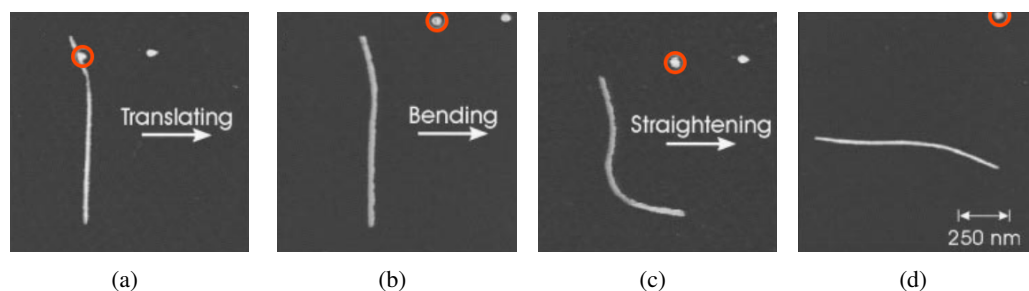


Figure 1.13: Manipulation of a CNT over a surface using a needle-type end-effector [Hertel et al., 1998].

These tools can be also used to cut and indent samples [Meyer et al., 2008]. Figure 1.14 demonstrates a cutting process over a thin (50 nm) polystyrene film using a thin needle probe inside a low-voltage SEM. The article remarks that, despite the brittle nature of this material, the sample does not crack or present further deformation due to the different behaviors of ultra thin films.

When more complex trajectories or 3D manipulation are required, adhesion forces can be used. If the interaction forces produced by the needle tip are higher than the ones generated by the substrate, samples can be lifted. To deposit the structure to a surface, the inverse is true. This behavior brings more complexity to manipulation task with a needle. Some solutions to this problem include the use of additional tool tips [Sitti et al., 2001, Xie et al., 2009], and the control of the tip orientation, reducing the contact area during deposition tasks [Koyano et al., 1996].

In some cases, however, adhesion forces are not sufficient to ensure that the sample will be correctly held. To solve this issue, fixation strategies (through gluing process, electron beam induced deposition, ...) [Yu et al., 1999, Fukuda et al., 2002] can be used. In [Rong et al., 2006], two AFM tips were used to test the tensile strength and Young modulus of nanoparticle chain

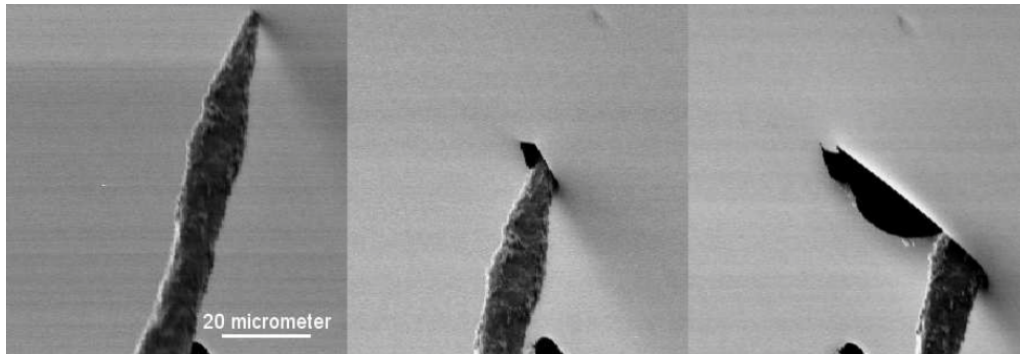


Figure 1.14: Cutting of a ultra thin (50 nm) polystyrene film using a sharp needle. [Meyer et al., 2008]

aggregates (NCA). These chains are formed of branches structures, composed of particles between 1 and 50 nm, and have applications in structure reinforcement, flexible electronics and gas sensors. To test these particles, a soft and a hard AFM tips were mounted on independent manipulators. The NCA were firmly attached to each tip through electron beam induced deposition, and the AFM tips were separated. Through inspection of the SEM images, it was possible to estimate the mechanical characteristics of the sample by measuring deflections in the soft tip. Figure 1.15 shows some steps of this process. In the left image, an individual NCA is captured by the soft cantilever. In the right image, the end-effectors are distanced, elongating the trapped structure.

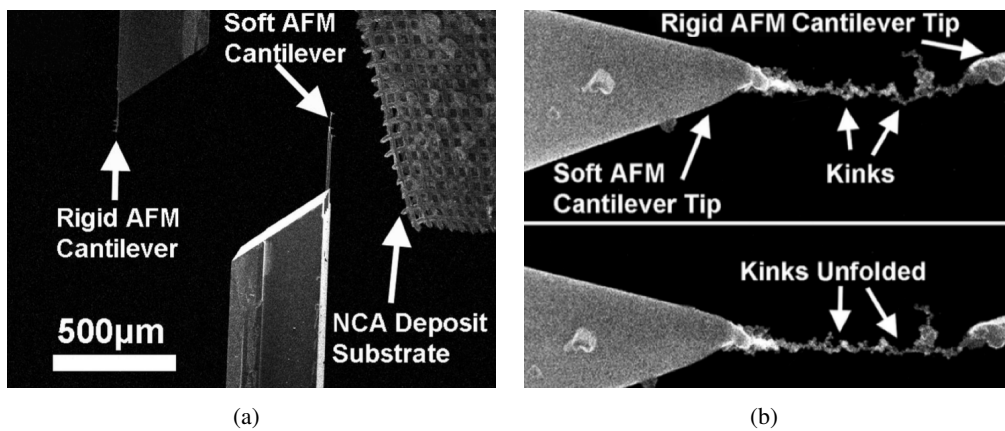


Figure 1.15: Two AFM tips with different stiffness were used to hold and perform traction test on a nanoparticle chain aggregate [Rong et al., 2006].

### 1.3.3.2/ MICRO-GRIPPERS

Grippers are structures composed of two or more fingers, that can be closed around a sample to grasp it. This can be used to avoid the fixation and separation processes often employed when using needles for 3D manipulation. They are the most used tools for handling micro-objects [Clévy et al., 2006], and can be passive or active, with one or more degrees of freedom, and be equipped with different sensors.

The use of passive, compliant grippers, was described in [Dechev et al., 2004, Tsai et al., 2005]. They were designed so that it can elastically deform when facing external forces.

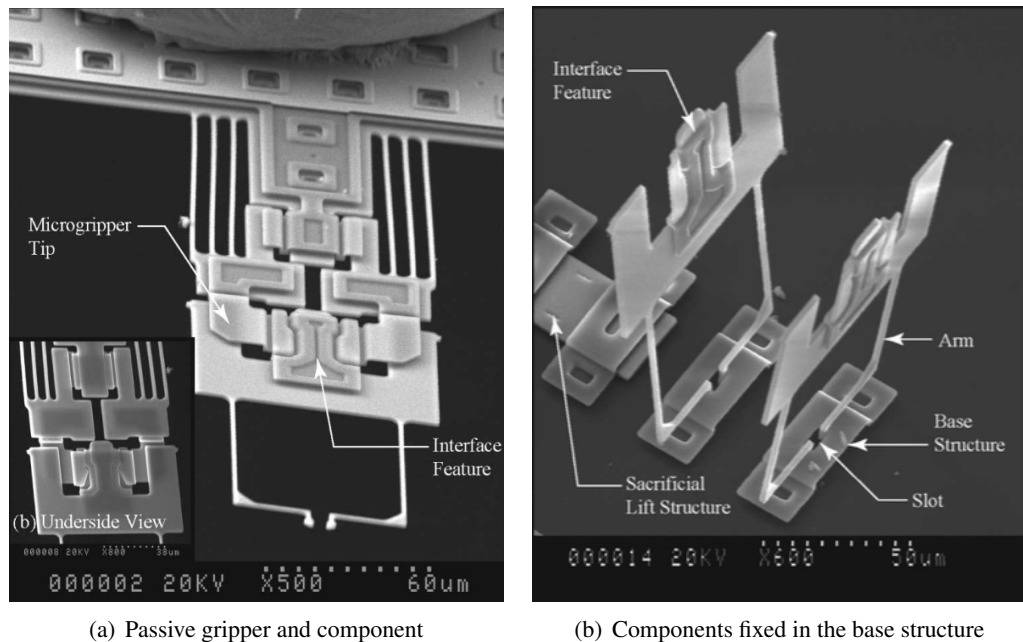


Figure 1.16: A passive gripper used to assemble 3D structures inside the SEM [Dechev et al., 2004].

By adapting the structure of both gripper and sample, a passive grasping and releasing mechanism was produced. This kind of approach has a low degree of flexibility, as the end-effector design was strongly dependent of the manipulated object. In Figure 1.16, an example of this passive grasping mechanism is shown. To grab a part, the manipulator should approach the structure and exert enough force so that the mechanism firmly locks it. The sample could then be manipulated in 3D, and positioned over the substrate, where it was fixed with the aid of another especially conceived mechanism. The fixation force between samples and substrate should be large enough to overcome the gripper's adhesion forces, so that the passive mechanism can open and releases the structure easily.

Although possible to be used for manipulation and assembly tasks, these grippers may require large modifications in the end-effector, in the sample and in the deposit surface. Due to this added complexity, active grippers are more commonly used. In these structures, finger movements can be controlled. Their actuation system can be based on various methods, where the most commonly found are:

- **Electro-thermal:** Takes advantage of the local thermal expansion due to Joule effects. They can be constructed by two principles: the difference in thermal properties between two materials (i.e. bimorph effect on beams) [Chu, 1994, Park et al., 2010] or the difference between dilatation on areas of the same material [Nordström Andersen et al., 2009, Sardan et al., 2008]. These methods allow producing large forces with relatively compact structures. Some designs are capable of active opening and closing movements, what can be convenient for real applications. They often require high temperatures (up to 1000 K), what can be dangerous to the gripper and to the manipulated sample. Also, when operating in different environments (air and vacuum), the actuator presents different behavior due to the thermal dissipation difference. In [Park et al., 2010], a displacement of 250 nm was produced for a given actuator under a constant current in air, while the same input induced a displacement of 900 nm in the vacuum. Figure 1.17 shows the end-effector developed in

[Nordström Andersen et al., 2009], where controlling the current flow in each of the three parallel connectors forming the fingers allows to open and to close the grasp.

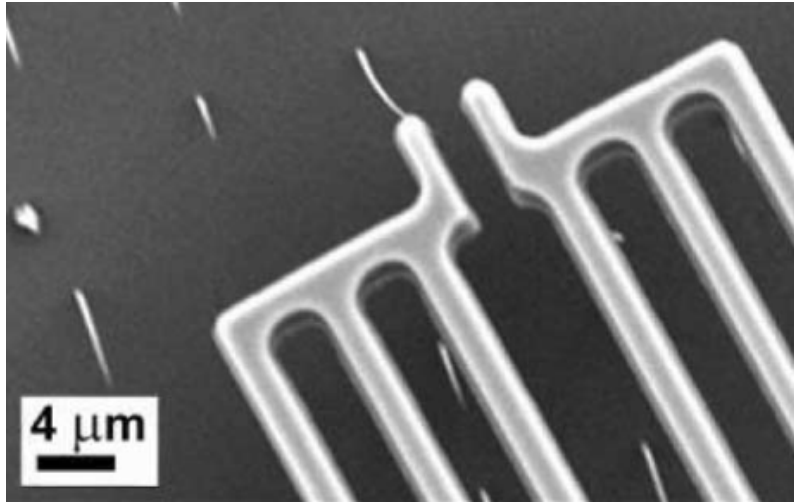


Figure 1.17: Thermo-electric micro-gripper. By heating different parts of each finger, open and close movements could be produced [Nordström Andersen et al., 2009].

- **Piezoelectric:** these materials are capable of transforming mechanical energy into electrical energy. The reverse process is also possible, where an electric potential can generate deformation in certain directions. Piezoelectric grippers can achieve high resolution and fast response times. They are generally built by using piezoelectric actuation to deform a compliant structure [Salim et al., 1997, Goldfarb et al., 1999, Agnus et al., 2005], or by using a bimorph configuration [Haddab et al., 2000, Pérez et al., 2005, Tamadazte et al., 2012, Ivan et al., 2013]. When using piezoelectric actuators, the achievable stroke is usually reduced, requiring multiple piezoelectric elements to be stacked or an amplification system to be included, augmenting the size and complexity of the device. Furthermore, devices using this actuation method can also present hysteresis and creep effects. In [Ivan et al., 2013], a dual bi-morph gripper was developed using an alternative piezoelectric material (lead magnesium niobate - lead titanate, PMN-PT), allowing to achieve 6D of movement (Figure 1.18). This end-effector could produce larger displacements than equivalent constructions, with lower hysteresis effects thanks to the use of PMN-PT. This gripper was only tested in air, although its structure is also compatible for operation in high-vacuum environments.
- **Electrostatic:** use the Coulomb attraction forces produced between differently charged plates, where one element is fixed and the other is free to move. By using this principle, different structures can be conceived. Planar parallel surfaces were used in [Chu et al., 1994]. Due to the nonlinear characteristic for this kind of actuators, multiple equilibrium points can appear, what is a challenge from the control point of view. After a certain displacement, the attraction force increases quickly, producing high accelerations and possible collisions between the two charged plates. This effect is called *pull in instability*. The use of interdigitated comb-drives [Beyeler et al., 2007] can reduce this problem, by keeping the distance between plates constant. The direction of movement in this case is parallel to the plate surface. Figure 1.19 shows a monolithically fabricated micro-gripper, actuated by a comb-drive system. This device could achieve strokes up to 100  $\mu\text{m}$ , and possessed an integrated force sensor, to manipulate and characterize delicate sample.

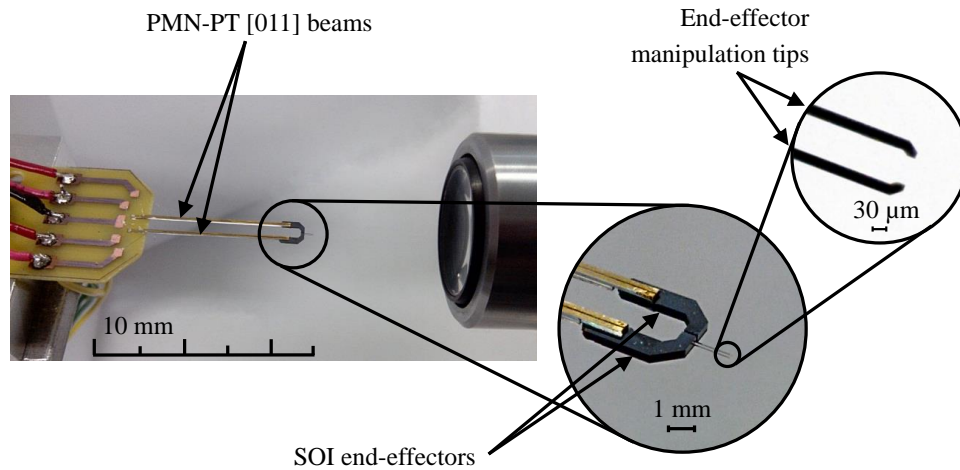


Figure 1.18: Piezoelectric actuated gripper. The arms are composed of dual bi-morph structures, giving the end effector 6 DoF [Ciubotariu, 2015].

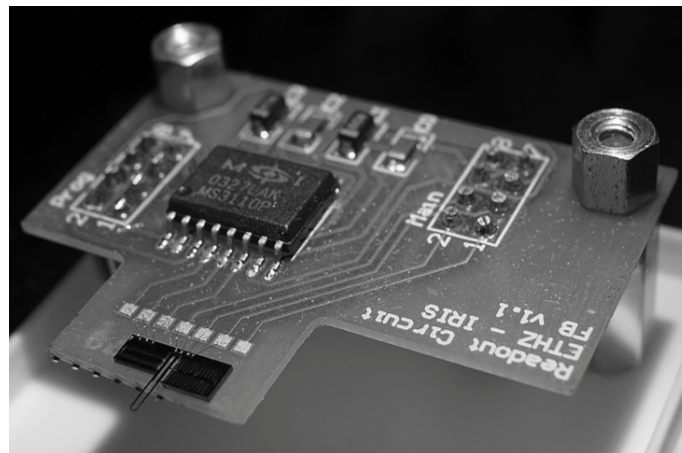


Figure 1.19: Electrostatic comb-drive actuated gripper, located at the extremity of the circuit board (lower left corner of the image) [Beyeler et al., 2007].

Grippers have relatively large contact surfaces interacting with the samples. In addition, the capacity of exert prehensile forces on the object ensures they can be safely held. One of the challenges for this class of end-effector lies on the releasing phase. When the gripper opens, the adhesion forces between fingers and the manipulated object are generally large, resulting in failure to release the part. Various methods aim to facilitate this step, by reducing the grippers contact area or by introducing active releasing methods, such as the repulsive charges or mechanical aid [Arai et al., 1996, Régnier, 2006, Gauthier et al., 2011, Chen et al., 2009].

It is important to consider that, when operating in a vacuum environment, some of the characteristics for those elements can be modified. It is clear, in the case of thermal based actuators, reduced heat dissipation to the environment should be examined to avoid damaging gripper and sample. However, the effects of pressure variation between air and vacuum may also affect these systems and its dynamics, similarly as occurs in cantilever structures

[Sandberg et al., 2005, Mertens et al., 2003], where the environment composition and pressure alter their vibration characteristics. These effects over system dynamics are often overlooked, and can contribute to their performance degradation.

### 1.3.4/ SENSORS

The characterization of the different material and structure properties can be performed through various sensors inside the SEM. They can offer information over position and surface, forces, temperature, currents, ..., and may help during object handling (detecting contacts, deformations and other phenomena).

The SEM itself is, primarily, a powerful sensing device, offering topographical and morphological information about the sample surface, detecting features up to a few nanometers. Through image, it is also possible to estimate the mechanical characteristics (stiffness, Young modulus, ...) of materials, by measuring its deformations under the effects of a known force. The image capabilities of the SEM are also widely explored to offer position information during robotic operation. As seen earlier in this chapter, the compromise between image acquisition speed and resolution is an important tradeoff to be considered. Despite this limitation, the SEM is an useful and flexible tool. It allows studying crystalline structures and its orientation on the surface of specimens (through the use of backscattered electron diffraction [Matteson et al., 2002]) and to acquire compositional information through the use of characteristic x-rays. Modern x-ray detectors are capable of detecting the x-ray emissions of all elements above atomic number 4 at typical electron beam currents used in SEMs [Newbury et al., 2003].

Force and torque sensors are also usual tools to be found during manipulation and characterization tasks. Some end-effectors possess integrated force sensing capabilities [Beyeler et al., 2007, Komati et al., 2014, Mokrane Boudaoud, 2014], (i.e. strain gauges, capacitive and piezo-resistive sensors, optical methods), but dedicated force sensors can be applied. In [Beyeler et al., 2009], a complete six-axis force-torque sensor was demonstrated (Figure 1.20). AFM tips are also commonly used for force estimation, where the well known stiffness for this structure and the measurement of its deformation allows to estimate some sample's characteristics. In some cases, the AFM can be used as both sensor and end-effector.

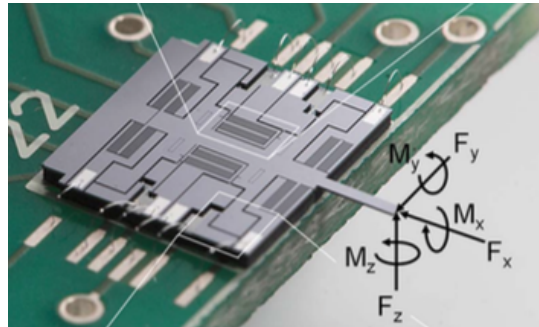
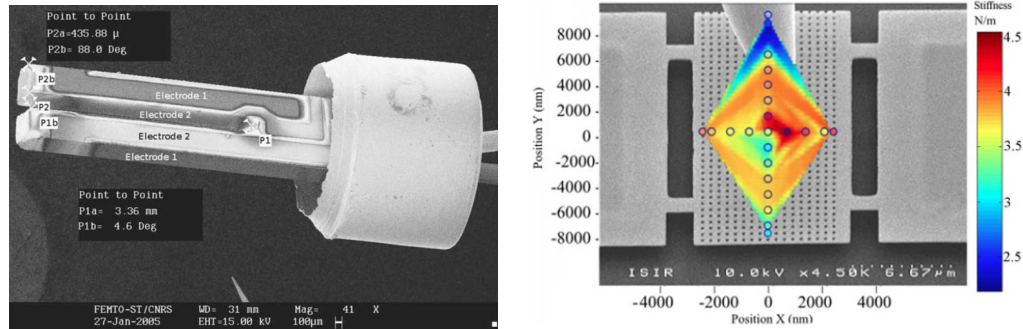


Figure 1.20: 6 DoF force sensor [Beyeler et al., 2009].

The use of tuning forks has been reported in various SEM applications. When operating in vacuum, its quality factor increases drastically, resulting in more precise measurements. In [Friedt et al., 2007], a quartz tuning fork was used as a scanning probe, to obtain a 3D representation of a surface. As this device presents a stable resonance frequency, its variations can be precisely measured. The same principle was used to estimate forces and stiffness [Acosta et al., 2011, Abrahamians et al., 2014, Polyakov et al., 2014] of fragile and flexible materials. Figure 1.21 shows an example of a quartz tuning fork (left) and a possible application for stiffness mapping in a thin membrane surface (right), a task requiring high position accuracy over the 3 directions.



(a) Quartz tuning fork, uses for dynamic force measurement and 3D topography mapping [Abrahamians et al., 2014] [Friedt et al., 2007]. (b) Stiffness chartography of a thin (200 nm) InP measurement and 3D topography mapping membrane [Abrahamians et al., 2014] [Friedt et al., 2007].

Figure 1.21: Tuning fork and application in characterization inside a SEM.

The characterization of electric properties for nano-materials has been explored by various authors. This process can be performed with aid of testing probes [Lim et al., 2005, de Jonge et al., 2003, Hwang et al., 2009, Wei et al., 2010], or over specially constructed surfaces [Suga et al., 2009, Franklin et al., 2012]. The correct positioning of probes and samples, and the need to ensure sustained contact between, are essential. In the case of fragile samples, such as CNTs, the contact forces exert by the probe, pushing the sample against a surface, may cause deformations and alter the results [Yu et al., 1999]. Performing measurements in free space or in measurement stages can reduce this effect. In [Suga et al., 2009], nano-spheres with diameters between 50 and 200 nanometers were deposited over a specially designed junction between gold electrodes (Figure 1.22), allowing to measure the electric conductivity for multiple samples. However, these methods still rely on the careful manipulation of samples.

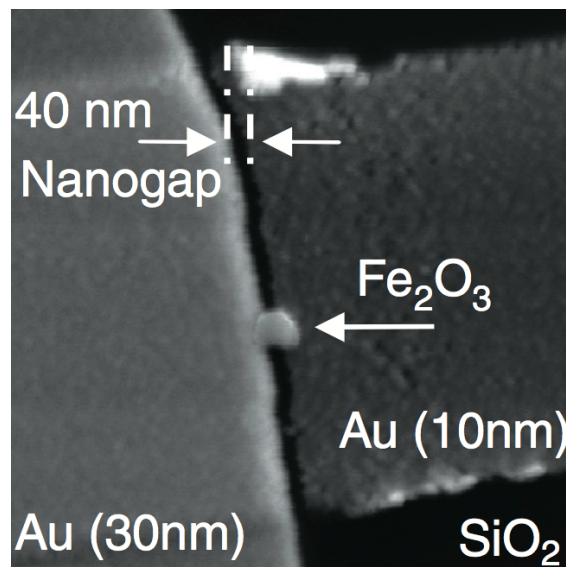


Figure 1.22: Electric characterization surface for nano-objects. It is composed of two gold covered pads, separated by 40 nm. Objects were carefully placed over the gap, and tested for its electric properties. [Suga et al., 2009].

The precise positioning of sensors is essential to ensure the quality of measurement, and

can be challenging when contact with fragile structures, such as nano-objects, is required. Controlling the position and forces exerted by these devices, statically and dynamically, is an important step towards improving the success rates.

### 1.3.5/ EXAMPLES OF ROBOTIZED TASKS CARRIED IN SEMs

To successfully perform the different task required for a complete operation in SEM (preparation, transport and assembly/characterization), the elements previously described (manipulators, end-effectors, sensors, and SEM) are used and combined in different forms. The following examples of real applications help to illustrate the evolution of SEM manipulation and the current challenges faced in this field.

#### 1.3.5.1/ TELE-OPERATED MANIPULATION AND CHARACTERIZATION IN SEMs

In the 1990's, the first reported research for SEM-based nanomanipulation was presented in Japan [Hatamura et al., 1990]. The idea was to obtain a direct relation between manufacturing methods in the macro and micro-world, where objects with dimensions as small as  $10\ \mu\text{m}$  could be handled. It described the use of the stereo scanning electron microscope to provide a magnified 3-dimensional image of the working environment, while two nanorobotic systems, controlled by joysticks and emulating the operator's left and right hand. An schematic of the proposed experimental setup is presented in Figure 1.23. One hand was used to control the tools, while the other held the sample. A scaled feedback on the forces involved during the manipulation of micro-components was available. The article recognized that some nano-manipulation problems were too difficult to be tackled at the time. It highlighted issues related to the need of extended manipulation capabilities and additional challenges posed by operating in an isolated environment, such as tool changing.

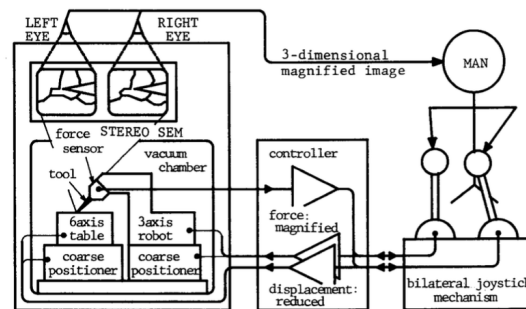


Figure 1.23: Proposed schematics for the first nano-manipulation station inside a SEM [Hatamura et al., 1990].

A different workstation was proposed in [Koyano et al., 1996], consisting of two manipulators (with 5 DoF each) and a workstation (3 DoF). The setup included an optical microscope, placed laterally to offer an improved vision over the interest zone. Improvements in the operation were achieved by using the additional angle of view, and the inclusion of rotational degrees of freedom in the manipulators and in the worktable. The article also proposed the use of different handling strategies to counter adhesive forces that become important at this scale. By cooperation of two tools with different tip diameters, this system could perform pick-and-place tasks of spheres between  $20$  and  $30\ \mu\text{m}$ . Figure 1.24 shows a schematic for the proposed manipulation system (left) and the actual implementation inside the SEM chamber (right), illustrating how most of the available space was cluttered by the workstation's structure.

In the following years, the ideas proposed by these pioneer articles were further developed. Quickly, the study of carbon nanotubes was extensively explored with the aid of SEMs and robotic interfaces. In [Yu et al., 1999], a dedicated platform was developed to investigate the

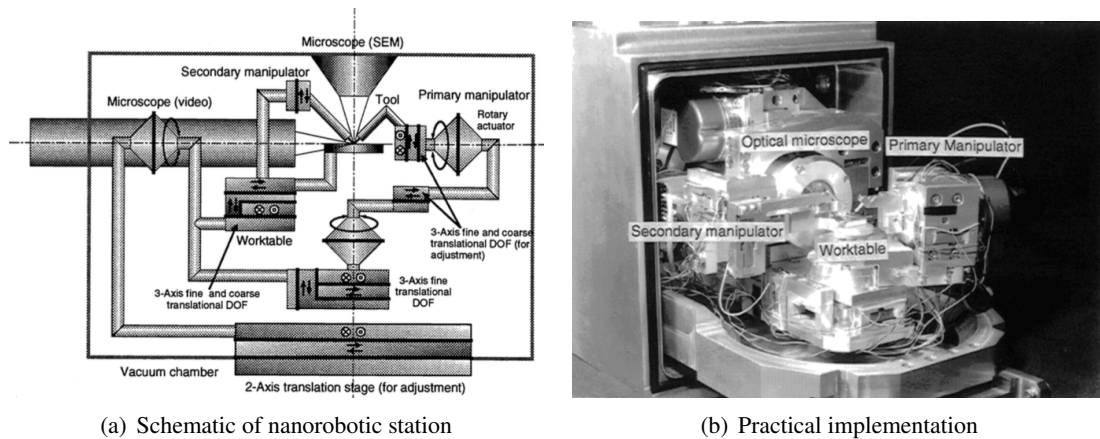


Figure 1.24: SEM nanorobotic station. (a) Scheme for the station, which included 1 moving stage, 2 manipulators and an optical microscope to give lateral vision over the system. (b) Actual implementation, where all the components should be arranged to fit the vacuum chamber tight space [Koyano et al., 1996].

properties of single CNT structures after liberating them from the substrate. It supposed the large differences in CNT characteristics found in literature at the time were due to the sample preparation process employed, that could deform the samples. It proposed to free the samples from its growth substrate and to characterize them in a free space, without the need of posing the CNTs against a rigid measurement surface. Figure 1.25 shows the developed robotic manipulator, with 3 linear and 1 rotational axis, and a SEM image of a carbon nanotube suspended between two AFM tips. This setup was used for simultaneous measurement of tensile strength and conductivity in the samples.

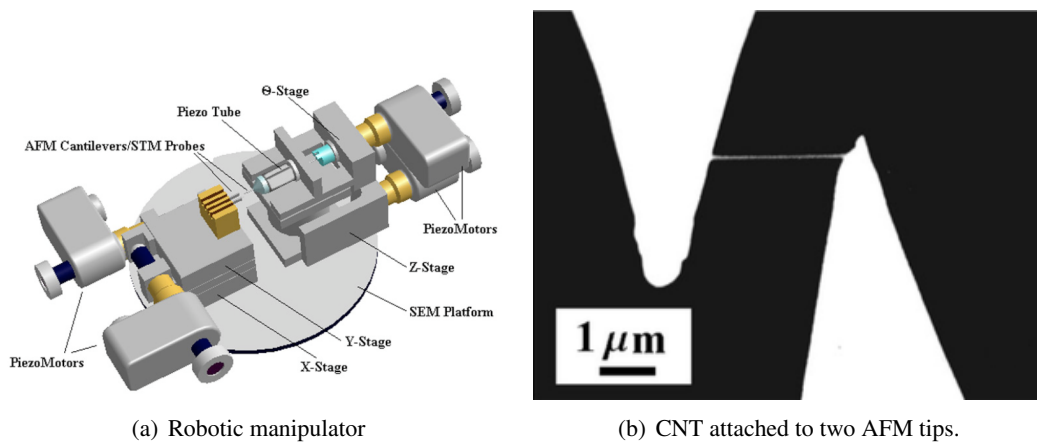


Figure 1.25: Robotic manipulator developed in [Yu et al., 1999], to test CNTs in a free space, without the substrate interference.

In [Akita et al., 2002], two carbon nanotubes were attached to an AFM tip and used as tweezers, to manipulate and characterize other nano-objects. By inducing a small DC voltage on this system, the separation between CNTs could be controlled. The tweezers assembly process was performed inside a SEM by a specially designed working platform, named nano-factory. It possessed three independent stages, each one with four degrees of freedom. Figure 1.26 shows the fabricated tweezers, and how a small voltage induced the nanotubes approxima-

tion. During manipulation, the contact forces between the substrate and target strongly influenced its performance. Other articles dealing with the attachment of individual carbon nanotubes to probe tips indicate that this procedure, when teleoperated, can take up to 30 minutes [de Jonge et al., 2003, Fahlbusch et al., 2005].

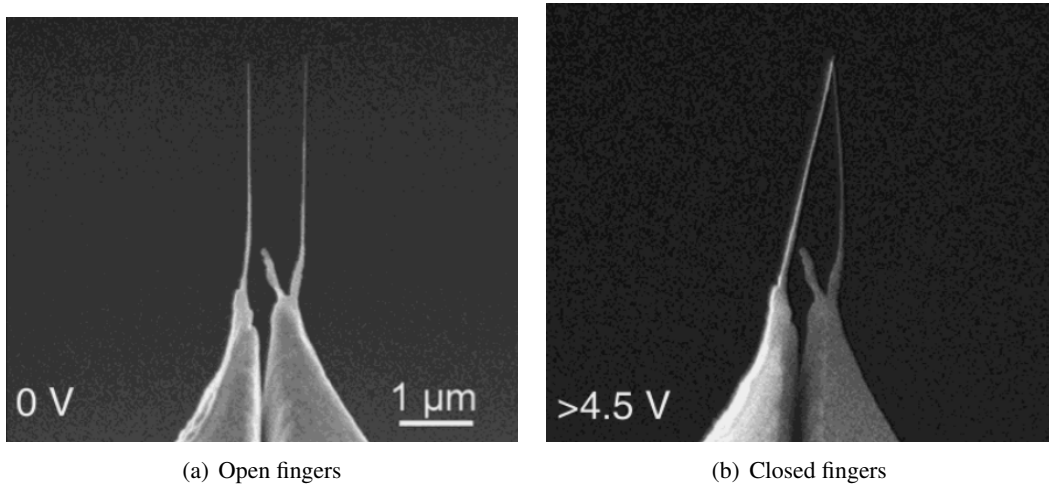


Figure 1.26: CNT nano-tweezer fabricated on an AFM tip. Fingers could be controlled by applying a small voltage [Akita et al., 2002].

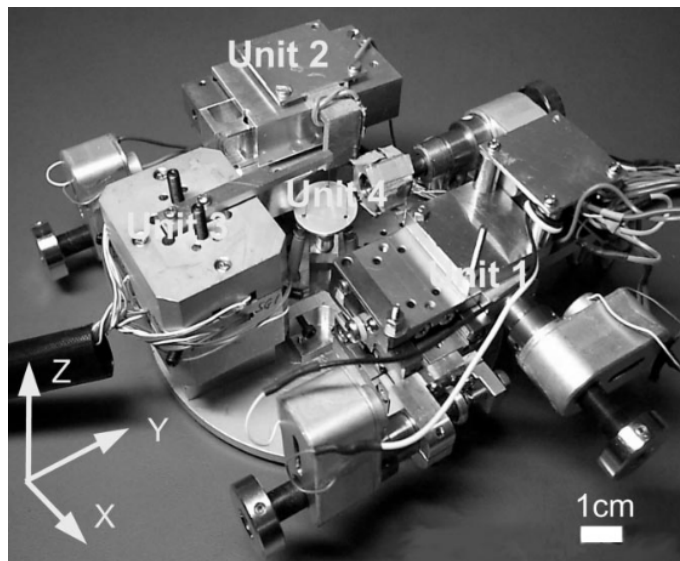


Figure 1.27: SEM robotic station composed of 4 independent manipulators, for a total of 16 DoF. [Fukuda et al., 2003].

In [Fukuda et al., 2003], a robotic station composed of 4 independent manipulators totalizing 16 DoF was proposed. This robotic platform, shown in Figure 1.27, aimed to perform manipulation and *in situ* characterization of nano-structures inside the SEM. These nano-structures were intended to be used as the building blocks for the fabrication of more complex devices. Tests shown adequate manipulation on carbon nanotubes for tasks such as picking and connecting individual structures, as also destructive characterization tests. The different tasks necessary to execute one complete operation were carried out individually and manually. The article concluded that, although numerous operations could be performed by an operator in this nano-laboratory, devel-

opments in task automation and better knowledge over the nano-world phenomena are necessary to further develop the manipulation in SEM.

CNT-based transistors (Figure 1.28) were produced in [Kim et al., 2003], using two commercial piezo-actuated micro-manipulators and carbon nanotubes based probes, by carefully placing the CNTs over pre-fabricated connections pads. The authors remarked that, even as the actuator used in the micro-manipulators possessed nominal resolutions close to 1 nanometer, a minimal attained displacement of 10 nanometers when moving objects was obtained during practical application inside the SEM. This degradation was attributed to the presence of surrounding vibrations. Although no further indication was offered in the article about the relation of external disturbance to the loss in performance, it serves as an important indication that these phenomena can have a significant impact over nano-manipulation systems in SEMs.

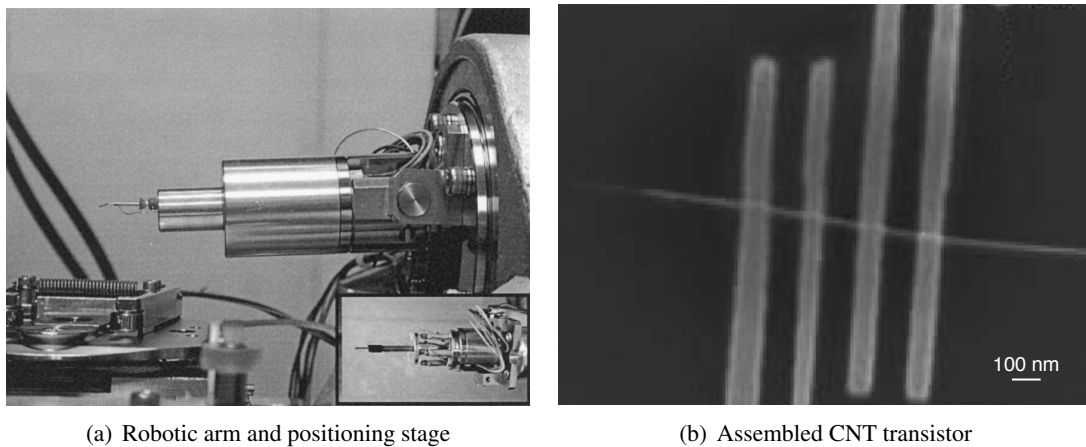


Figure 1.28: Basic CNT transistor, build manually by placing the nanowire over pre-patterned electrodes [Kim et al., 2003].

Another example on the importance of precise assembling is found in [Aoki et al., 2008]. This paper dealt with the construction of 3D photonic crystals from 2D structures. Photonic crystals are composed of patterned structures capable of controlling and manipulating light flow, with large interest in fundamental and applied research. By changing the patterns on its otherwise periodic lattice, new functionalities can be added, allowing light to flow or to be blocked in particular paths, or even creating micro-resonators [Busch et al., 2004]. These 3D structures were built by stacking thin ( $12.5 \times 12.5 \times 0.2 \mu\text{m}$ ) 2D crystals with the aid of two triaxial positioning stages installed inside a SEM. The stacks were positioned with under 50 nm of precision, what was considered adequate for the task, yet far away from the sub-nanometric precision of the piezo-electric nanostages used for positioning. Figure 1.29 shows an example of one assembled 17 layers structure. The three square pillars are used to facilitate the alignment during stacking phase. The assembly strategy required careful tele-operation to capture, transport and deposit correctly each

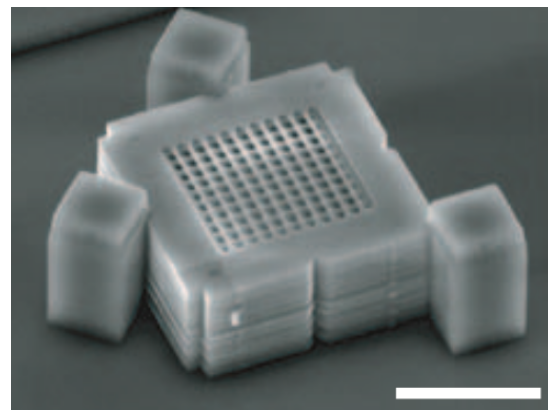


Figure 1.29: 3D photonic crystal, built by stacking multiple planar structures. Scale bar of  $5 \mu\text{m}$  [Aoki et al., 2008].

layer.

These studies were based on tele-operated, static and quasi-static manipulation and characterization of micro- and nano-structures. Despite the various positive results obtained, researchers contemplated the automation of tasks to improve productivity during nano-manipulations, reducing times and the variability induced by human-operated methods. Furthermore, they highlighted the necessity of better understating the phenomena occurring inside the vacuum chamber, including the effects of disturbances, dynamics and interactions between components.

#### 1.3.5.2/ DEVELOPMENT OF AUTONOMOUS TASKS IN SEM

Since the start of manipulation in SEM, researchers pointed the importance of autonomous tasks in this environment to achieve higher performances and speeds. A work dealing with image processing for automated precise positioning is presented in [Gong et al., 2013]. The authors were interested in obtaining the highest accuracy for automatic position of probes, intended to perform electric measurements on electronic devices. The probe tip radius were smaller than 100 nm, and the targets were concentric lines with 130 nm width separated by 125 nm spacings. It employed a high-accuracy robotic platform system with two independent probing systems, each with nominal fine positioning resolution close to 1 nm. After images were acquired and filtered to reduce noise, a visual tracking algorithm controlled the probes in the X-Y plane, to be positioned over selected points. Next, the Z axis was slowly moved, also automatically, until it touched the sample on desired spots. As no forces were directly measured, image processing was used to detect contact between probes and substrate automatically. Figure 1.30(a) shows the robotic station, with two independent 3 DoF Cartesian platforms used for the experiments inside a SEM. Figure 1.30(b) illustrates the automatic nanopositioning task, as seen by the SEM. It shows the test targets (I), followed by the selection of the probing points (II). Next, the system automatically approached the selected spots, in order (III and IV). The article indicated a 100% success rate at low-magnifications (1000x), and values between 80% for X-Y and 60% for Z positioning at large magnifications (80000x), where image drift and noise, shallower dept of field and external disturbances were more evident. Nevertheless, this setup was able to perform the task at least three times faster than a skilled operator.

In [Zhang et al., 2012], a method for fabricating a nanowire field-effect transistors (Nano-FET) inside SEMs was described. The Nano-FET is a highly sensitive device capable of molecular label-free sensing. The response sensitivity for this kind of sensor is affected by construction parameters, such as the number and diameter of employed nanowires bridging the electrodes. To improve the performance, multiple CNT were deposited over the electrodes, connecting them. By inspection, nanotubes with similar diameters bridging the electrodes were selected, and all the other connections were removed (Figure 1.31). With this method, the electrical connection properties across the device presented similar values, which increased performance. By introducing an automatic detection and selection of the appropriate wires, and later automatic removal of unwanted connections by a needle probe, success rates up to 95% were reported, a large gain when compared with a 40-60% rate during tele-operated manipulation. Furthermore, the production time was reduced, from 10 min/device for manual nanomanipulation to 1 min/device by the proposed automated method. One of the critical parameters in the automation algorithm was the minimal distance between the target CNT (to be kept) and the other nanotubes. If this distance was too small, the chance of accidentally damaging the target increased, up to approximately 12% fail rate when a minimal distance of 500 nm was selected. By increasing this minimal distance, the change of failure was reduced. However, this imposed an additional constraint and reduced the number

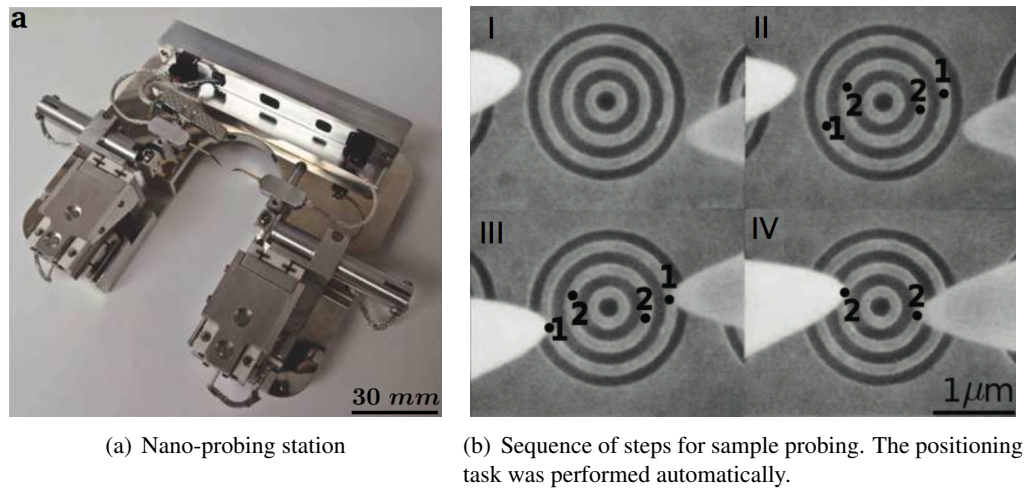


Figure 1.30: Robotic probing station. Combining vision servoing, the testing probes are automatically positioned over the desired spots. Contact between probes and substrate were detected by image inspection [Gong et al., 2013].

of candidate nanowires meeting the requirements. As consequence, a balanced minimal distance ( $1 \mu\text{m}$ ) value was experimentally found, to ensure the automated system would be able to find a successful combination of CNTs connecting the electrodes and the manipulation process had an acceptable risk of failure, estimated to be around 4% in this case.

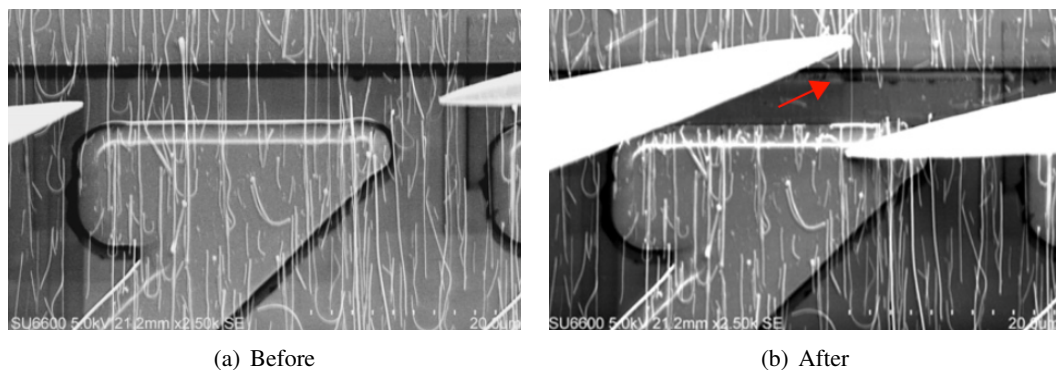


Figure 1.31: Automatic selection and isolation of single carbon nanotubes, signaled by the red arrow in the image. Needle tips were used to sever undesired connections between two electrodes [Zhang et al., 2012].

These examples demonstrate how certain degrees of automation in positioning tasks can be achieved, but limitations on performance do exist when high-precision, fine motions are required. In the examples, positioning tasks find its limitations, indicated by the increase in failure rates, for values that are many times larger than the nominal actuator resolutions. Again, these issues might be associated with the difficulty in obtaining fast, reliable data over the end-effector position, where disturbances and dynamic effects are often neglected. Other approaches were developed, not only using images provided by the SEM but also integrating different sensory information and models, to obtain a more complete panorama over the system's behavior.

### 1.3.5.3/ IMPROVING PERFORMANCE AND PRECISION IN SEM THROUGH THE USE OF MODELS

The use of 3D representations and virtual reality tools were most commonly found in atomic force microscopy operations. This kind of microscope returns 3D information about the surface, but normally its acquisition times are slow (from a few seconds up to minutes). Using the provided information to build a virtual model allows to plan tasks more efficiently, an important feature in this kind of device [Sharma et al., 2005, Korayem et al., 2012]. However, in SEMs, these methods have found so far limited applications. In [Abrahamians et al., 2014], virtual environments were explored to create a replica of the manipulation system (sample, positioning stage and micro-actuators) installed inside the SEM. The virtual model used information from the manipulator internal sensors to estimate its configuration. This allowed to improve the planning in 3D characterization tasks, effectively increasing the throughput and reducing the occurrence of failures. Figure 1.32 shows the virtual robot and how the different components interacted during manipulation.

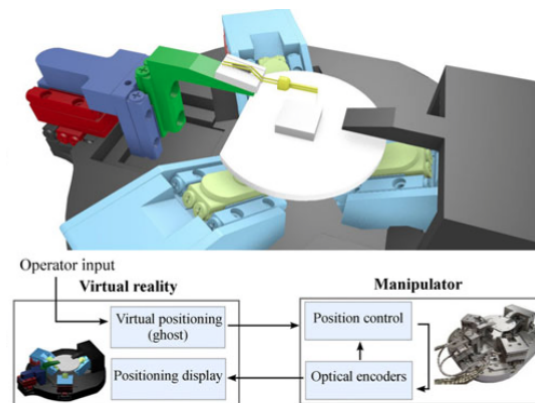


Figure 1.32: Virtual manipulator model and interaction between virtual and real components. [Abrahamians et al., 2014].

To enhance the positioning accuracy on robotics devices, other alternatives to image position are available. The work of [Saeidpourazar et al., 2008] described a method to fuse image and force sensors. It was developed based on a micro-robot without any position sensor. In this kind of robot, feedback information should be entirely provided by images (operator or image processing algorithm), what limited its accuracy and speed, depending on image resolution and acquisition times. To ameliorate these characteristics independently from image-based methods, a force sensor was added to the end-effector. By measuring the interaction forces between effector and sample, distances separating both elements could be estimated based on an interaction force model. The proposed system presented, in simulations, faster responses (less than 1 second) with no oscillations, and allowed a certain degree of control over the end-effector dynamics.

A custom micro-robotic structures was proposed in [Gorman et al., 2006, Gorman et al., 2007]. It consisted of a nanoassembly system to be contained in a chip, composed of four MEMS probe manipulators placed around a central port where samples were placed. The manipulators, with 3 linear axis and actuated by combination of thermal and electromagnetic elements, could be used individually or collaboratively to manipulate and characterize samples. Figure 1.33 shows the design of the structure and a SEM image for one of the manipulators mechanism. The positioning system was characterized, both dynamically and statically, with aid of external sensors in air only, and presented a nonlinear response and under-damped first mode characteristics. In open loop, the position resolution was found to be under 12 nm, with step repeatability around 7 nm for small displacements, with large degradations in those values when large steps were required, what limited its practical application. To improve the results, multiple control strategy were implemented, including the use of inverse models to compensate the non-linearity and a PI controller. The controllers were tested, in simulation only, considering uncertainties of up to 5% in the parametric estimation. Even though good tracking results could be achieved, it was clear that the performances depended on the correctness of the

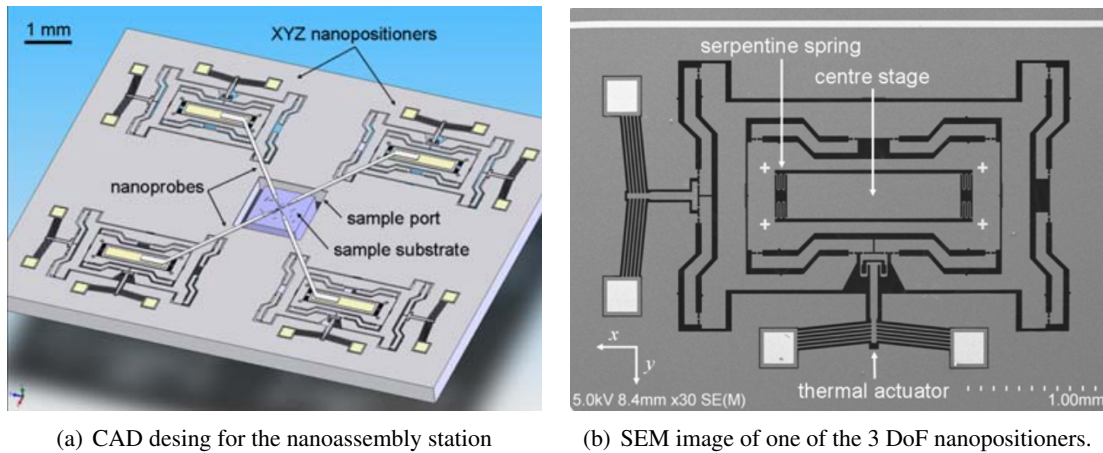


Figure 1.33: Desing of a microscale nanoassembly system to be fully contained on a chip, for operation in small environments, such as the SEM [Gorman et al., 2007].

models.

These examples bring up another issue: how to obtain adequate models considering environment effects over the system? In the considered examples, geometric parameters for the manipulators could be obtained with relative ease, yet the effects of low pressure operation in various components (manipulators, end-effectors, sensors and actuators) were often disregarded.

## 1.4/ THESIS CONTEXT

In the past couple of decades, numerous examples of manipulation, characterization and assembly of micro- and nano-structures in SEMs were reported, covering a large number of fields: physics, chemistry, biology, material science, among others. The evolution of fabrication methods, allowing to produce more complex structures in larger quantities with relative ease, demands for higher throughput, precision and accuracies when handling and examining with these components. In this chapter, the main components employed in SEM manipulations were reviewed, together with real-applications issues and other limitations found in the literature. Based on this information, an approach for improving the position accuracy of end-effectors is delimited.

### 1.4.1/ REVIEW OF THE ISSUES PRESENTED

The manipulation and characterization of micro- and specially nano-metric structures inside the SEM still presents multiple challenges, as seen earlier. A brief summary of the issues found in the literature collaborating to reduce the attainable performance on nano-manipulation in SEMs is presented in Table 1.1.

These issues effectively limit the processing speed of samples. SEM imaging, often takes as a ground-truth to detect displacements, struggle to capture dynamic events and require post-processing strategies that may not be suitable for real-time applications. For this reason, the behavior of manipulators, end-effectors and sensors inside the vacuum chamber is not well known.

As result of these uncertainties and reduced dynamic information, tasks inside the SEM are often limited in speed and in accuracy, in both tele-operated and autonomous/semi-autonomous

Component	Issues
SEM	<p>Operation in the vacuum restricts samples/components.  Limited volume available for instrumentation.  Image acquisition rates of a few Hertz restricts its use to static or slow dynamic events.  Localization in the 3D space can be difficult.</p>
Nanomanipulators	<p>Multiple/complex robots needed to improve the system's dexterity.  Difficult to fully characterize their behavior in vacuum.  Nanometric positioning precision and accuracies depend on image feedback (slow) or internal sensors (limited by resolution and speed, drift effects).</p>
End-effectors	<p>Adhesion and other effects during manipulation.  Subject to disturbances and uncertainties.  Precise information over the positioning/orientation of this device is not often available.</p>
Sensors	<p>Signal-to-noise ratios can be unfavorable.  Precise information over the positioning/orientation of this device is not often available.</p>

Table 1.1: Summary of issues presented during nano-manipulation tasks inside the SEM.

task, with outcomes including damaged samples and components, an increase in operation time per sample and a higher variability in results. If more in depth data about the phenomena harming the performance of components in SEM is available, improved strategies could be implemented for nano-manipulation tasks, bringing a direct gain on the overall system performance.

The project NanoRobust, of which this thesis works are part, aims to improve several different parts of the nano-manipulation task, including image processing, calibration and visual servoing, and also component manipulation and handing. The goal is to perform, with nanometric accuracy, the manipulation and characterization of fragile micro and nano-structures entirely in the SEM environment. By doing so, the risk of damaging and contaminating samples during transport between tools is reduced. Furthermore, performing locally multiple tasks helps to improve the processing speed of parts. In the scope of the NanoRobust project, various expertise fields were gathered together to enhance different aspects for the tasks, aiming to boost speed, accuracy, reliability and robustness of the complete nano-manipulation system.

In this context, this thesis works on exploring directly the dynamic behavior of structures and the existence of disturbances in the vacuum chamber environment, to improve the quality of fine motions performed by end-effectors. By measuring displacements and vibrations inside the vacuum chamber, it is possible to compare results between both air and vacuum environments, helping to quantify its influence on the overall positioning performance. Disturbance effects from the environment were reported to have impact over the attainable performance, yet they have not been deeply studied and understood.

If these information were available, precise positioning tasks inside SEMs could be improved in various stages: SEM room and nano-manipulation design and constructions, and during

the development of dynamic control strategies for an end-effector for high accuracy tasks.

#### 1.4.2/ THESIS OBJECTIVES

This thesis aims to contribute to nano-manipulation by investigating the nano-positioning task inside the SEM. In this environment, various different phenomena occur and can have significant impact when dealing with nanometer precisions.

The objectives for this thesis can be summarized into three main points:

- 1. Characterization of the most important mechanical disturbances that affect components inside the scanning microscope:** The investigation of these effects may allow to better tackle the issue and to attenuate it more effectively. By comprehending its frequency spectrum, systems can be developed with characteristics outside its range. Conversely, if the disturbance sources were known, it could be possible to actuate directly on them.
- 2. Identification of the pressure influences over a micro-actuator dynamic response, and development of a representative model for its dynamics in vacuum:** Structures operating in the vacuum of a SEM can behave differently from when operating in air. These uncertainties can have a large impact when developing controllers and estimation strategies based on models. By comparing a system response in both conditions, it would be possible to reduce those uncertainties in the future.
- 3. Development of positioning control laws capable of improving the system performance in this environment:** Through the better understanding of the mechanisms degrading the performance on high-precision positioning tasks, more suitable control laws can be obtained, integrating fast dynamic responses and real time disturbances attenuation strategies. These strategies can be then explored to achieve higher levels of repeatability and robustness for end-effectors during handling and characterization of nano-objects and fragile structures.

One of the challenges limiting the achievement of these goals is directly related to the difficulty in obtaining precise and, at the same time, sufficiently fast positioning data on components inside the SEM. As stated earlier in this chapter, strategies based on the electron beam bombardment and integrated sensors may be not adequate, due to its low resolution and acquisition speed, unfavorable signal/noise ratios and problems such as heating and measurement drift when operation in vacuum environment. A different strategy should be employed to obtain reliable real-time information about the displacement of the systems. For this purpose, a dedicated vibrometer was used, allowing to explore their dynamics directly inside the SEM chamber.

In the next chapter, the proposed experimental setup is described, along with the study of mechanical disturbances, the first objective of this work towards improving nano-positioning tasks on SEM. Chapter 3 presents the end-effector that was studied during this work: the FT-G30 micro-gripper. This device was characterized in air and vacuum, to study the influence of environment pressure over its dynamics. Chapter 4 deals with the nano-positioning control problem of the studied gripper, focusing on SEM applications. Two strategies were considered during this work:  $H_\infty$  and Extended State Observer controllers, developed based on requirements for SEM applications and the available information over disturbances and dynamic characteristics of the considered micro-gripper. The robustness of these controllers were tested through simulation and experimentally validated. Finally, Chapter 5 presents some final remarks about this work and its contributions, and a brief discussion about perspectives for future developments.



## CHARACTERIZATION AND ANALYSIS OF DISTURBANCE ON SEM

The SEM is, as any other system, prone to the effects of disturbances. Those disturbances can be of various origins and may have significant impact on the precision of tasks developed on this device. Large portion of the literature on this subject focuses on how those perturbations deteriorate the images, with less regard to their effects on the elements inside the SEM. This chapter sketches an overview on the different disturbance sources and their impact on components in the microscope. Later, an experimental investigation is performed, to quantify what are the acting disturbances and their contributions to the displacement of samples in the vacuum chamber. For this purpose, the use of a dedicated vibrometer was proposed.

### 2.1/ OVERVIEW ON SOURCES OF DISTURBANCES OCCURRING IN THE SEM

When acquiring images with a SEM or using it as a base for performing complex tasks such as manipulation and characterization of samples, the best possible performance is desired. However, it is not rare to obtain sub-optimal results for a given device. In imaging, this could mean that the resulting resolution is lower than a nominal advertised value or the failure to reproduce these precisions and accuracies when manipulating objects in the vacuum. This document will focus on the second issue and how those perturbations affect components inside the vacuum chamber (samples, sensors, actuators), without concerning about the problem of image acquisition.

In practice, disturbances acting upon a system limit the achieved results, as environmental perturbation can not be eliminated, only attenuated. The following analysis aims to determine how sensitive the microscope and components placed inside it are to those perturbations and how it can affect its dynamic behavior. To organize the study, sources of perturbation are classified in three main groups:

- Mechanical: this category includes ground vibrations, transmitted from the surroundings to the microscope's base and acoustic disturbances.
- Electromagnetic: varying magnetic fields can interfere with the precise electronic components that allow the microscope to obtain high quality images.
- Thermal: fluctuations in the room temperature can have an impact on the microscope's performance, i.e., producing drifts in images. Furthermore, due to poor heat transfer in the vacuum chamber, sample temperatures tend to increase.

The effects of vibration in SEM imaging are known and are somehow reflected by the manufacturer recommendations over the microscope room vibration levels, described in its manual. For the Auriga60 SEM, from Carl Zeiss manufacturer, ground vibration should be limited to under  $0.04 \text{ mm/s}^2$  for frequencies lower than 9.5 Hz, and under 50 dB for acoustic disturbances with frequencies under 200 Hz. Electromagnetic fields should be limited to no more than 2 mG peak-to-peak for frequencies under 10 Hz, and temperature variation to  $0.5^\circ \text{ C/hour}$  [Aur, ]. The following subsections detail each one of the three disturbance kinds, exemplifying how they can alter a sample's behaviors and corrupt measurements.

### 2.1.1/ MECHANICAL AND ACOUSTIC DISTURBANCES

Mechanical disturbances can affect the microscope through floor (background vibration) and air (acoustic vibrations). The sensitivity characterization of a microscope to background and acoustic vibrations is a complex task, as it depends on the frequency and on each of the microscope's resonances, varying from instrument to instrument. In general, vibrations with frequency above 100 Hz are attenuated, while those from 1 to 10 Hz are in the microscope resonant frequency range and can become a problem [Muller et al., 2006]. Many studies about vibration on SEMs are focused on their effects to the image produced by the SEM, where the microscope's column is disturbed, resulting in low quality images. Figure 2.1 shows the effect of mechanical disturbance applied to the microscope column during image acquisitions. The work of [Vladar, 2003] summarized some practices and rules of thumb when preparing a room to receive a SEM. It recommended placing the microscope in an area with reduced structural vibration (ground floor or underground), and distant from air currents and water piping, avoiding movements that will degrade the images. However, no remark was made about the effect of vibrations on the elements in the vacuum chamber interior.

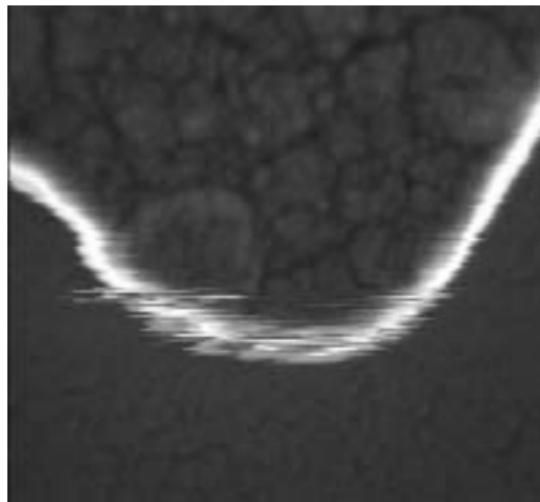


Figure 2.1: Effect of a short mechanical impulse to the SEM electron optical column (500000x amplification). From [Vladar, 2003].

Vibration measurement and its frequency analysis provides an efficient tool to detect, identify and isolate the noise (cooling fans, air conditioning, human speech, ...) and vibration sources (heavy machinery, vacuum pumps, human interference, ...). If those sources can be identified, it would be possible to eliminate them (turning off unnecessary equipment, rearranging instruments, ...) or to reduce their effects by adding acoustic shielding to attenuate a specific frequency band of interest. The later solution is generally more expensive and time consuming and implementing it can be challenging for low frequency acoustic noise. However, some disturbances are not constant, and do not work in a specific frequency range. This is the case of air currents, commonly caused in the laboratory environment by air conditioning system. Those distortions can be difficult to detect, as they are produced by turbulent air displacements and do not present themselves in a single band frequency of the spectrum.

If not taken into consideration, those disturbances can have an important impact in the performance of manipulation tasks. A few articles found in the literature can help to describe the

importance of those phenomena in practical SEM applications.

In [Kim et al., 2003], the electrical characterization of carbon nanotubes with diameters ranging from 30 to 50 nanometers was performed inside a Field Emission SEM. The tools were positioned with the aid of two commercial micro-manipulators, actuated by high-precision piezo-electric motors. While the nominal step size of the motors can be adjusted between 1 and 200 nm, the practical attained accuracy was close to 10 nanometers. The article concluded that external disturbances caused the response degradation, without further investigation on its possible sources.

Vacuum pump vibrations on images were studied in [Jung et al., 2012]. It remarked that, for high magnifications, these disturbances were transferred to the chamber despite the use of vibration suppressors. Through an external accelerometer, vibrations in the range between 0.05 to 500 Hz were measured. It demonstrated that passive anti-vibration dampers, installed on the SEM table and the vacuum pump, were not enough to ensure high-performance imaging at large magnifications (40000x or more). To attenuate those effects, an image filtering method was proposed, based on the measured vibration frequencies.

A different approach was proposed in [Iwaya et al., 2012] through the use of an active vibration damping system. The authors sought to reduce the influence of low-frequency vibrations transmitted from the ground to the vacuum chamber. Using accelerometers to estimate the disturbance frequencies acting in multiple directions, different foundation slabs were compared to infer and improve their vibration damping characteristics. Also, electronic components and human operator interference, that could produce acoustic noises, were re-positioned to minimize their effects on the microscope. Despite its effectiveness in reducing low-frequency disturbances, this method requires a large effort, including physical modifications to the SEM room, such as adequating its foundation bed and installing soundproof walls.

More recently, the work of [Pluska et al., 2015] studied the effects of acoustic influence on the focus ion beam (FIB). Through the use of an external noise source, the identification of resonant frequencies for the microscope's column, the FIB gun and the positioning table was achieved. It remarked that the SEM and its components can be a source of disturbance, and compared the noise levels before FIB installation (40 dB) and after (68 dB during its operation), corresponding to a 25 times increase. As conclusion, the study highlighted the microscope sensitivity to acoustic noises as it may contain significant harmonic components matching those of the mechanical elements of the instrument. In this case, oscillations of 90 nanometers were reported. In the reviewed literature, this was the first demonstration of external disturbances having effects on components inside the SEM, distinguished from the imaging system.

The reviewed literature indicates that external mechanical and acoustic vibrations play an important role in applications that aim to achieve nanometric precision. Besides the environment natural disturbances, SEM components can also contribute significantly as perturbation sources. While vibrations transmitted by the ground are limited to low frequencies (up to a few hundred hertz), acoustic noises may have a much larger band (up to 20 kHz). When these disturbances match the resonant modes of mechanical components inside the microscope, resulting vibrations can become sufficiently large and thus surpass acceptable levels for the task.

### 2.1.2/ ELECTROMAGNETIC DISTURBANCES

Environmental sources of alternated current can affect the SEMs imaging acquisition process, by distorting the electron beam path or the signals applied to the scanning coils caus-

ing periodic deformations in the registered image. In [Fatikow, 2007], the use of high-resolution SEM images as an alternative to on-board sensors for identification and manipulation of micro and nano-sized parts was reviewed. Taking images as ground truth when performing tasks in the microscope is a common practice. However, these strategies can be limited by noises, low acquisition frequency and the movement of objects in the scene (drift). In many cases, the images are used for measurements and even for calibration of sensors, what can lead to incorrect or imprecise results.

In [Muller et al., 2006], alternated current electromagnetic interference (EMI) on the scan coils of a scanning transmission electron microscope (STEM) was studied. The microscope column should shield radio frequency noise from the electron beam, but lower frequencies (less than 3000 Hz) are less effectively screened. To quantify the EMI, a large coil was built and placed at approximately 1 meter from the microscope, and the generated field was measured close to the microscope column. Images were recorded in the presence of induced alternated fields (32 mG peak to peak) as well as in their absence (0.2 mG peak to peak). The scanned structure, five unit cells of  $SrTiO_3$  grown on silicon, was 1.96 nm thick. The results shown in the figure exemplify these distortions caused to the images by large magnetic fields. For this set-up, average deviations of 48 pm/mG (peak-to-peak) were measured.

The effects of alternating magnetic fields were analyzed in [Pluska et al., 2009]. During this study, a separation between direct beam interference and coil signal distortion was made. It concluded that perturbations acting directly on beams were affected by the electron energy, where high energies are less susceptible to path deviations, while interference in the electromagnetic coil signals distorted the beam path, regardless its energy. An example of those effects are shown in Figure 2.2. A disturbance along the  $X$  scanning axis  $d_x$  was induced to the system, producing periodic deformations close to 200 nm peak-to-peak in the image.

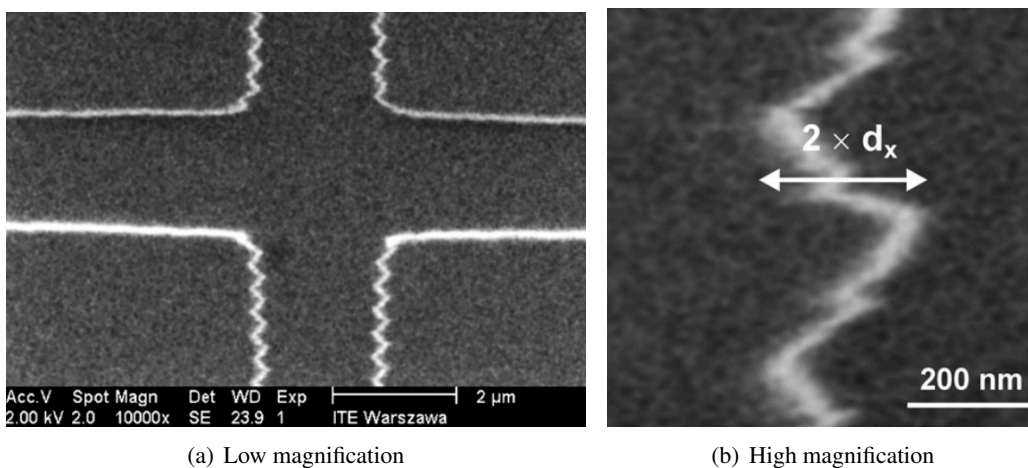


Figure 2.2: Effect of induced EMI disturbances on images [Pluska et al., 2009].

Electromagnetic interference can be difficult to detect and to distinguish from other disturbance sources. In [Vladar, 2003, Pluska et al., 2009], some characteristics of an adequate SEM room are described. They include avoiding placing the microscope in a room susceptible to electromagnetic and radio-frequency interference. If this is not possible, it is recommended to use active and passive shielding techniques to reduce these effects. It also suggested removing metal objects from the room, such as chairs and tables, as moving metallic masses can change the EM field around the SEM. Electric cables should be shielded, and positioned far from the microscope's column, as they can produce significant interference, depending on their currents.

Overall, the degradation over the SEM operation, due to EMI documented in the literature is related to the image acquisition process and is not a major concern on this thesis scope.

### 2.1.3/ THERMAL DISTURBANCES

The effects of temperature on devices constitute a problem when considering objects of micro or nanometric dimensions, as its measurement becomes complex, and the precise data acquisition can be affected by the sensor. In addition, systems in vacuum have a reduced heat exchange and its accumulation can be an issue. A particularity of SEMs lies on electron beam effects during image acquisition. Those accelerated particles, constantly colliding with the sample, can also generate considerable heat. Those thermal-related phenomena are discussed in the next subsections.

#### 2.1.3.1/ THERMAL NOISE

Johnson-Nyquist noise [Johnson, 1928], also known as thermal noise, is used to describe how temperature can induce random vibrations in a lattice structure. It is most commonly applied to electric circuits, describing the voltage fluctuations at the terminals of a conductor or semi-conductor material at equilibrium. As the noise is random in nature, it can affect the whole frequency spectrum [Stievater et al., 2002]. Its power spectral density  $V_i^2$  is given by Equation 2.1, and represents the expected voltage variance per Hertz of the bandwidth:

$$V_i^2 = 4k_B T R \quad (2.1)$$

with  $k_B$  the Boltzmann constant,  $T$  the absolute temperature in Kelvin, and  $R$  the resistance of the electronic circuit. The same principle can be applied to infer mechanical-thermal noises. In this case, the spectral density for the thermal driving force  $F_i^2$  is given by:

$$F_i^2 = 4k_B T R_{mech} \quad (2.2)$$

but considering  $R_{mech}$  the mechanical resistance (damping). In [Babic et al., 2003], the Young modulus for CNTs are estimated based on the mechanical-thermal induced excitation, relating the sample length and vibration amplitudes. For a CNT of 6  $\mu\text{m}$  length and 80 nm diameter at room temperature, displacements close to 2 nanometers were measured experimentally.

#### 2.1.3.2/ THERMAL EFFECTS ON SENSORS AND MICRO-STRUCTURES

The measurement of temperature variations inside the vacuum chamber is a complex challenge, even more difficult when dealing with microscopic samples, as their dimensions limit the direct non contact and contact method usage. Due to the reduced heat exchanges with the environment, it is important to consider the contribution of different elements to the heating problem (i.e. extended use of the electron beam, Joule effect on components, ...).

An example of how heat can compromise components was shown in [Toda et al., 2010], where a comparison on the pressure effects for the heating dissipation of bi-material cantilevers was performed. In this study, pre-bent silicon nitride and gold cantilevers (with dimensions 400  $\mu\text{m}$  x 20 – 70  $\mu\text{m}$  x 0.4  $\mu\text{m}$ ) were used as high-precision temperature sensors. By heating the cantilever's tip with a laser diode of varying power (from 0.5 to 13 mW) and measuring the resulting

deformation of the beam, temperature variations could be estimated. In experimental tests, an incident power of 4 mW resulted in a tip temperature increase from 19 to 143 °C in air, while the temperature at the cantilever's base only rose a few degrees. This produced an average radius variation of the pre-bent cantilever of a few  $\mu\text{m}$ . Increasing the incident beam power to its maximum produced an average radius variation of approximately 100  $\mu\text{m}$  in air. Performing a similar study in the vacuum revealed that, for a beam incident power of only 2.5 mW, an average radius change of 400  $\mu\text{m}$  is achieved, while a 5 mW incident beam causes permanent damage in the sample. This illustrates the importance of temperature exchanges with the air, and how accumulated heat can quickly become a problem when operating in vacuum environments.

The effects of heat in an optical encoder during long operation inside the SEM were also noticed in [Zhang et al., 2013a], where the axis of a 3 degree of freedom Cartesian micro-robot was analyzed in vacuum through image processing. The sensor characterization performed indicates a minimal resolution of 2 nm, while the nominal value indicated by the manufacturer was 1 nm. Also, the authors remarked the existence of long term drift. Figure 2.3 demonstrates this effect after long usage, attributed to the thermal expansion of the optical scale. In the tests, position values were measured by the encoder at 100 Hz for 10 minutes, with no action from the actuators. In this setup, the measured drift was approximately 1.2 nm/s. The averaged encoder accuracy for the device was within 98% of the travel distance.

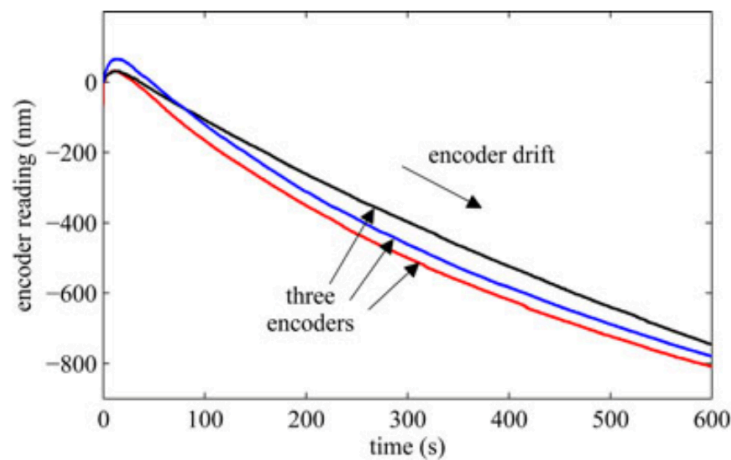


Figure 2.3: Drift quantification of optical encoders on long usage inside the vacuum chamber [Zhang et al., 2013a].

Some encoders allow a power save mode, where the sensor power supply is disabled most of the time, and activated in sparse time intervals or when a movement command is issued. This option is useful to reduce the generated heat [Sma, 2013] at cost of degrading the reaction time, as the sensor needs to be re-activated.

A similar study was performed in [Jasper et al., 2010], describing the use of a linear nanopositioner from Physik Instrumente, based on stacked piezoactuators, to achieve nanometer resolution with a large working range. For closed loop positioning, a capacitive position sensor was used. The downsides of this measurement strategy include frequent recalibration for long-term drift compensation, due to thermal variations. The difference between the sensor measured positions and image analysis indicates a deviation of up to 15 nm in precision positioning tasks.

The effects of temperature fluctuations on cantilevers in low-pressure environments are described in several articles. In [Mertens et al., 2003], the use of cantilevers as precise thermal

sensors was studied, describing how small temperature variations ( $\Delta T = 0 \dots 30$  K) can affect the frequency response of bending beams (silicon nitride cantilevers, dimensions  $200 \times 20 \times 0.5 \mu\text{m}$ , with added gold layers of different thickness). In experimental tests, variations smaller than 0.5% in the first mode were found for the defined  $\Delta T$ , and a relation between temperature and Young's modulus  $E$  was established. The relation  $\Delta E/\Delta T$  could be considered linear for mono-material beams, while on bi-material cantilevers a nonlinear behavior appeared. This can be related to the difference of thermal expansion coefficients between the two materials, resulting on changes on the bi-material cantilevers deflection and frequency. The results are summarized in Figure 2.4, where four cantilevers (A for a mono-material and B, C and D for bi-material, with increasing gold coating thickness, cantilevers) had their deflection and frequency measured under temperature variations.

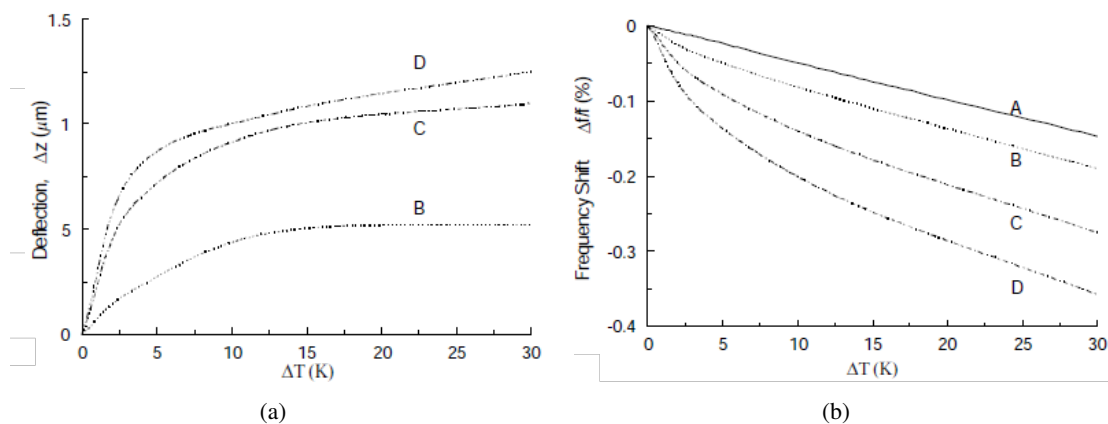


Figure 2.4: Deflection (a) and first resonance frequency (b) as a function of temperature for mono (silicon nitride, Cantilever A) and bi-material (silicon nitride with gold coating of different thickness, Cantilevers B, C and D) samples. [Mertens et al., 2003].

In a related work, [Sandberg et al., 2005] analyzed the influence of temperature on the first five resonant modes of cantilevers. Two silicon dioxide cantilevers (dimensions  $195 \mu\text{m} \times 10 \mu\text{m} \times 850 \text{ nm}$ ) were tested. One of them was coated with a thin layer of gold (400 nm), and the differences in its behavior due to temperature changes (from  $30^\circ$  to  $80^\circ$  C) were observed. Figure 2.5 demonstrates how the resonant frequencies change as functions of temperature for (a) the uncoated and (b) coated cantilever.

Material properties, such as the density  $\rho$  and the Young's modulus of elasticity  $E$ , are linked to the temperature. For uncoated cantilevers, the linear dependence between frequency and temperature was clear, in accordance with previous results in the literature. It was possible to verify that the thermal expansion effects are small and most of the time negligible for these samples. The elasticity thermal dependence was presumed the dominating effect in this change. For coated cantilevers, the behavior of different modes were non-trivial and attributed to the non-homogeneous coating structure (Figure 2.5(b)), that could influence internal frictions and affect the individual modes differently.

### 2.1.3.3/ HEATING DUE TO ELECTRON BEAM

As explained in Section 1.3.1.1, the different image acquisition processes in a SEM and TEM are based on the interaction of high-energy electrons with matter. Those interactions, however, can have important effects over the studied sample. In [Egerton et al., 2004], the conse-

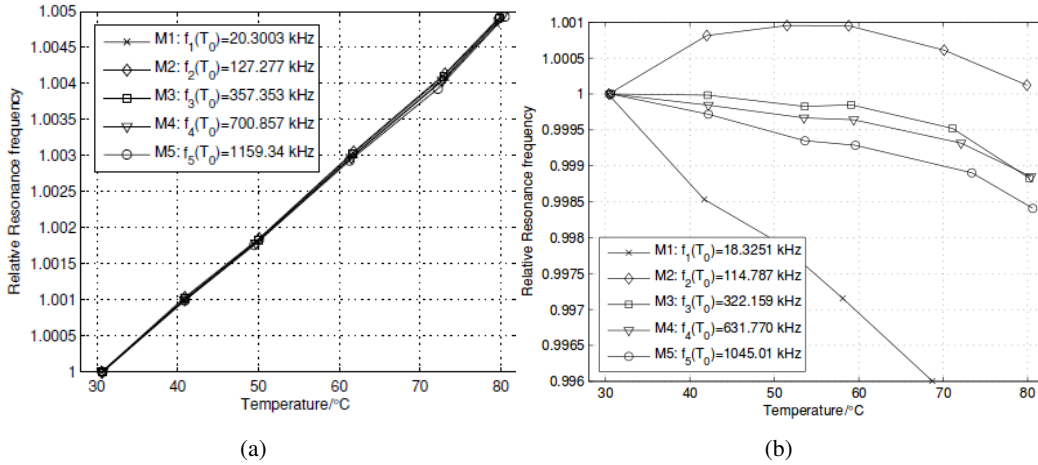


Figure 2.5: Normalized resonance frequencies of the first five flexural modes (M1–M5) of (a) the uncoated and (b) the gold-coated cantilever as functions of temperature [Sandberg et al., 2005].

quences of such interactions on TEMs and SEMs were summarized. These effects include heating, electrostatic charging, permanent sample damage, and others. As the common accelerating voltage for a SEM is much lower than the needed ones for TEM imagery (from 1 to 30 kV in the first against 100 to 300 kV in the later), most of the electron-irradiation problems have a reduced impact in scanning electron microscopes. However, heating and electrostatic charging can still have significant influence in prolonged exposure situations.

When an electron beam is focused on a material, various elastic and inelastic interactions can occur between electrons and the material. During inelastic scattering, most of the energy created is dissipated as heat within the specimen, causing a local rise in temperature. Materials with low thermal conductivity, such as polymers, are more sensitive to heating and may experience thermal degradation. Another important aspect to be considered is the sample geometry, as bulk specimens benefit from a radial heat flow in three dimensions, something not true for thin structures. The works of [Polyakov et al., 2014] remarked that, during the manipulation of gold nano-particles (nominal radius between 100 and 280 nm), as the diameter of structures decreases, so does its melting temperature. In the example discussed in the article, partial sample deformation was reported during the image acquisition process inside the SEM, due to the electron beam radiation.

For experimental measuring of the temperature variation due to electron beam, different methods can be applied. Thermocouples can be employed for direct measures, but with limited spatial resolution. Another method consists in using low fusion point samples bombarded with different beam powers. A third method was proposed in [Bouscaud et al., 2012], measuring the lattice parameters of materials under the electron beam using the Kossel micro-diffraction technique. Knowing the linear thermal coefficient of the material, temperature variations could be deduced from the lattice dilatation. This method is attractive, as modern techniques can determine lattice parameters with high precision. In this article, two materials (copper and germanium) were chosen, due to the differences in their thermal conductivity. The study consisted in changing the incident beam power  $P$  and measuring variations in the lattice structure.

The local temperature rise  $\Delta T$  induced by the electron beam on the bulk specimen can be calculated using Equation 2.3:

$$\Delta T = \frac{P}{2\pi\lambda}(q^{-1} - Q^{-1}) \quad (2.3)$$

where  $\lambda$  is the thermal conductivity of the specimen,  $Q$  is the approximated sample dimension and  $q$  is the distance from the probed zone on the material corresponding to the x-ray source used for the micro-diffraction technique. The true lattice parameter without heating  $a_{true}$  and the measured lattice parameter with beam heating  $a_{meas}$  are related by Equation 2.4, with  $\alpha_t$  the linear thermal expansion coefficient.

$$a_{meas} = a_{true}(1 + \alpha_t\Delta T) \quad (2.4)$$

Equations 2.3 and 2.4 established a linear relationship between lattice parameter and electron beam power. By measuring those quantities and its uncertainties, it was possible to determine the relation between local temperature variations and beam power. The experiments performed in [Bouscaud et al., 2012] led to the following relations between beam power and temperature variations for the two metals:

$$\Delta T(Cu) = 102(\pm 22).P$$

$$\Delta T(Ge) = 606(\pm 11).P$$

As the normal operating power could vary from 0.003 to 0.03 Watts, the local temperature increase in bulk materials, due to the electron beam, could achieve values close to 3 degrees for copper and 27 for germanium. While these temperature variations were still small in this case, they could be greatly increased if the studied materials were less conductive and their geometry restricted the heat dissipation. It was reported in [Egerton et al., 2004], for the analysis of thin film of low conductivity samples, temperature increases of a few hundred degrees for a stationary scan, even considering lower energy electrons (from 0.5 to 2 keV). In this situation, the beam energy was deposited in the sample, where the heat flow is only two dimensional. Considering normal raster scan, the temperature rise could be reduced by a factor of ten.

#### 2.1.4/ CONCLUSION

Despite the best efforts to attenuate their effects, external disturbances are still a limiting factor for high-performance imaging and manipulation in the SEM. Mechanical vibrations from the surroundings and the microscope itself can affect components placed inside, even when passive and active damping techniques are implemented. Acoustic disturbances can affect significantly systems in vacuum through mechanical coupling, and even relatively small noise levels may result in a large degradation of the positioning accuracy. A SEM is a complex system, and these perturbations can excite the vibration modes of various components (robotic stage, micro-manipulators, samples, ...).

Electromagnetic interference can affect electronic devices in the SEM and the natural caution should be exerted. The major problem caused by this kind of perturbation is related to the image acquisition process. As the microscope imaging mechanism is based on large voltages and the use of magnetic fields, special attention should be given when preparing the SEM room, to avoid image deterioration. However, they represent artifacts in the image, and not real displacement of components.

Thermal disturbances can become a serious issue in the vacuum, due to the low heat transfer characteristics and the reduced object dimensions. The effects of heat accumulation can degrade measurements and modify the characteristics of components, to the point of generating premature failure in the device. A special case should be made over the heating due to electron

beam incidence, a particularity in this family of microscopes. The incident beam can generate considerable amounts of heat during image scanning processes. If the beam bombardment is too frequent (i.e. when defining a small scanning area to improve the acquisition frame rate), and has enough energy, heat is added faster to the systems than they can dissipate. This effect is emphasized when considering thin or small samples and poorly conductive materials.

## 2.2/ VIBRATION MEASUREMENT INSIDE A SEM

From the previous section, there are clues indicating that disturbances on electron microscopes can be of various origins (mechanical, thermal and electromagnetic). A complete analysis of each one of those sources would be ideal for the development of precise and detailed nano-manipulation systems. In this work, only mechanical and acoustic excitations will be studied, as, based on the literature review, these are believed to be the major contributors for the positioning task degrading in the SEM environment. Disturbance sources, such as vacuum pump vibrations and acoustic noises, are present in most of SEMs operation environments.

The influence of these disturbances poses a recurring challenge when performing precise micro- and nano-manipulation tasks, as the induced vibrations (from 0 to a few kilo-Hertz) can excite the vibration modes of components inside the microscope. These vibrations can affect samples, end-effectors and other components inside the vacuum chamber, which limit the achievable accuracy of a manipulation system.

To characterize these disturbances, it would be interesting to measure how they can affect elements of the microscope. The two main vibration measurement methods found in the literature are based on:

- **Electron beam bombardment:** Processes images (or parts of them) and estimate the vibration amplitudes and frequencies. However, it may be difficult to separate sample vibrations from electron gun column vibrations. This analysis may take a long time and requires multiple image acquisitions, which reduces usage in real-time applications. An example is the stroboscopic electron scanning microscopy [Fujioka et al., 1980, Ishikawa et al., 1993]. Reducing the scanned area (i.e. a single line, instead of the full image [Wong et al., 2007, Jasper, 2011]) improves the acquisition and processing speed, while losing the images capabilities of the SEM.
- **Accelerometers:** The use of these instruments allows retrieving information in real time for multiple axes. So far this method is limited to measurement of disturbances of the vacuum chamber and other large components, as high-sensitivity sensors are bulky (up to hundreds of grams) and their measurement ranges may be limited.

While accelerometers can offer an interesting approach to estimating vibrations effects over the vacuum chamber, this method does not capture the actual behavior of components inside the chamber. On the other hand, electron beam methods can measure information directly on components of interest inside the SEM. However, it may require extensive post-processing of a large amount of images to retrieve this information. Furthermore, these methods may not achieve enough spacial resolution to identify vibrations at the nanometric scale.

To overcome these limitations, a different method is proposed based on the use of a dedicated laser vibrometer. This kind of sensor performs non-contact displacement measurements, with great accuracy over a large spectrum, without interfering with the image acquisition process.

Through this device, the displacement information of an object can be measured directly inside the vacuum chamber, and is available in real-time, with minimal need of post-processing.

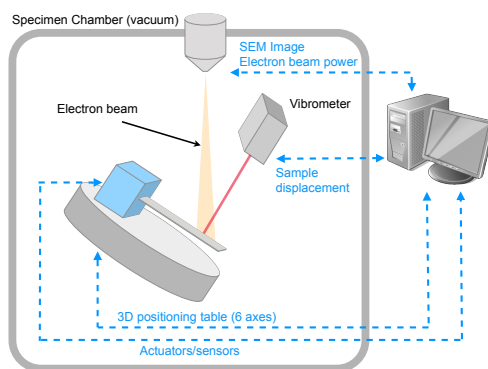


Figure 2.6: Carl Zeiss SEM Auriga 60, from the EQUIPEX ROBOTEX project, where the experiments were performed.

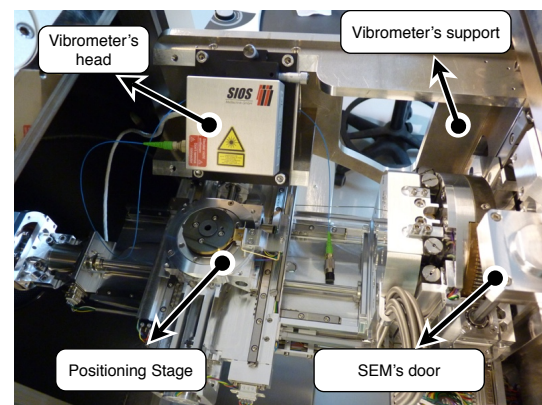
The setup consists of fixing a vibrometer (SP-120, vacuum compatible, from SIOS Meßtechnik GmbH) inside a SEM (Carl Zeiss SEM Auriga 60, shown in Figure 2.6). They are fixed at a relative  $45^\circ$  angle, so both the laser and the electron beam intersect. This allows acquiring images and perform displacement measurements simultaneously. For this purpose, a rigid metallic support was designed and fixed to the SEM door, independently from the microscope six degrees-of-freedom positioning stage (four translations and two rotations), allowing relative movement between both structures.

Samples were fixed through an appropriate support to the stage, that positions it inside the vacuum chamber. The sample can be

remotely positioned using a joystick or by a software interface, as it is necessary to adjust the laser beam's incident angle and will be described later in this chapter. Finally, the sensor is connected to its external processing unit through the appropriate feed-through ports (optical fiber and electrical connection). This processing unit can then transmit the data to other devices, via digital or analog signals, in real time. Figure 2.7(a) illustrates the proposed setup, with the measured and control signals available to the user. Figure 2.7(b) shows its implementation inside the microscope, where the vibrometer head was attached to the SEM door through an aluminum support at a  $45^\circ$  angle.



(a)



(b)

Figure 2.7: (a) Scheme of the experimental setup proposed and (b) implementation inside the SEM.

### 2.2.1/ VIBROMETER CHARACTERIZATION

To correctly estimate the disturbance levels in the system, it is necessary to first quantify the intrinsic noise levels existent in the measurement system and the practical attainable resolu-

tions achieved by the transducer. This can be estimated by measuring the vibration of a rigid metal block at different reflection levels. During the characterization process, the metal block and the vibrometer were fixed to a pneumatic anti-vibration table, to minimize ground vibration interferences.

The measurements were acquired through the vibrometer analog output, and digitized by a 12 bits A/D converter (dSPACE DS1103 PPC Controller Board). When operating in analog mode, the vibrometer allows users to select an analog output gain. This gain regulates the measurement range (maximum vibration amplitude before saturating the output signal). These values, described in the manufacturer manual [SP1, 2012], are summarized in Table 2.1 for each output gain named as G0, G1, G2 and G3.

Analog output gain	Maximum oscillation amplitude (in $\mu\text{m}$ )	Measurement gain K (in $\mu\text{m}/\text{V}$ )
G0	0.63	0.24
G1	2.50	0.97
G2	10.10	3.87
G3	40.30	15.48

Table 2.1: The vibrometer offers several analog output gain options, with different operation ranges.

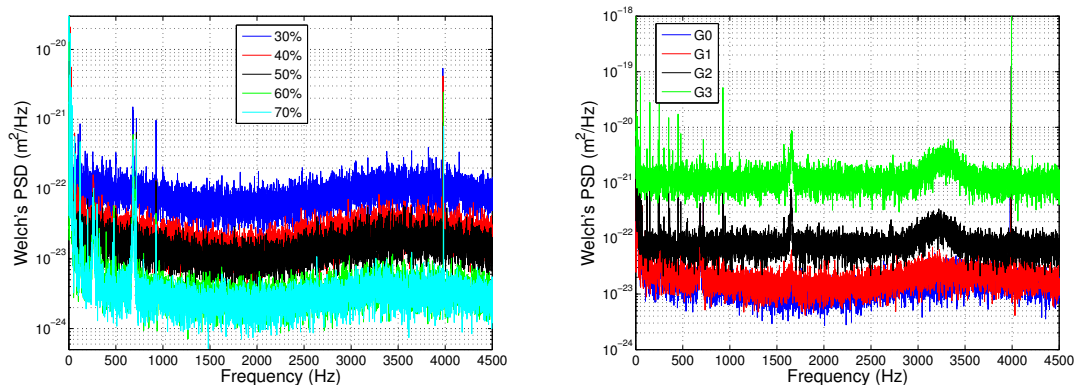
To estimate the noise levels for these gains, a series of measurements were performed for different reflection levels, representing a metric, indicating the laser beam percentage reflected back by the sample and captured by the sensor. It can be interpreted as the signal quality, where a higher value ensures a lower noise level.

The measurements for the calibration tests were performed with an acquisition frequency of 25 kHz. For each one of the four analog output gains to be tested, and for each studied reflection level (30, 40, 50, 60 and 70%), ten measurements were performed. These twenty different scenarios intent to represent common values found in normal operation conditions. The manufacturer recommends reflection levels greater than 50% to ensure measurement precision. However, in real applications, these values depends on the studied surface and its roughness, where high reflection can be difficult to achieve.

Each acquired measurement was processed using Welch's power spectral density (PSD) method [Welch, 1967]. The ten resulting frequency spectra for each scenario were then averaged, to obtain an estimation of the sensor's frequency response. Figure 2.8(a) shows, for the analog output gain G0, the reflection level influence over the measurements and how high levels can improve the signal quality, up to a limit. In this case, it is close to a 60% reflection level. The graph shows significant peaks around 700 and 4000 Hz. These frequencies were considered part of the sensor's characteristic response (measurement noise).

Figure 2.8(b) shows, for a close reflection level (50%), how the analog output gain influences the measurements. There is a loss in signal quality as the gain increases, reflecting the resolution reduction with measurement range increase. Furthermore, it is possible to notice for gains G2 and G3 peaks at 1600 and 3200 Hz, in addition to the ones mentioned before.

Table 2.2 resumes the sensor's analog output results, considering different reflection levels. The measures performed with gains G0 and G1 have shown similar noise levels, credited to



(a) Averaged PSD for G0 input gain, considering different reflection levels. (b) Averaged PSD for a constant reflection level of 50%, considering different output gains.

Figure 2.8: Vibrometer PSD results, considering different reflection levels and analog output gains.

Gain	Average RMS noise level and standard deviation (in nm)					Resolution (nm)
	Reflection level (%)					
	30	40	50	60	70	
G0	$1.1 \pm 0.07$	$0.68 \pm 0.12$	$0.55 \pm 0.16$	$0.37 \pm 0.06$	$0.42 \pm 0.14$	0.07
G1	$0.9 \pm 0.17$	$0.56 \pm 0.09$	$0.57 \pm 0.02$	$0.48 \pm 0.04$	$0.48 \pm 0.15$	0.3
G2	$1.3 \pm 0.02$	$1.2 \pm 0.02$	$1.2 \pm 0.01$	$1.2 \pm 0.04$	$1.1 \pm 0.03$	1.2
G3	$4.6 \pm 0.06$	$4.4 \pm 0.02$	$4.4 \pm 0.05$	$4.4 \pm 0.08$	$4.4 \pm 0.03$	4.7

Table 2.2: Measurement noise RMS value and standard deviation for different output analog gains and reflection levels, and maximal measurement resolution for each gain.

residual disturbances not compensated by the anti-vibration table (i.e. acoustic perturbations from devices in the room, such as computers and cooling fans) and electronic noise. It is possible to see that, for the gains G2 and G3, resolution becomes a limiting factor. The effects of quantization are shown in Figure 2.9, where the loss of information becomes evident. Therefore, a trade-off should be achieved between desired resolution and measurement range. Hence, G1 will be used for all measurements, except when the desired displacement range exceeds the limit value of  $2.5 \mu\text{m}$ . In that case, the gain value G3 is applied.

### 2.2.2/ SEM DISTURBANCES AND NOISES IDENTIFICATION

As stated in Section 2.1, components inside the SEM are subject to unknown disturbances that may produce undesired vibrations during micro- and nano-manipulation tasks. From the possible sources of disturbance, mechanical disturbances appear to be the major contributor. Its precise identification and quantification can offer valuable information to researchers aiming for extreme high accuracies for positioning tasks in SEM.

To study the influence of external mechanical disturbances over components inside the SEM, two different tests were proposed. The first observed the perturbations constantly affecting

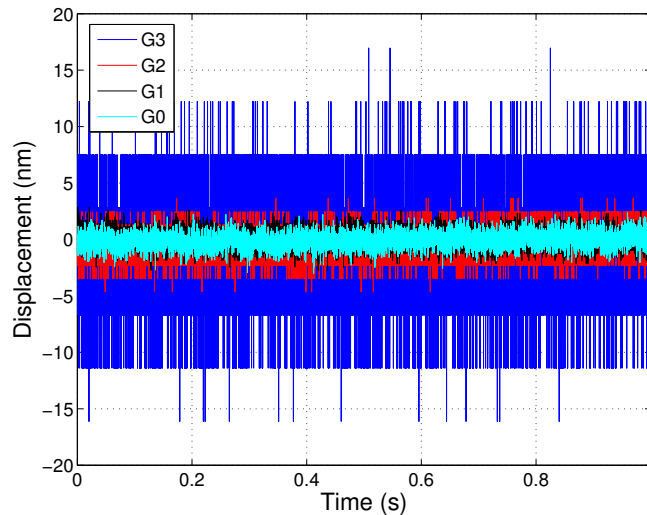


Figure 2.9: Acquired signals for different output analog gains, at a constant reflection level of 50%.

the microscope are under regular operation conditions. In the second test, a controlled external acoustic disturbance source was added in the environment to investigate how these excitations can be transmitted to structures inside the vacuum chamber.

#### 2.2.2.1/ SYSTEM UNDER REGULAR OPERATION CONDITION

This step considered tests performed in conditions close to real practical tasks and aimed to identify the most important disturbances frequencies and to characterize its sources. It was performed in the SEM chamber at high-vacuum ( $10^{-4}$  Pa), with reduced human activity in the room. The sample, a set of silicon cantilevers of different lengths, was fixed in the sample holder and placed in the microscope positioning table (Figure 2.10).

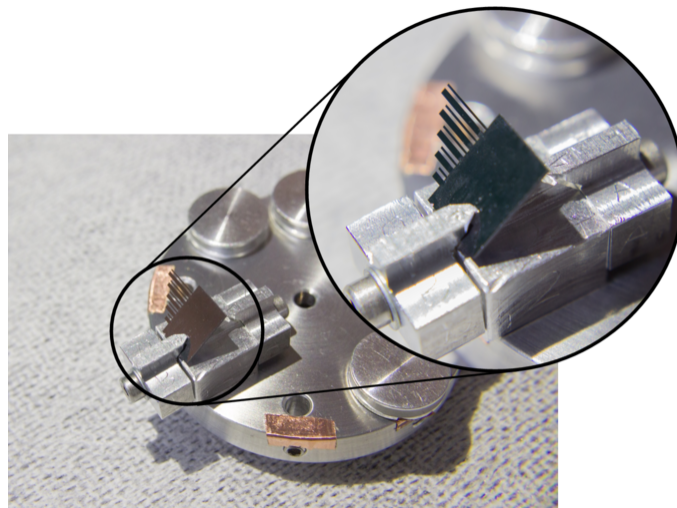


Figure 2.10: Silicon cantilevers in the sample holder.

The cantilevers approximated dimensions are given in Table 2.3, together with the measured first resonant frequency in air,  $f_{1_{air}}$ . These samples are interesting during the identification process due to its reflective surface, allowing for better reflection levels and, consequently, improved displacement readings. In addition, the different cantilever lengths and first modes may emulate the behavior of various structures, as those are roughly similar to values found in micro-grippers and other micro-positioning tools.

Name	Dimensions ( $l \times w \times t$ , in $\mu\text{m}$ )	$f_{1_{air}}$ (Hz)
Cantilever 1	5000 x 400 x 20	1162.0
Cantilever 2	4000 x 400 x 20	2013.4
Cantilever 3	3000 x 400 x 20	3649.1
Cantilever 4	2000 x 400 x 20	8337.4

Table 2.3: Nominal dimensions (length  $l$ , width  $w$  and thickness  $t$ ) and first resonance mode measured at atmospheric pressure for the different silicon cantilevers.

The silicon samples do not possess any kind of actuators or electrical connections, and therefore all the displacements measured were caused by mechanical vibrations (from inside and outside the SEM) transmitted to the cantilever, or sensor noise. The laser reflection calibration, as stated before, is essential to ensure good measurement quality. However, once that all the setup is sealed inside the vacuum chamber, the only visual hint to aid in calibration comes from an infrared camera, which can become tiresome when dealing with micro-elements. Therefore, an initial calibration process is performed manually while the SEM door is open, when rotation angles and positions are adjusted. Once the chamber is closed and sealed, only small adjustments can be performed. In this particular case, the high reflection for the silicon cantilevers simplifies the laser calibration process. In consequence, reflection values larger than 50% are usually encountered.

For each silicon cantilever, twenty separated measurements were acquired and had Welch's PSD method applied to each of them. To further reduce measurement noises and the effects of sporadic disturbances, the obtained PSD's were averaged for each cantilever. Figure 2.11 shows the resulting curves for silicon cantilevers from 0 to 1 kHz.

From the graph, six major peaks (56.1, 95.4, 140, 235.7, 688.55, and 955.2 Hz) in the spectrum frequency were identified, besides the cantilevers resonant modes (not shown in the figure) and other minor peaks with smaller contributions. The influence of sensor noise is present in the measurement through a high frequency peak close to 4010 Hz that is not shown in the graph.

The root mean square (RMS) vibration level measured for the different cantilevers ranged from 1.07 to 2.55 nm, depending on the sample's length. Performing similar measurements at the cantilevers' base, to eliminate the first vibration mode influence, found RMS displacements values between 0.86 and 0.98 nm. As expected, both tip and base showed similar frequency spectra, with exception of the first cantilever mode, responsible for this difference in the computed RMS value. It is possible to infer that, for longer cantilevers, its first vibration mode presents a larger contribution to the total vibration.

The following step in the disturbance analysis is to identify the origins for each one of the six main vibrations peaks. In this phase, new sets of measurements were acquired for the cantilevers, considering small variations in the environment. Comparing results obtained before and after these variations can help isolate each one of the disturbance's origin.

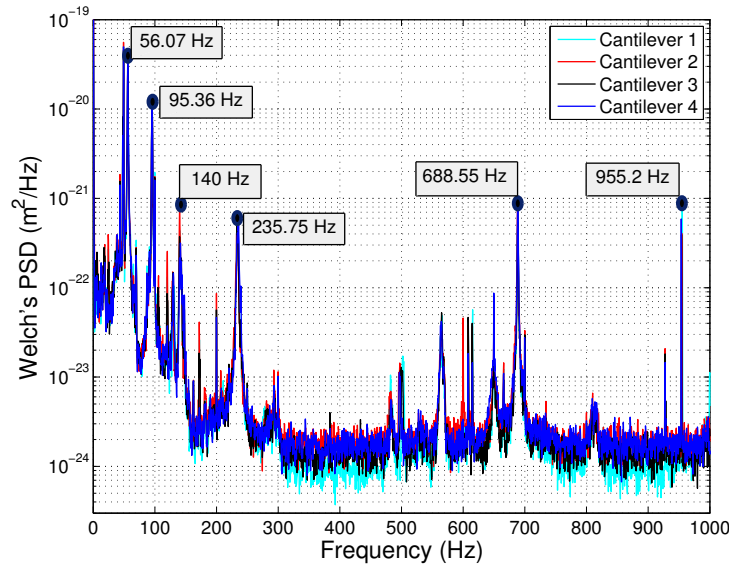


Figure 2.11: Averaged power spectrum density of the silicon cantilevers, detailing the frequencies with larger amplitude.

The vibrometer support was fixed to the SEM door at one extremity and free at the other. It can therefore be interpreted as a clamped beam, and may have a vibration mode in the studied range. To verify this assumption, the finite element analysis shown that the expected vibration mode for this component is close to 120 Hz, within the frequency range of the experimental values (Figure 2.12). An experiment was proposed to validate this numerical result. It consisted in changing the vibrometer's head placement on the support, as this component has a considerable mass (approximately 300g). Positioning it closer to the support fixed end resulted in the frequencies located at 56.1 and 95.4 Hz to shift to 82.3 and 122.5 Hz, respectively, while other frequencies in the spectrum remained mostly unchanged.

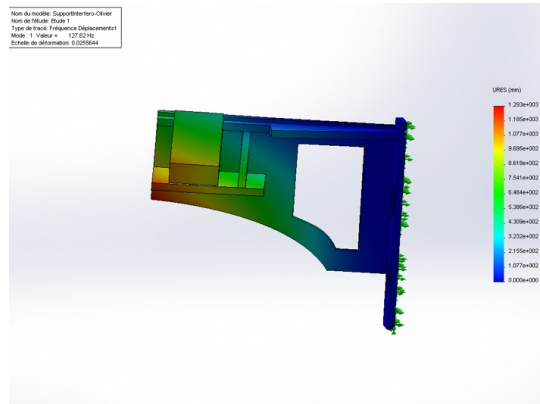


Figure 2.12: Finite element analysis for the vibrometer's support.

Following the same analysis, the microscope stage itself is also fixed to the SEM door and free in the other end. In this case, the finite element analysis was not possible, as no model for this component is available. Therefore, a different experiment is proposed, consisting in adding weights (metal blocks of approximately 185g) to the support and to the positioning table, alternately.

When placing weights on the vibrometer support, frequency variations at the same peaks as before (56.1 and 95.4 Hz) were observed. It is possible to conclude that these are measurement noises and do not represent actual sample displacements. When placing the weight over the SEM positioning table, the peaks previously located at 140 and 235.7 Hz shifted in frequency. These

peaks were then attributed to mechanical vibrations of the positioning table. These values are within the frequency range of the positioning stage obtained in [Pluska et al., 2015] for a different SEM.

To help identify the remaining frequency peak sources, an additional experiment was proposed. It aims to investigate the proposition found in literature that the SEM itself and its components could be the cause of some observed disturbances. For this purpose, measurements were acquired under two different conditions:

- Condition 1: SEM under normal operation conditions, with a high vacuum ( $10^{-4}$  Pa) but no electron beam bombardment.
- Condition 2: SEM powered off (electricity shut off), with a high vacuum ( $10^{-4}$  Pa).

Enforcing Condition 2 ensures that all SEM elements (i.e. vacuum pumps, cooling fans, ...) were turned off, allowing to verify if those elements had significant contribution in the measured disturbance spectrum. As the specimen chamber stayed sealed, the vacuum was kept in similar conditions as the normal SEM operation levels.

In Figure 2.13 the PSD for 688.5 and 955.2 Hz frequencies are compared in both conditions. It became evident these disturbances sources were related to the microscope. The frequency around 700 Hz is attributed to the turbo-molecular pump. Differently from the main rotary pump, this component is always active to ensure the high-vacuum level necessary for the SEM correct operation. In this particular case, this pump has a nominal rotation frequency of 42000 rpm (700 Hz), in agreement with the experimental values. It is worth to remark that the pumps are placed over passive damping systems, and connected to the SEM using components to minimize the vibrations.

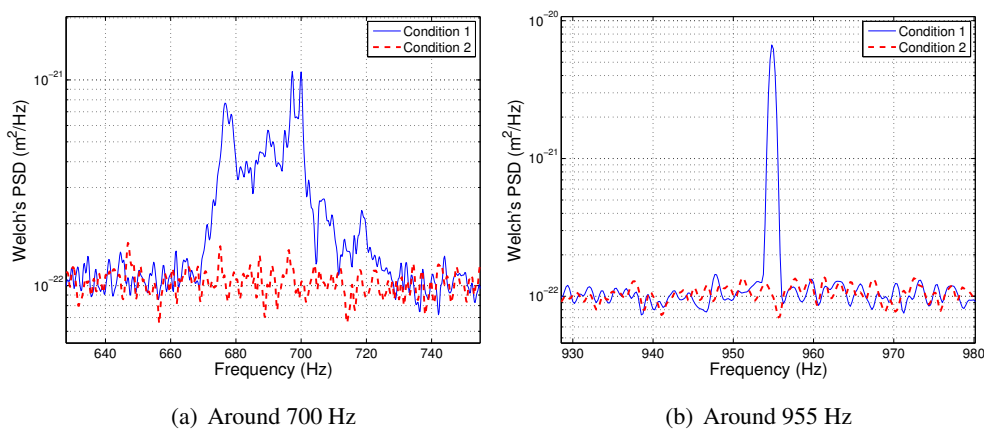


Figure 2.13: PSD around 700 (a) and 955 Hz (b) comparing the SEM in two conditions. It indicates that the SEM could be the possible origin for these disturbances.

The 955.2 Hz frequency can also be related to the SEM operation, as shown in Figure 2.13(b). This peak presents some interesting characteristics. When performing multiple measurements, for the same cantilever, at different times and over a span of several days, the peak varies between 949 and 957 Hz, always with similar amplitudes. These characteristics are also present when considering the other silicon cantilevers. This effect was attributed to electronic interference over the vibrometer signal, as it presents itself in a well defined frequency, similarly to the effects

of 50 Hz noise and its harmonics. However, the nature of this phenomenon is not known precisely, except the fact that its origin is related to the SEM.

The identification of disturbance sources in the SEM represents an important step towards improving the micro- and nano-manipulation in this environment. It allows designing improved systems that operate outside the disturbance ranges and offers an insight on how external and internal SEM components can affect samples in the vacuum chamber. However, as stated before, the major disturbance contribution are due to first mode vibrations.

Figure 2.14 shows the PSD around Cantilever 1's first mode, comparing between both test conditions. It is important to remark that, during normal operation (Condition 1), the PSD level for this peak is two orders of magnitude higher than any other peak presented in the spectrum. The cantilever vibration was largely reduced when the SEM was turned off, even though there were no evident disturbances acting close to the sample resonant mode. Other disturbance frequencies related to mechanical components, namely vibrations in the positioning stage and in the vibrometer support, also showed decreased amplitudes, with the average RMS displacement in Condition 2 of approximately 0.84 nm.

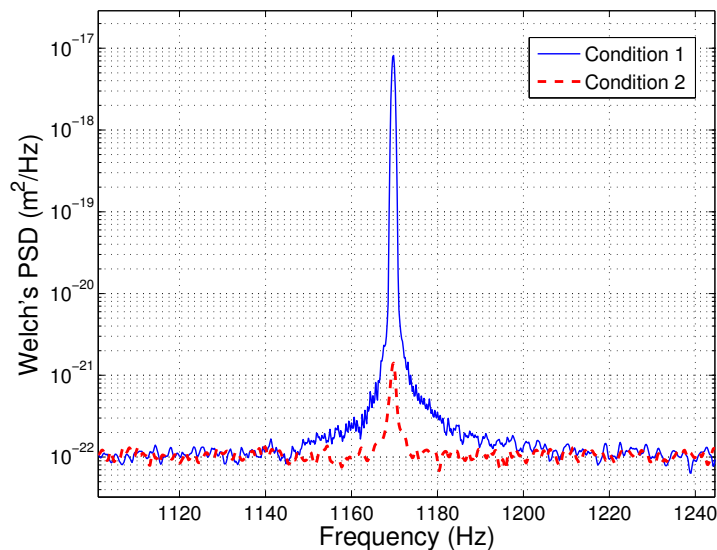


Figure 2.14: PSD of Cantilever 1, detailed for its first mode (1169.8 Hz), comparing both test conditions.

The experiments shown above demonstrated that elements inside the vacuum chamber are prone to the effects of external mechanical disturbances. Furthermore, the microscope can contribute as a source of disturbance. This experimental identification also offers an approximated idea for each disturbance contribution to the overall vibration level. This information is valuable when considering systems to be operated in the SEM environment, trying to avoid those critical frequencies when possible.

### 2.2.2.2/ SYSTEM UNDER EXTERNAL ACOUSTIC EXCITATION

The existence of acoustic vibrations in the working environment is a recurring problem when dealing with micro- and nano-manipulation tasks. During previous experimental measurements, it became clear that acoustic noises can have a substantial impact on systems inside the

SEM. As the system operates in a vacuum environment, perturbations can only be transmitted through mechanical coupling. In the case where acoustic excitations carry enough energy to produce displacements in the SEM chamber, these can be transmitted to the positioning stage and, consequently, to samples and manipulators.

Those vibrations can be generated by human interference and surrounding equipment, are not necessary continuously affecting the system and can cover a wide range of frequencies and amplitudes. To better understand the coupling between external acoustic excitations and components located inside the SEM, a different experimental setup was proposed (Figure 2.15). Through the use of a signal generator and a loud-speaker positioned at 1 meter from the SEM, controlled acoustic noises with different frequencies and amplitudes were introduced as an external disturbance source, while sample displacements inside the vacuum chamber were measured. The loudspeaker employed for this test has an approximate constant response for frequencies between 1 kHz and 10 kHz (approximately  $90 \pm 4$  dB for a 2.83Vrms signal at 1 meter), so sinusoidal excitations within this range should produce similar dB sound levels for a given voltage input. Additional information on its response characteristics can be found in Appendix A.

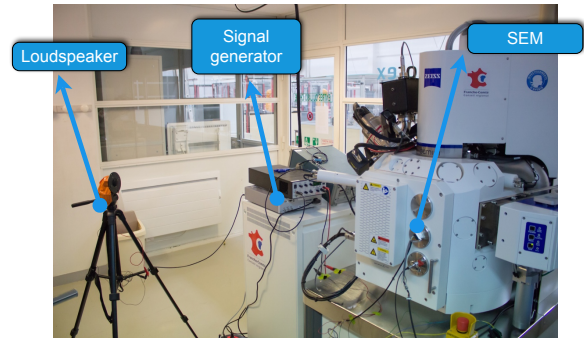


Figure 2.15: Photo of the experimental setup for external acoustic excitation, with the SEM, the loudspeaker and signal generator.

The worst case scenario was tested, where the system was subjected to a constant sine wave disturbance. A set of sample displacement measurements was acquired before activating the loudspeaker, and the average RMS displacement obtained after ten measurements was 1.07 nm. Generating a sinusoidal signal of 1000 Hz through the loudspeaker (outside the range of any resonant frequency previously measured), produced small displacements of the sample. These vibrations were only noticeable through a careful analysis of the frequency spectrum, and for large noise amplitudes (70 dB or greater). In this case, the added disturbance had a small effect, and other mechanical disturbances previously measured were still dominant. For comparison, a 70 dB external acoustic excitation with a frequency not matching any resonant mode produced an average RMS vibration level of 1.15 nm, slightly above the previous measured vibration levels.

Nonetheless, if the frequency applied matches a resonant mode (in this case, 1169.8 Hz), much lower excitation power can have a large impact over the vibration amplitude. For Cantilever 1, the system achieved a constant 21 nm peak-to-peak vibration for an approximated excitation level of 50 dB (normal conversation level) and more than 70 nm peak-to-peak for a 60 dB perturbation. Figure 2.16 shows the obtained result for this measure. In the graph, external excitation starts at 1 second. This meaningful increase in vibration amplitude for a relatively small acoustic excitation shows how easily external disturbances can affect components in the SEM chamber.

The scenario described above, where an external acoustic disturbance frequency matches those of components inside the chamber for an extended period, is difficult to be found in real work environments. In reality, a laboratory is prone to different acoustic disturbances and pressure variations. They originate from the environment and may present themselves in a large frequency band, affecting one or multiple resonant modes of components in the specimen chamber. This test exemplifies how even low amplitude noises may have a large impact on the positioning accuracy

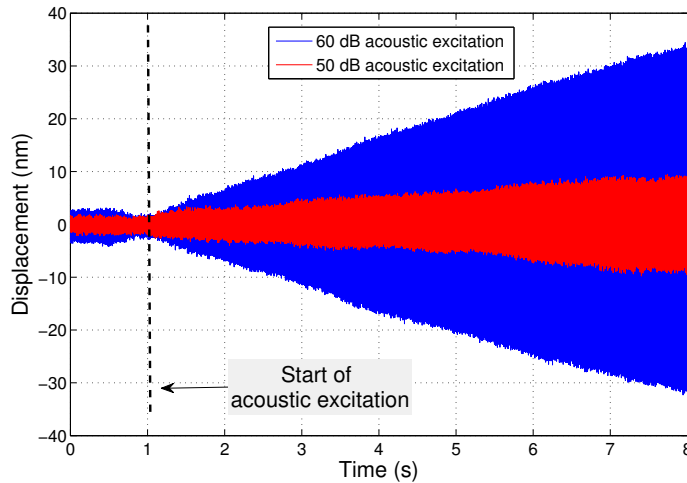


Figure 2.16: Displacements measured on Cantilever 1 under the influence of an external noise source of different powers, generated by the loudspeaker. A sinusoidal wave with frequency matching the sample's first mode is applied as the disturbance signal. The black dashed line indicates when the external excitation starts.

inside the SEM. Even in a high vacuum environment, it is evident structures are still subject to acoustic disturbances through mechanical coupling.

### 2.2.3/ CONCLUSION

To analyze the disturbances acting inside a SEM without resorting to its electron gun or imaging methods, a new setup was proposed based on the use of a dedicated vibrometer. It was placed inside the SEM vacuum chamber and allowed to measure the displacements over a set of samples with sub-nanometric precision and with sampling rates up to tens of kilo-Hertz. This original structure allowed to obtain a unique insight on the disturbances in this environment. The work focused on mechanical and acoustic disturbances effects on the vacuum chamber.

The analysis of collected data, through extensive experimental investigation, reveals that the scanning electron microscope itself contributes largely as a disturbance source. Figure 2.17 resumes the results found experimentally, showing the sources for each one of the most significant disturbances. The largest contribution, however, is due to the sample's oscillations. Experiments indicate that this mode can be excited by the SEM during normal operation.

Another effect commonly overlooked is the influence of external acoustic perturbations. Through the use of a loudspeaker, to control the acoustic disturbance power and frequency, it was possible to witness how even small noises can produce significant vibrations on elements inside the vacuum chamber. As acoustic disturbances are present in real operation environment and can cover a large band in the frequency spectrum, they constitute an authentic issue when high accuracies are required.

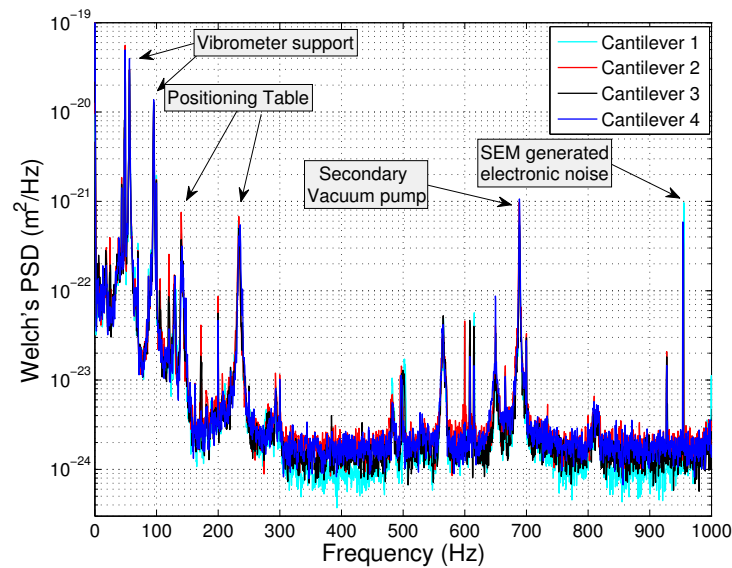


Figure 2.17: Summary of the most important measured sources of disturbance.

## 2.3/ CONCLUSION

In this chapter, a literature survey indicates the presence of four possible sources of disturbance in the SEM: mechanical vibrations, acoustic noises, electromagnetic interferences and thermal related disturbances. When considering SEMs, studies concerning disturbances focus mainly on imaging and how those perturbations affect the electron beam column or the beam itself. However, a few results indicate that the column is not the only influenced component, and that other elements inside the SEM are also subject to those effects. The literature also indicates that, from those possible sources, mechanical and acoustic disturbances should present the largest contribution in producing undesired vibrations. The identification and quantification of those contributions in micro- and nano-devices is a challenge, where the local conditions (limited volume, vacuum environment) impose additional restrictions making precise position measurements of components inside the microscope not always possible.

Through the use of a dedicated vibrometer, some of those difficulties have been overcome, allowing the measurement of disturbances acting over samples inside the SEM in real-time, independently of the imaging system. The performed measurements concerned real movements of components in the vacuum chamber, and not artifacts generated by the SEM image acquisition system, as those commonly caused by EMI.

The samples consisted of silicon cantilevers of different lengths. During this experimental study, it became clear that the major vibration frequency was linked to the excitation of the sample vibration modes. Other mechanical components inside the SEM (positioning stage, vibrometer support) and the secondary vacuum-pump produced additional vibrations. Experimental tests demonstrate that the microscope is especially sensitive to acoustic disturbances.

Figure 2.18 shows, in a simplified graph, how different sources of disturbance affect systems in relation to their scale. The curves are rough estimates, as they depend on multiple parameters (geometry, material, vibration modes, disturbance amplitudes and frequencies, ...). In this work, the studied cantilevers have lengths of a few millimeters. In the tests performed, the

frequency band of acoustic noises encompass the vibration mode of various components, while mechanical vibrations have a limited effect in high frequencies.

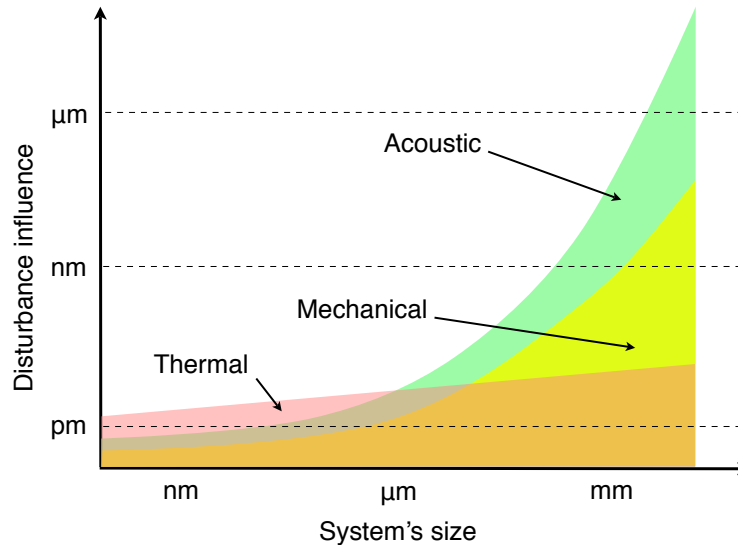


Figure 2.18: Diagram relating the different sources of disturbances and their influence over systems of various sizes.

Thermal noise affects a large frequency range, and should be the dominant effect in systems with high resonant frequencies. From the literature, it is possible to infer that it has a reduced influence on our system, where the expected induced displacement rests close to or under the resolution limits of the vibrometer used in the test. Another issue presented is related to heat accumulation, that becomes a critical factor in the vacuum that can change a system dynamic characteristics or even damage components, if no caution is taken. The reviewed literature indicates that thermal noise effects become more important as the dimensions of the samples are reduced. In this case, those effects are not considered as the tested cantilevers are sufficiently large.

Mechanical vibrations, transmitted from the surroundings through the ground, act at much lower frequencies (generally from 0 up to 400 Hz, although some devices may achieve higher frequencies). SEMs are generally equipped with passive and active dampers, aiming for lower frequencies, what improves their performances in this range, yet those effects can still be observed. Although in this work the mechanical vibrations generated by the vacuum pump had a limited contribution, it could still be measured.

Acoustic noises, however, act on a larger band (from 0 to 20 kHz normally) and are damped less effectively by the SEM. These variations in pressure can have various sources (human conversation, operating devices, air flow due to air conditioning, ...). In this study, acoustic disturbances of relatively low levels with frequencies matching the sample's vibration modes can induce large displacements. These induced vibrations were sustained for a long time due to the low damping in the vacuum environment. In this study, acoustic excitation was the most important source of disturbance.

## MICRO-GRIPPER DYNAMICS IDENTIFICATION IN VACUUM AND AT ATMOSPHERIC PRESSURE

The identification of micro-grippers and actuated cantilevers in air is widely spread in the literature, presenting several models, each one with its own specific characteristics depending on the studied system ([Carrozza et al., 2000, Eisinberg et al., 2001, Boudaoud et al., 2010, Rakotondrabe et al., 2010], to cite a few). However, the dynamic characterization of those structures in vacuum is not well documented. Studies about the pressure effects focus on simpler components, such as passive cantilevers and plates ([Epp et al., 2004, Zhang et al., 2005, Sandberg et al., 2005]), and only general information is available. In this chapter, the identification of an electrostatic micro-gripper actuation system, encompassing comb-drive and finger, is performed in air and vacuum, and its differences are analyzed. In the end, two models capable of representing the system's most important dynamics in all operation range are presented.

### 3.1/ THE FT-G30 MICRO-GRIPPER

For this work, commercially available micro-grippers (model FT-G30, from Femto-Tools GmbH.) were used. The micro-gripper consists of two fingers: a comb-drive mechanics actuates one of them, while the other is passive and capable of force measurements through a built-in capacitive sensor. Figure 3.1 shows a SEM image of one gripper and its components.

The objective is to precisely characterize the gripper actuation system, including the comb-drive and the actuated finger, during its free movement (no contact interaction with samples or the sensing finger). The actuated finger dimensions are approximately  $4000 \times 120 \times 50 \mu\text{m}$ , and the nominal distance between its fingers is  $30 \mu\text{m}$ , which defines its working range. An example of its dynamic response is presented in Figure 3.2 for a 30 V step input, acquired at atmospheric pressure. It reveals the behavior of a low damped oscillatory system, with overshoot close to 100% and settling time around 0.1 second.

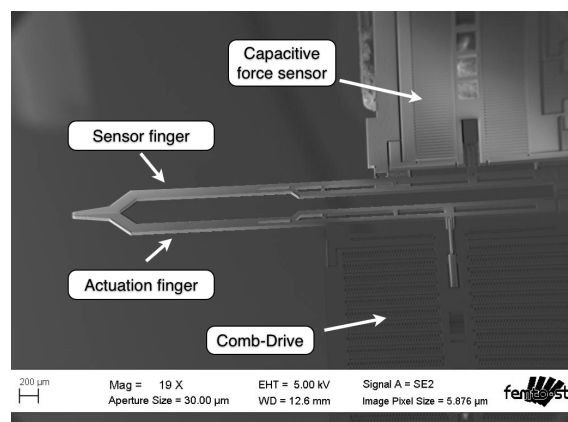


Figure 3.1: SEM image of the micro-gripper FT-G30 and its main components.

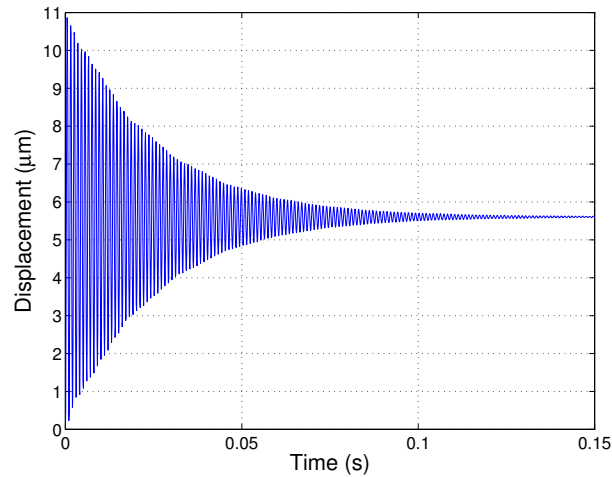


Figure 3.2: Example of the gripper's step response in air, for a 30 V input.

In [Boudaoud, 2012], the actuation mechanism of a similar electrostatic micro-gripper was modeled, considering the forces and moments on the comb-drive system. Its parameters were experimentally estimated for atmospheric pressure, in a gray-model identification process. The actuation system, detailed in Figure 3.3, is composed of a central shuttle (connecting the comb-drive and the finger), a set of suspensions responsible for holding the shuttle, and a hinge serving as rotation point for the finger and connecting it to the base of the structure..

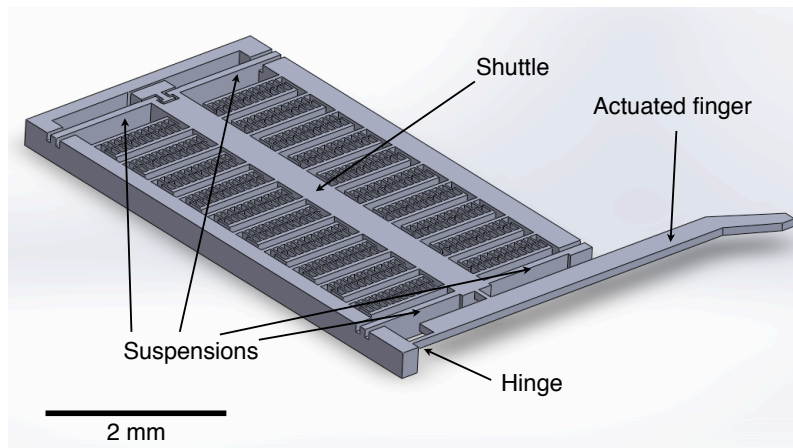


Figure 3.3: Micro-gripper actuated finger and comb-drive system representation, showing its main components.

Applying a voltage to the comb-drive mechanism produces an attraction force between the inter-digital structure. This force moves the shuttle, and consequently the finger. Therefore, their movements are related. Displacements of the shuttle are amplified by the geometric relation between the finger length and the distance between the hinge and the shuttle-finger connecting point. This way, small comb-drive movements can generate large tip displacements. The suspension mechanism holds the shuttle and gives some structural damping. It is also responsible to bring the system back to its initial position when no voltage is applied.

The first resonant modes found for the studied devices in [Boudaoud, 2012] were located

between 1000 and 2000 Hz, and were attributed to the comb drive's suspension mechanism. This work also shown that the finger's first mode has a much higher frequency (close to 30000 Hz). Therefore, reasonable agreement with experimental data was possible considering a second-order model, with nonlinear, varying stiffness and damping, to model only the suspension behavior. This representation served as a base for the gripper model in air used during this work.

When using the vibrometer, the measured displacements for the actuated finger tip depended on the laser beam incident point. Positioning the beam precisely at its extremity is not possible in reality due to the gripper geometry. Furthermore, the incident point in one experiment may not be the same as in a later moment, as relative movements between the sensor and gripper (i.e. during the vibrometer calibration process) will alter it. Figure 3.4 helps to illustrate these obstacles.

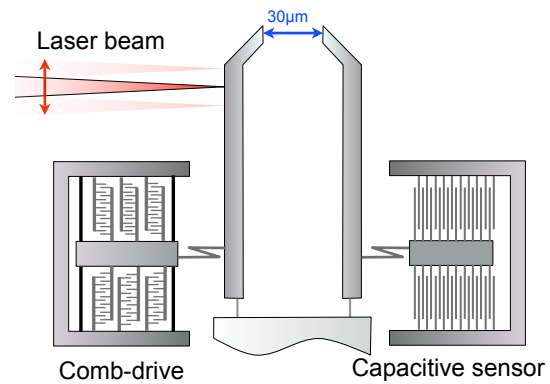


Figure 3.4: Micro-gripper representation, indicating that the laser beam measurement is not performed at the finger's tip and that variations on the laser incident point can occur.

To minimize their effect and ensure that all measurements correctly represent the same quantities (the actuated finger tip displacement), a correction process is performed. A triangular wave, with slope small enough to avoid inducing vibrations in the system, is applied to the gripper until its actuated finger touches the sensor finger. The contact between them can be easily noticed, as the displacement curve slope changes significantly. The obtained contact distance is then compared with the nominal distance between fingers ( $30\mu\text{m}$ ). This process is repeated every time the working conditions are changed. Figure 3.5 shows an example of acquired data in function of the input voltage, detailing the contact between fingers. In this case, the measured displacement is approximately  $25.5\mu\text{m}$ , for an input voltage of approximately 68 Volts. The ratio between nominal and measured distance gives a correction factor that approximates the real grippers tip displacement.

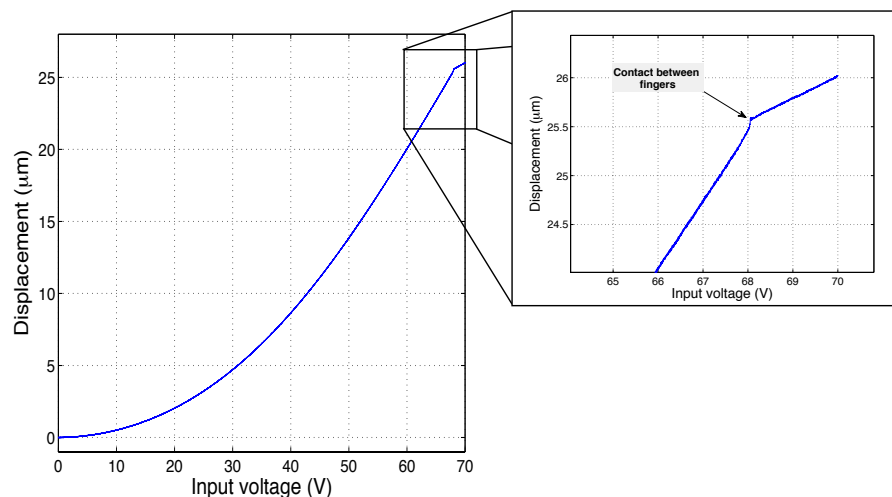


Figure 3.5: Experimental data used for estimating the relation between measured and actual tip displacement. The zoom box illustrates the contact between fingers.

The electrostatic force  $F_{elec}$  produced by this comb drive can be approximated by Equation 3.1:

$$F_{elec} = K_{elec} V_{in}^2 \quad (3.1)$$

where  $K_{elec}$  is the electrostatic gain of a comb-drive and  $V_{in}$  is the input voltage applied. The electrostatic gain  $K_{elec}$  can be estimated by Equation 3.2:

$$K_{elec} = \frac{N_a \cdot \xi \cdot h_z}{2 \cdot g} \quad (3.2)$$

with  $N_a = 992$  the total number of fingers in the comb-drive,  $\xi = 8.85e^{-12}$  F/m the dielectric permittivity of the medium,  $h_z = 50\mu\text{m}$  the comb drive fingers thickness and  $g = 6\mu\text{m}$  the gap distance between two comb-drive electrodes [Boudaoud et al., 2013]. As the electrostatic force is not applied to the finger extremity, a correction factor is introduced. It represents the lever effect, and is a ratio between two distances: from the hinge to the point of force application, and from the hinge to the finger tip.

From Equation 3.1, the produced force is expected to show a quadratic relation with the applied voltage. Comparing the obtained displacement curves as functions of inputs voltages (after the correction factor is applied) to the ideal function of  $V_{in}^2$  verifies this assumption. Figure 3.6 shows the error between the experimental curve and an ideal quadratic response. This error is lower than 380 nanometers for all the free movement range, and could be explained by fabrication process imperfections and unaccounted forces present in this gripper structure. The error increases rapidly after 68 Volts with the contact between fingers.

These information over the actuation mechanisms on the FT-G30 gripper will be used in the next sections to help modeling and identifying its dynamic behavior in air and vacuum.

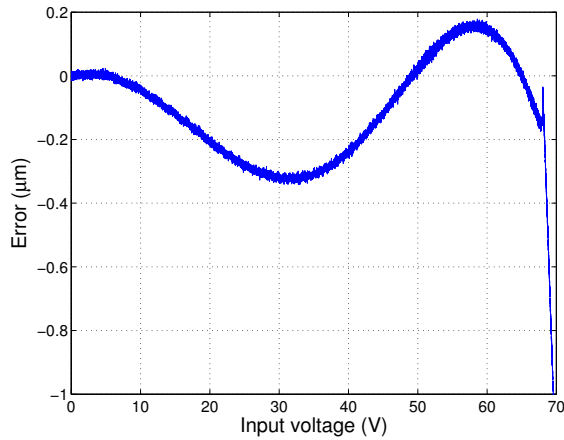


Figure 3.6: Difference between experimentally measured and theoretical displacements for the micro-gripper electrostatic actuator.

### 3.2/ IDENTIFICATION OF ACTUATED FINGER AT ATMOSPHERIC PRESSURE

This section explains the experimental identification process employed to obtain a model capable of representing the most important dynamics of the micro-gripper actuated finger in air. The proposed model was derived from other authors works on comb-drives, modified to better accommodate particularities of the studied device, and validated experimentally. During the identification process, the influence of electronic input noises related to instruments in the experimental setup used to generate the driving voltage was observed.

## 3.2.1/ EXPERIMENTAL IDENTIFICATION FOR THE GRIPPER IN AIR

For the identification process in air, the vibrometer and the sample were placed on an anti-vibration table, and small voltage steps ( $\Delta V = 0.5$  Volts) were applied at 23 different operation points ( $V_0 = [5...60]$  Volts). Based on previous works [Boudaoud, 2012, Boudaoud et al., 2013], the gray-box model in air assumes the form shown by Equation 3.3:

$$M\ddot{x} + C_i^a \dot{x} + K_i^a x = G_i^a K_{elec} V_{in}^2 \quad (3.3)$$

where  $M$  represents the mass,  $C^a$  the damping in air,  $K^a$  the stiffness in air,  $K_{elec}$  the electrostatic gain of the comb drive actuator and  $G^a$  the input gain in air (ideally  $G^a = 1$ ) for each one of the  $i$  operation points. The parameter  $M$  is considered the same for all the models. The parameter  $G^a$ , not present in previous works, is introduced here to compensate for variations in the electrostatic force, as shown in the previous section.

The gray-box identification was performed manually for each one of the operation points. This was necessary as automatic methods available in the Matlab<sup>®</sup> software did not present satisfactory and consistent results estimating the parameters for this low-damped system. This was specially true when considering systems in vacuum, as will be seen later in this chapter, where the acquisition period necessary to capture the whole system dynamics was relatively long (up to 15 or more seconds for a single excitation). Therefore, the parametric identification was performed manually.

To obtain the parameters, the experimental response curves, in time and frequency domains (via FFT), were studied. The system model described in Equation 3.3 was simulated considering different parameter values. Each one of them were adjusted individually and iteratively, so model and experimental responses were similar. Firstly, the stiffness  $K_i^a$  was chosen, with aid of the experimental data in frequency domain, to match the first vibration mode frequencies between model and experimental data, so their difference was considered acceptable (less than 1 Hz). Next,  $G_i^a$  was selected, considering the responses in time domain, to drive steady state responses to similar values. In this step, steady state errors lower than 12 nanometers were obtained when comparing experimental and simulation data. Finally, the damping  $C_i^a$  was chosen to closely capture the settling times presented by the system. Once all parameters for one of the operation points were completely identified, they were employed as an initial guesses for the model in a slightly different operation point.

During this estimation phase, the stiffness  $K^a$  and the input gain  $G^a$  presented a significant variation on their values over the studied range, while the damping  $C^a$  remained almost unchanged, therefore being considered constant. Figure 3.7 shows the relation between parameters and the operation point  $V_{in} = V_0 + \Delta V$ . The variation for the estimated stiffness and input gain was relatively small at low voltages, becoming more important with the increase of the applied tension. From experimental data, up to 25% of variation in the input gain  $G_i^a$  and more than 18% of variation in the stiffness  $K_i^a$  were observed. This variation in stiffness is translated into a shift on the first mode frequency, ranging from 992 Hz to 1090 Hz.

The obtained set of models describes the system behavior at specific operation points. Using this information, it was possible to obtain a single general model, capable of representing the actuated finger behavior over all the working range. For this purpose, the sets of parameters  $K_i^a$  and  $G_i^a$  were used to compute fitting functions  $K^a(V_{in})$  and  $G^a(V_{in})$ . These continuous functions, 3rd order polynomials computed by the linear least square method, are represented in Figure 3.7 together with the individual values computed for each operation point. Equation 3.4 gives the general model describing the actuation system in air, with stiffness and input gain defined as

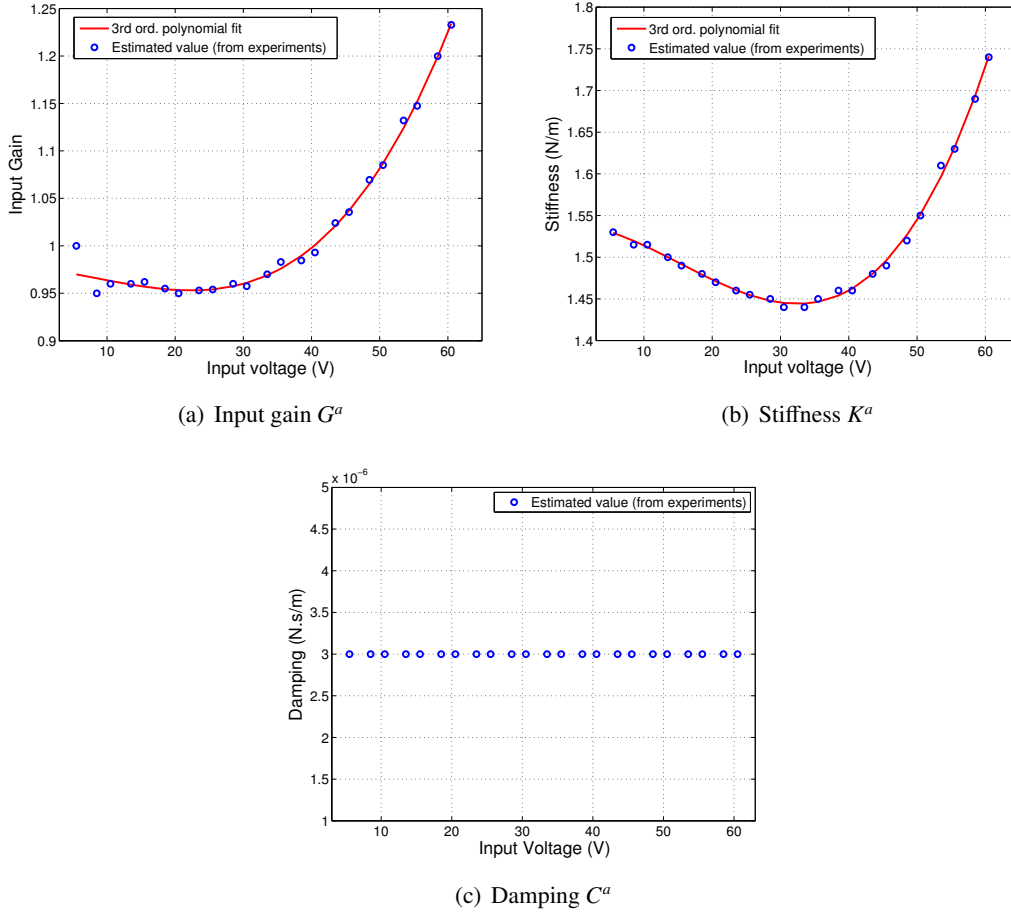


Figure 3.7: Variation of model parameters for different input voltages, in air.

polynomial functions of the input voltage:

$$M\ddot{x} + C^a\dot{x} + K^a(V_{in})x = G^a(V_{in})K_{elec}V_{in}^2 \quad (3.4)$$

A validation process was then performed by comparing the general model with a new set of experimental data in frequency and time domains, this time considering large input steps. Figure 3.8 shows the comparison between fast Fourier transforms (FFT) for experimental data and simulated models. The results show a good agreement between simulation and experimental data, with first mode frequency estimation errors smaller than 8 Hz and a steady state displacement errors lower than 110 nm across all range. For input steps larger than 35 V, a second peak can be noticed in the experimental data. In air, its effects are small when compared with the first oscillation mode, and therefore was not included in the model. However, these effects will play an important role when placing the system in vacuum, as will be seen later in this chapter. The validation step demonstrated the accuracy of the proposed general model for the operation range, and therefore it will be used as a base for comparison with the same system in the vacuum.

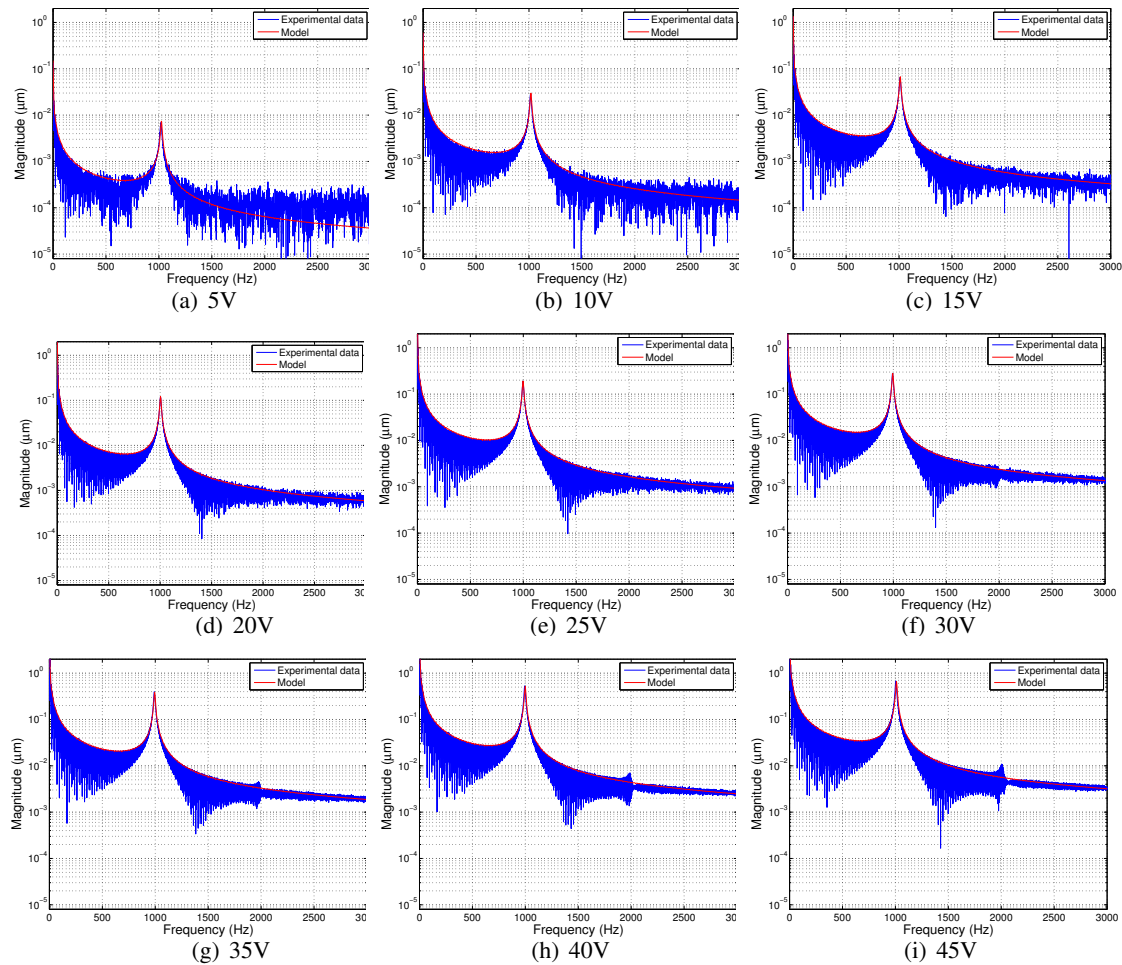


Figure 3.8: Comparison between responses for large step inputs (ranging from 5 to 45 V) in frequency domain. Experimental data is shown in blue, and simulated response based on the second order model is shown in red.

### 3.2.2/ EFFECTS OF ELECTRONIC INPUT DISTURBANCE OVER THE ELECTROSTATIC COMB-DRIVE IN AIR

An unexpected phenomenon observed during the characterization stage was the influence of electronic disturbance in the system. These effects presented little visible impact in most of the experiment, becoming evident only when computing the frequency spectrum for a constant input signal. In this case, the electronic noise injected by the power system used to control the gripper (the dSPACE controller and the power amplifier) could be noticed, generating disturbances within the 50 Hz frequency and its harmonics, and resulted in finger tip displacements of a few nanometers.

This disturbance signal can be modeled as a series of impulses, with 50 Hz frequency (Figure 3.9(a)). By simulating the system considering the general model in air and the proposed input disturbance signal, it was possible to achieve a close approximation for the results obtained experimentally. Figure 3.9(b) shows the results for the simulated and the real data in frequency domain. Both peaks amplitudes and frequencies are closely matched across the spectrum, including the decaying characteristics around the first vibration mode frequency.

This undesired external disturbance serves as an example of the problems faced on real operation situations. This issue will be further analyzed when considering the system in a vacuum

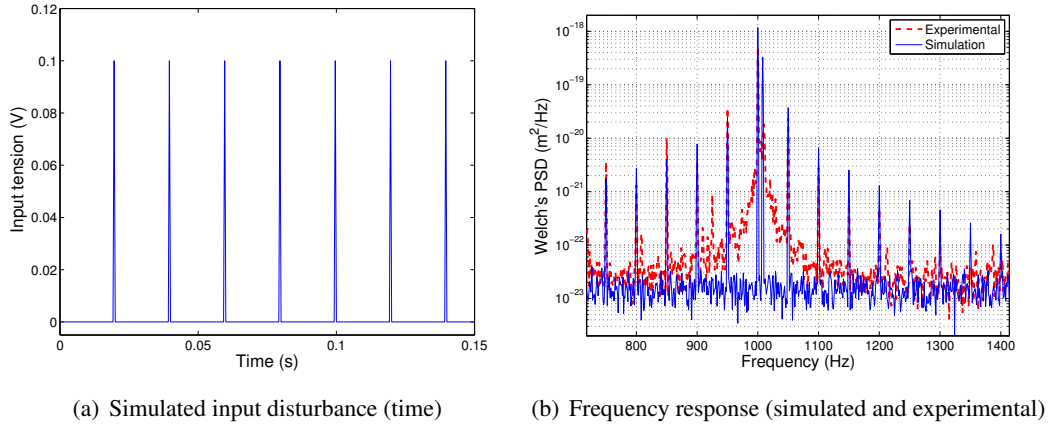


Figure 3.9: Influence of electronic input disturbance on the system in air.

environment.

### 3.3/ IDENTIFICATION OF ACTUATED FINGER IN VACUUM

This section describes measurements performed over the micro-gripper inside the SEM, at a high-vacuum in the range of  $10^{-4}$  Pa, using the vibrometer set-up described in Section 2.2. The identification in vacuum was performed similarly as in air. However, some remarks should be made in consideration to the process. In vacuum, the damping is reduced as there is no fluidic drag to slow down the movement. Consequently, longer settling times and a larger sensitivity to excitations are expected. This effect is shown for the electronic input disturbance. In addition, the existence of non-linear stiffness in this system appears more clearly in vacuum.

#### 3.3.1/ NONLINEAR STIFFNESS EFFECTS

The consequences of low pressure in the micro-gripper's behavior are visible in Figure 3.10. On the left, the time-domain data indicates a large reduction in the damping on this environment, with a settling times increasing two orders of magnitude. On the right, its frequency spectrum reveals the presence of other effects on this system, where a second peak, firstly neglected in air due to its low amplitude, became more prominent even at lower voltages. This peak does not represent the second vibration mode of our system, but a geometric non-linearity [Villanueva et al., 2013, Miller, 2005]. This phenomenon, found in literature, can be represented by the Duffing equation (Equation 3.5):

$$\ddot{x} + \iota\dot{x} + \kappa x + \beta x^3 = U \quad (3.5)$$

where the variable  $x$  represents the position,  $\dot{x}$  the velocity and  $\ddot{x}$  the acceleration for this system, and the parameters  $\iota$ ,  $\kappa$ ,  $\beta$  are constants for the damping, linear and nonlinear stiffness respectively. The input signal  $U$  is usually a sinusoidal signal. This equation describes a damped oscillator where its stiffness does not follow Hooke's law. The coefficient  $\kappa$  describes the initial linear-elastic deformation, while  $\beta$  represents the stress-strain curve for large displacements.

The non-linear term is responsible for deforming the main frequency peak and inducing

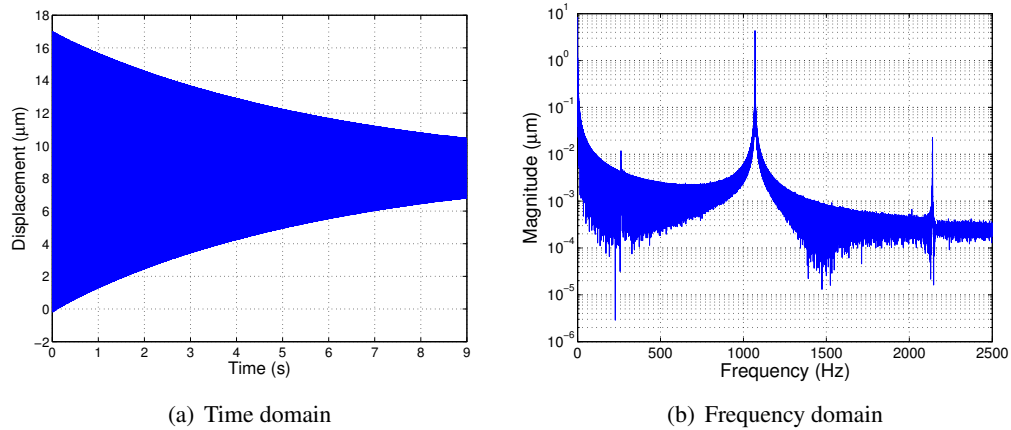


Figure 3.10: Step response for the micro-gripper in vacuum, for a 40 V step input.

others modes. A positive value of  $\beta$  is named *hardening*, and a negative, *softening* non-linearity. Although there is no general analytic solution for Equation 3.5, approximations and numerical solutions can be determined. If the input signal  $U$  excites certain frequencies on this system, and if the damping  $\iota$  is sufficiently small, the system may present multiple solutions.

The effects of the non-linear stiffness can be seen in Figure 3.11(a), representing the deformation caused by a negative  $\beta$  in a system with sufficiently small damping coefficient. The red and blue dots represent bifurcation points, where the number of roots in Equation 3.5 changes in function of the frequency. At these points, jumps in magnitude can occur (dashed lines). Figure 3.11(b) shows the experimental frequency response around the first vibration mode for an input step applied to the gripper (red continuous line) compared with a linear second order response (blue dashed line). The experimental curve is bent, similarly to the expected response for a system with a non-linear stiffness, and the presence of bifurcation points can be hypothesized.

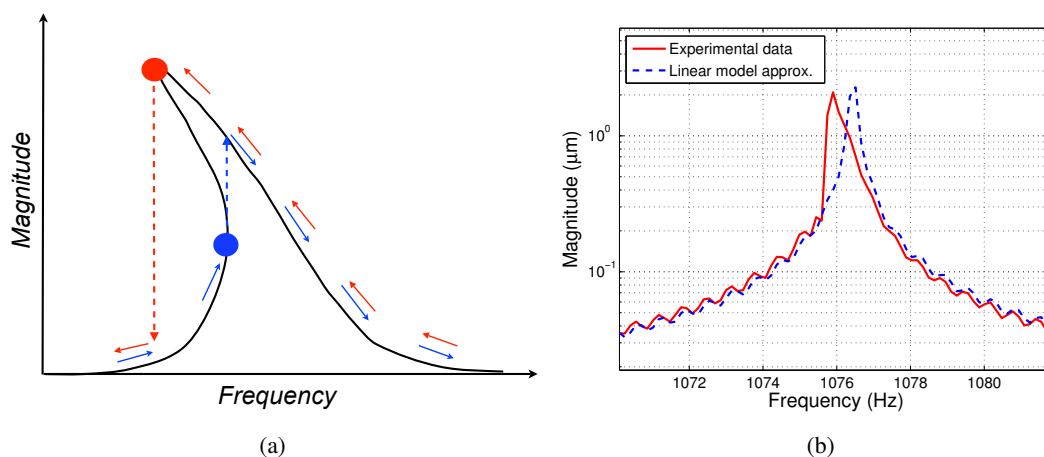


Figure 3.11: Duffing equation frequency responses. (a) shows the bifurcations (blue and red dots) for a softening non-linearity ( $\beta < 0$ ). (b) shows experimental response for the micro-gripper compared to a linear simulated response.

Although the nonlinear Duffing equation can approximate the phenomena acting over the

system, this nonlinear identification can be troublesome. The approach based on small displacements used in air is not adequate for this task, and the use of large input steps disfavors the linear parameters estimation. Even as the Duffing equation could be used to represent specific input steps (i.e. 0 to 30 V), the derivation of a single general model for all range is not straightforward. Through polynomial fitting, a good matching capable of correctly capturing the frequency peaks variation was not achieved, with errors as large as 100 Hz. For these reason, a linear representation capable of approximating both vibration peaks was favored. However, the knowledge over the system behavior will be used later in Section 4.3.2, when developing a controller for this system.

### 3.3.2/ EXPERIMENTAL IDENTIFICATION FOR THE GRIPPER IN VACUUM

Based on the collected data over the system behavior in vacuum, a different model structure was proposed considering a linear 4th order system given by Equation 3.6.

$$\begin{cases} M\ddot{x}_1 + C_i^{v1}\dot{x}_1 + K_i^{v1}x_1 = G_i^{v1}K_{elec}V_{in}^2 \\ M\ddot{x}_2 + C_i^{v2}\dot{x}_2 + K_i^{v2}x_2 = G_i^{v2}K_{elec}V_{in}^2 \\ y = x_1 + x_2 \end{cases} \quad (3.6)$$

The system consists of two parallel second order models, with independent parameters for damping, stiffness and input gain. The parameters for this model are obtained in two consecutive steps, one for each second order system, where the first equation encompasses the first oscillation mode and the second, the peak generated by the nonlinear stiffness behavior.

Using data acquired by applying small voltage steps to the system along its operation range, the parameters in vacuum  $C_i^{v1}$ ,  $K_i^{v1}$  and  $G_i^{v1}$  were estimated using the process described in the Section 3.3, while  $M$  was considered the same as identified in air. The obtained parameters showed similar trends as those obtained for the system at atmospheric pressure. The damping displayed a small variation across the studied operation points, and was considered as a constant value (Figure 3.12(a)), while stiffness  $K_i^{v1}$  and input gain  $G_i^{v1}$  presented significant variations. In the vacuum, the observed frequency range due to stiffness variations was located between 1070 and 1133 Hz.

A similar process was performed for the parameters of the non-linear stiffness equation. However, as the phenomenon is only noticeable when considering large displacements, appropriate input signals should be applied. In this case, large input steps were used to excite the system, from 0 V to values between 5 to 50 V. Results showed small variation in the parameters  $G^{v2}$  and  $C^{v2}$ , then considered constants. However, the stiffness  $K^{v2}$  presented important variations, following a slope tendency similar to  $K^{v1}$ .

To encapsulate the obtained family of models into a single one, the varying parameters were also approximated by a polynomial function of the input  $V_{in}$ . The results are presented in Figures 3.12(b) and 3.12(c), together with the corresponding polynomial function, obtained through the linear least mean square method. Figure 3.12(d) shows the obtained experimental values for  $K^{v2}$  and its fit function, capable of capturing the slope tendency of  $K^{v1}$ , its expected behavior, even if only limited number of measurement points were used.

The system of Equations 3.7 gives the final model for the micro-gripper's actuated finger operating in vacuum, where the three parameters presenting significant variation across the operation range were considered as functions of the input voltage  $V_{in}$ : the stiffness  $K^{v1}$  and  $K^{v2}$ , and the input gain  $G^{v1}$ .

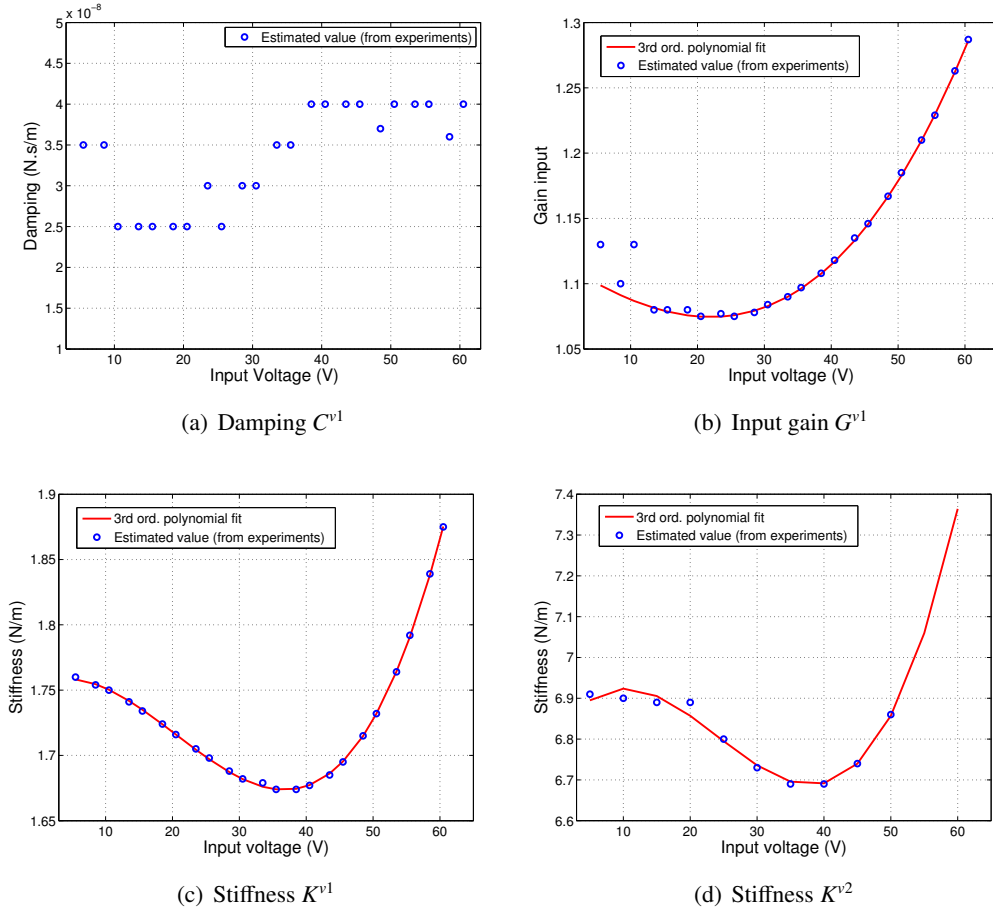


Figure 3.12: Variation of model parameters for different input voltages, in vacuum.

$$\begin{cases} M\ddot{x}_1 + C^{v1}\dot{x}_1 + K^{v1}(V_{in})x_1 = G^{v1}(V_{in})K_{elec}V_{in}^2 \\ M\ddot{x}_2 + C^{v2}\dot{x}_2 + K^{v2}(V_{in})x_2 = G^{v2}K_{elec}V_{in}^2 \\ y = x_1 + x_2 \end{cases} \quad (3.7)$$

The validation process was performed by comparing its results with experimental data obtained when applying large input steps. A comparison of experimental and simulated curves is shown in Figure 3.13. Overall, the frequency estimation error was smaller than 4 Hz for the first vibration mode and 5 Hz for the second peak, while steady state errors were lower than 400 nanometers across the measured operation points. The smaller error in frequency estimation is due to the sharper peak present on its frequency spectrum, facilitating the definition of its value in relation to air measurements. Conversely, the constant oscillation present in the time-domain data helped to increase the errors for steady state estimations.

The fourth order linear model reveals to be sufficiently precise to estimate, in frequency and time domains, the oscillatory characteristics for this system. Furthermore, the development of linear control methods is straightforward, and will be explored in the next chapter. Still, the obtained results were less accurate than those for the system in air, as demonstrated by the higher steady state error. One of the difficulties presented in this process was related to the experimental acquisition of data. The reduced damping makes the system sensible to external disturbances, and

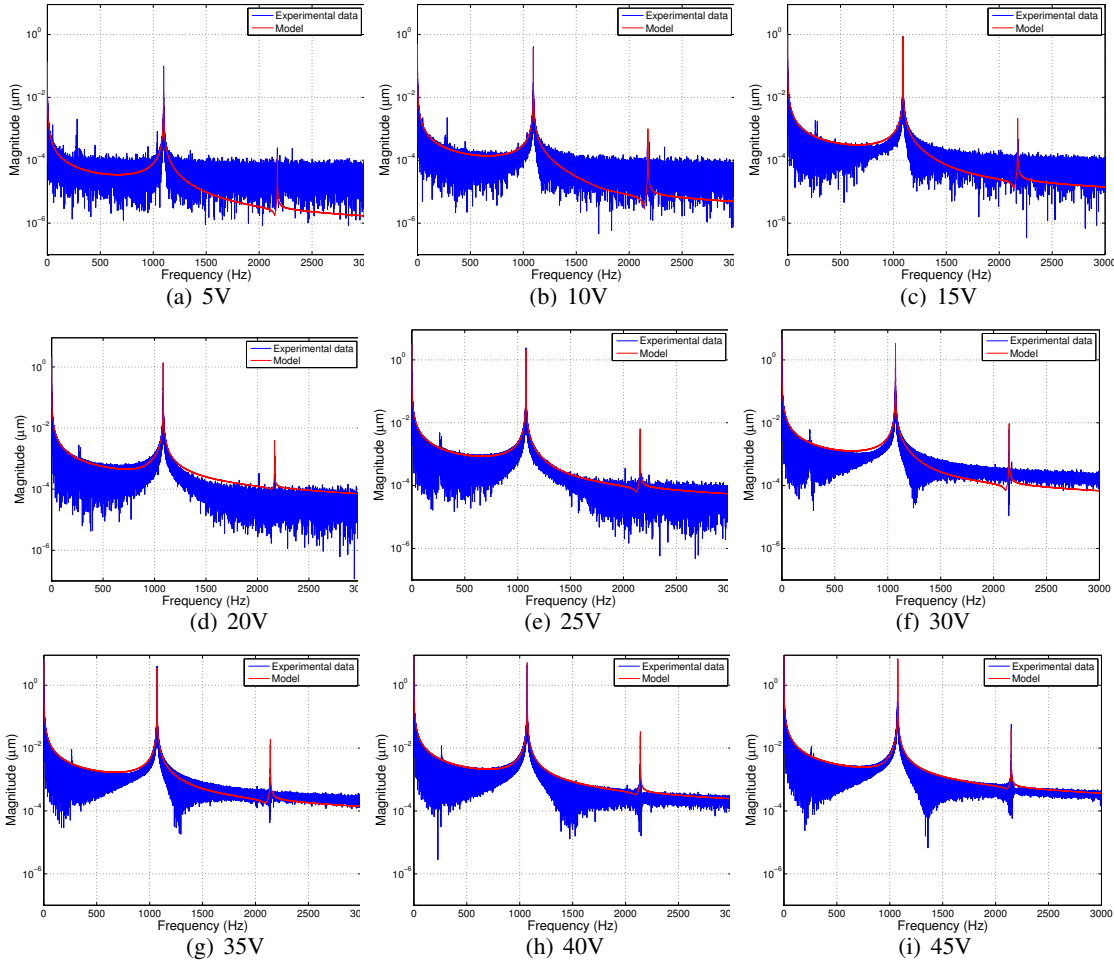


Figure 3.13: Comparison between responses for large step inputs (ranging from 5 to 45 V) in frequency domain, considering the gripper in vacuum. Experimental data is shown in blue, and simulated response based on the second order model is shown in red.

the precise data acquisition becomes more critical and time consuming.

### 3.3.3/ EFFECTS OF ELECTRONIC INPUT DISTURBANCES OVER THE ELECTROSTATIC COMB-DRIVE IN VACUUM

While operating in air, electronic input disturbances were attenuated by the added environmental damping, only noticeable under certain conditions. This is not the case the case in vacuum, where its effects gain importance and become an issue in many cases. These disturbances are easily visible in the frequency spectrum, as shown in Figure 3.14(a). This curve illustrates the Welch's PSD averaged from five measurements for a constant input of 10 V, in air and vacuum. This result indicates that the phenomenon has a much larger influence in at lower pressures, specially around the first vibration mode.

However, while this effect was limited to a few nanometers in air, the low damping aggravate its impact over in vacuum. Its influence over the gripper's behavior in this environment can be seen in Figure 3.14(b), where for a given operation point (in this case, around 53 V or  $18.7\mu\text{m}$ ), the comb-drive first mode matched one of the disturbance frequencies (in this case, 1050 Hz), producing large oscillations. In this example, vibrations up to 200 nanometers peak-to-peak

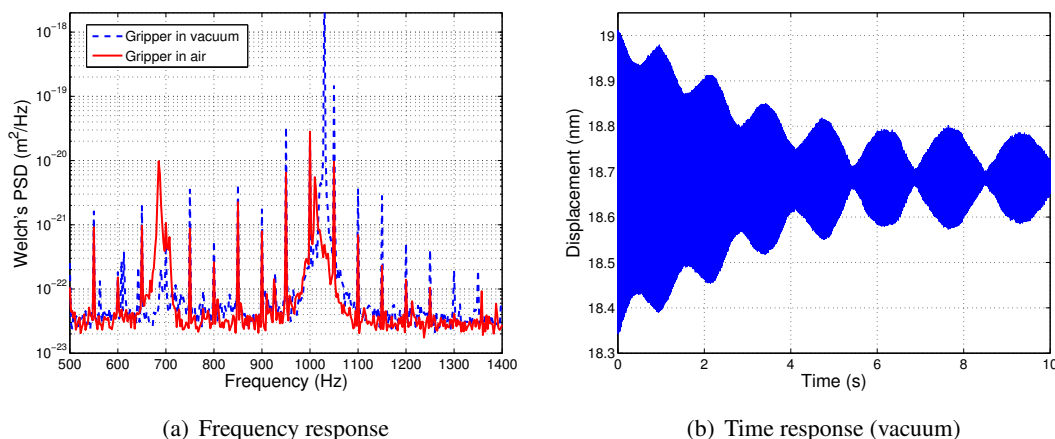


Figure 3.14: Effects of electronic input noise on the system.

were observed. These values are large in relation to the desired accuracies for this work, and imposed additional difficulties during the identification process. Although this problem was directly related to the hardware implementation of the setup, changes in the equipment were not possible at the time. This issue will be addressed in the next chapter, where the controllers should take this disturbance into account to effectively attenuate it .

### 3.4/ RESUME OF DIFFERENCES BETWEEN AIR AND VACUUM

Through the results obtained during the identification phase, the influence of pressure variation on the behavior of the tested micro-gripper is undeniable. In this work, the differences lie on a large damping variation, shifts in the resonant frequencies and on a more noticeable non-linear effects. The experimentally identified parameters are given in Table 3.1.

In [Chen et al., 2003], the relation between comb-drive parameters (thickness, electrodes separation, and others) was studied through numerical simulations, considering the flow and squeeze film generated when operating in a fluid (normally air). It concluded that, in this environment, the largest contribution to the comb-drive energy dissipation is due to the compression of fluid between fingers. Accordingly to its results, the quality factor of MEMS in air and vacuum can present variations up to 3 orders of magnitude, depending on various construction parameters [Nguyen, 1995].

The effects of gas damping can be investigated by dividing it in three regions (also called flow regimes). In the first, the pressure influence is small enough so gas damping is negligible when compared to other sources. In this region, most of the energy dissipation is related and dependent on the surface-volume ratio, the material and surface characteristics, and the gas slips with respect to the surface. A second region is defined in the opposing extreme, where pressures are high enough so gas molecules often collide with each other. In this case, the gas viscous damping is the most important dissipation mechanism, inducing a temporary mass increase in the system. The third region represents an intermediate scenario, where molecules do not interact with each other, but are still present in enough amounts so when they collide with the system, moment is transferred between them [Ho et al., 1998].

These different regions can be formally classified with the aid of the Knudsen number  $K_n$

Environment	Parameters						
	$M$	$K^{\square 1}$	$K^{\square 2}$	$G^{\square 1}$	$G^{\square 2}$	$C^{\square 1}$	$C^{\square 2}$
Air	$3.7e^{-8}$	[1.44 – 1.74]	-	[0.95 – 1.233]	-	$3e^{-6}$	-
Vacuum	$3.7e^{-8}$	[1.674 – 1.875]	[6.69 – 6.91]	[1.075 – 1.287]	$4e^{-2}$	$2e^{-8}$	$2e^{-6}$

Table 3.1: Summary of the identified parameter for the micro-gripper in different working environments.

[Mertens et al., 2003], defined by Equation 3.8:

$$K_n = \frac{\lambda}{w} = \frac{1}{D\eta w} \quad (3.8)$$

where  $\lambda$  is the mean free path the gas molecule can move before colliding with another,  $w$  is the gas layer motion width,  $D$  the gas number density and  $\eta$  the collision cross section of the gas molecule. The three regions described above are classified and named as: free molecule regime ( $K_n > 10$ ), transition regime ( $10 > K_n > 0.01$ ) and viscous regime ( $K_n < 0.01$ ). If  $K_n \ll 1$ , the gas obeys the Navier-Stokes equations of hydrodynamics, while a  $K_n \gg 1$  indicates a system following the rarefied gas dynamics theory.

The precise computation of the Knudsen number for complex shapes, like the comb-drive structure, can become a laborious exercise. From experimental results found in literature [Mertens et al., 2003, Sandberg et al., 2005, Sumali et al., 2008] the free molecule regime is attained for different micro-structures at pressures between  $10^1$  and  $10^2$  Pa, values several orders of magnitude larger than the ones usually found in SEMs. Therefore, we assumed these systems as operating in the free molecular regime, where the environment influence on its damping is negligible.

This large reduction in damping is traduced into an increase in the settling time, from 0.1 second in air to more than 10 seconds in vacuum. Figure 3.15(a) demonstrates this effect comparing both responses together, where the absence of air to brake the oscillation results in a sustained vibration for a longer period, while maintaining similar overshoot and steady state values for both environments.

Due to the low damping, the non-linearities are more discernible in vacuum. During this work, the observed effects of a non-linear stiffness resulted in the intensification of a second oscillation peak, with frequency two times the comb-drive first vibration mode. In addition, the first mode appears to be bent, indicating the presence of a softening non-linearity. Figure 3.15(b) shows a comparison between step responses for both environments in the frequency domain.

Finally, the variation in stiffness is studied. Figure 3.16 shows the values related to the first vibration mode obtained for both environments. In the literature, there are analytic models to describe the influence of pressure over the frequency mode of simple structures, such as cantilevers [Sandberg et al., 2005]. For a cantilever of thickness  $t$  and width  $w$ , these phenomena can be approximated by Equation 3.9 :

$$f_{gas} = f_{vac} \left( 1 + \frac{\pi p w M_{gas}}{4RT\rho t} \right)^{-1/2} \quad (3.9)$$

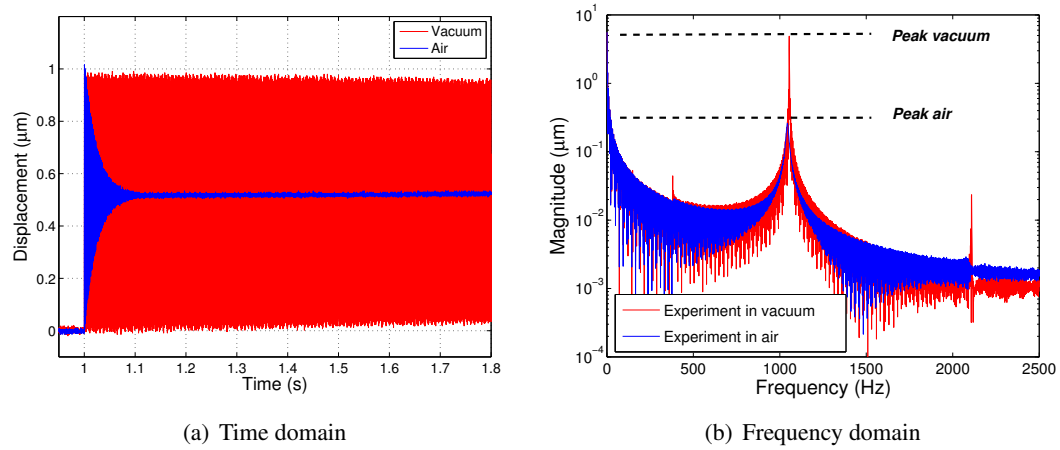


Figure 3.15: Response comparison for micro-gripper step in air (blue) and vacuum (red).

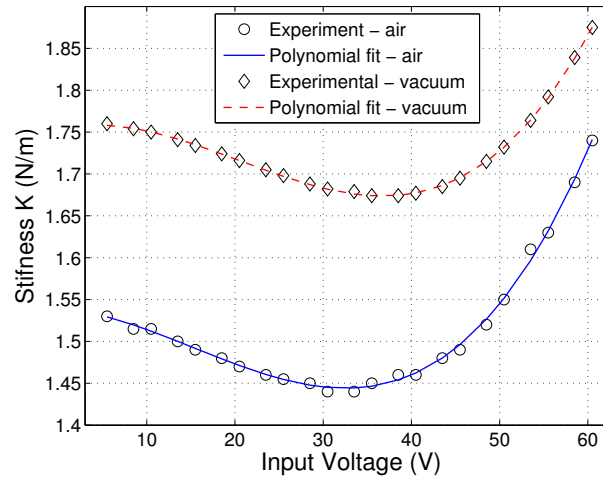


Figure 3.16: Stiffness comparison for gripper in different environments, together with its corresponding polynomial fit functions.

with  $M_{gas}$  the molar mass of the gas,  $p$  the environment pressure,  $R$  the gas constant,  $T$  the absolute temperature,  $w$  and  $t$  the cantilever width and thickness, respectively, and  $\rho$  the material density. Experimental results found in the literature shown a reasonable agreement with the theory for single and multi-layered cantilevers. However, the precise frequency shift estimation for more complex geometries is still a challenge, relying on numerical simulations.

The measured frequency shift due to pressure variations for samples with simple geometry (single and V-shaped cantilevers) was smaller than 4% in the studied references [Sandberg et al., 2005, Sumali et al., 2008, Epp et al., 2004, Zhang et al., 2005, Sader et al., 1995], while the obtained values for the comb-drive in this work ranged between 3.8% and 8.2%. This can be explained by the large contact surface between the comb-drive mechanism when compared with other cantilever structure (larger surface/volume ratio). Overall, the comparison between obtained models, in air and vacuum, highlights the difficulties in estimating the parameter variations due to pressure changes, where experimental methods are still the most spread method for obtaining reliable results.

### 3.5/ CONCLUSION

To obtain the dynamic model for the micro-gripper actuated finger, a gray-box model approach was used, where the parameters for a pre-defined dynamic equation were found. The identification process, performed in air and vacuum, showed how pressure influences its dynamic behavior, modifying its damping, stiffness and exposing non-linearities, present in vacuum and usually hidden when operating in air. To obtain models capable of capturing the most important characteristics of the system in each environment, parameters were identified at different operation points. These parameters were then employed to develop a general model for each pressure condition capable of representing the system in all its operation range, which were experimentally validated. The two general models encompass the most important system dynamics in both environments (main vibration modes, parameter variation in the working range, steady state responses) and can be used, together with information about disturbance obtained in the previous chapter, in the synthesis and simulation of controllers.

These results emphasize the importance of considering different models and parameters when operating in a vacuum environments. Although the literature offers general clues about what to expect, their precise system behavior requires in dept analysis, often recurring to experimental observation. The data acquisition process in vacuum can be challenging, even when using strategies such as these applied in this chapter, and even more when methods base on image analysis are used. Due to the especially low damping shown in vacuum, external perturbation effects are much more noticeable and require additional attention. In this work, electronic perturbations injected by the circuit responsible for generating the input voltage required a greater effort during data acquisition and processing phases. This unexpected disturbance represents a real issue for the positioning of the studied micro-gripper inside a SEM, and will be addressed during the controller development.

## POSITION CONTROL IN THE MICRO-WORLD

The precise positioning of structures with micro and nano-metric accuracies is currently a challenge restricting the grasping, handling and characterization of fragile small samples. As presented in early chapters, the limiting issues on precise position control in the micro-world include difficulties in instrumentation, reducing our ability to measure dynamic behaviors and disturbances. This work employs different robust control strategies to explore the end-effector dynamic aspects, taking advantage of the available experimental setup. The positional information supplied by the vibrometer was used to correct, in real time, undesired gripper behaviors, leading to a significant improvement in its response characteristics.

This chapter describes strategies for positioning stages and micro/nano-manipulators, highlighting their strengths and limitations. Next, the control problem inside the SEM is addressed, offering some clues about the specific challenge of operating in vacuum. Based on this information, two control strategies were selected and developed for the considered micro-gripper. Finally, simulation and experimental results are compared, validating these strategies and concluding about their strengths and weaknesses .

### 4.1/ CONTROL STRATEGIES FOR NANO-POSITIONING

All systems, and more particularly micro-systems, are subject to uncertainties. This means the output of a real system cannot be exactly predicted, and may arise from two sources: inputs (i.e. noises and disturbances) and non-considered dynamics. A model should be able to represent the input-output relation in a system, so that a resulting controller is able to impose a desired performance in closed loop to the real system. As the model cannot be fully known, uncertainties will be present, thus resulting in a degradation of the real system performance. However, effects of disturbances and uncertainties can be taken in consideration up to some extent through effective modeling, analysis and design techniques. Robustness is achieved when the system response is insensitive to these effects.

In the past years, different methods were developed and applied for researches to improve response characteristics of positioning systems. Figure 4.1 gives an overview of the different approaches found in the literature when considering control strategies applied for micro and nano-positioning of several devices (stages, cantilevers, grippers and piezotubes). This survey deals mostly with systems operating in air, and classifies the control methods in: proportional (P)-integral (I)-derivative (D),  $H_\infty$  methods, sliding modes based approaches (SM), model predictive control (MPC), open-loop control (OL), observer based control and others. It is important to remark that two or more of the strategies/control structures mentioned above can be applied simultaneously in the same controller.

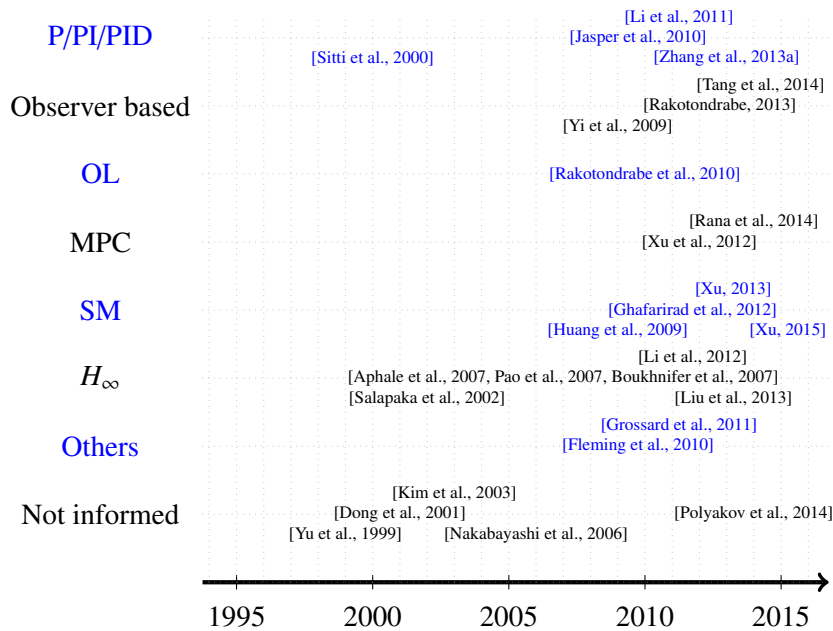


Figure 4.1: Summary on several published works considering nano-positioning control in air and vacuum, accordingly to the main strategy employed and year of publication.

- P/PI/PID: These error-based controllers are popular, with various applications in commercial devices. Their simplicity and intuitive parameter selection are major aspects making these methods attractive. In [Li et al., 2011], a PID controller was combined with an hysteresis model to control a micro-positioning stage, showing how the pre-compensation of this non-linearity can greatly improve the system response. In [Zhang et al., 2013a], two PID controllers were applied to regulate the positioning dynamics of a piezomotor. The controllers were switched depending on the desired operation mode (fine or coarse movement).
- Observer based control: This category includes disturbance observers (DO) [Yi et al., 2009], unknown input observers (UIO) [Rakotondrabe, 2013] and extended state observer (ESO)[Tang et al., 2014]. These strategies rely on estimating external disturbances in real-time based on output measurements. By modifying the control signal using this estimation, an effect similar to a disturbance feed-forward controller can be obtained. This attenuation strategy is considered proactive, while methods based on the regulation of errors, such as PID, are considered reactive and present in general slower responses to perturbations. While DO and UIO rely on the knowledge over disturbances and plant dynamics, ESO makes less restrictive assumptions as it estimates states, disturbances and plant uncertainties simultaneously. This reduced dependency on plant models, and the potential to efficiently reject disturbances are attractive properties for practical control implementations. As these are only observers, a feedback controller is still required.
- Open-loop: The use of open loop control is discussed in [Borovic et al., 2005], together with methods such as input shaping and inverse models to compensate hysteresis and other undesired effects [Rakotondrabe et al., 2010]. It was argued that, if a good model for the system is available, the control problem could be simplified though the use of open loop control methods, thus reducing the need for instrumentation.

- Model predictive control: The MPC controller relies on a constant on-line optimization process to find and simulate future plant outputs. In [Rana et al., 2014], a MPC based position controller for an AFM positioning stage was developed, aiming to reduce the piezoelectric actuator non-linearities and improve its scan speed. In the paper, it was shown how the MPC strategy can improve the stage's performance, producing faster and more accurate responses when compared to traditional proportional-integral controllers, often used for controlling this kind of device. However, this process requires constant optimization and considerable computational power, and may not be applicable for systems with fast dynamics.
- Sliding mode: This method is based on altering the dynamics of a system by applying a discontinuous, switching control signal. It presents naturally robust characteristics, with low sensitivity to parameter variations and disturbances. In [Huang et al., 2009] a mixed sliding mode/fuzzy controller for a long range nano-positioning mechanism was described. The sliding surface was used to modify the fuzzy controller gains, reducing the chattering, characteristic for this kind of controller, while presenting a small non-zero tracking error. In [Ghafari-rad et al., 2012] the control of a multi-axial piezoelectric actuator was described. In this article, the effects of hysteresis present in this kind of actuator were pre-compensated through an experimentally estimated inverse model. To further reduce errors and non-modeled dynamic effects, a sliding mode structure coupled with a neural network was proposed. A discrete sliding mode coupled with a force observer and impedance filter, to control force and position of a micro-gripper under effect of external disturbances and non-linearities, was proposed in [Xu, 2013]. The disturbances and non-linearities were estimated as a lumped parameter, based on the system's nominal model. The authors remark that, in cases of sufficiently large uncertainties and disturbances, additional control terms should be added to ensure the closed loop convergence to the sliding surface. One of the drawbacks for SM based controllers is the generated control signal, introducing chattering on the system and degrading its response. Furthermore, this signal can be harmful to actuators. Methods to reduce the chattering exist and can be implemented at the cost of complexity and added tracking error [Xu, 2015]. One of the alternative methods to reduce chattering is presented in [Xu et al., 2012], where a model predictive controller was included in the loop.
- $H_\infty$ : This class of controller relies on translating design requirements into a small-gain robust control optimization problem to be solved. In [Salapaka et al., 2002], this method was applied to improve the bandwidth and precision of nano-positioning device actuated by piezoelectric stacks over standard proportional-integral approaches, while increasing the system robustness to non-linearities and uncertainties. In [Aphale et al., 2007], a similar control structure has been applied to reduce the resonant peak amplitude for a piezo-tube. Displacements were estimated based on external shunt measurements and did not require a dedicated displacement sensor. Other control structures were explored in [Pao et al., 2007, Li et al., 2012, Liu et al., 2013], with the addition of filters and feed-forward elements to improve response times and disturbance attenuation characteristics. The challenge for this method lies on the selection of adequate weighting functions to build the optimization problem, what depends on knowledge about the plant, uncertainties and disturbance.
- Others: Different structures can be found in the literature not belonging to any of the described categories. In [Fleming et al., 2010], a linear structure called Integral Resonant Control was used to damp multiple resonant modes of a scanning probe microscope, improving its bandwidth and stability. In [Grossard et al., 2011], a mixed High Authority Control/Low

Authority Control strategy was presented. It consisted of a two degrees-of-freedom nested controller, where the inner loop damping to the system while the outer loop focused on robustness and stability issues.

- **Not Informed:** In some cases, no information about the controller was given (i.e. the micro-manipulator manufacturer provided the controller). In general, these articles described practical micro- and nano-manipulation tasks, where their goals (biological material manipulation, characterization of nano-tubes) required high-precision.

The presented survey offers a general idea about the development of control strategies for precise positioning devices. In recent years, researchers proposed different strategies, indicating that this particular problem is still open. The controller selection should take into consideration the specificities of precise positioning in SEMs. In the following subsection, a few examples of positioning task in this environment are briefly described.

#### 4.1.1/ EXAMPLES OF POSITIONING TASKS INSIDE THE SEM

Micro- and nano-manipulation inside a SEM was reported for the first time in the 1990's in Japan with the handling of micro-objects (less than  $100 \mu\text{m}$ ). It consisted of two manipulators and a working table, producing several translational and rotational degrees of freedom, driven by ultra-sonic motors for coarse and piezoelectric actuators for fine motions [Mazerolle et al., 2005]. Since then, several research groups focused their work on improving the robotic and the automation aspect of manipulation tasks, trying to achieve higher positioning resolutions. However, only a limited success was obtained. While specific cases of automation were implemented, the large majority of tasks is still being performed by human operators. In addition, closed-loop methods for controlling robotic structures rely on SEM imaging and internal sensing capabilities methods, often disregarding fast dynamic effects.

In [Yu et al., 1999], a custom build 3 DoF stage for manipulation and characterization of carbon nanotubes with approximately 50 nm thickness was proposed, using linear piezoelectric actuators and piezo-tubes to generate motion. It described the delicate operations required for separating individual samples from the substrate. These processes, made by an operator, were based on SEM image feedback while the stage was controlled by incremental steps. The authors noticed that the distance traveled by one-step displacements was not constant. Depending on the direction of movement (forward or backward), displacements between 4 and 12 nanometers per step could be produced, with occasional jumps of approximately 30 nm. The settling time for this construction in vacuum was estimated to be around 3 seconds. Similarly, the work of [Dong et al., 2002] developed a 10 DoF manipulator for carbon nanotubes with diameter varying between 30 to 50 nm. In this case, picomotors were used for coarse and piezoelectric actuators for fine motions, resulting in a system with nominal accuracy near one nanometer. The added degrees of freedom improved the manipulation capabilities of the setup. Both articles stated that, despite SEMs at the time being able to achieve image resolutions under 6 nm with slow scan speeds (improved signal/noise ratio), real-time manipulation requires faster acquisition speeds. This penalizes the image quality, resulting in effective achievable resolutions between 20 and 30 nanometers, further decreasing the positioning accuracy of tasks depending on image feedback.

In [Saeidpourazar et al., 2008], the effects of non-linearities and uncertainties limiting the dynamics of micro-manipulators inside SEM were put in evidence when using only image feedback. In this work, a commercial nano-manipulator was adopted, possessing 3 DoF and nominal precisions close to 1 nanometer. However, it did not include any position or velocity sensor. Move-

ment steps were applied in open loop, and relied on external feedback (i.e. image from the SEM) to determine its position. To improve the system, a force sensor was attached to the manipulator extremity in order to capture the interaction forces between samples and the sensing tip. With this information, and by modeling the interaction forces between both components, it was possible to estimate their separating distance. By alternating the use of position information from image and force sensor (as proposed in [Zhou et al., 1998] for a micro-manipulator in air), the closed loop control was performed. To overcome the uncertainties and non-linearities existing in the manipulator, a modified sliding mode controller was implemented. This closed loop system was then simulated, producing a faster, non-oscillatory response for step reference tracking when compared with PID controllers, even under the effects of measurement noise and small errors in the system.

In [Jasper et al., 2010], a piezo-actuated micro mobile robot to operate inside the SEM vacuum chamber was described. In this work, its position was controlled by performing line scans with the electron beam tracking a specific pattern in the robot. Using only line scans instead of full images improved the acquisition speed, capable of obtaining position data with frequencies up to 1 kHz, a large improvement from standard image acquisition and processing strategies, limited to values near 50 Hz in best case scenarios. This sensing strategy was used together with a proportional feedback gain, selected experimentally, to control the mobile micro-robot displacements with precision close to 20 nm. However, later studies shown carbon deposits around the scanned pattern after long exposures times, degrading its accuracy [Dahmen et al., 2013].

More recently, [Zhang et al., 2013a] described the development of a manipulation platform composed of two nano-manipulators, each one with 3 DoF, mounted and dismounted from a SEM through the specimen exchange chamber. This feature avoided breaking the main chamber vacuum, reducing contamination and simplifying the exchange of end-effectors. The manipulator displacements were measured through optical encoders, embedded in the actuators, with nominal resolution of 1 nanometer. During the system characterization, an encoder drift of approximately 1.2 nm/s was measured, together with an averaged precision of 98% over the traveled distance. PID controllers were developed for coarse and fine motions, and a combination of internal sensor and image servicing allowed to refine and obtain a reasonably accurate and fast positioning (under 1 second).

Another example illustrating the importance of precise position control in a SEM environment is found in [Abrahamians et al., 2014]. It describes the stiffness characterization of thin (200 nanometers) suspended membranes through the use of a vibrating tip coupled to a tuning fork. To reduce failures, sensory information from the robotic system were used to update in real-time a virtual 3D model of the SEM's interior, including positioning stage and manipulators, offering an interesting complement to the SEM image for position control and task planning. This allowed to improve the efficiency of precise positioning, specially in the Z axis. The authors commented that the probe approach phase needed to be done through nanometric steps to increase the success rate. Their remarks extended to future works when, considering even more delicate samples, sub-nanometric accuracies may be required and the effects of disturbances, uncertainties in the manipulator motion and other effects must be considered.

The available literature focusing on the positioning problem inside the SEM or in the vacuum environment is limited. The examples described above offer some insight about the specific challenges of micro- and nano-manipulation inside the scanning electron microscope, summarized next:

1. The global image produced by the SEM is one of the main sources for position feedback information. Due to its low frame rate, it limits position control to static behaviors.

2. The use of additional sensors to measure positions, velocities and forces are still limited. Furthermore, sensors and actuators may behave in unexpected ways in vacuum environment (i.e. due to the poor heat transfer).
3. Disturbances and uncertainties will disrupt the operation of components, reducing its effective performance.
4. Knowledge about the system behavior in vacuum is rarely explicitly considered on the applications.

#### 4.1.2/ CONCLUSION

Through inspecting the literature related to position control of micro and nano-manipulators, positioners and stages, it was possible to identify certain challenges present on the development of high-performance controllers for the SEM environment.

One of the most important issues is the difficulty to measure the dynamics of end-effectors position inside the SEM. A great amount of studies for positioning of end-effectors and other robotic structures were based on SEM imaging methods, and therefore limited to static and quasi-static position control. The use of image to supply feedback information for those devices, despite popular, faces a strong limitation due to its acquisition speed. By introducing other methods for position measurement and estimation, it was possible to improve overall response characteristics when positioning devices in SEM. However, as researchers shown, internal sensors can have their performance degraded in vacuum, and the characterization of components in this environment is necessary.

Due to difficulties in obtaining accurate real-time positional information for those structures, disturbance effects were rarely considered and constrained to low frequencies/static domain. Additionally, system uncertainties and variations on their dynamics were often overlooked or roughly estimated.

When considering control strategies for positioning, a wide range of different methods can be found in literature. Although most of the reviewed research deals with tasks at atmospheric pressure and the use of different sensing methods, it offers a rich panorama over the tools to be used for position control. By using the information obtained in previous chapters about disturbances acting in the SEM environment, together with a reasonably accurate dynamic model for the system, the design of control laws better adapted for this problem can be envisioned. By taking advantage of the existing experimental setup and its precise, fast, real-time data acquisition capabilities, advances in the end-effector dynamic positioning can be foreseen. It would be valuable to quantify the improvements brought by the use of specially conceived control laws to nano-manipulation.

#### 4.2/ ROBUST POSITION CONTROL STRATEGIES FOR A MICRO-GRIPPER IN VACUUM

In the previous section, various control strategies explored for position control in the micro-world were briefly presented. An essential step in control design is to identify the strategies better suited for the problem. In this particular case, the controller should present robustness to uncertainties and parametric variations, while being able to attenuate effects of disturbances.

Taking in consideration these goals, open-loop control and classic P/PI/PID controllers would require considerable efforts to achieve good performances and robustness characteristics

in all operation range. In addition, open-loop control is not capable of attenuating disturbances that, as seen in the previous chapters, are an important issue when operating in vacuum. Model predictive control offers an interesting alternative, and the optimization control problem can be formulated taking directly into consideration specific design objectives (i.e. control signal saturation, limitations on the system velocity, model uncertainties, ...). However, as it requires the online resolution of an optimization problem, the computational overhead may limit, at the current time, its practical implementation to systems with slower dynamics.

Both sliding mode and  $H_\infty$  methods can present good robustness characteristics in the face of disturbed and uncertain plants, and shown considerable performance improvements in the reviewed references over classic PID methods. Both methods, in their standard forms, were developed assuming reasonable well-known system models. The  $H_\infty$  framework offers more tools when selecting desired response characteristics, an interesting feature for this application. Furthermore, the intrinsic chattering phenomenon present in the sliding mode approach requires the use of more complex solutions, such as fuzzy or adaptive-sliding mode [Gu et al., 2014].

An alternative control strategy is the use of observer structures to estimate undesired effects in the system. This category includes Disturbance Observers (DO), Unknown Input Observers (UIO) and Extended State Observers (ESO), among others. A perturbation in the system can be estimated in real-time from the inputs and outputs. This estimation can be then used to directly attenuate its effects, similarly to a disturbance feed-forward strategy. As these are only estimators, they need to be used together with feedback control methods.

Based on this information, two strategies were selected:  $H_\infty$  and Extended State Observers. They represent two different philosophies on the controller synthesis. The  $H_\infty$  controller aims to obtain a robust controller, given that accurate information about the plant, its uncertainty range, the incident disturbance and its characteristics are available. This knowledge is then applied in the construction of an optimization problem, specific for this scenario. The resulting controller is obtained in the minimization of this problem. This strategy also allows a greater control over the requirements, the disturbances and the uncertainties to be taken into consideration, as these can be introduced separately into the problem formulation via the use of separated weighting function, as will be seen later in this chapter.

The second proposed controller was based on the Extended State Observer. This estimator aims to identify, in real-time, the effects of disturbances acting upon a system, as well as to counter them. Contrary to the  $H_\infty$  method, and to other perturbation observers such as DO and UIO, the ESO aims to reduce the need of accurate models, acknowledging that those are not often accessible or easy to obtain in many practical applications. This strategy is made possible by introducing a virtual state, called total disturbance, into the system approximate model. This total disturbance contains all external, unknown disturbance, together with plant uncertainties. The core idea consists of recognizing both disturbance and uncertainties as undesired quantities to be eliminated and, therefore, their separation into individual components, as often seen in other control strategies, is not necessary. By estimating this virtual state, it is possible to reduce disturbance effects and to improve the system robustness to uncertainties at the same time.

Both control strategies present relevant characteristics to solve the robust position control problem. This work took advantage of the available setup to obtain displacement measurements with nanometric accuracy and fast sample rates inside the SEM vacuum chamber. The setup, applied for identifying the disturbances inside the SEM and micro-gripper dynamics in vacuum, was used to perform real-time, dynamic closed-loop control, where these control strategies could be tested. This section reviews the  $H_\infty$  theory and the associated optimization problem formulation, and introduces the ESO structure and the observer gain selection, where high-gain strategy was

chosen. Before starting the controller development, a short review on linear fraction transformation (LFT) and the representations of uncertain systems is presented, summarizing how these tools are used in the context of robust control analysis and synthesis.

#### 4.2.1/ UNCERTAIN SYSTEMS AND THE LFT REPRESENTATION

In practice, all models are uncertain representations of a real system, where uncertainty is the price to be paid in exchange of reduced complexity. These uncertainties can comprise unknown/neglected dynamics and parametric variations. An accurate model is capable of correctly mapping the plants input/output set, for all possible cases. If the selected model is too simple, this assumption may be not valid for all input/output pairs. However, a set of simple models may contain enough elements to model complex behaviors.

The LFT representation is widely used to express uncertainties and to study its effects on closed loop systems. This structure is briefly introduced, and additional considerations can be found in Appendix B. The standard form for this representation is given by Figure 4.2.

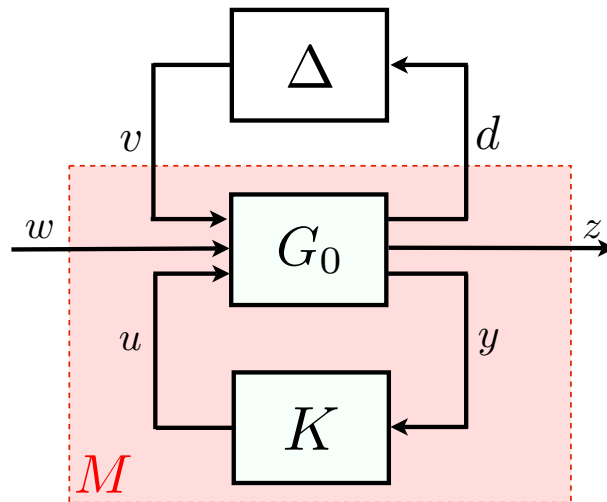


Figure 4.2: General LFT representation, containing the nominal system  $G_0$ , the uncertainty block  $\Delta$  and the controller  $K$ . During robustness analysis, the nominal plant and controller are considered as a single system  $M$ .

This representation assumes a nominal plant model  $G_0$ , where multiple dynamic uncertainties affecting it can be lumped into a single perturbation block  $\Delta$ . This block representation is usually referred as the system's uncertainty. Assuming its dynamics are not perfectly known, but norm-bounded, it is possible to represent the block  $\Delta$  by a transfer function, describing its limits that are assumed to be known. This transfer function follows a relation  $\bar{\sigma}(\delta(j\omega)) \geq \delta(j\omega)$ , with  $\bar{\sigma}$  the supreme of the singular value and  $\delta$  a known function. Uncertainties are often used to represent non-modeled time delays, high-order dynamics, hysteresis and other non-linearities.

When uncertainty comes from inaccurate description of parameters, another representation can be used, to model variations or uncertainties of some elements inside a possible bounded value range (i.e.  $a = a_0 + r\Delta$ , where the parameter  $a$  is described by a nominal value  $a_0$  and a variation range  $r$  regulated by the uncertainty  $|\Delta| < 1$ ). This can be used to represent the effects of wearing, deterioration or other alterations (i.e. due to temperature variation) present in a system.

If  $G_0$  is a matrix where each element is a transfer function between its inputs and outputs signals, the LFT becomes the closed loop transfer between  $w$  and  $z$  under the feedback effects of  $K$  (a controller) and  $\Delta$  (the system uncertainties). These connections are called  $F_l$  and  $F_u$  (lower and upper LFT), and defined in Appendix B. A common notation considers the lower feedback system as a nominal closed loop  $M$ , that is interconnected to the uncertain block  $\Delta$  by the feedback signals  $v$  and  $d$ , and the transfer map from external signals  $w$  to  $z$  can be written as:

$$\begin{aligned} z &= F_l(F_u(P, \Delta), K)w \\ &= F_u(F_l(P, K), \Delta)w \\ &= F_u(M, \Delta)w \end{aligned} \quad (4.1)$$

This structure, called the  $M-\Delta$  representation, establishes a framework to perform stability and performance robustness analysis, through the use of another tool: the Structured Singular Value, discussed next.

#### 4.2.2/ $\mu$ ANALYSIS - A TOOL FOR ROBUST STABILITY AND PERFORMANCE EVALUATION

One of the most popular methods to analyze the robustness of uncertain time-invariant systems is based on the analysis of the singular value  $\sigma$ . This value, computed as the square root of the the eigenvalues of a matrix multiplied by its transpose conjugate, is a measure of the system magnification at each frequency and its maximum value can give some information about the stability and robustness. However, this metric revealed to be conservative, as the only assumption made about the uncertainty  $\Delta$  was its boundedness. To improve this result, the structured singular value (SSV), also denoted  $\mu$ , was introduced. The analysis based on the SSV aims to refine the small-gain condition, that is based on  $\sigma$ , through the imposition of a structure to the perturbation [Doyle, 1982]. Before introducing this tool, some concepts are defined.

##### Definition 1: Infinity norm

The  $\infty$ -norm, also known as  $H_\infty$  norm, maximum norm or uniform norm, of a vector  $v(\cdot)$  is denoted  $v_\infty$  and defined as the maximum of the absolute value of their components.

$$\|v\|_\infty := \sup |v(\cdot)| \quad (4.2)$$

The  $\infty$ -norm of a linear, time-invariant, causal system  $G(s)$ , is the peak value on a bode magnitude plot of  $G(j\omega)$ , or the maximum of its singular value across the frequencies.

$$\|G(s)\|_\infty := \max_{\omega} \bar{\sigma}(G(j\omega)) \quad (4.3)$$

The  $\infty$ -norm is an important metric for many control problems, as will be seen later. A second concept that is fundamental for control system investigation is the small-gain.

##### Theorem 1: Small-gain Theorem

If two systems  $G_1$  and  $G_2$  are stable, then the closed loop formed by them (Figure 4.3) is internally stable if:

$$\|G_1 G_2\|_\infty < 1 \quad \text{and} \quad \|G_2 G_1\|_\infty < 1 \quad (4.4)$$

The theorem states that, if a system gain is lower than 1 in all directions (for all eigenvalues), for all frequencies, the energy in this loop will eventually be completely dissipated [Skogestad et al., 2007]. It is also possible to express the small-gain theorem by using LFTs.

Considering the  $M - \Delta$  structure (Figure 4.2), the internal stability can be evaluated by only considering the feedback loop. If the system  $M$  is stable, and the uncertainty block is bounded in norm  $\|\Delta\|_\infty < \beta$ , with  $\beta > 0$ , the interconnection will be stable as soon as  $\|M\|_\infty < \beta^{-1}$ .

The small-gain theorem can be used to infer about the stability of plants in a closed loop with a given controller  $K$  and, more interestingly, when a nominal system is perturbed by an uncertainty matrix  $\Delta$ . However, its application to practical problems is limited. The assumption that  $\Delta$  does not possess any particular structure (therefore being a full matrix) and only has a limited  $\infty$ -norm defines an excessively general problem. To obtain an improved, less conservative estimation of stability for more realistic problems, SSV can be applied by assuming that  $\Delta$  has a well-defined structure.

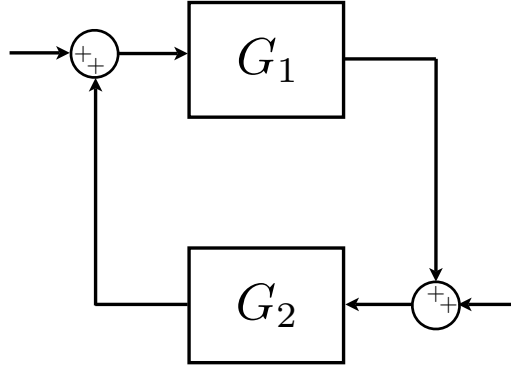


Figure 4.3: Feedback configuration for the small gain theorem.

The matrix  $\Delta$  is said structured if the uncertainties are organized accordingly to its nature, in a block diagonal form. It is always possible to find an interconnection matrix  $M$  so that  $\Delta$  will be structured [Doyle, 1985]. A general form for  $\Delta_s$  is given in Equation 4.5:

$$\Delta_s(s) = \text{diag}[\delta_1 I_{r_1}, \dots, \delta_s I_{r_s}, \Delta_1, \dots, \Delta_r] : \delta_i \in \mathcal{C}, \Delta_j \in \mathcal{C}^{m_j \times m_j} \quad (4.5)$$

where  $\delta_i$  represents the parametric uncertainties,  $I_r$  are identity matrices with adequate dimensions, and  $\Delta_j$  describes dynamic uncertainties and can contain complex elements. The block diagonal matrix  $\Delta_s$  is assumed bounded. The stability condition for a SSV is written as:

$$\det(I - M(j\omega)\Delta_s(j\omega)) \neq 0, \forall \omega \in \mathcal{R}, \forall \Delta \quad (4.6)$$

where the nominal closed loop system  $M$  is assumed to be stable. The condition implies all uncertainties in the structure small enough so Equation 4.6 does not become singular at any frequency. Analog to this result, is possible to estimate the smallest uncertainty value, for a given structure, capable of destabilizing the closed loop system. This is the structured singular value  $\mu$ , and can be used as a metric to describe the robustness of a system.

#### Definition 2: Structured singular value

The structured singular value  $\mu_\Delta(M)$  of  $M \in \mathcal{C}^{n \times n}$  with respect to  $\Delta_s$  is defined as:

$$\mu_\Delta(M) := \frac{1}{\min_{\Delta_s \in \Delta_s} \{\bar{\sigma}(\Delta_s) : \det(I - M\Delta_s) = 0\}} \quad (4.7)$$

where  $\sigma(\Delta_s)$  is the singular value of  $\Delta_s$ . If there is no value of  $\Delta_s \in \Delta_s$  so that  $(I - M\Delta_s)$  is singular, then  $\mu_\Delta(M) := 0$ .

Definition 2 is, in essence, similar to the small-gain theorem. If the uncertainty  $\Delta_s$  is bounded by  $\|\Delta_s\|_\infty < \beta$ ,  $\forall \Delta_s \in \Delta_s$ , the perturbed system  $M$  is robustly stable, with respect to  $\Delta_s$ , if and only if  $\mu_\Delta(M) \leq \beta^{-1}$ . Furthermore, if the disturbance matrix set is normalized, such as:

$$\mathbf{B}\Delta_s := \{\Delta : \bar{\sigma}(\Delta) < 1, \Delta \in \Delta_s\} \quad (4.8)$$

the stability condition becomes  $\mu_{\Delta}(M(s)) \leq 1$ . In this case, the value of  $\mu_{\Delta}(M)$  can provide an estimation on how much uncertainty  $\Delta_s$  can be tolerated before destabilizing the closed loop.

The search of  $\mu_{\Delta}(M)$  constitutes a NP-complete problem, growing in complexity for large dimension, and the computation of its exact value can be prohibitive. Fortunately, there are different methods to estimate its upper and lower bounds  $\mu_{u\Delta} > \mu_{\Delta} > \mu_{l\Delta}$ . These values can be computed with relative simplicity for cases where the structured uncertainty matrix is composed of purely complex or complex/real elements. In the cases where its elements are purely real values, the lower boundary estimation may present large imprecision. To improve this computation, adding a small magnitude complex component to the uncertainties is a common practice. More details in the boundary computation methods can be found in [Packard et al., 1993, Braatz et al., 1994].

Apart from stability, robustness in performance is also highly desired in practical applications. The resulting regulation and tracking characteristics between nominal and real system can vary largely, specially when external disturbances are considered. This variation can render a controller unacceptable for a task, despite still being stable. The robust performance test is developed to indicate how the controller can handle this degradation.

To analyze closed-loop performances, the transfer from input to output becomes a function of  $\Delta$ , and the complete matrix  $M$  needs to be considered. Robust performances can be studied by introducing fictitious uncertainty blocks  $\Delta_f$  across the inputs and outputs channels, thus generating an augmented uncertainty block  $\Delta_{aug}$  (Figure 4.4). By introducing this block, it is always possible to reformulate the robust performance problem in the stability framework [Doyle, 1985, Skogestad et al., 2007]. Therefore, the bounds for performance indicators  $\mu_{u\Delta}^{perf}$  and  $\mu_{l\Delta}^{perf}$  are obtained in the same manner as for the stability analysis problem.

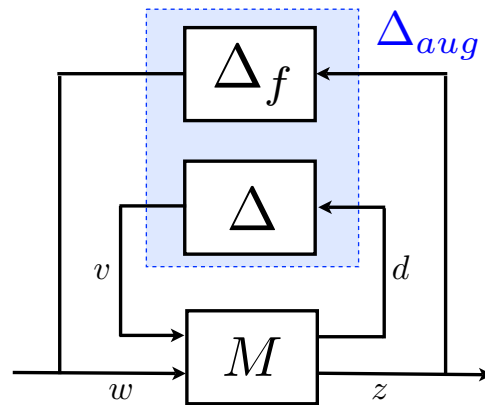


Figure 4.4: LFT representation for the augmented structured disturbance  $\Delta_{aug}$ , applied in the case of robust performance analysis.

#### 4.2.3/ $H_{\infty}$ CONTROLLER

Following the development of uncertainty representation and the small gain theorem in the late 1960's, George Zames [Zames, 1981] proposed the solution of feedback gain selection as an optimization problem, aiming to minimize an operator norm. The  $H_{\infty}$  was originated to solve a fundamental problem of sensitivity in a feedback loop, constraining signals in the loop to achieve a desired requirement, expressed in terms of a  $\infty$ -norm.

Consider a linear, time invariant system  $P(s)$  with two sets of inputs and outputs, represented in Figure 4.5. The  $H_{\infty}$  framework aims to minimize the relation between external input signals  $w$  (representing disturbances, reference signals, noises, ...) and output  $z$  containing tracking errors, control actions and other signals of interest. To achieve this goal, the measurement  $y$  is used to derive an input signal  $u$ . This mapping between  $y$  and  $u$  is given by a dynamic controller  $K$ , rendering the loop stable. This structure can be easily represented in the LFT framework.

The loop transfer functions can offer further insight on how to define specific design requirements into the  $H_\infty$  framework. For a given plant  $G_0$ , and considering a classical feedback loop structure, different relations between inputs and outputs are obtained:<sup>1</sup>:

- Loop transfer function:  $L(s) = K(s)G_0(s)$ ;
- Sensitivity function:  $S(s) = \frac{1}{1+K(s)G_0(s)} = (1 + L)^{-1} = \frac{e}{r}$
- Complementary sensitivity function:  $T(s) = \frac{K(s)G_0(s)}{1+K(s)G_0(s)} = S(s)L(s) = \frac{y}{r}$
- Control sensitivity function :  $\frac{K(s)}{1+K(s)G_0(s)} = K(s)S(s) = \frac{u}{r}$

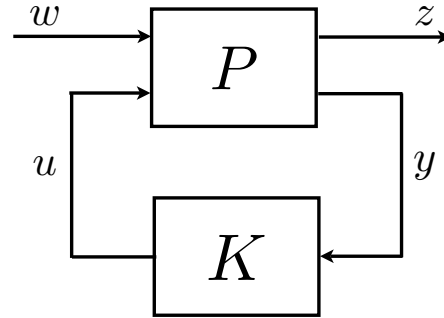


Figure 4.5: Basic structure for the  $H_\infty$  problem, in the LFT representation.

In Figure 4.6, the closed loop scheme is shown. The external reference signal  $r$ , the disturbance  $d$  and the noise  $n$  form the exogenous vector  $w$  while  $z_1, z_2$  and  $z_3$  are the signals forming the output vector  $z$ . The system  $G$ , together with weighting functions  $W_1, W_2, W_3$  (used to shape the desired response during the minimization process) and  $W_d$  (describing the disturbance characteristics) form the augmented system  $P$ , resulting in a loop structure equivalent to the one presented in Figure 4.5.

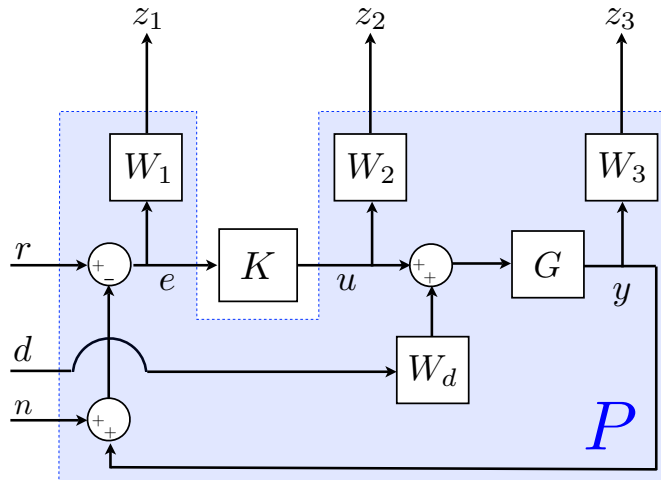


Figure 4.6: Block diagram representing the augmented plant  $P$ , obtained from a nominal system  $G$  and the weight functions  $W$ . This structure is applied in the framework of  $H_\infty$  synthesis to obtain the controller  $K$  minimizing a relation between inputs ( $r, d, n$ ) and outputs in  $z$ .

Sensitivity and complementary sensitivity are connected by the algebraic constraint  $T = 1 - S$ . It imposes a trade-off in the closed loop response, put in evidence by Equation 4.9. It describes the influence of each input over the output  $y$ .

<sup>1</sup>In this case, the sensor dynamics was not considered

$$y = \underbrace{(I+L)^{-1}Lr}_T + \underbrace{(I+L)^{-1}Gd}_S - \underbrace{(I+L)^{-1}Ln}_T \quad (4.9)$$

To obtain zero tracking error,  $S \rightarrow 0$ , or equivalently  $T \rightarrow I$ , the loop transfer  $L$  must have a large value. However, this also implies a direct transfer from noise. In addition, a large value of  $L$  is related to large control gains, what can be undesired, saturating the control signal and even damaging the actuators.

This conflict can be partially solved by selecting different gains accordingly to the frequency ranges. By choosing  $|L| > 1$  over low frequencies ensures that sufficiently slow reference transitions will be correctly tracked, while disturbances in these frequencies will have reduced effects. At high frequencies, where measurement noises are usually found, the gain  $L$  is made sufficiently small to disregard this effects. The selection of  $L$ , therefore, defines performance trade-offs to be made during controller synthesis.

In the framework of  $H_\infty$  control, desired performances can be imposed by the selection of appropriate weighting functions  $W_1$ ,  $W_2$  and  $W_3$ . By selecting them as frequency dependent ( $W(j\omega)$ ), complex requirements and specifications can be defined, and additional information (i.e. the disturbance dynamics) can be included in the problem. When multiple weighting functions are employed, the requirement conditions are written as:

$$\begin{cases} \|W_1(s)S(s)\|_\infty < \gamma^{opt} \\ \|W_2(s)S(s)K(s)\|_\infty < \gamma^{opt} \\ \|W_3T(s)\|_\infty < \gamma^{opt} \end{cases} \quad (4.10)$$

where  $\gamma^{opt}$  is the minimal (optimal) value, representing its performance level. The solution for this problem is not unique except in the scalar case. If  $\gamma^{opt} \leq 1$ , all the requirements are achieved. In practical design, the computation of an optimal controller may be too numerically demanding. Hence, it is common to accept sub-optimal stabilizing controllers, so that the norm value is  $\gamma \rightarrow \gamma^{opt}$ , with  $\gamma > \gamma^{opt}$ .

The optimization process in the  $H_\infty$  methodology searches for the dynamic controller  $K(s)$  that stabilizes the system and, at the same time, minimizes the positive scalar  $\gamma$  value in the Inequation system 4.10.

By representing the augmented plant  $P$  and partitioning it as shown in Equation 4.11:

$$\begin{cases} \dot{x} = Ax + B_1w + B_2u \\ z = C_1x + D_{11}w + D_{12}u \\ y = C_2x + D_{21}w + D_{22}u \end{cases} = \begin{bmatrix} A & B_1 & B_2 \\ C_1 & D_{11} & D_{12} \\ C_2 & D_{21} & D_{22} \end{bmatrix} = \begin{bmatrix} P_{11} & P_{12} \\ P_{21} & P_{22} \end{bmatrix} \quad (4.11)$$

the system can be easily represented by a lower LFT, and the resolution a sub-optimal  $H_\infty$  problem is summarized as:

$$\min_K \|F_l(P, K)\|_\infty, \text{ given that } K \text{ stabilizes } P \quad (4.12)$$

Several methods are available to solve Equation 4.12 and to find the controller  $K(s)$  that minimizes  $\gamma$ . The most popular are based on the DGKF algorithm [Doyle et al., 1989] (that solves simultaneously two algebraic Riccati equations) and based on linear matrices inequalities (LMIs) [Gahinet et al., 1994]. The DGKF algorithm, firstly limited by assumptions on the problem's structure, was later expanded to encompass larger classes of systems

[Green et al., 1990, Stoorvogel, 1991, Scherer, 1992]. In other hand, the LMI based approach [Gahinet et al., 1994] presented a less restrictive algorithm for minimizing the cost function, at the expenses of larger computational effort. In [Liu et al., 2006], a demonstration for duality between this two methods shown, under certain assumptions.

#### 4.2.4/ EXTENDED STATE OBSERVER STRUCTURE

In the  $H_\infty$  approach, the controller is obtained based on information about the model, its range of uncertainty and parametric variations, and also over the characteristics of disturbances affecting the system (frequencies and amplitudes). This approach is, among others, heavily dependent on modeling and plant characterization. In the middle of the 1990's, Jingqing Han proposed a new control structure, named Extended State Observer (ESO). He argued that modern control theory was too much focused on modeling, model-based analysis and synthesis [Gao et al., 2001]. Despite bringing important advances in the field, this paradigm had fundamental limitations, mostly when dealing with robustness issues, relying heavily on accurate plant representation. Han contemplated if effective control could be achieved only based on general information of the physical process and measurement data obtained in real time.

The goal of perturbation observers is to identify, in real time, an unmeasured signal/uncertainty responsible for deviating the system from its desired/nominal performance and to compensate it. The core difference between ESO and other disturbance rejection methods, like Unknown Input Observer, Disturbance Observer and Perturbation Observer is that this method does not distinguish between external disturbances and model uncertainties, while others rely explicitly on the mathematical modeling of one or both elements [Schrijver et al., 2002, Radke et al., 2006]. This apparent small difference represented an important design methodology shift, focusing on system perturbations instead of modeling. Its structure addresses realistic disturbances and plant uncertainties while maintaining its simplicity. The main ideas shaping the ESO methodology are presented next.

Considering a generic, nonlinear, single-input single-output system in state space representation:

$$\begin{cases} \dot{x}_1 &= x_2 \\ \dot{x}_2 &= x_3 \\ &\vdots \\ \dot{x}_n &= a(x, d) + b(x, d)u \\ y &= x_1 \end{cases} \quad (4.13)$$

where  $x_i$ ,  $i = 1, \dots, n$  represents the system states,  $u$  the control input,  $y$  the measured output,  $d$  an external, bounded disturbance and  $a(x, d)$  and  $b(x, d)$  are nonlinear functions describing the system dynamics. It is assumed the existence of a state feedback controller  $\Phi(x)$  stabilizing the system origin  $x = 0$  in closed loop. To implement this controller only using the available output measurements, state estimation is necessary.

In most practical applications, values for  $a(x, d)$  and  $b(x, d)$  can be approximated through physical modeling and identification techniques, with varying degrees of accuracy. Supposing these functions can be approximated by nominal models,  $\hat{a}(x)$  and  $\hat{b}(x)$ . Next, an auxiliary variable is introduced,  $\sigma$ , and it is defined as:

$$\sigma = a(x, d) - \hat{a}(x) + [b(x, d) - \hat{b}(x)]u \quad (4.14)$$

This variable represents the sum of modeling errors and external disturbance acting over the system, and is called total disturbance. By combining Equations 4.13 and 4.14, and introducing  $\sigma$  as a new virtual state, it is possible to obtain an equivalent, augmented representation of the original system:

$$\begin{cases} \dot{x}_1 = x_2 \\ \dot{x}_2 = x_3 \\ \vdots \\ \dot{x}_n = \sigma + \hat{a}(x) + \hat{b}(x)u \\ \dot{\sigma} = \phi(x, d, \dot{d}, u, \dot{u}) \\ y = x_1 \end{cases} \quad (4.15)$$

Instead of estimating the original states, it is possible to develop an observer for the augmented representation, assuming the virtual state dynamics  $\phi(x, d, \dot{d}, u, \dot{u})$  is bounded. An observer structure for the augmented system takes the general form of Equation 4.16, where  $h_i$  are function of the estimation error.

$$\begin{cases} \dot{\hat{x}}_1 = \hat{x}_2 + h_1(y - \hat{x}_1) \\ \dot{\hat{x}}_2 = \hat{x}_3 + h_2(y - \hat{x}_1) \\ \vdots \\ \dot{\hat{x}}_n = \hat{\sigma} + \hat{a}(\hat{x}) + \hat{b}(\hat{x})u + h_n(y - \hat{x}_1) \\ \dot{\hat{\sigma}} = h_{n+1}(y - \hat{x}_1) \end{cases} \quad (4.16)$$

The core idea of the ESO methodology is that, if the states can be closely tracked by the observer, then a controller can use the estimated states and total disturbance in the feedback. Building the control signal  $u$  as:

$$u = \frac{1}{\hat{b}(\hat{x})}(-\hat{\sigma} - \Phi(\hat{x})) \quad (4.17)$$

and substituting it in Equation 4.15, results in a Equation 4.18:

$$\begin{cases} \dot{x}_1 = x_2 \\ \dot{x}_2 = x_3 \\ \vdots \\ \dot{x}_n = \hat{a}(x) - \Phi(\hat{x}) \\ y = x_1 \end{cases} \quad (4.18)$$

assuming the estimation of  $\sigma$  is sufficiently close to its real value. This equation indicates the system will follow the dynamics defined by the nominal model  $\hat{a}(x)$ , and a state feedback control  $\Phi(\hat{x})$  can be designed for this nominal system. Furthermore, if the observer is sufficiently fast, dynamic external disturbances can be estimated and attenuated.

An interesting advantage of this method is that it requires only an approximated knowledge about the system dynamics, and only supposes the boundedness of external disturbances.

However, some remarks should be made about the selection of the function  $\hat{a}$ . The ESO method is often robust enough to accept  $\hat{a} = 0$ , what indicates that the whole plant dynamics is unknown and will be estimated by  $\hat{\sigma}$ . Nonetheless, [Zheng et al., 2012] demonstrated how this function can have a significant impact over the its transient response. The article shown that, as  $\hat{a}$  approximated the real value, better results could be achieved (faster disturbance rejection and settling times, and less oscillatory responses). Therefore, any knowledge about these dynamics should be considered.

Choosing the observer functions  $h_i$  is the final design step. In the literature, several methods are proposed, but [Guo et al., 2011] points out its tuning process in various of those strategies remains largely experimental. The original work of Han proposed the use of a special function, combining linear and nonlinear elements [Gao et al., 2001, Tang et al., 2014]. Classic linear Luenberger observers have also been used in [Yang et al., 2009]. The use of sliding mode observers has been reported with good results in [Wang et al., 2003], as well as the development of hybrid tuning methods, which include switching gains and the use of optimized filters to reduce the influence of noise [Madoński et al., 2015].

Another method is funded on the use of high-gains [Freidovich et al., 2008, Guo et al., 2011, Khalil et al., 2014] for the function selection. In this case,  $h_i$  are chosen as linear functions, selected as constant large gains to be multiplied by the observer estimation error. This class of observers presents performance recovery properties, indicating that a controller considering output feedback and estimated states will behave similarly to a state feedback one. This includes recovering the region of attraction on non-linear controllers. In addition, [Tian et al., 2009] highlighted the stability demonstration of the ESO with  $h_i$  selected by the high-gain method can be achieved for problems with less restrictive assumptions. From the practical point of view, it can be easily parametrized, reducing the number of tuning variables and resulting in a straightforward design approach. Due to these characteristics, the observer gains  $h_i$  will be chosen accordingly to the high-gain methodology.

#### 4.2.4.1/ HIGH-GAIN OBSERVER

High-gain observers firstly appeared in the context linear feedback, to provide robust properties [Doyle et al., 1979]. The need for robust observers arose from the fact that state feedback methods, such as linear quadratic regulators, presented impressive robustness properties for gain and phase margins only for the full state-feedback case. However, in practice, only a limited number of states are available for measurement, and the use of observers and Kalman filters is necessary. In this case, no guaranteed robustness properties by the controller was held, and every design needed to be analyzed individually. This problem became known as the loop transfer recovery (LTR) [Athans, 1986]. Through the use of high gains, a trade-off is proposed, where closed-loop stability margins can be improved to the point of recovering the full-state feedback performance, at the cost of reduced noise rejection.

Similar properties were later shown for classes of nonlinear systems. A demonstration of the separation principle for a class of nonlinear systems is shown in [Atassi et al., 1999], where it was possible to independently design the controller and a sufficiently fast high-gain observer. Furthermore, it also indicated, for adequately selected parameters, the convergence of the state feedback and output feedback trajectories. This difference could be made sufficiently small to recover certain closed loop characteristics for some nonlinear systems, including their region of attraction and asymptotic stability at the origin [Khalil et al., 2014].

The following example, based on a second order dynamic system, is taken to explain the methodology, and its generalization for high-order systems is straightforward. Assuming a general

system given by Equation 4.19:

$$\begin{cases} \dot{x}_1 = x_2 \\ \dot{x}_2 = f(x, u, w, d) \\ y = x_1 \end{cases} \quad (4.19)$$

where  $d$  the vector of disturbance inputs,  $w$  the vector of known exogenous signals,  $u$  the control input and  $y$  the measured output. The function  $f$  is locally Lipschitz in  $(x, u)$  and continuous in  $(d, w)$ . If a state feedback control  $u = \Phi(x, w)$  stabilizes the closed loop system at  $x = 0$  is available, its implementation will depend on the correct state estimation. An observer taking the form described by Equation 4.20 is proposed:

$$\begin{cases} \dot{\hat{x}}_1 = \hat{x}_2 + h_1(y - \hat{x}_1) \\ \dot{\hat{x}}_2 = \hat{f}(\hat{x}, u, w) + h_2(y - \hat{x}_1) \end{cases} \quad (4.20)$$

where  $\hat{f}(x, u, w)$  is the nominal model of  $f(x, u, w, d)$ . If the function  $f$  its sufficiently known, it is possible to assume  $\hat{f} = f$ . In most cases, however, this is not valid. The estimation error for the observer is defined as the vector  $\tilde{x}_i = x_i - \hat{x}_i$ . The estimation of error dynamics  $\dot{\tilde{x}}$  can be obtained using Equations 4.19 and 4.20, resulting in Equation 4.21:

$$\begin{cases} \dot{\tilde{x}}_1 = -h_1\tilde{x}_1 + \tilde{x}_2 \\ \dot{\tilde{x}}_2 = -h_2\tilde{x}_1 + \delta(x, \tilde{x}, w, d) \end{cases} \quad (4.21)$$

where  $\delta(x, \tilde{x}, w, d)$  is a function representing the error estimation in the system dynamics  $f - \hat{f}$ . To verify the observer stability, two cases must be studied. Considering the ideal case, where the function  $\delta(\cdot)$  is zero (representing a system with no external disturbances and with a perfectly known model), the asymptotic convergence of Equation 4.21 is achieved when its characteristic matrix,

$$\begin{bmatrix} -h_1 & 1 \\ -h_2 & 0 \end{bmatrix}$$

is Hurwitz. This holds for any positive constant values of  $h_1$  and  $h_2$ . However, this is hardly the case, and  $\delta(\cdot)$  should be considered. In this situation, it would be interesting to minimize the influence of uncertainties over the estimation error. By examining Equation 4.21, the transfer function from  $\delta(\cdot)$  to  $\tilde{x}_i$  can be represented by:

$$T_{\delta\tilde{x}}(s) = \frac{1}{s^2 + h_1s + h_2} \begin{bmatrix} 1 & 1 \\ s + h_1 & 0 \end{bmatrix} \quad (4.22)$$

Equation 4.22 puts in evidence the impossibility to completely eliminate uncertainties and disturbance influences over the estimation error. Still, it can be reduced to a sufficiently small value over all frequency range by minimizing  $\sup_{\omega} \|T_{\delta\tilde{x}}(j\omega)\|$ . Rewriting Equation 4.22 in the following form:

$$T_{\delta\tilde{x}}(s) = \frac{\frac{1}{\sqrt{h_2}}}{\left(\frac{s}{\sqrt{h_2}}\right)^2 + \frac{h_1}{\sqrt{h_2}} \frac{s}{\sqrt{h_2}} + 1} \begin{bmatrix} \frac{1}{\sqrt{h_2}} \\ \frac{s}{\sqrt{h_2}} + \frac{h_1}{\sqrt{h_2}} \end{bmatrix} \quad (4.23)$$

indicates this minimization objective can be met if the ratio  $\frac{h_i}{\sqrt{h_2}}$  is a constant positive real number, and the value of  $h_2$  tends to infinity. This can be implemented by selecting the observer gains as:

$$h_i = \frac{\alpha_i}{\varepsilon^i} \quad (4.24)$$

for positive constant values of  $\alpha$ , and with a positive value of  $\varepsilon \ll 1$ . This assigns the observer eigenvalues to be  $1/\varepsilon$  times the roots of the polynomial  $s^2 + \alpha_1 s + \alpha_2$ . Therefore, for a small enough value of  $\varepsilon$ , the observer dynamics can be made much faster than the system response under state feedback, and the influence of  $\delta$  over it can be reduced.

Further investigation on the observer characteristics can be performed in the time-domain. For this purpose, the estimation errors should be scaled as:

$$\zeta_1 = \frac{\tilde{x}_1}{\varepsilon}, \quad \zeta_2 = \tilde{x}_2 \quad (4.25)$$

Combining the scaled variables with Equation 4.21 results in the following singularly perturbed equation:

$$\begin{aligned} \varepsilon \dot{\zeta}_1 &= -\alpha_1 \zeta_1 + \zeta_2 \\ \varepsilon \dot{\zeta}_2 &= -\alpha_2 \zeta_1 + \varepsilon \delta(x, \tilde{x}, w, d) \end{aligned} \quad (4.26)$$

Equation 4.26 shows the effect of  $\varepsilon$  on the response: smaller its value is, smaller will be the effects of modeling errors and disturbances  $\delta$  over the estimation, and faster the observer dynamics will be. However, Equation 4.25 also indicates the transient response can be large when the initial conditions  $x_1(0) \neq \hat{x}_1(0)$ , in what is called peaking phenomenon [Esfandiari et al., 1989, Esfandiari et al., 1992].

Although the estimation error may decay fast and converge to its true value, the peak value tends to an impulsive-like behavior when  $\varepsilon \rightarrow 0$ , which degrades the response and may even destabilize the closed loop system and damage actuators and other components. As this peak is an artifact introduced by the observer, it can be safely disregarded, what can be achieved by designing the control law and the function  $\hat{f}(\hat{x}, u, w)$  to be globally bounded in  $\hat{x}$ . In practice, this means limiting the operation range of our system by saturating the control  $u$  and/or the estimation  $\hat{x}$  outside a compact set of interest.

Due to the fast high-gain observer dynamics, the estimation error should be of order  $O(\varepsilon)$  after this short transient period. By introducing saturation, the real plant state  $x$  is limited during the peaking phenomena, and the observer converges faster to the real value. In [Freidovich et al., 2008, Khalil, 2008], it was shown that, for sufficiently small values of  $\varepsilon$ , an output feedback controller using the states estimated by this method will closely approach the trajectories of a full state feedback controller, with errors of order  $O(\varepsilon)$ , and will recover its stability and performance characteristics.

This controller is based on the separation procedure, where it is designed as if the full states were available, and the observer is designed independently. The separation principle is well known in the context of linear systems, and similar forms for different classes of non-linear systems can be found. However, [Khalil et al., 2014] emphasized that in high-gain observers, trajectory recovery can be achieved by making the observer sufficiently fast. This feature allows designing state feedback controllers to meet design specifications and, by tuning the observer with decreasing values of  $\varepsilon$ , bringing output feedback trajectories closer to the state feedback ones.

As stated in the start of the discussion about high-gain observers, its recovery properties and robustness come at the cost of an increased sensibility to measurement noises, due to the fact

that this observer approximates a differentiator. In the presence of high frequency noises, this derivation effect can lead to a reduction in the signal/noise ratio. Assuming a measurement noise  $n$  is limited by  $\mu = \sup |n|$ , its effect on the state estimation error takes the form:

$$\|x(t) - \hat{x}(t)\| \leq c_1 \varepsilon + c_2 \frac{\mu}{\varepsilon}, \quad \forall t \geq T \quad (4.27)$$

for positive constants  $c_1$ ,  $c_2$ ,  $T$  [Khalil et al., 2014]. Appendix C details the procedure to obtain Equation 4.27. The first part of this inequation right-side shows the direct influence of the gain  $\varepsilon$  in the state estimation accuracy. Yet, the second element indicates that, for small values of  $\varepsilon$ , the error will tend to infinity. This bound, represented in Figure 4.7, illustrates how the presence of measurement noise limits the observer convergence velocity in practice. The trajectories in a noisy closed loop system under this feedback approach asymptotically the  $O(\sqrt{\mu})$  neighborhood ( $k_a \sqrt{\mu}$ , where  $k_a = 2\sqrt{c_1 c_2}$ ) as  $\varepsilon$  tends to an optimal value ( $c_a \sqrt{\mu}$ , where  $c_a = \sqrt{c_2/c_1}$ ).

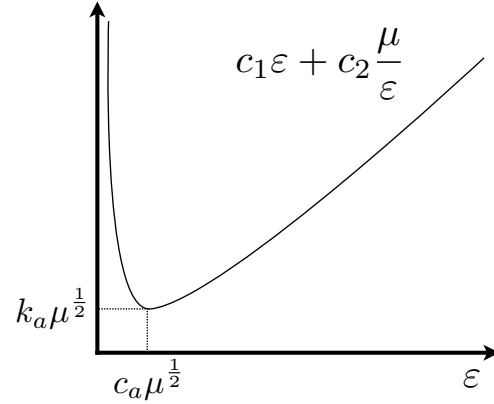


Figure 4.7: Sketch of the noise effects on the observer error. From [Khalil et al., 2014].

The high-gain observer presented here has a similar form to a standard ESO problem, and the interconnection between both methodologies can be made without large efforts. The resulting controller is called extended high-gain observer (EHGO).

### 4.3/ CONTROLLER DESIGN

When dealing with fragile components in the micro and nano-scales, requirements for the end-effector precision, accuracy, response times and robustness become more strict. During manipulation and characterization of such elements, it would be ideal to minimize the processing time and the chances of damaging components (samples and end-effectors). In this stage, the position control for the actuated micro-gripper finger is considered. By taking in consideration the open-loop dynamics of this device (obtained in Chapter 3), the goal requirements to be achieved by the closed loop systems are defined as follows:

1. The system settling time for a reference step input in vacuum should be lower than 30 ms. This is approximately three times faster than its response in air, and more than three hundred times faster than the open loop response in the vacuum.
2. The response overshoot to a reference step input should be zero, to avoid undesired collisions between the gripper and fragile samples.
3. Steady state error to a reference step input should be smaller than 0.1%.
4. An end-effector variation to perturbations of 1 nanometer (RMS) was set as goal challenge, once that it presents a genuine test when considering other works dealing with the precise positioning task at this scale.

In addition, as the system behavior changes for different operation points, the controllers should be robust enough to hold these characteristics for the whole operational range. These requirements consider the micro-gripper as a tool responsible for fine-position control, capable of quickly respond to events in the chamber. In the following subsections,  $H_\infty$  and EHGO controllers are developed based on the above design requirements. These controllers were selected for this work based on their capabilities to deal with plant uncertainties and attenuate disturbances. While the  $H_\infty$  strategy requires a good knowledge over those perturbations, the EHGO method relies on on-line estimation for these quantities based on reduced models and on-line measurements.

A remark should be made about the input non-linearity present in the model. As the input electrostatic force is proportional to the square of  $V_{in}$ , the control signal is assumed to be  $U = V_{in}^2$ . This alteration is possible because the voltages applied to the gripper should always be positive, accordingly to the manufacturer specifications.

The controllers then had their performances compared through simulation. The robustness levels achieved were investigated by considering an uncertain model for the gripper, taking in consideration the estimated parametric variations obtained during its identification process.

#### 4.3.1/ CONTROLLER SYNTHESIS USING $H_\infty$

As shown in Section 4.2.3, the optimization process to obtain an  $H_\infty$  controller requires the construction of an augmented plant  $P$ , where design requirements are introduced by means of weighting functions  $W$ . The control design depends on their choice and may be not always evident when dealing with concurrent objectives. The process employed in this phase can be summarized as follows:

- (a) Define the weighting functions that will shape the desired response characteristics, and construct the augmented plant  $P$ , considering the nominal transfer function of the plant model  $G_0$ .
- (b) Perform the optimization process, and obtain a controller  $K$  and the sub-optimal  $\gamma$  value. If no controller is found and the optimization fails, redefine the weighting functions.
- (c) If the obtained  $\gamma < 1$ , the controller achieves all the requirements imposed by the weighting functions. In this case, the performance requirements can be modified to more restrictive ones (i.e. faster response, better disturbance rejection, ...). If  $\gamma > 1$ , investigate which requirements could not be achieved, and try to balance them if necessary by changing the weighting functions.
- (d) If a satisfactory controller is obtained for a nominal model, test its robustness for all the family of models  $G$ . If it does not achieve the desired performances, modify the weighting functions.

##### 4.3.1.1/ SELECTION OF THE WEIGHTING FUNCTIONS

In the multi-objective  $H_\infty$  problem formulation, three functions can be used:  $W_1$ ,  $W_2$  and  $W_3$ , each one defining a specific desired characteristic. However, using all of them may be not necessary. In a first instance, only  $W_1$  will be used, to introduce the first three design requirements in the optimization problem.

These requirements can be expressed with the aid of a target closed loop function. The closed-loop response  $T_d$  (Equation 4.28) represents a desired transfer function from the reference signal to the system output and will be used as a base to obtain the weighting function  $W_1$ .

$$T_d = \frac{K_d \omega_d^2}{s^2 + 2\xi_d \omega_d s + \omega_d^2} \quad (4.28)$$

Following the first three design requirements, and using a second-order transfer functions as target for the closed loop system, its parameter can be selected to achieve the desired response. In this case,  $K_d = 0.999$  defines the allowed static error of 0.1%,  $\omega_d = 100 \text{ rad/s}$  the time response characteristics and  $\xi_d = 1.8$  the system damping.

The weighting function  $W_1$  is obtained through the relation 4.10, resulting in:

$$W_1 = \frac{1}{S_d} = \frac{1}{1 - T_d} \quad (4.29)$$

In this first iteration, when only the minimization of  $\|S W_1\|_\infty$  was considered, the resulting controller was able to achieved the second and third design requirements while obtaining a steady state error of 0.14% for the nominal plant, slight above the desired value. Analyzing the singular value diagram from a disturbance input  $d$  to the system output  $y$  revealed that the obtained controller could only reject low frequency disturbances. This means disturbances with frequencies close to the gripper's oscillation modes would be still transmitted to the output. As the transfer function from the disturbance signal  $d$  to the error signal  $e$  is given by  $GS$ , it was possible to improve the response by modifying  $W_1$ , taking this requirement into consideration.

In an ideal case, the weighting function should only include the frequencies to attenuate, avoiding introducing unnecessary and conservative requirements. To include this design requirement, indicating how disturbances around the two vibration modes present in the system should be attenuated, a band-stop filter with narrow band approaching the characteristics of notch filters is used:

$$T_f = \frac{s^2 + a_{bs} + \omega_{bs}^2}{s^2 + 2\xi_{bs}\omega_{bs}s + \omega_{bs}^2} \quad (4.30)$$

where  $\omega_{bs}$  is the central frequency of the filter in rad/s,  $\xi_{bs}$  is the damping defining the peak width, and  $a_{bs}$  is a parameter regulating the filtering peak amplitude. Two band-stop filters were added to  $W_1$ , one for each resonant mode:

$$W_1 = \frac{1}{1 - T_d} \frac{1}{T_{f_1} T_{f_2}} \quad (4.31)$$

To improve the performance, a function  $W_{dist}$  describing the input disturbances acting on the system was added. It was constructed to take into account the environmental disturbances described in Chapter 2, and the input electronic noise, generated in the hardware that produces the gripper actuation voltage and commented in Sections 3.2.2 and 3.3.3.

To avoid using a function with elevated order,  $W_{dist}$  was designed as a high-pass filter to represent the influence of electronic noise close to the oscillation modes, combined with a band pass filter covering the environmental disturbances between 100 and 700 Hz. A new controller was obtained for the new augmented plant  $P$ , and the improvement in disturbance rejection can be seen in Figure 4.8. It shows the singular value from the disturbance signal  $d$  to the measured

output signal  $y$ . The graph indicates attenuation levels up to 50 dB for disturbances exciting the first mode in relation to the previous controller, with only a few decibels of improvement for the second oscillation mode. The improved response at high frequencies demands a small degradation in the attenuation capabilities at low frequencies, but still within acceptable values.

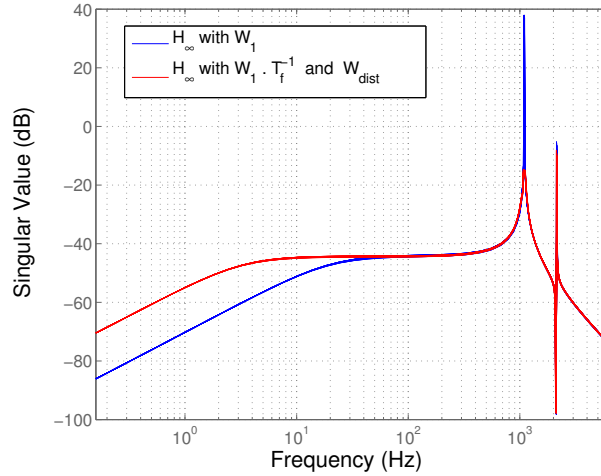


Figure 4.8: Singular value plot from disturbance input  $d$  to tracking error  $e$ . Two different controllers were compared: one obtained through  $H_\infty$  optimization when only reference tracking characteristics were considered ( $W_1$ , in blue), and another considering reference tracking and disturbance effects on the system ( $W_1 T_f^{-1}$  and disturbance characteristics  $W_{dist}$ , in red).

While the obtained controller for the augmented system  $P$  considering the weighting functions  $W_1$  and  $W_{dist}$  presents good characteristics for step reference inputs and disturbance attenuation it also leads to larger control signals  $u$ . By adding the weighting function  $W_2$ , limit control actions can be imposed in the loop at different frequencies. This can, in practice, reduce saturation and high-frequency shattering. The function  $W_2$  was selected as:

$$W_2 = K_p \frac{s/\omega_z + 1}{s/\omega_p + 1} \quad (4.32)$$

where  $K_p$  represents the allowed gain relation between input and output, and the parameters  $\omega_z = 300$  and  $\omega_p = 900$  were selected to shape  $W_2$  as a high-pass filter, penalizing high-frequency control. The gain  $K_p$ , selected as  $20/60^2$ , indicates that displacements of  $20 \mu\text{m}$  in the gripper should not surpass a 60 Volts input. The squared value was introduced to match the nonlinear input relation present in the electrostatic actuator.

The resulting multi-objective optimization problem returned a  $\gamma$  value of 2.10. Figure 4.9 shows the comparison between desired requirements and obtained responses. The limitation in the control signal is achieved for the most of the frequencies, except for those close to the second oscillation peak present in the model. Although not all performance requirements were achieved, the resulting controller approached them closely, with a steady state error of 0.2% instead of the required 0.1%, while the other design requirements related to settling time and system damping were respected. Further modifications in the weighting functions, to improve the steady state error, resulted in a loss of performance over other characteristics.

The obtained  $H_\infty$  controller is of  $14^{\text{th}}$  order (same dimension as the augmented plant  $P$ ),

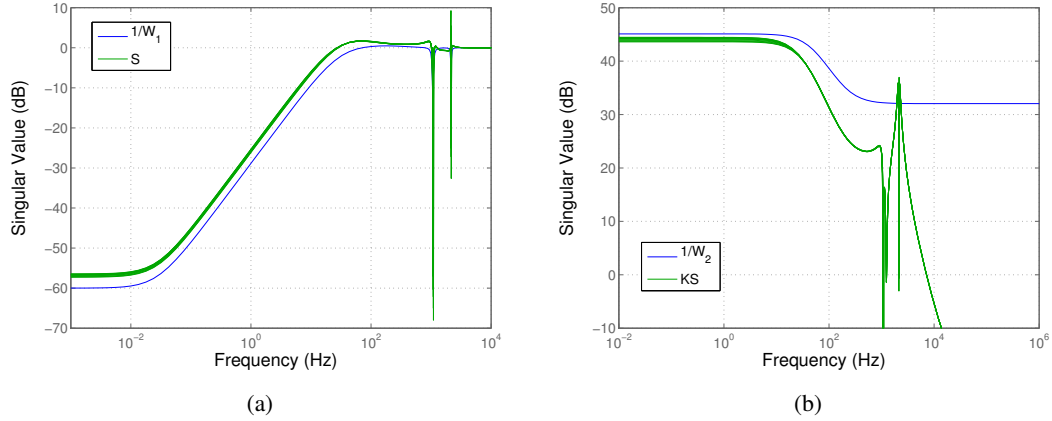


Figure 4.9: Resulting sensitivity function  $S$  and control sensitivity function  $KS$  for the obtained  $H_\infty$  controller (green line), compared with the target function (blue line).

and reached a balance between the achievable performances for this structure considering the different requirements. This design process is a practical example of the limits and difficulties that can be found when pushing performances to an extreme, where compromises should be made between desirable and achievable. It is important to highlight that the weighting functions could have been developed differently, considering different structures and parameters, what could result in radically different controllers. In [Bibel et al., 1992], it is stated that the relation between weighting function in the multi-objective  $H_\infty$  problem is complex and often non-linear. This means a small variation in one of the weighting functions may lead to a drastically different controller after the optimization process. As results, performing fine adjustments of these functions to improve a certain aspect of the response may be not obvious.

#### 4.3.2/ CONTROLLER SYNTHESIS USING ESO

Contrasting with the  $H_\infty$  control framework, the ESO design focus on disturbance rejection based on fewer information about plant and perturbations, where undesired effects are evaluated and compensated on-line. Therefore, the approximations made during the identification process, where a forth-order model with varying parameters is considered, can be relaxed. In this case, modeling the system as a second order Duffing equation with a unknown nonlinear stiffness can help to simplify the problem.

Assuming the system has the form described by Equation 4.33, where the functions  $a(x, d)$  and  $b(x)$  hold the non-linear gripper behavior in vacuum, not perfectly known, and  $d$  is a bounded disturbance signal with bounded derivatives.

$$\begin{cases} \dot{x}_1 = x_2 \\ \dot{x}_2 = a(x, d) + b(x)u \\ y = x_1 \end{cases} \quad (4.33)$$

Considering the gripper behavior, the nonlinear stiffness effects were included on the unknown dynamics of  $a(x, d)$ , and  $b(x)$  includes the varying input gain for the system. These functions were approximated by defining its nominal models  $a_0$  and  $b_0$  as:

$$a_0 = -\frac{K_0}{M_0}x_1 - \frac{C_0}{M_0}x_2 \quad (4.34)$$

$$b_0 = \frac{K_{elec_0}}{M_0} \quad (4.35)$$

where  $M_0$ ,  $K_0$ ,  $C_0$  and  $K_{elec_0}$  are nominal values for the systems mass, stiffness, damping and electrostatic gain, respectively. These parameters were precisely identified in Chapter 3 and their approximated values are summarized in Table 4.1. These values reflect the gripper dynamic behavior in air, intentionally selected to test the efficacy and robustness of the ESO in face of larger parametric uncertainties.

	$M_0$	$K_0$	$C_0$	$K_{elec_0}$
Value	$3.7e^{-8}$	1.6	$3e^{-6}$	0.01

Table 4.1: Nominal parameters used for the micro-gripper dynamics, considered for the ESO.

A variable change was performed to introduce the tracking control task, where the signal  $x_1$  should follow a bounded reference signal  $r$ , with derivatives also bounded. Reformulating the problem as a function of the tracking error, using the relations  $e_1 = x_1 - r$  and  $e_2 = x_2 - \dot{r}$ , allows to rewrite Equation 4.33 as:

$$\begin{cases} \dot{e}_1 = e_2 \\ \dot{e}_2 = a(e, r, \dot{r}, \ddot{r}, d) + b(e, r)u \\ y_e = e_1 \end{cases} \quad (4.36)$$

The observer was designed based on this tracking error dynamic equation. An augmented equivalent system, with the addition of a virtual state  $\sigma$  considering the nominal model, is easily derivable, and is given by Equation 4.37:

$$\begin{cases} \dot{e}_1 = e_2 \\ \dot{e}_2 = \sigma + a_0(e) + b_0u \\ \dot{\sigma} = \varphi(e, d, \dot{d}, u, \dot{u}, r, \dot{r}, \ddot{r}) \\ y_e = e_1 \end{cases} \quad (4.37)$$

In this form, an observer can be obtained by the method described in Section 4.2.4.1, resulting in the system given by Equation 4.38:

$$\begin{cases} \dot{\hat{e}}_1 = \hat{e}_2 + h_1(y_e - \hat{e}_1) \\ \dot{\hat{e}}_2 = \hat{\sigma} + a_0(\hat{e}) + b_0u + h_2(y_e - \hat{e}_1) \\ \dot{\hat{\sigma}} = h_3(y_e - \hat{e}_1) \end{cases} \quad (4.38)$$

The observer gain functions  $h_i$ , selected using the high-gain methodology, took the form of a large gain multiplied by the observer estimation error  $y_e - \hat{e}_1$ , given by Equation 4.24 and repeated here for convenience:

$$h_i = \frac{\alpha_i}{\epsilon^i}$$

The values for  $\alpha_i$  were selected so the polynomial  $s^3 + \alpha_1 s^2 + \alpha_2 s + \alpha_3$  is Hurwitz. It was possible to parametrize this selection by choosing  $\alpha_i$  as the coefficients of a Hurwitz polynomial, such as  $(s + 1)^3$ .

Consequently, a single parameter,  $\varepsilon \ll 1$ , remained to be tuned. It defined the convergence rate for the observer, and selected taking in consideration measurement noise effects. This parameter was chosen experimentally, by reducing its value iteratively. Selecting a sufficiently small value for  $\varepsilon$  renders a quick convergence for the observer, so that the estimated total disturbance  $\hat{\sigma}$  approaches the real value of  $\sigma$ . If the convergence is made sufficiently fast, dynamic disturbances can be estimated and compensated, while keeping the tracking error small.

The state feedback controller was designed independently from the observer, considering the nominal plant dynamics. It can be obtained through different methods (pole allocation, linear quadratic regulator, ...). For simplicity, this work used a static state feedback, considering pole placement, to obtain a system response with no overshoot and with settling time close to 1 millisecond, a value much faster than required in the specifications. The considered state feedback controller assumes the form  $\Phi = [\phi_1 \ \phi_2]$ .

The final feedback control is given by:

$$u = \frac{1}{b_0}(-\hat{\sigma} + \Phi \hat{e}) \quad (4.39)$$

This control action was saturated between 0 and 70 Volts, a selected operation range for the gripper comprising positions between 0 and 30  $\mu\text{m}$ , to limit possible undesired effects caused by peaking phenomena. In addition, a reference filter  $F_{ref}$ :

$$F_{ref} = \frac{1000}{s + 1000}$$

was included, to ensure a sufficiently smooth reference signal with bounded derivatives. This filter slows the settling time to around 4 ms. Faster filters could still be applied, at the cost of some degradation in the initial transitory response.

Figure 4.10 shows the final ESO structure. The observer, selected using the high-gain method, supplies estimations for position and velocity errors to the controller, as well as the estimated disturbances and model uncertainties  $\hat{\sigma}$ . These values were used to construct the control signal  $u$  given by Equation 4.39.

#### 4.3.3/ ROBUSTNESS ANALYSIS

This section resumes the robustness properties for the controllers described above, comparing both performances in the face of uncertainties, external disturbances and measurement noises. The closed loop system was built considering the uncertain plant  $G(\Delta)$  as a structured uncertain model (based on the parametric variation range previously identified in Table 3.1) and the obtained,  $H_\infty$  and EHGO controllers. It is important to remark that this polytopic uncertainty representation can generate parameter combinations that may not be obtainable by the real system, hence results may be conservative. However, this method still offered an interesting tool for comparing its robustness.

The tests were performed via simulation in the  $\mu$  analysis framework, by rearranging the closed loop systems in the  $M - \Delta$  structure for the different controllers. Bounds for the real SSV value  $\mu_\Delta(M)$  allowed estimating the controller's stability and performance in the frequency spectrum.

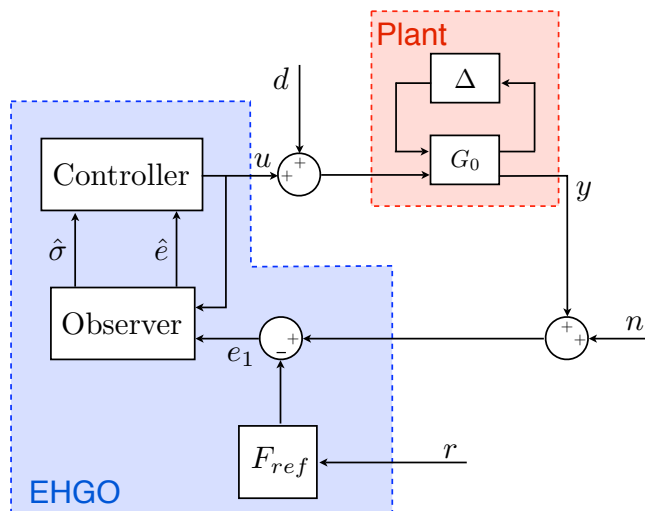


Figure 4.10: The block diagram for the ESO controller implementation.

The first result concerning the stability of these closed loop systems can be seen in Figure 4.11. Both controllers achieved robust stability for all the considered parametric range, as the upper bounds values are smaller than 1 for all frequencies. The critical frequencies for the  $H_\infty$  controller were located around the two resonant frequencies. A maximum calculated upper bound value of 0.89 indicates that the closed loop system should hold for an uncertainty up to 112% of the considered range. In other hand, the controller based on ESO led to lower limit bounds ( $\mu_u = 0.53$ ). This indicates that the ESO control structure can stand much larger uncertainties (up to 188% of the present value).

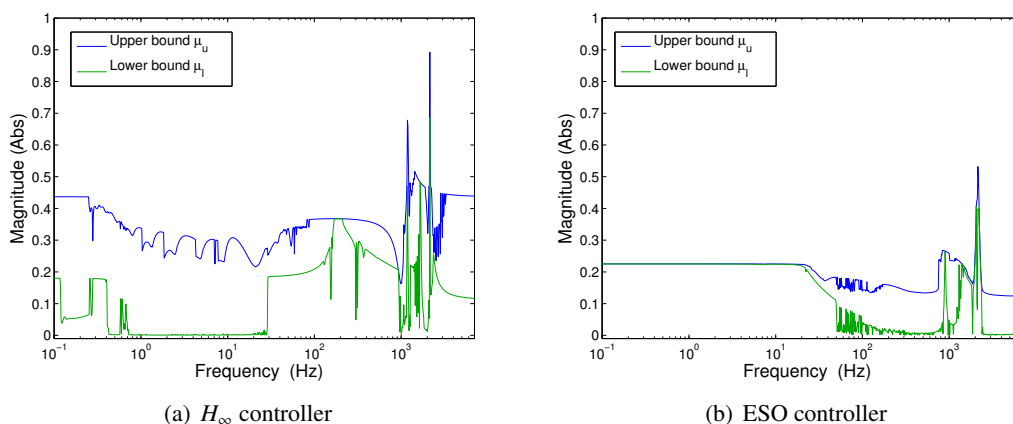


Figure 4.11: Robust stability index for the controllers. The curves show minimum and maximum bounds for the true value  $\mu_\Delta$ .

The next step in the analysis focused on the response characteristics considering the three first design requirements, testing if the transfer maps from inputs  $w$  to outputs  $z$  were insensitive to uncertainties. If the upper bounds  $\mu_u^{perf}$  is smaller than 1, or similarly  $\|T_{wz}\|_\infty < 1$ , the system achieves robust performance for the modeled uncertainty.

Considering the  $H_\infty$  controller, it was possible to know beforehand that its reference

tracking performance is not robust, as the  $H_\infty$  norm of the nominal plant was greater than 1. Reexamining Figure 4.9(a) demonstrates this aspect, a consequence for the controller not being able to achieve the desired steady state error requirements. The resulting  $\mu_\Delta^{perf}(M)$  curve (Figure 4.12(a)) reflects this property at lower frequencies. At higher frequencies, a peak was present in the upper limit boundary close to 2000 Hz, indicating that signals in this frequency may be close to infringing some performance requirements.

The same simulation was made for the ESO controller structure (Figure 4.12(b)), and revealed the reference tracking performance requirements were met with ease. Two peaks were present at high frequency range, but the upper boundary values were still considerably far from accepted unitary limit. This indicates the controller can ensure current performance requirements an even larger range in the parametric uncertainty.

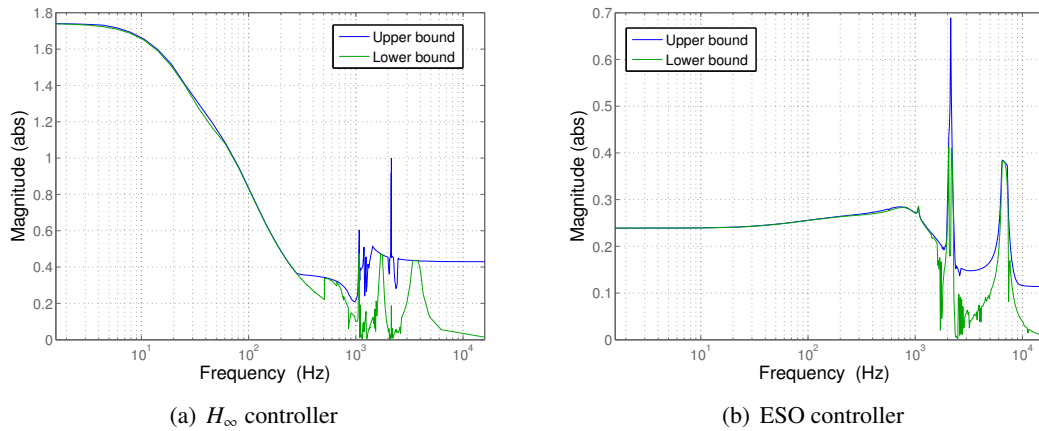


Figure 4.12: Robust performance index for the obtained controllers. The curves show minimum and maximum bounds for the true value  $\mu_\Delta^{perf}$ .

To better interpret these results, the closed loop systems responses for a unitary reference step signal, in the time domain, are given in Figures 4.13(a) and 4.13(b). Twenty responses (blue continuous lines) were obtained for each controller, considering different plants obtained randomly from the family models set. The vertical black dashed lines indicates the time when a response enters its steady state, defined as 98% of the final value.

The curve shows, for the  $H_\infty$  controller, the defined settling time requirement of 30 milliseconds is achieved for almost all the samples model, with times varying between 19 to 33 ms. For the second controller, faster response times were obtained with settling times about 4 ms. This time is close to the selected reference filter  $F_{ref}$  response, indicating the controller is sufficiently fast to closely track such fast reference changes with a small dispersion among responses.

Figures 4.13(c) and 4.13(d) show the respective control signals applied during the reference step. The ESO controller presents a sharp increase in the control signal in the initial moments, due to the peaking phenomenon. However, as the observer converges to the true value, this effect is eliminated and the control signal behaves normally. This occurs quickly (under 0.2 millisecond), with almost unnoticeable consequences over its displacement.

The second design requirement was attained by both controllers in all range, as no overshoot was present in the responses. Finally, steady state errors 0.2 and 0.14% we obtained for the  $H_\infty$  controller, where the latter value corresponds to the one obtained for the nominal plant during

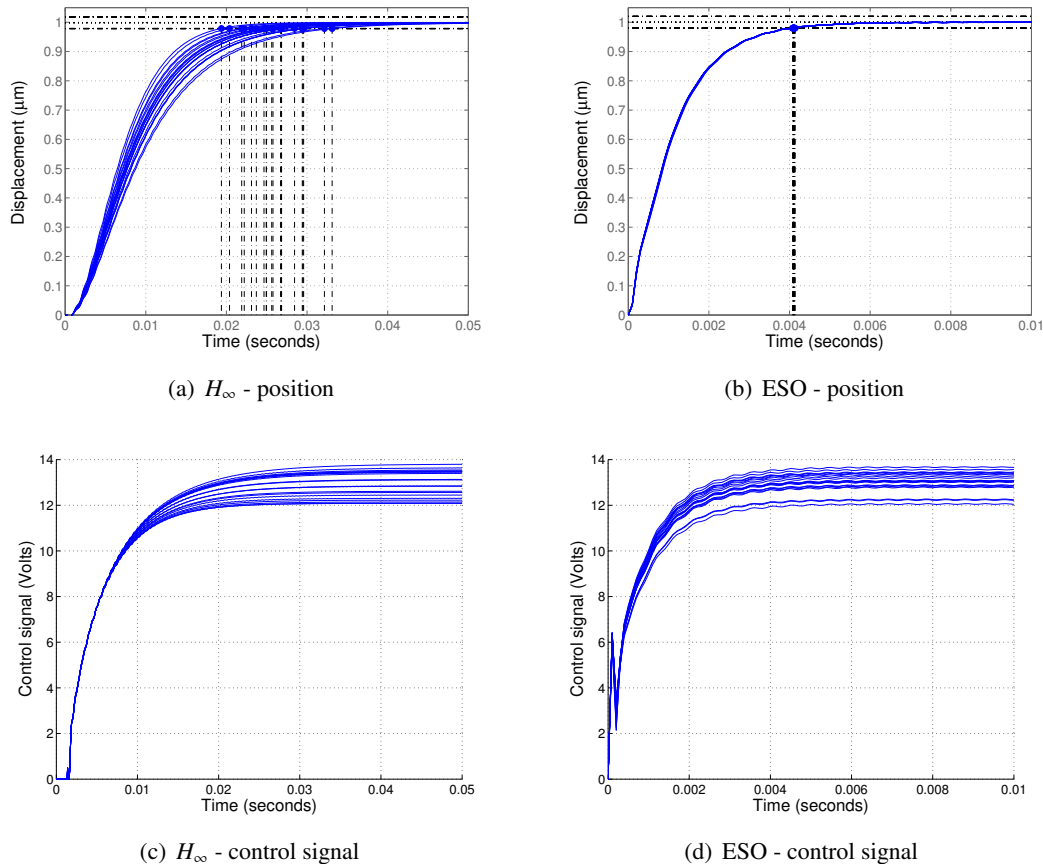


Figure 4.13: Simulated response to unitary step reference change considering various plants within the parametric variation range. (a) and (b) show the responses for a unitary reference step. The dashed-dot lined indicate the settling time ( $t_{98\%}$ ). (c) and (d) indicate the respective control signals applied.

the controller synthesis. As commented before, the design objective of 0.1% could not be achieved for the  $H_\infty$  controller without sacrificing other aspects of the response. For the EHGO controller, close to null error is obtained for all plants.

Up to this point, the analysis concerned just signal tracking characteristics. The last design requirement, disturbance rejection, is addressed next. Recalling the results from Chapter 2, mechanical and acoustic vibrations operating in different frequencies can affect elements inside the microscope. If these undesired excitation frequencies match the vibration modes of the components in the SEM chamber, large displacements can be generated as result.

Figure 4.14 shows the Bode diagram for the closed loop systems, from disturbance to the gripper tip position. The graphs show two curves for each case, one representing the nominal system (blue continuous line) and another the response obtained for the worst-case gain model (red dashed line). The worst-case gain is the parameter combination, within the defined variation range, producing the largest singular value.

Perturbations acting in frequencies under 700 Hz and above 2 kHz presented a large attenuation for both controllers. The critical point occurs for perturbations in frequencies close to the system's oscillation modes. For the  $H_\infty$  controller, attenuation values between -15 and -10.8

dB for the first and -36 to -20 dB for the second mode were obtained. This presented a large improvement in relation to the open loop response, where amplifications close to 40 dB for the first mode could be achieved.

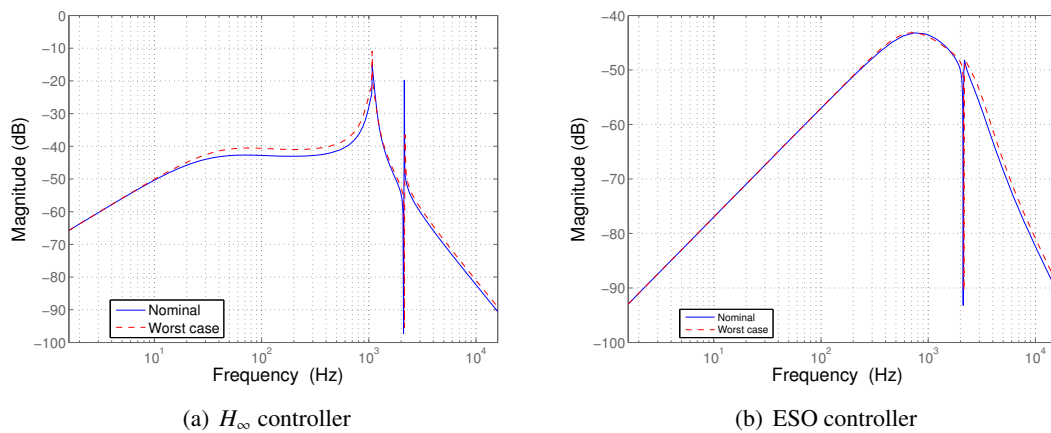


Figure 4.14: Closed-loop Bode diagram, from the input disturbance  $d$  to the system output  $y$ , considering the nominal plant response (blue continuous line) and the worst case result (red, dashed line) achievable within the defined parametric variation range.

The ESO based control analysis indicated a larger disturbance attenuation capability, where values between 43.5 to 42 dB, and 48.1 to 49.8 dB, were achieved for the first and second vibration peaks, respectively. As this controller presents a proactive disturbance compensation structure, improved attenuation capabilities were already expected. Yet, it is worth to remark how its intrinsic perturbation rejection properties can be obtained without any *a priori* knowledge over the disturbances, a valuable characteristic for many practical applications.

The influence of noise in the control signal is another aspect to be considered. The Bode curves, shown in Figure 4.15, demonstrate this limitation in the high-gain observers, as mentioned previously. As the observer gain increases, its dynamics become faster, improving its tracking and disturbance rejection capabilities. At the same time, the noise impact in the closed loop also increases, up to a limit where higher observer gains would degrade the estimation performance as the signal/noise ratio in the estimated states is reduced. Comparing both graphs, the larger impact of measurement noise in the control signal for the current observer parameters is evident, although it appeared to have small effects in the overall system response for simulations considering the expected noise levels delivered by the vibrometer.

#### 4.3.4/ CONCLUSION

After the controller synthesis using the two selected methods, some important points should be highlighted. The  $H_\infty$  controller depends directly on the choice of weighting functions and may show a large sensibility to it, where small variations in one of these functions can have large impact on the optimality index  $\gamma$ , resulting in large changes over the response. This is one of the main drawbacks of this method, and the fine-tuning process required to improve a response characteristics may be troublesome. In this specific work, the found  $\gamma$  value of 2.1 indicates that the design requirements are not fully met, and therefore a compromise should be made in its performance.

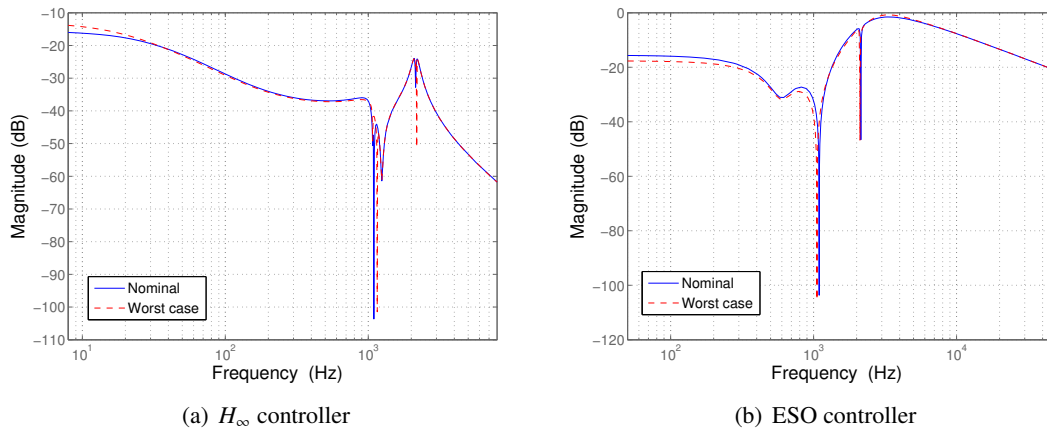


Figure 4.15: Closed-loop Bode diagram, from measurement noise  $n$  to control signal  $u$ , considering the nominal plant response (blue continuous line) and the worst case result (red, dashed line) achievable within the defined parametric variation range.

The ESO methodology is based on a different approach. Observer and feedback control can be designed separately. The observer estimates in real time the difference between the real plant and a nominal model. This difference, including effects of external disturbances and unmodeled plant dynamics, is compensated and results in a plant behaving as the nominal, undisturbed model. The feedback control, designed for this ideal case, gives the dynamic characteristics for the closed loop behavior. When considering high-gain observers, its convergence is made sufficiently fast through the selection of a single parameter  $\varepsilon$ . It may be selected so the system can estimate static and dynamic disturbances and behaviors.

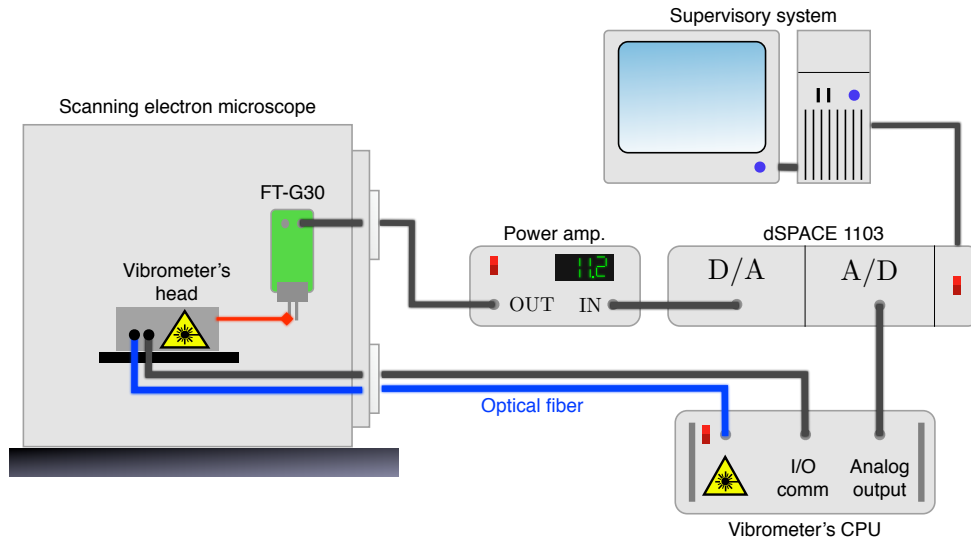
Through simulation analysis, the two controllers have shown to be robustly stable with respect to the parametric variations in the operational range. Considering performances, the  $H_\infty$  controller, despite not being able to precisely achieve the initial requirements, approaches them sufficiently to be regarded as successful. It achieved adequate disturbance attenuation characteristics and a sufficiently small tracking error (less than 0.2 %). In contrast, the EHGO could achieve zero error in tracking and a faster settling time. The proactive disturbance attenuation strategy obtained improved responses in relation to the first controller, specially around the system natural vibration frequencies.

#### 4.4/ EXPERIMENTAL VALIDATION AND RESULTS

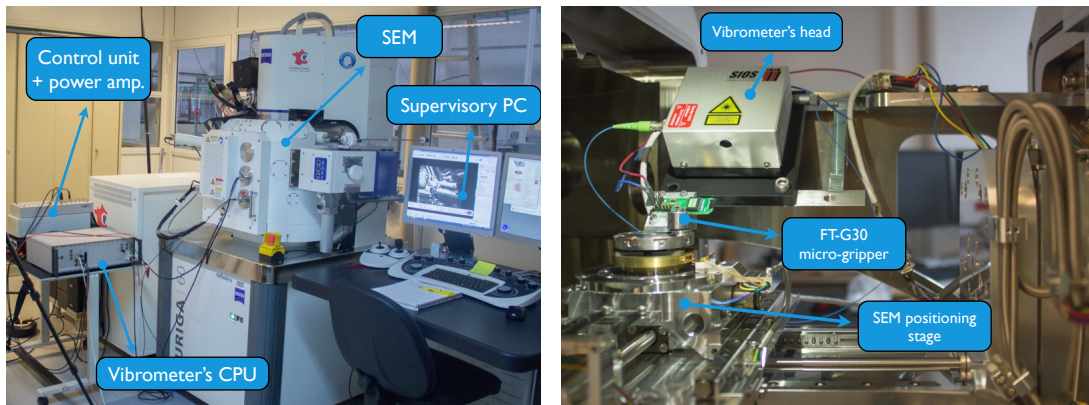
As a final stage of controller development, an experimental validation was performed to ratify the simulations. For this purpose, several scenarios were devised to check stability, robustness and disturbance rejection characteristics.

A scheme and the real setup for the experimental closed loop implementation are shown in Figures 4.16(a) and 4.16(b), respectively. The tests were performed inside the SEM vacuum chamber at pressures between  $6e^{-4}$  and  $2e^{-4}$  Pa. During the experiments, the micro-gripper FT-G30 was fixed over the SEM's stage. The vibrometer, also placed inside the SEM, measured displacements over the micro-gripper actuated finger (Figure 4.16(c)).

The controllers, designed in continuous time, were implemented in Simulink<sup>®</sup> software



(a) Scheme detailing the interconnection between elements.



(b) Experimental setup: exterior

(c) Experimental setup: inside the SEM

Figure 4.16: Experimental setup for validation of closed-loop control strategies.

and uploaded to a dSPACE<sup>®</sup> card responsible for handling conversions between digital and analog signals. The generated control signal computed by the card were amplified to produce the voltage levels required by the comb-drive for its operation. Finally, a supervisory system, communicating with the control board, allowed the operator to activate the controllers, to define set points and test parameters, and to store various variables of interest.

Before starting the experiments, dSPACE sampling frequency needed to be specified. During tests considering the  $H_{\infty}$  controller, this frequency was set to 10 kHz, a constraint imposed by the available hardware to ensure the real time computation for this 14<sup>th</sup> order controller. The same hardware was able to achieve, for the ESO based controller, update frequencies up to 80 kHz, indicating a significant difference in their required computational power.

## 4.4.1/ REFERENCE TRACKING AND STEADY STATE ERROR UNDER ENVIRONMENTAL DISTURBANCES

To confirm the closed loop stability for the whole operation range, a series of step inputs with different amplitudes was used as reference signal. Due to measurement range limits imposed by the vibrometer, two sets of measurements were performed. One comprised steps between 50 nm and 2.5  $\mu\text{m}$  (using the vibrometer analog output gain G1, with a measurement range of 2.6  $\mu\text{m}$  and a resolution of 0.3 nm), and another with reference steps ranging from 500 nm to 25  $\mu\text{m}$  (using vibrometer gain G3, range up to 40  $\mu\text{m}$  and a resolution of 4 nm). Figure 4.17 displays the obtained responses and respective control signals, normalized and juxtaposed against each other. Besides verifying their stability, this analysis allowed to estimate the influence of parametric variations in each controller, so they could be compared with the simulated values (shown in Figure 4.13). The experimental results are well within the range of response obtained in simulation, with experimental settling times, approximated due to the present of measurement noise, between 28 and 33 ms for the  $H_\infty$  controller and close to 4 ms for the ESO based controller.

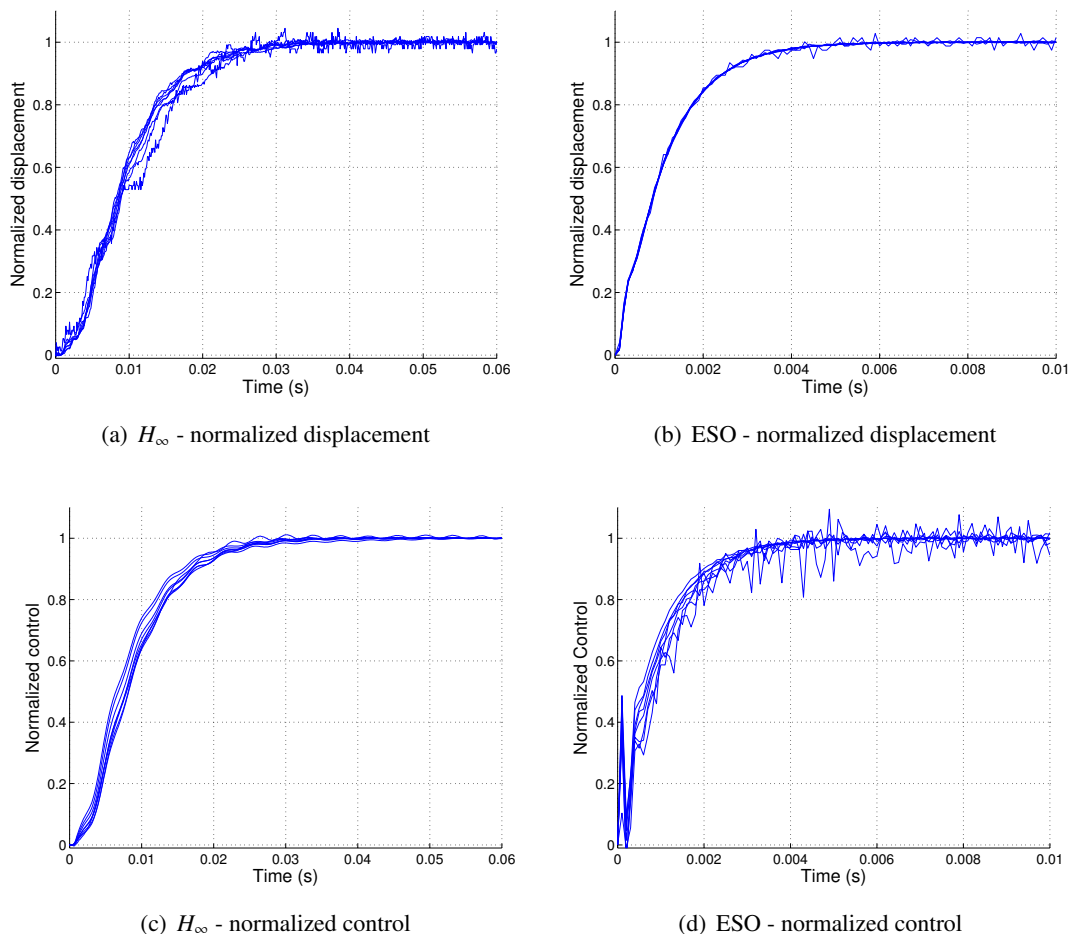


Figure 4.17: Experimental response to step reference change of different amplitudes (between 50 nanometers and 25 micrometers). The responses are normalized, to contrast differences due to parametric variations.

A second test focused on the constant reference regulation, observing how well controllers sustain a desired fixed position when confronted with the perturbation levels present in our SEM room. The measurements were performed at different operation points (constant ref-

erences signals between 0 to 50 V), using the vibrometer analog output gain G1 to obtain measurements with sub-nanometric resolution. Each test set, considering different controllers and operation points, was performed five times, and RMS values for the displacements were computed and averaged. The results are summarized in Table 4.2, and compared against open loop responses in air (performed over an anti-vibration table) and in vacuum.

Test condition	Average RMS disturbance (in nm)					
	0V	10V	20V	30V	40V	50V
Open loop (air)	2.7	2.5	2.3	3.2	3.1	5.1
Open loop (vacuum)	5.4	4.4	4.3	29.4	89.9	14.2
Closed loop ( $H_\infty$ vacuum)	2.2	2.3	2.8	3.7	4.9	4.2
Closed loop ( $ESO$ vacuum)	0.61	0.59	0.62	0.61	0.63	0.63

Table 4.2: Measured average RMS disturbance for the micro-gripper's tip, for different constant input voltage values, considering four operation conditions.

From the obtained results, several interesting points arise. Firstly, it was possible to notice how open loop responses in vacuum presented larger RMS displacements values than when the same experiment was performed in air. Two factors may have contributed for this result: the increased sensitivity due to the lower damping in vacuum, and the improved performance of the anti-vibration table when compared to the SEM structure and dampers. Also, effects of input electronic disturbance (demonstrated in Section 3.3.3) can be easily noticed, resulting in the large displacements for 30, 40 and 50 Volts when in open loop in vacuum. In this context, responses to lower voltages were less affected by it. At lower voltages, it can be assumed that vibrations were mostly produced by other external sources (ground vibration, acoustic, ...), as seen Chapter 2. These values exemplify the vibration levels commonly found for this setup during real applications in SEM .

The degradation due to electronic input disturbance at larger voltages is harsher in vacuum, where the reduced damping and the first harmonic excitation can generate displacements in the order of hundreds of nanometers. In this case, it becomes the most important source of disturbance in the system, while the same effect in air is limited to a few nanometers thanks to the damping provided by the air. It is important to notice that, as the cantilever stiffness varies with the pressure, this harmonic excitation will occur at different operation voltages. In this example, the frequency match in vacuum is located close to 40 V. A further increase in the input voltage in vacuum reduced the disturbance amplitude, as the micro-gripper's resonant frequency shifted.

The  $H_\infty$  controller was able to attenuate disturbances significantly. At lower voltages, the RMS displacement in vacuum attained values compatibles to those obtained in air over the anti-vibration table, with RMS vibration levels between 35 to 60% lower. At higher voltages, when the electronic disturbance became dominant, the attained RMS level was slightly larger, yet displaying a great improvement when compared to the open loop response in vacuum. Overall, this controller appears to be able to operate within a 5 nm RMS displacement margin in the worst case scenario. The EHGO controller, in other hand, achieved an almost constant RMS value around 0.6 nm for all measured range, being less affected by the presence of input electronic noise. This result is impressive, as the controller can keep the tracking error near the sensor resolution level for the whole operation range, even in the face of unexpected, dynamic disturbances.

A direct comparison between controller responses to a constant reference signal in the time domain is shown in Figure 4.18. The curves were obtained around 40 V, the operation point with the largest vibrations due to disturbances. The top graph shows the position variations around this operation point, and the bottom graph reveals the applied control signals. The control signal generated by the EHGO controller presented quicker transitions and was able to track closer the reference with lower amplitude oscillation. This also resulted in a less smooth control signal, with the presence of random peaks due to measurement noise. The noise influence was still too small to introduce significant degradation in the response, yet any increase in the observer gain should be made with caution. In other hand, the  $H_\infty$  controller presents a much smoother, conservative control signal.

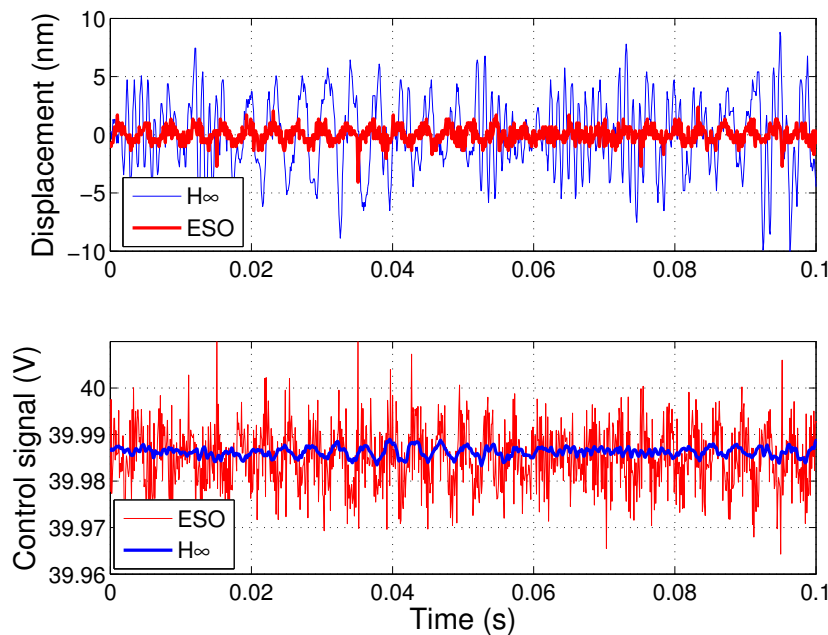


Figure 4.18: Experimental closed-loop response to a constant reference signal, and control signal  $u$  for each controller. No additional external disturbance is added.

#### 4.4.2/ DISTURBANCE REJECTION FOR EXTERNAL MECHANICAL AND ACOUSTIC PERTURBATIONS

The previous tests considered only background perturbations that existed in the environment and the electronic noise introduced by the control hardware. To further explore the attenuation feature of the controllers, artificial disturbances were introduced.

To test the effects of external acoustic excitations in closed-loop, a loudspeaker was placed in the room at 1 meter from the SEM chamber and directed at it. A signal generator was used to produce sinusoidal waves in different frequencies and amplitudes, as performed during the noise characterization phase in Section 2.2.2.2.

The obtained curves are summarized in Figure 4.19. The graph compares the controllers under external excitation of a high-amplitude noise (approximately 70 dB), with frequency close to the first vibration mode. At the start, the controllers were disabled, allowing the finger to oscillate with increasing amplitudes. The operation point was selected around 3 V, to ensure control signals would not be negative. The EHGO controller, activated at  $t = 5.5$  seconds, quickly attenuated the

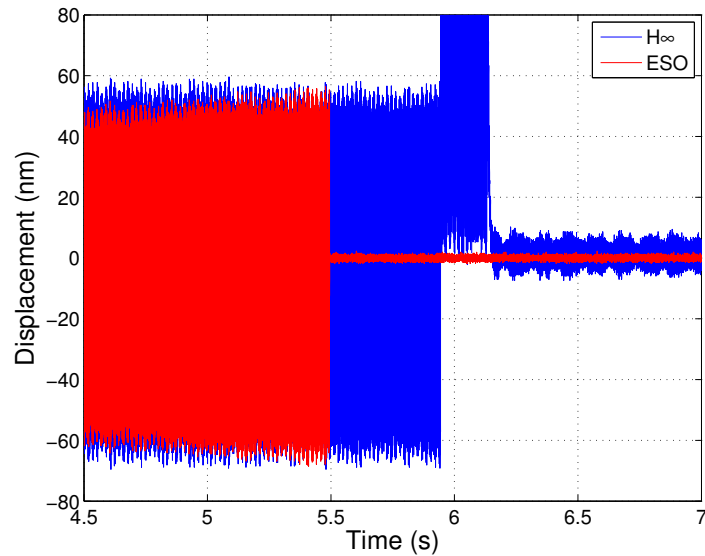


Figure 4.19: Experimental responses for external acoustic excitations, considering the two controllers. The disturbance signal frequency is 1080 Hz with an intensity of 70 dB. The controllers are disabled at the start, to better illustrate their efficacy.

acoustic effects, achieving steady state values similar to those obtained previously (0.64 nm RMS of vibration). The  $H_\infty$  controller was activated near  $t = 6$  seconds, and after a short transitory phase, steady state was achieved with a RMS displacement value of 2.4 nm. This demonstrates their capacity to quickly attenuate the effects of sustained acoustic excitations over the tested end-effector.

The last experiment performed consisted of an impact test. A small rigid plastic half-sphere, with a radius of 2 centimeters and mass  $m = 10.8$  grams, was dropped directly besides the vacuum chamber and over the SEM table, so vibrations could be transmitted to the SEM interior more easily. The half-sphere was dropped from a height  $h_0$  of approximately 3 centimeters (Figure 4.20), to mimic an impulsive disturbance exciting a wide frequency range. During tests, the half-sphere bounced back after the first impact, resulting in multiple consecutive impulsive excitations.

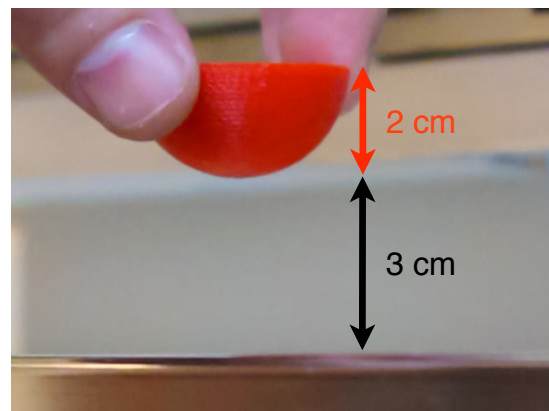


Figure 4.20: Impact test example, showing the sphere and approximated drop height.

Even if the resulting impact force could not be directly measured, its value was estimated from the impact velocity and the contact time between surfaces for the first impact by the relation  $F = (2mv)/t_i$ . The half-sphere velocity at the instant of impact was estimated using  $v = \sqrt{2h_0g} = 0.76$  m/s. The impact time  $t_i$  was approximated by recording the experiment on video at 60 frames per second. Through the study of these images, the moment of impact could be determined to occur between frames, and therefore its duration was less than 1/60 of a second. If the impact time is taken as  $t_i = 0.01$  second,

an approximated force value of  $F = 1.6$  N is obtained. The response obtained for the open loop test is shown in Figure 4.21(a). The first impact induced a displacement of over 50 nm, followed by a second impact and the sustained vibration due to the excitation of the low damped first mode.

Repeating the experiment with the controllers in closed loop yields the curves shown in Figure 4.21(b). The ESO controller greatly reduced the disturbance effects, with a more noticeable degradation at the moment of first and subsequent impacts, when a maximum peak displacement of 11 nm was measured. Nevertheless, the vibrations were quickly attenuated (0.1 seconds). Regarding the  $H_\infty$  controller, its response reveals the initial impact amplitude is only slightly attenuated in relation to the open loop case, with the subsequent vibrations suppressed in around 0.5 seconds. This test corroborates the excellent disturbance attenuation of the EHGO structure. The  $H_\infty$  controller still presented a considerable reduction in the settling time, but its limited effectiveness for this special case of disturbance is clear.

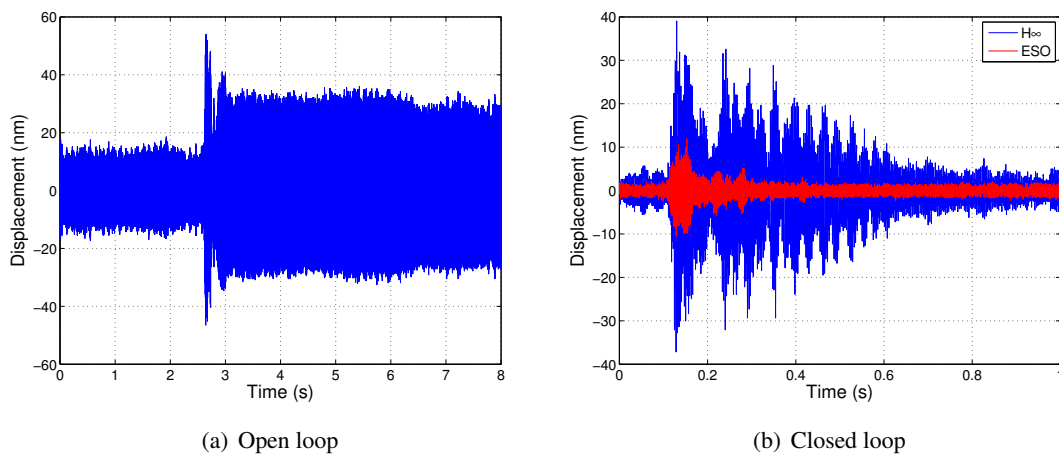


Figure 4.21: Experimental impact test response, when a half-sphere of mass 10.8 grams is dropped near the microscope to mimic an impulsive disturbance on the system.

#### 4.4.3/ CONCLUSION

The validation process presented in this section confirmed the expected results from simulation. Both controllers behaved as designed, were stable in the grippers operational range and improved, to different degrees, the achievable performance in relation to the open loop.

The disturbance attenuation characteristics presented by the ESO are a strong argument in favor of this method, achieving accuracies in the sub-nanometric range (close to sensor's resolution values), while the  $H_\infty$  controller obtained values ranging from 2.2 to 4.9 nanometers RMS when considering natural background vibrations and electronic input perturbation, the later playing an important role in the experimental validation process. Although it could not be removed within the current hardware implementation, future works should consider the use of new devices to reduce/eliminate it, an essential step for real nano-positioning applications. Regardless, the remarkable ESO properties allowed countering its effects. The  $H_\infty$  controller was also able to greatly reduced its impact on the gripper's position. However, the existence of this disturbance needed to be explicitly considered when constructing the weighting functions.

When additional external disturbances were applied to the system (acoustic and mechanical impact), both controllers were capable of attenuating the first vibration mode excitations,

greatly improving the system performance and settling times. However, the vibration amplitudes produced by this test varied significantly, with the ESO based controller presented 4 times less peak-to-peak displacements than the  $H_\infty$  controller.

#### 4.5/ CONCLUSION

This chapter described the issue of precision control of nano-positioning devices inside the SEM. In literature, various methods were proposed to control micro- and nano-positioning devices. However, few was said when considering control strategies for similar systems in vacuum.

The challenges restricting the precise micro- and nano-manipulation in SEM are strongly linked to the obstacles in obtaining fast and accurate positional information over components located in the vacuum chamber. Difficulties in instrumenting and measuring devices and components of interest (due to the operation environment and limited work volume), and the strict requirements in resolution and dynamic range demanded by sensing devices (the reduced dimension of objects, unfavorable signal/noise ratios) contribute to it. Thanks to the available setup, consisting on a fast acquisition, sub-nanometric resolution vibrometer placed inside the SEM's specimen chamber, the implementation of real-time, dynamic control laws in this environment and the improvements brought by it to precise position control could be demonstrated.

Two control strategies were carried out in this work. The  $H_\infty$  controller was computed based on an optimization process, where different weighting functions were selected to achieve desired closed loop characteristics, attenuation specific disturbance frequencies and limiting the control signal. The ESO controller, developed more recently in the late 1990's and still under study, is based on the on-line reconstruction and compensation of external disturbances and plant uncertainties. Both methods are regarded as robust and able to improve the overall system responses and disturbance attenuation characteristics.

The  $H_\infty$  synthesis required reasonable precise knowledge over the system and its disturbances, and the selection of weighting functions can be a complex task when requirements are too strict and conflicting. In the ESO framework, the use of high-gain method for the observer reduced the total number of parameters to be selected, in this studied case, to four: the feedback proportional and derivative gains, the reference filter pole  $F_{ref}$ , and the observer gain  $\varepsilon$ . The need of only an approximated model is an interesting feature for practical applications, as it can greatly simplify the identification and controller synthesis processes.

Overall, the EHGO controller delivered better reference tracking and disturbance rejection characteristics, as simulations indicated this framework as presenting larger robustness margins. Using real-time measurements, this control structure consistently achieved nanometric resolution, even under the effects of disturbances. This consists of an important and promising result to be further explored, that may lead to more accurate, faster, and more accessible nano-manipulation.



## CONCLUSIONS AND PERSPECTIVES

This work aimed to explore one of the current challenges in nanotechnology: the correct and safe manipulation of small and fragile structures. It was seen that, when approaching these structures to perform tasks such as characterization and grasping, precise position control of the end-effector is essential, specially when dealing with nano-objects. Various examples of manipulation in SEMs, scattered in the literature, indicated that the precision and accuracy limits of currently available methods may be not sufficient to ensure the repeatability and success rates required for characterizing and assembling structures in this scale, restricting their applications. Failing to achieve the required positional precision can result in broken components, unreliable measurements and large variations on the tasks outcome. This work main contributions towards improving the quality of nano-manipulations in the SEM environment are summarized next, together with perspectives and ideas for future developments.

### 5.1/ CONCLUSIONS

In this thesis, the difficulty to measure and account for system dynamics on the vacuum chamber was pointed as one of the major limitation on SEM manipulation. This work proposed the use of a dedicated vibrometer, placed inside the vacuum chamber, to directly measure displacements of samples and end-effectors. This allowed to capture data about the position dynamics of components in real time. The sensor characterization process indicated that it could capture displacements in the sub-nanometric range with acquisition frequencies of tens of kHz, being therefore an effective tool for this investigation.

The study of mechanical disturbances in SEM revealed that, despite operating in a vacuum chamber placed over an active damping system and other efforts to reduce perturbations in the room, components were still affected by surrounding vibrations. The identified vibrations included those produced by the secondary vacuum pump and those induced over the SEM positioning stage. Although these vibrations resulted in small displacements, they could become important if their frequencies match the oscillation modes of components in the chamber (samples, actuators, end-effectors, ...). During experimental tests, perturbations from the environment achieved RMS values close to 2.55 nm for a silicon cantilever with 5 mm length, and up to 5 nm RMS for the considered FTG-30 micro-gripper, significant values when nanometric precisions are desired. This effect became clear when adding a source of acoustic perturbation, transmitted to the interior of the SEM via mechanical coupling. When these excitations matched the first mode of a sample, large displacements could be produced. From experiments, vibrations amplitudes over 50 nm could be easily produced by the external acoustic noise source, and even low intensity noises (50 dB) were sufficient to significantly degrade the response, with oscillations close to 20 nm peak-to-peak.

The analysis of pressure influence was performed by taking an electrostatic micro-gripper as a case-of-study. Its actuated finger was characterized both in air and vacuum. During experiments, damping presented the most noticeable variation, where its settling time for a voltage step input changed from 0.1 second in air to more than 10 seconds in the vacuum. This indicates the air drag was the responsible for dissipating the major part of the energy in this micro-system and corresponded to a near 100 times increase in the quality factor. Also, changes in the vibration frequencies were observed due to pressure influence, where the first mode presented up to 8.2% variation on its frequency between both environments. The full characterization of the actuated finger revealed the non-linear nature of its behavior, with parameters varying according to its operation point, and the presence of a non-linear stiffness became more evident in the vacuum. Through the acquired data, general models for the gripper operating in air and vacuum were derived and validated. It is important to stress that some of the effects shown in vacuum may be difficult to predict accurately, requiring extensive analysis and simulations, while an experimental study in vacuum, as presented here, can be laborious, time consuming, and require special instrumentation and components.

After considering the disturbance effects in SEM and the micro-gripper characteristics in vacuum obtained during the previous stages of this work, the necessity of improved position control in this environment inspired the development of two strategies: one based on the  $H_\infty$  methodology, and other based on the Extended State Observer approach. While the first took advantage of the available information over the system dynamics, its parametric variations and existing disturbances, the second presented a structure less dependent on models and based on real-time estimation of plants disturbances and uncertainties. Both controllers succeeded in obtaining improved response for reference step signals, with settling times of 30 ms for the  $H_\infty$  and 4 ms for the ESO and both presenting zero overshoot. More interesting, the disturbance attenuation properties achieved on both controllers allowed to greatly improve its performance when compared with open-loop. The designed ESO controller presented encouraging results, capable of achieving a RMS displacement level under 0.64 nm for all operation range, even under the effects of constant acoustic disturbance and electronic input noises.

These results demonstrated the importance of taking into consideration the system dynamics when high-accuracy positioning tasks are required, and how overlooking disturbances and its effects can produce large degradation in the final position. The performed test revealed that vibrations levels up to 15 nm peak-to-peak were not uncommon for the case of study considered, achieving even higher values (100 nanometers or above) under specific acoustic excitations. These vibrations attenuation is essential for tasks requiring high precision and accuracies. From the control point of view, the ESO framework offers an interesting alternative to speed up the development of positioning controllers, which is interesting for practical applications, given that reliable and fast sensor information is available. Its robustness to plant uncertainty and disturbance attenuation characteristics could be further explored for tasks in micro and nano-scale, where both uncertainty and perturbations are present and largely influential in the outcome.

## 5.2/ FUTURE PERSPECTIVES

The experimental setup employed for this thesis served to demonstrate how real-time information over the system dynamics can improve the precise positioning task in the SEM environment. However, the actual implementation, serving as a proof of concept, lacked in flexibility and some problems were encountered. To improve these limitations, a few modifications are necessary.

The sensor used had a considerable size (9 cm x 9 cm x 4 cm for the sensing head) and required to be positioned over a rigid, large support, limiting the operations that could be realized in the SEM. The miniaturization of the vibrometer head is essential to facilitate its positioning inside the chamber, minimizing the required space and its interference with other components. Commercial devices with compact sensor heads (few millimeters in diameter and less than 2 cm in length) are available, as well as the possibility to developing custom miniaturized devices for this application.

The sensor fixed support could be changed for a robotic structure, increasing the setup flexibility. A robotic arm (Figure 5.1) was designed specifically for the SEM used during this thesis and possesses 6 DoF (3 translations in the arm and 3 rotations in the wrist). It is fixed at the vacuum chamber's ceiling and can be extended and retracted, reducing its interference during other operations. This setup could be used as a flexible measurement device to characterize the vibrations and dynamic behaviors of various components in SEM.

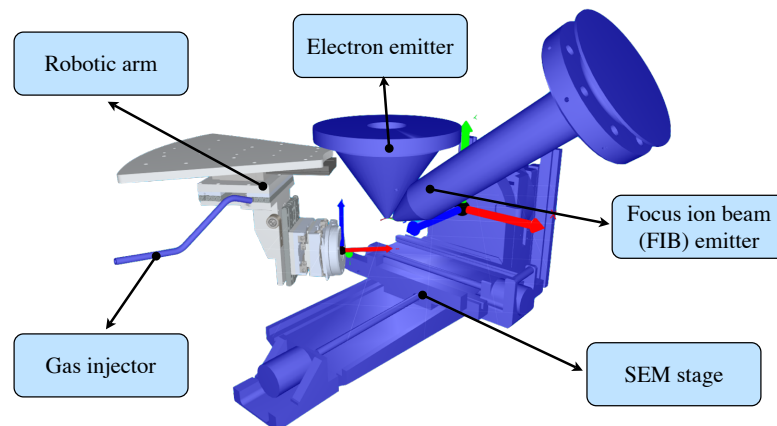


Figure 5.1: CAD representation of a serial 6 DoF robot for SEM developed at the FEMTO-ST laboratory, showing how it is positioned inside the SEM chamber.

In addition, modifications should be considered to eliminate or at least reduce the electronic input disturbance. As seen in the electrostatic micro-gripper identification phase, these disturbances could be dominant for an important part of the operation range. Tests should be performed with other processing boards and signal converters to find one suited for delivering noise and disturbances compatible with this application.

The results over disturbance influence can be explored to other tasks in SEM such as fabrication via FIB/e-beam lithography, where vibrations in the stage can reduce their attainable resolution. It is evident how SEM room preparation require special care, and the development of remote supervision strategies to eliminate non-essential interferences in the environment can be contemplated. In this situation, the SEM controlling computer, pumps and all robotic interface components (i.e. joysticks, ...) can be installed farther from the microscope, in a separated room.

In the scope of the NanoRobust project, the results obtained are expected to be integrated in a prototype for complete autonomous SEM manipulation cell. The works developed during this thesis would be used at the approach phase and characterization in real-world problems, and would serve as a final validation for this strategy. Combining the precise positioning strategy for the approach phases and force control during component handling could improve manipulation and characterization tasks, while reducing the risks of damaging components. A possible complete setup to be explored includes the use of end-effectors to counter vibrations and displacement errors

for the robotic arm or other positioning elements. In this case, coarse positioning of a robotic structure may be obtained via standard methods (i.e. visual servoing), while fine position control of the end-effector compensating any undesired effects present at the extremity.

Figure 5.2 exemplifies a real problem to be tackled: the characterization and manipulation of a nano-helix. So far, only traction tests were made with aid of AFM tips, where the pads at each extremity were glued to testing probes and displacements were measured via image processing techniques. The use of grippers with force-sensing capabilities could simplify the whole manipulation processing, while allowing to perform compression test with the aid of real time positioning data.

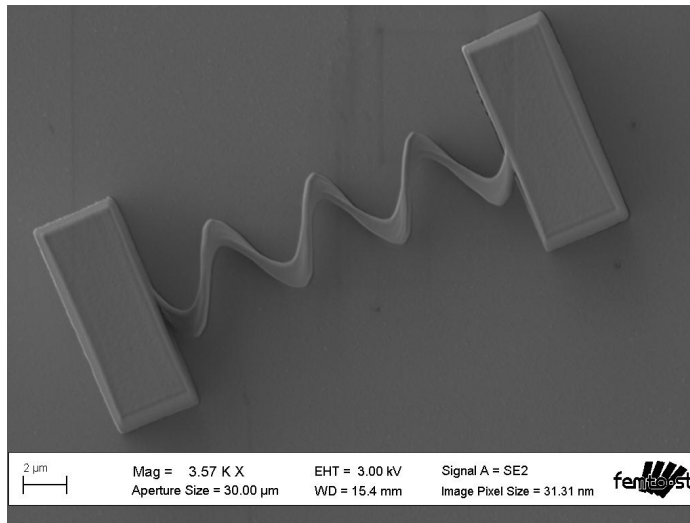


Figure 5.2: Nano-helix between pads, to facilitate manipulation tasks without damaging the sample. Fabricated and kindly offered by the Laboratory of Photonics and Nanostructures (LPN) in Marcoussis, France.

## PERSONAL PUBLICATIONS

- [Boudaoud et al., 2014a] Boudaoud, M., De Faria, M. G., Haddab, Y., Haliyo, S., Le Gorrec, Y., Lutz, P., et Régnier, S. (2014a). **Robust microscale grasping using a self scheduled dynamic controller**. In *World Congress*, volume 19, pages 7492–7498.
- [Boudaoud et al., 2015] Boudaoud, M., De Faria, M. G., Haddab, Y., Haliyo, S., Le Gorrec, Y., Lutz, P., et Régnier, S. (2015). **Robust microscale grasping through a multimodel design: synthesis and real time implementation**. *Control Engineering Practice*, 39:12–22.
- [Boudaoud et al., 2014b] Boudaoud, M., De Faria, M. G., Le Gorrec, Y., Haddab, Y., et Lutz, P. (2014b). **An output feedback l<sub>p</sub>v control strategy of a nonlinear electrostatic microgripper through a singular implicit modeling**. *Control Engineering Practice*, 28:97–111.
- [de Faria et al., 2015a] de Faria, M. G., Haddab, Y., Le Gorrec, Y., et Lutz, P. (2015a). **Extended high-gain observer for robust position control of a micro-gripper in air and vacuum**. In *IEEE Conference on Automation Science and Engineering (CASE)*.
- [de Faria et al., 2015b] de Faria, M. G., Haddab, Y., Le Gorrec, Y., et Lutz, P. (2015b). **Influence of mechanical noise inside a scanning electron microscope**. *Review of Scientific Instruments*, 86(4):045105.



## REFERENCES

- [Aur, ] **Auriga 60 Modular Crossbeam workstation - Installation requirements manual.** Carl Zeiss Microscopy.
- [kle, ] **Kleindiek MM3A-EM nano prober.** <http://www.nanotechnik.com/mm3a-em.html>. (accessed September 16, 2015).
- [pi, ] **P-911KNMV UHV-Compatible Miniature Piezo Hexapod.** <http://www.physikinstrumente.com/product-detail-page/p-911knmv-700850.html>. (accessed September 16, 2015).
- [sma, ] **SmarAct 15D manipulator.** <http://www.smaract.de/index.php/manipulators>. (accessed September 16, 2015).
- [zyv, ] **Zyvex nProber.** <http://www.zyvex.com/Documents/nProber.pdf>. (accessed September 16, 2015).
- [SP1, 2012] (2012). **Plane-mirror Miniature Interferometer Series SP120/2000 User's Guide.** SIOS Meßtechnik GmbH, 4 edition.
- [Sma, 2013] (2013). **MCS - Modular Control System Programmer's Guide.** Smaract GmbH.
- [Abrahamians et al., 2014] Abrahamians, J.-O., Sauvet, B., Polesel-Maris, J., Braive, R., et Régner, S. (2014). **A nanorobotic system for in situ stiffness measurements on membranes.** *Robotics, IEEE Transactions on*, 30(1):119–124.
- [Acosta et al., 2011] Acosta, J. C., Hwang, G., Polesel-Maris, J., et Régner, S. (2011). **A tuning fork based wide range mechanical characterization tool with nanorobotic manipulators inside a scanning electron microscope.** *Review of Scientific Instruments*, 82(3):035116.
- [Agnus et al., 2005] Agnus, J., Nectoux, P., et Chaillet, N. (2005). **Overview of microgrippers and design of a micromanipulation station based on a mmoc microgripper.** In *Computational Intelligence in Robotics and Automation, 2005. CIRA 2005. Proceedings. 2005 IEEE International Symposium on*, pages 117–123. IEEE.
- [Akita et al., 2002] Akita, S., et Nakayama, Y. (2002). **Manipulation of nanomaterial by carbon nanotube nanotweezers in scanning probe microscope.** *Japanese journal of applied physics*, 41(6S):4242.
- [Aoki et al., 2008] Aoki, K., Guimard, D., Nishioka, M., Nomura, M., Iwamoto, S., et Arakawa, Y. (2008). **Coupling of quantum-dot light emission with a three-dimensional photonic-crystal nanocavity.** *Nature Photonics*, 2(11):688–692.
- [Aphale et al., 2007] Aphale, S., Fleming, A., et Moheimani, S. (2007). **High speed nano-scale positioning using a piezoelectric tube actuator with active shunt control.** *Micro & Nano Letters*, 2(1):9–12.

- [Arai et al., 1996] Arai, F., Andou, D., et Fukuda, T. (1996). **Adhesion forces reduction for micro manipulation based on micro physics**. In *Micro Electro Mechanical Systems, 1996, MEMS'96, Proceedings. An Investigation of Micro Structures, Sensors, Actuators, Machines and Systems. IEEE, The Ninth Annual International Workshop on*, pages 354–359. IEEE.
- [Atassi et al., 1999] Atassi, A. N., et Khalil, H. K. (1999). **A separation principle for the stabilization of a class of nonlinear systems**. *IEEE Transactions on Automatic Control*, 44(9):1672–1687.
- [Aten et al., 2014] Aten, Q. T., Jensen, B. D., Burnett, S. H., et Howell, L. L. (2014). **A self-reconfiguring metamorphic nanoinjector for injection into mouse zygotes**. *Review of Scientific Instruments*, 85(5):055005.
- [Athans, 1986] Athans, M. (1986). **A tutorial on the LQG/LTR method**. Citeseer.
- [Babic et al., 2003] Babic, B., Furer, J., Sahoo, S., Farhangfar, S., et Schönenberger, C. (2003). **Intrinsic thermal vibrations of suspended doubly clamped single-wall carbon nanotubes**. *Nano Letters*, 3(11):1577–1580.
- [Beyeler et al., 2009] Beyeler, F., Muntwyler, S., et Nelson, B. J. (2009). **A six-axis mems force-torque sensor with micro-newton and nano-newtonmeter resolution**. *Microelectromechanical Systems, Journal of*, 18(2):433–441.
- [Beyeler et al., 2007] Beyeler, F., Neild, A., Oberti, S., Bell, D. J., Sun, Y., Dual, J., et Nelson, B. J. (2007). **Monolithically fabricated microgripper with integrated force sensor for manipulating microobjects and biological cells aligned in an ultrasonic field**. *Microelectromechanical Systems, Journal of*, 16(1):7–15.
- [Bibel et al., 1992] Bibel, J. E., et Malyevac, D. S. (1992). **Guidelines for the selection of weighting functions for h-infinity control**. Technical Report, DTIC Document.
- [Borovic et al., 2005] Borovic, B., Liu, A., Popa, D., Cai, H., et Lewis, F. (2005). **Open-loop versus closed-loop control of mems devices: choices and issues**. *Journal of Micromechanics and Microengineering*, 15(10):1917.
- [Boudaoud, 2012] Boudaoud, M. (2012). **Caracterisation dynamique des bruits a lechelle nanometrique et commande robuste LPV de systemes de micromanipulation**. PhD thesis, Universite de Franche-Comte, Besancon, France.
- [Boudaoud et al., 2010] Boudaoud, M., Haddab, Y., et Le Gorrec, Y. (2010). **Modelling of a mems-based microgripper: application to dexterous micromanipulation**. In *Intelligent Robots and Systems (IROS), 2010 IEEE/RSJ International Conference on*, pages 5634–5639. IEEE.
- [Boudaoud et al., 2013] Boudaoud, M., Haddab, Y., et Le Gorrec, Y. (2013). **Modeling and optimal force control of a nonlinear electrostatic microgripper**. *Mechatronics, IEEE/ASME Transactions on*, 18(3):1130–1139.
- [Boukhnifer et al., 2007] Boukhnifer, M., et Ferreira, A. (2007). **H $\infty$  loop shaping bilateral controller for a two-fingered tele-micromanipulation system**. *Control Systems Technology, IEEE Transactions on*, 15(5):891–905.
- [Bouscaud et al., 2012] Bouscaud, D., Pesci, R., Berveiller, S., et Patoor, E. (2012). **Estimation of the electron beam-induced specimen heating and the emitted x-rays spatial resolution by Kossel microdiffraction in a scanning electron microscope**. *Ultramicroscopy*, 115:115–119.

- [Braatz et al., 1994] Braatz, R. P., Young, P. M., Doyle, J. C., et Morari, M. (1994). **Computational complexity of  $\mu$  calculation**. *Automatic Control, IEEE Transactions on*, 39(5):1000–1002.
- [Busch et al., 2004] Busch, K., Lölkes, S., Wehrspohn, R. B., et Föll, H. (2004). **Photonic crystals**. *New York: Wiley*, pages 241–247.
- [Carrozza et al., 2000] Carrozza, M. C., Eisinger, A., Menciassi, A., Campolo, D., Micera, S., et Dario, P. (2000). **Towards a force-controlled microgripper for assembling biomedical microdevices**. *Journal of Micromechanics and Microengineering*, 10(2):271.
- [Chen et al., 2009] Chen, B. K., Zhang, Y., et Sun, Y. (2009). **Active release of microobjects using a mems microgripper to overcome adhesion forces**. *Microelectromechanical Systems, Journal of*, 18(3):652–659.
- [Chen et al., 2003] Chen, C.-S., et Kuo, W.-J. (2003). **Squeeze and viscous dampings in micro electrostatic comb drives**. *Sensors and Actuators A: Physical*, 107(2):193–203.
- [Chu et al., 1994] Chu, P. B., et Pister, K. S. (1994). **Analysis of closed-loop control of parallel-plate electrostatic microgrippers**. In *Robotics and Automation, 1994. Proceedings., 1994 IEEE International Conference on*, pages 820–825. IEEE.
- [Chu, 1994] Chu, W.-H. M. (1994). **Microfabricated tweezers with a large gripping force and a large range of motion**. PhD thesis, Case Western Reserve University.
- [Ciubotariu, 2015] Ciubotariu, A. (2015). **Pmn-pt based integrated actuator for 6 dof micro-gripper**. Technical Report, FEMTO-ST Institute.
- [Clévy et al., 2006] Clévy, C., et Chaillet, N. (2006). **Micromanipulation and micro-assembly systems**. In *IEEE/RAS International Advanced Robotics Programm, IARP'06.*, pages sur–CD.
- [Cui, 2009] Cui, Z. (2009). **Nanofabrication: principles, capabilities and limits**. Springer Science & Business Media.
- [Dahmen et al., 2013] Dahmen, C., et Tiemerding, T. (2013). **Fast and robust position determination in the scanning electron microscope**. In *Australasian Conference on Robotics and Automation*.
- [de Jonge et al., 2003] de Jonge, N., Lamy, Y., et Kaiser, M. (2003). **Controlled mounting of individual multiwalled carbon nanotubes on support tips**. *Nano Letters*, 3(12):1621–1624.
- [Dechev et al., 2004] Dechev, N., Cleghorn, W. L., et Mills, J. K. (2004). **Microassembly of 3-d microstructures using a compliant, passive microgripper**. *Microelectromechanical Systems, Journal of*, 13(2):176–189.
- [Dong et al., 2001] Dong, L., Arai, F., et Fukuda, T. (2001). **Three-dimensional nanoassembly of multi-walled carbon nanotubes through nanorobotic manipulations by using electron-beam-induced deposition**. In *Nanotechnology, 2001. IEEE-NANO 2001. Proceedings of the 2001 1st IEEE Conference on*, pages 93–98. IEEE.
- [Dong et al., 2002] Dong, L., Arai, F., et Fukuda, T. (2002). **Three-dimensional nanorobotic manipulations of carbon nanotubes**. *Journal of Robotics and Mechatronics*, 14(3):245–252.
- [Doyle, 1982] Doyle, J. (1982). **Analysis of feedback systems with structured uncertainties**. In *IEE Proceedings D (Control Theory and Applications)*, volume 129, pages 242–250. IET.

- [Doyle, 1985] Doyle, J. (1985). **Structured uncertainty in control system design**. In *1985 24th IEEE Conference on Decision and Control*, number 24, pages 260–265.
- [Doyle et al., 1991] Doyle, J., Packard, A., et Zhou, K. (1991). **Review of lfts, lmis, and  $\mu$** . In *Decision and Control, 1991., Proceedings of the 30th IEEE Conference on*, pages 1227–1232. IEEE.
- [Doyle et al., 1989] Doyle, J. C., Glover, K., Khargonekar, P. P., Francis, B., et others (1989). **State-space solutions to standard h 2 and h $\infty$  control problems**. *Automatic Control, IEEE Transactions on*, 34(8):831–847.
- [Doyle et al., 1979] Doyle, J. C., et Stein, G. (1979). **Robustness with observers**. Technical Report, DTIC Document.
- [Driesen et al., 2005] Driesen, W., Varidel, T., Régnier, S., et Breguet, J.-M. (2005). **Micro manipulation by adhesion with two collaborating mobile micro robots**. *Journal of Micromechanics and Microengineering*, 15(10):S259.
- [Egerton et al., 2004] Egerton, R., Li, P., et Malac, M. (2004). **Radiation damage in the TEM and SEM**. *Micron*, 35(6):399–409.
- [Eisenberg et al., 2001] Eisenberg, A., Menciassi, A., Micera, S., Campolo, D., Carrozza, M., et Dario, P. (2001). **Pi force control of a microgripper for assembling biomedical microdevices**. *IEE Proceedings-Circuits, Devices and Systems*, 148(6):348–352.
- [Epp et al., 2004] Epp, D. S., Ozdoganlar, O. B., et Sumali, H. (2004). **Dynamic measurement of gas damping effects in MEMS**. In *Current Proceedings, SEM International Congress X*.
- [Esfandiari et al., 1989] Esfandiari, F., et Khalil, H. (1989). **Observer-based control of uncertain linear systems: Recovering state feedback robustness under matching condition**. In *American Control Conference, 1989*, pages 931–936. IEEE.
- [Esfandiari et al., 1992] Esfandiari, F., et Khalil, H. K. (1992). **Output feedback stabilization of fully linearizable systems**. *International Journal of control*, 56(5):1007–1037.
- [Fahlbusch et al., 1999] Fahlbusch, S., Fatikow, S., Seyfried, J., et Buerkle, A. (1999). **Flexible microrobotic system miniman: design, actuation principle and control**. In *Advanced Intelligent Mechatronics, 1999. Proceedings. 1999 IEEE/ASME International Conference on*, pages 156–161. IEEE.
- [Fahlbusch et al., 2005] Fahlbusch, S., Mazerolle, S., Breguet, J.-M., Steinecker, A., Agnus, J., Pérez, R., et Michler, J. (2005). **Nanomanipulation in a scanning electron microscope**. *Journal of materials processing technology*, 167(2):371–382.
- [Falvo et al., 1997] Falvo, M., Clary, G., Taylor, R., Chi, V., Brooks, F., Washburn, S., et Superfine, R. (1997). **Bending and buckling of carbon nanotubes under large strain**. *Nature*, 389(6651):582–584.
- [Fatikow, 2007] Fatikow, S. (2007). **Automated nanohandling by microrobots**. Springer Publishing Company, Incorporated.
- [Fatikow et al., 2000] Fatikow, S., Seyfried, J., Buerkle, A., Schmoeckel, F., et others (2000). **A flexible microrobot-based microassembly station**. *Journal of Intelligent and Robotic Systems*, 27(1-2):135–169.

- [Fleming et al., 2010] Fleming, A. J., Aphale, S. S., et Moheimani, S. R. (2010). **A new method for robust damping and tracking control of scanning probe microscope positioning stages.** *Nanotechnology, IEEE Transactions on*, 9(4):438–448.
- [Franklin et al., 2012] Franklin, A. D., Luisier, M., Han, S.-J., Tulevski, G., Breslin, C. M., Gignac, L., Lundstrom, M. S., et Haensch, W. (2012). **Sub-10 nm carbon nanotube transistor.** *Nano letters*, 12(2):758–762.
- [Freidovich et al., 2008] Freidovich, L. B., et Khalil, H. K. (2008). **Performance recovery of feedback-linearization-based designs.** *Automatic Control, IEEE Transactions on*, 53(10):2324–2334.
- [Friedt et al., 2007] Friedt, J.-M., et Carry, E. (2007). **Introduction to the quartz tuning fork.** *American Journal of Physics*, 75(5):415–422.
- [Fujioka et al., 1980] Fujioka, H., Nakamae, K., et Ura, K. (1980). **Function testing of bipolar ics and lsis with the stroboscopic scanning electron microscope.** *Solid-State Circuits, IEEE Journal of*, 15(2):177–183.
- [Fukuda et al., 2002] Fukuda, T., Arai, F., et Dong, L. (2002). **Fabrication and property analysis of mwnt junctions through nanorobotic manipulations.** *International Journal of Nonlinear Sciences and Numerical Simulation*, 3(3-4):753–758.
- [Fukuda et al., 2003] Fukuda, T., Arai, F., et Dong, L. (2003). **Assembly of nanodevices with carbon nanotubes through nanorobotic manipulations.** *Proceedings of the IEEE*, 91(11):1803–1818.
- [Fukuda et al., 2013] Fukuda, T., Arai, F., et Nakajima, M. (2013). **Micro-nanorobotic manipulation systems and their applications.** Springer Science & Business Media.
- [Gahinet et al., 1994] Gahinet, P., et Apkarian, P. (1994). **A linear matrix inequality approach to  $h_\infty$  control.** *International journal of robust and nonlinear control*, 4(4):421–448.
- [Gao et al., 2001] Gao, Z., Huang, Y., et Han, J. (2001). **An alternative paradigm for control system design.** In *Decision and Control, 2001. Proceedings of the 40th IEEE Conference on*, volume 5, pages 4578–4585. IEEE.
- [Gauthier et al., 2011] Gauthier, M., et Régnier, S. (2011). **Robotic micro-assembly.** John Wiley & Sons.
- [Ghafari-rad et al., 2012] Ghafari-rad, H., Rezaei, S., Zareinejad, M., Hamdi, M., et Ansari, R. J. (2012). **Robust control with unknown dynamic estimation for multi-axial piezoelectric actuators with coupled dynamics.** *Comptes Rendus Mecanique*, 340(9):646–660.
- [Gjerde et al., 2006] Gjerde, K., Kjelstrup-Hansen, J., Clausen, C. H., Teo, K. B., Milne, W. I., Rubahn, H.-G., et Bøggild, P. (2006). **Carbon nanotube forests: a non-stick workbench for nanomanipulation.** *Nanotechnology*, 17(19):4917.
- [Goldfarb et al., 1999] Goldfarb, M., et Celanovic, N. (1999). **A flexure-based gripper for small-scale manipulation.** *Robotica*, 17(02):181–187.
- [Gong et al., 2013] Gong, Z., Chen, B. K., Liu, J., et Sun, Y. (2013). **Automated nanoprob-ing under scanning electron microscopy.** In *Robotics and Automation (ICRA), 2013 IEEE International Conference on*, pages 1433–1438. IEEE.

- [Gorman et al., 2006] Gorman, J. J., Kim, Y.-S., et Dagalakis, N. G. (2006). **Control of mems nanopositioners with nano-scale resolution**. In *ASME 2006 International Mechanical Engineering Congress and Exposition*, pages 151–159. American Society of Mechanical Engineers.
- [Gorman et al., 2007] Gorman, J. J., Kim, Y.-S., Vladar, A. E., et Dagalakis, N. G. (2007). **Design of an on-chip microscale nanoassembly system**. *International Journal of Nanomanufacturing*, 1(6):710–721.
- [Green et al., 1990] Green, M., Glover, K., Limebeer, D., et Doyle, J. (1990). **Aj-spectral factorization approach to  $h_\infty$** . *SIAM Journal on Control and Optimization*, 28(6):1350–1371.
- [Grossard et al., 2011] Grossard, M., Boukallel, M., Chaillet, N., et Rotinat-Libersa, C. (2011). **Modeling and robust control strategy for a control-optimized piezoelectric microgripper**. *Mechatronics, IEEE/ASME Transactions on*, 16(4):674–683.
- [Gu et al., 2014] Gu, G.-Y., Zhu, L.-M., Su, C.-Y., Ding, H., et Fatikow, S. (2014). **Modeling and control of piezo-actuated nanopositioning stages: a survey**. *IEEE Transactions on Automation Science and Engineering*.
- [Guo et al., 2011] Guo, B.-Z., et Zhao, Z.-l. (2011). **On the convergence of an extended state observer for nonlinear systems with uncertainty**. *Systems & Control Letters*, 60(6):420–430.
- [Haddab et al., 2000] Haddab, Y., Chaillet, N., et Bourjault, A. (2000). **A microgripper using smart piezoelectric actuators**. In *Intelligent Robots and Systems, 2000.(IROS 2000). Proceedings. 2000 IEEE/RSJ International Conference on*, volume 1, pages 659–664. IEEE.
- [Hatamura et al., 1990] Hatamura, Y., et Morishita, H. (1990). **Direct coupling system between nanometer world and human world**. In *Micro Electro Mechanical Systems, 1990. Proceedings, An Investigation of Micro Structures, Sensors, Actuators, Machines and Robots. IEEE*, pages 203–208. IEEE.
- [Hertel et al., 1998] Hertel, T., Martel, R., et Avouris, P. (1998). **Manipulation of individual carbon nanotubes and their interaction with surfaces**. *The Journal of Physical Chemistry B*, 102(6):910–915.
- [Ho et al., 1998] Ho, C.-M., et Tai, Y.-C. (1998). **Micro-electro-mechanical-systems (mems) and fluid flows**. *Annual Review of Fluid Mechanics*, 30(1):579–612.
- [Horsley et al., 1998] Horsley, D., Cohn, M. B., Singh, A., Horowitz, R., Pisano, A. P., et others (1998). **Design and fabrication of an angular microactuator for magnetic disk drives**. *Microelectromechanical Systems, Journal of*, 7(2):141–148.
- [Huang et al., 2009] Huang, S.-J., et Wang, S.-S. (2009). **Mechatronics and control of a long-range nanometer positioning servomechanism**. *Mechatronics*, 19(1):14–28.
- [Hwang et al., 2009] Hwang, G., Acosta, J. C., Vela, E., Haliyo, S., et Régnier, S. (2009). **Graphene as thin film infrared optoelectronic sensor**. In *Optomechatronic Technologies, 2009. ISOT 2009. International Symposium on*, pages 169–174. IEEE.
- [Ishikawa et al., 1993] Ishikawa, H., Dobashi, H., Kodama, T., Furuhashi, T., et Uchikawa, Y. (1993). **Investigation of micro mechanical vibration of piezoelectric actuators using a stroboscopic sem**. *Journal of electron microscopy*, 42(1):35–40.

- [Ivan et al., 2013] Ivan, I. A., Ciubotariu, D. A., Clévy, C., Lutz, P., et Chaillet, N. (2013). **Duo-bimorph actuator made of pmn-pt [011]: 3d modeling, development and characterization.** In *Advanced Intelligent Mechatronics (AIM), 2013 IEEE/ASME International Conference on*, pages 140–145. IEEE.
- [Iwaya et al., 2012] Iwaya, K., Shimizu, R., Teramura, A., Sasaki, S., Itagaki, T., et Hitosugi, T. (2012). **Design of an effective vibration isolation system for measurements sensitive to low-frequency vibrations.** *Journal of Vacuum Science & Technology A*, 30(6):063201.
- [Jasper, 2011] Jasper, D. (2011). **SEM-based motion control for automated robotic nanohandling.** PhD thesis, Carl von Ossietzky Universität, Oldenburg.
- [Jasper et al., 2010] Jasper, D., Diederichs, C., Edeler, C., et Fatikow, S. (2010). **High-speed nanorobot position control inside a scanning electron microscope.** In *Electrical Engineering/Electronics Computer Telecommunications and Information Technology (ECTI-CON), 2010 International Conference on*, pages 513–517. IEEE.
- [Johnson, 1928] Johnson, J. B. (1928). **Thermal agitation of electricity in conductors.** *Physical review*, 32(1):97.
- [Jung et al., 2012] Jung, K. O., Kim, S. J., et Kim, D. H. (2012). **An approach to reducing the distortion caused by vibration in scanning electron microscope images.** *Nuclear Instruments and Methods in Physics Research Section A: Accelerators, Spectrometers, Detectors and Associated Equipment*, 676:5–17.
- [Khalil, 2008] Khalil, H. K. (2008). **High-gain observers in nonlinear feedback control.** In *Control, Automation and Systems, 2008. ICCAS 2008. International Conference on*, pages xlvii–lvii. IEEE.
- [Khalil et al., 2014] Khalil, H. K., et Praly, L. (2014). **High-gain observers in nonlinear feedback control.** *International Journal of Robust and Nonlinear Control*, 24(6):993–1015.
- [Kim et al., 2003] Kim, K., Lim, S., Lee, I., An, K., Bae, D., Choi, S., Yoo, J., et Lee, Y. (2003). **In situ manipulation and characterizations using nanomanipulators inside a field emission-scanning electron microscope.** *Review of scientific instruments*, 74(9):4021–4025.
- [Komati et al., 2014] Komati, B., Agnus, J., Clévy, C., et Lutz, P. (2014). **Prototyping of a highly performant and integrated piezoresistive force sensor for microscale applications.** *Journal of Micromechanics and Microengineering*, 24(3):035018.
- [Korayem et al., 2012] Korayem, M., et Esmailzadehha, S. (2012). **Virtual reality interface for nano-manipulation based on enhanced images.** *The International Journal of Advanced Manufacturing Technology*, 63(9-12):1153–1166.
- [Koyano et al., 1996] Koyano, K., et Sato, T. (1996). **Micro-object handling system with concentrated visual fields and new handling skills.** In *Photonics East'96*, pages 130–140. International Society for Optics and Photonics.
- [Li et al., 2011] Li, Y., et Xu, Q. (2011). **A totally decoupled piezo-driven xyz flexure parallel micropositioning stage for micro/nanomanipulation.** *Automation Science and Engineering, IEEE Transactions on*, 8(2):265–279.
- [Li et al., 2012] Li, Y., et Xu, Q. (2012). **Design and robust repetitive control of a new parallel-kinematic xy piezostage for micro/nanomanipulation.** *Mechatronics, IEEE/ASME Transactions on*, 17(6):1120–1132.

- [Lim et al., 2005] Lim, S. C., Kim, K. S., Jeong, S. Y., Cho, S., Yoo, J.-E., Lee, Y. H., et others (2005). **Nanomanipulator-assisted fabrication and characterization of carbon nanotubes inside scanning electron microscope**. *Micron*, 36(5):471–476.
- [Liu et al., 2006] Liu, K.-Z., et He, R. (2006). **A simple derivation of are solutions to the standard  $h_\infty$  control problem based on lmi solution**. *Systems & control letters*, 55(6):487–493.
- [Liu et al., 2013] Liu, L., Bai, Y.-G., Zhang, D.-L., et Wu, Z.-G. (2013). **Ultra-precision measurement and control of angle motion in piezo-based platforms using strain gauge sensors and a robust composite controller**. *Sensors*, 13(7):9070–9084.
- [Madoński et al., 2015] Madoński, R., et Herman, P. (2015). **Survey on methods of increasing the efficiency of extended state disturbance observers**. *ISA transactions*, 56:18–27.
- [Matteson et al., 2002] Matteson, T., Schwarz, S., Houge, E., Kempshall, B., et Giannuzzi, L. (2002). **Electron backscattering diffraction investigation of focused ion beam surfaces**. *Journal of Electronic Materials*, 31(1):33–39.
- [Mazerolle et al., 2005] Mazerolle, S., Breguet, J.-M., Steinecker, A., Agnus, J., Pérez, R., Michler, J., et others (2005). **Nanomanipulation in a scanning electron microscope**. *Journal of Materials Processing Technology*, 167(2):371–382.
- [Mertens et al., 2003] Mertens, J., Finot, E., Thundat, T., Fabre, A., Nadal, M.-H., Eyraud, V., et Bourillot, E. (2003). **Effects of temperature and pressure on microcantilever resonance response**. *Ultramicroscopy*, 97(1):119–126.
- [Meyer et al., 2008] Meyer, E., et Braun, H.-G. (2008). **Micro-and nanomanipulation inside the sem**. In *Journal of Physics: Conference Series*, volume 126, page 012074. IOP Publishing.
- [Miller, 2005] Miller, L. A. (2005). **Structural dynamics and resonance in plants with nonlinear stiffness**. *Journal of theoretical biology*, 234(4):511–524.
- [Mokrane Boudaoud, 2014] Mokrane Boudaoud, S. R. (2014). **An overview of gripping force measurement at the micro and nano-scales using two-fingered microrobotic systems**. *Int J Adv Robot Syst*, 11:45.
- [Muller et al., 2006] Muller, D., Kirkland, E., Thomas, M., Grazul, J., Fitting, L., et Weyland, M. (2006). **Room design for high-performance electron microscopy**. *Ultramicroscopy*, 106(11):1033–1040.
- [Nakabayashi et al., 2007] Nakabayashi, D., Silva, P., et Ugarte, D. (2007). **Inexpensive two-tip nanomanipulator for a SEM**. *Applied Surface Science*, 254(1):405–411.
- [Nakabayashi et al., 2006] Nakabayashi, D., Silva, P. C., González, J. C., Rodrigues, V., et Ugarte, D. (2006). **Low-cost nanomanipulator for in situ experiments in a sem**. *Microscopy and Microanalysis*, 12(04):311–316.
- [Nakazato et al., 2009] Nakazato, Y., Yuasa, T., Sekine, G., Miyazawa, H., Jin, M., Takeuchi, S., Ariga, Y., et Murakawa, M. (2009). **Micromanipulation system using scanning electron microscope**. *Microsystem technologies*, 15(6):859–864.
- [Newbury et al., 2003] Newbury, D. E., Joy, D. C., Echlin, P., Fiori, C. E., et Goldstein, J. I. (2003). **Scanning electron microscopy and X-ray microanalysis**. Springer.

- [Nguyen, 1995] Nguyen, C. T. (1995). **Micromechanical resonators for oscillators and filters.** In *Ultrasonics Symposium, 1995. Proceedings., 1995 IEEE*, volume 1, pages 489–499. IEEE.
- [Nordström Andersen et al., 2009] Nordström Andersen, K., Petersen, D. H., Carlson, K., Møhlhave, K., Sardan Sukas, Ö., Horsewell, A., Eichhorn, V., Fatikow, S., et Bøggild, P. (2009). **Multimodal electrothermal silicon microgrippers for nanotube manipulation.** *IEEE Transactions on Nanotechnology*, 8(1):76–85.
- [Otsuka et al., 2012] Otsuka, H., Nagasaki, Y., et Kataoka, K. (2012). **Pegylated nanoparticles for biological and pharmaceutical applications.** *Advanced drug delivery reviews*, 64:246–255.
- [Packard et al., 1993] Packard, A., et Doyle, J. (1993). **The complex structured singular value.** *Automatica*, 29(1):71–109.
- [Pao et al., 2007] Pao, L. Y., Butterworth, J., Abramovitch, D. Y., et others (2007). **Combined feedforward/feedback control of atomic force microscopes.** In *American Control Conference, 2007. ACC'07*, pages 3509–3515. IEEE.
- [Park et al., 2010] Park, D. S.-W., Nallani, A. K., Cha, D., Lee, G.-S., Kim, M. J., Skidmore, G., Lee, J.-B., et Lee, J.-S. (2010). **A sub-micron metallic electrothermal gripper.** *Microsystem technologies*, 16(3):367–373.
- [Peralta et al., 2013] Peralta, E., Soong, K., England, R., Colby, E., Wu, Z., Montazeri, B., McGuinness, C., McNeur, J., Leedle, K., Walz, D., et others (2013). **Demonstration of electron acceleration in a laser-driven dielectric microstructure.** *Nature*, 503(7474):91–94.
- [Pérez et al., 2005] Pérez, R., Agnus, J., Clévy, C., Hubert, A., et Chaillet, N. (2005). **Modeling, fabrication, and validation of a high-performance 2-dof piezoactuator for micromanipulation.** *Mechatronics, IEEE/ASME Transactions on*, 10(2):161–171.
- [Pluska et al., 2009] Pluska, M., Czerwinski, A., Ratajczak, J., Katcki, J., Oskwarek, L., et Rak, R. (2009). **Separation of image-distortion sources and magnetic-field measurement in scanning electron microscope (sem).** *Micron*, 40(1):46–50.
- [Pluska et al., 2015] Pluska, M., Czerwinski, A., Wzorek, M., Juchniewicz, M., et Katcki, J. (2015). **Identification and reduction of acoustic-noise influence on focused ion beam (fib).** *Nuclear Instruments and Methods in Physics Research Section B: Beam Interactions with Materials and Atoms*, 348:106–110.
- [Polyakov et al., 2014] Polyakov, B., Vlassov, S., Dorogin, L. M., Butikova, J., Antsov, M., Oras, S., Löhmus, R., et Kink, I. (2014). **Manipulation of nanoparticles of different shapes inside a scanning electron microscope.** *Beilstein journal of nanotechnology*, 5(1):133–140.
- [Postma et al., 2000] Postma, H. W., Sellmeijer, A., et Dekker, C. (2000). **Manipulation and imaging of individual single-walled carbon nanotubes with an atomic force microscope.** *Advanced Materials*, 12(17):1299–1302.
- [Radke et al., 2006] Radke, A., et Gao, Z. (2006). **A survey of state and disturbance observers for practitioners.** In *American Control Conference, 2006*, pages 6–pp. IEEE.
- [Rakotondrabe, 2013] Rakotondrabe, M. (2013). **Combining self-sensing with an unknown-input-observer to estimate the displacement, the force and the state in piezoelectric cantilevered actuators.** In *American Control Conference (ACC), 2013*, pages 4516–4523. IEEE.

- [Rakotondrabe et al., 2010] Rakotondrabe, M., Clévy, C., et Lutz, P. (2010). **Complete open loop control of hysteretic, creeped, and oscillating piezoelectric cantilevers**. *Automation Science and Engineering, IEEE Transactions on*, 7(3):440–450.
- [Rana et al., 2014] Rana, M. S., Pota, H. R., et Petersen, I. R. (2014). **The design of model predictive control for an afm and its impact on piezo nonlinearities**. *European Journal of Control*, 20(4):188–198.
- [Régnier, 2006] Régnier, S. (2006). **La manipulation aux échelles microscopiques**. *Habilitation à diriger des recherches, Université Pierre et Marie Curie (Paris 6, France)*.
- [Rong et al., 2006] Rong, W., Ding, W., Maedler, L., Ruoff, R. S., et Friedlander, S. K. (2006). **Mechanical properties of nanoparticle chain aggregates by combined afm and sem: Isolated aggregates and networks**. *Nano letters*, 6(12):2646–2655.
- [Sader et al., 1995] Sader, J. E., Larson, I., Mulvaney, P., et White, L. R. (1995). **Method for the calibration of atomic force microscope cantilevers**. *Review of Scientific Instruments*, 66(7):3789–3798.
- [Saeidpourazar et al., 2008] Saeidpourazar, R., et Jalili, N. (2008). **Towards fused vision and force robust feedback control of nanorobotic-based manipulation and grasping**. *Mechanics*, 18(10):566–577.
- [Salapaka et al., 2002] Salapaka, S., Sebastian, A., Cleveland, J. P., et Salapaka, M. V. (2002). **High bandwidth nano-positioner: A robust control approach**. *Review of scientific instruments*, 73(9):3232–3241.
- [Salim et al., 1997] Salim, R., Wurmus, H., Harnisch, A., et Hülsenberg, D. (1997). **Microgrippers created in microstructurable glass**. *Microsystem technologies*, 4(1):32–34.
- [Sandberg et al., 2005] Sandberg, R., Svendsen, W., Mølhave, K., et Boisen, A. (2005). **Temperature and pressure dependence of resonance in multi-layer microcantilevers**. *Journal of Micromechanics and Microengineering*, 15(8):1454.
- [Sardan et al., 2008] Sardan, O., Eichhorn, V., Petersen, D., Fatikow, S., Sigmund, O., et Bøggild, P. (2008). **Rapid prototyping of nanotube-based devices using topology-optimized microgrippers**. *Nanotechnology*, 19(49):495503.
- [Scherer, 1992] Scherer, C. (1992).  **$H_\infty$ -optimization without assumptions on finite or infinite zeros**. *SIAM Journal on Control and Optimization*, 30(1):143–166.
- [Schmoeckel et al., 2001] Schmoeckel, F., et Worn, H. (2001). **Remotely controllable mobile microrobots acting as nano positioners and intelligent tweezers in scanning electron microscopes (sems)**. In *Robotics and Automation, 2001. Proceedings 2001 ICRA. IEEE International Conference on*, volume 4, pages 3909–3913. IEEE.
- [Schrijver et al., 2002] Schrijver, E., et Van Dijk, J. (2002). **Disturbance observers for rigid mechanical systems: equivalence, stability, and design**. *Journal of Dynamic Systems, Measurement, and Control*, 124(4):539–548.
- [Semonin et al., 2011] Semonin, O. E., Luther, J. M., Choi, S., Chen, H.-Y., Gao, J., Nozik, A. J., et Beard, M. C. (2011). **Peak external photocurrent quantum efficiency exceeding 100% via meg in a quantum dot solar cell**. *Science*, 334(6062):1530–1533.

- [Sharma et al., 2005] Sharma, G., Mavroidis, C., et Ferreira, A. (2005). **Virtual reality and haptics in nano-and bionanotechnology**. *Handbook of theoretical and computational nanotechnology*, 10:1–33.
- [Sievers, 2011] Sievers, T. (2011). **Global sensor feedback for automatic nanohandling inside a scanning electron microscope**. In *Intelligent Production Machines and Systems-2nd I\* PROMS Virtual International Conference 3-14 July 2006*, page 289. Elsevier.
- [Sitti, 2001] Sitti, M. (2001). **Survey of nanomanipulation systems**. In *Nanotechnology, 2001. IEEE-NANO 2001. Proceedings of the 2001 1st IEEE Conference on*, pages 75–80. IEEE.
- [Sitti et al., 2001] Sitti, M., Aruk, B., Shintani, H., et Hashimoto, H. (2001). **Development of a scaled teleoperation system for nano scale interaction and manipulation**. In *Robotics and Automation, 2001. Proceedings 2001 ICRA. IEEE International Conference on*, volume 1, pages 860–867. IEEE.
- [Sitti et al., 2000] Sitti, M., et Hashimoto, H. (2000). **Two-dimensional fine particle positioning under an optical microscope using a piezoresistive cantilever as a manipulator**. *journal of Micromechatronics*, 1(1):25–48.
- [Skogestad et al., 2007] Skogestad, S., et Postlethwaite, I. (2007). **Multivariable feedback control: analysis and design**, volume 2. Wiley New York.
- [Stievater et al., 2002] Stievater, T., Rabinovich, W., Newman, H., Mahon, R., Goetz, P., Ebel, J., et McGee, D. (2002). **Measurement of thermal-mechanical noise in microelectromechanical systems**. *Applied physics letters*, 81(10):1779–1781.
- [Stoorvogel, 1991] Stoorvogel, A. A. (1991). **The singular  $h_\infty$  control problem with dynamic measurement feedback**. *SIAM journal on control and optimization*, 29(1):160–184.
- [Suga et al., 2009] Suga, H., Naitoh, Y., Tanaka, M., Horikawa, M., Kobori, H., et Shimizu, T. (2009). **Nanomanipulation of single nanoparticle using a carbon nanotube probe in a scanning electron microscope**. *Applied Physics Express*, 2(5):055004.
- [Sumali et al., 2008] Sumali, H., et Carne, T. G. (2008). **Air-drag damping on micro-cantilever beams**. In *XXVI International Modal Analysis Conference (IMAC): Conference & Exposition on Structural Dynamics*. Society of Experimental Mechanics.
- [Tamadazte et al., 2012] Tamadazte, B., Painsavoine, M., Agnus, J., Pétrini, V., et Le-Fort Piat, N. (2012). **Four dof piezoelectric microgripper equipped with a smart cmos camera**. *Micro-electromechanical Systems, Journal of*, 21(2):256–258.
- [Tang et al., 2014] Tang, H., et Li, Y. (2014). **Development and active disturbance rejection control of a compliant micro-/nanopositioning piezostage with dual mode**. *Industrial Electronics, IEEE Transactions on*, 61(3):1475–1492.
- [Tian et al., 2009] Tian, G., et Gao, Z. (2009). **From poncelet’s invariance principle to active disturbance rejection**. In *American Control Conference, 2009. ACC’09.*, pages 2451–2457. IEEE.
- [Toda et al., 2010] Toda, M., Ono, T., Liu, F., et Voiculescu, I. (2010). **Evaluation of bimaterial cantilever beam for heat sensing at atmospheric pressure**. *Review of Scientific Instruments*, 81(5).

- [Tsai et al., 2005] Tsai, Y.-C., Lei, S. H., et Sudin, H. (2005). **Design and analysis of planar compliant microgripper based on kinematic approach.** *Journal of Micromechanics and Microengineering*, 15(1):143.
- [Villanueva et al., 2013] Villanueva, L., Karabalin, R., Matheny, M., Chi, D., Sader, J., et Roukes, M. (2013). **Nonlinearity in nanomechanical cantilevers.** *Physical Review B*, 87(2):024304.
- [Vladar, 2003] Vladar, A. (2003). **Scanning electron microscopy in real world environment.**
- [Wang et al., 2003] Wang, W., et Gao, Z. (2003). **A comparison study of advanced state observer design techniques.** In *American Control Conference, 2003. Proceedings of the 2003*, volume 6, pages 4754–4759. IEEE.
- [Wei et al., 2010] Wei, X., Chen, Q., Peng, L., Cui, R., et Li, Y. (2010). **In situ measurements on individual thin carbon nanotubes using nanomanipulators inside a scanning electron microscope.** *Ultramicroscopy*, 110(3):182–189.
- [Welch, 1967] Welch, P. D. (1967). **The use of fast fourier transform for the estimation of power spectra: A method based on time averaging over short, modified periodograms.** *IEEE Transactions on audio and electroacoustics*, 15(2):70–73.
- [Wong et al., 2007] Wong, C.-L., et Wong, W.-K. (2007). **In-plane motion characterization of mems resonators using stroboscopic scanning electron microscopy.** *Sensors and Actuators A: Physical*, 138(1):167–178.
- [Wong et al., 1997] Wong, E. W., Sheehan, P. E., et Lieber, C. M. (1997). **Nanobeam mechanics: elasticity, strength, and toughness of nanorods and nanotubes.** *Science*, 277(5334):1971–1975.
- [Wu et al., 2013] Wu, Z.-S., Parvez, K., Feng, X., et Müllen, K. (2013). **Graphene-based in-plane micro-supercapacitors with high power and energy densities.** *Nature communications*, 4.
- [Xie et al., 2009] Xie, H., et Régnier, S. (2009). **Three-dimensional automated micromanipulation using a nanotip gripper with multi-feedback.** *Journal of Micromechanics and Microengineering*, 19(7):075009.
- [Xu, 2013] Xu, Q. (2013). **Precision position/force interaction control of a piezoelectric multi-morph microgripper for microassembly.** *Automation Science and Engineering, IEEE Transactions on*, 10(3):503–514.
- [Xu, 2015] Xu, Q. (2015). **Robust impedance control of a compliant microgripper for high-speed position/force regulation.** *Industrial Electronics, IEEE Transactions on*, 62(2):1201–1209.
- [Xu et al., 2012] Xu, Q., et Li, Y. (2012). **Micro-/nanopositioning using model predictive output integral discrete sliding mode control.** *Industrial Electronics, IEEE Transactions on*, 59(2):1161–1170.
- [Yamamoto et al., 2003] Yamamoto, Y., Konishi, R., Negishi, Y., et Kawakami, T. (2003). **Prototyping ubiquitous micro-manipulation system.** In *Advanced Intelligent Mechatronics, 2003. AIM 2003. Proceedings. 2003 IEEE/ASME International Conference on*, volume 2, pages 709–714. IEEE.

- [Yang et al., 2009] Yang, X., et Huang, Y. (2009). **Capabilities of extended state observer for estimating uncertainties**. In *American Control Conference, 2009. ACC'09.*, pages 3700–3705. IEEE.
- [Yi et al., 2009] Yi, J., Chang, S., et Shen, Y. (2009). **Disturbance-observer-based hysteresis compensation for piezoelectric actuators**. *Mechatronics, IEEE/ASME Transactions on*, 14(4):456–464.
- [Yu et al., 1999] Yu, M., Dyer, M. J., Skidmore, G. D., Rohrs, H. W., Lu, X., Ausman, K. D., Von Ehr, J. R., et Ruoff, R. S. (1999). **Three-dimensional manipulation of carbon nanotubes under a scanning electron microscope**. *Nanotechnology*, 10(3):244.
- [Zadegan et al., 2012] Zadegan, R. M., et Norton, M. L. (2012). **Structural dna nanotechnology: From design to applications**. *Int. J. Mol. Sci*, 13:7149–7162.
- [Zames, 1981] Zames, G. (1981). **Feedback and optimal sensitivity: Model reference transformations, multiplicative seminorms, and approximate inverses**. *Automatic Control, IEEE Transactions on*, 26(2):301–320.
- [Zhang et al., 2005] Zhang, W., et Turner, K. L. (2005). **Pressure-dependent damping characteristics of microsilicon beam resonators for different resonant modes**. In *Sensors, 2005 IEEE*, pages 4–pp. IEEE.
- [Zhang et al., 2013a] Zhang, Y., Zhang, Y., Ru, C., Chen, B., et Sun, Y. (2013a). **A load-lock-compatible nanomanipulation system for scanning electron microscope**. *ASME Transactions on Mechatronics*, 18(1).
- [Zhang et al., 2012] Zhang, Y. L., Li, J., To, S., Zhang, Y., Ye, X., You, L., et Sun, Y. (2012). **Automated nanomanipulation for nanodevice construction**. *Nanotechnology*, 23(6):065304.
- [Zhang et al., 2013b] Zhang, Y. L., Zhang, Y., Ru, C., Li, J., et Sun, Y. (2013b). **Nanorobotic manipulation of 1d nanomaterials in scanning electron microscopes**. In *Nanorobotics*, pages 155–165. Springer.
- [Zheng et al., 2012] Zheng, Q., Gao, L. Q., et Gao, Z. (2012). **On validation of extended state observer through analysis and experimentation**. *Journal of Dynamic Systems, Measurement, and Control*, 134(2):024505.
- [Zhou et al., 1998] Zhou, Y., Nelson, B. J., et Vikramaditya, B. (1998). **Fusing force and vision feedback for micromanipulation**. In *Robotics and Automation, 1998. Proceedings. 1998 IEEE International Conference on*, volume 2, pages 1220–1225. IEEE.
- [Zhu et al., 2015] Zhu, S., Cheng, H.-H., Blakey, I., Stokes, N., Ostrikov, K. K., et Cortie, M. (2015). **Plasmonic ‘top-hat’ nano-star arrays by electron beam lithography**. *Microelectronic Engineering*, 139:13–18.
- [Ziaie et al., 2007] Ziaie, B., Baldi, A., et Atashbar, M. (2007). **Introduction to micro/nanofabrication**. In *Springer Handbook of Nanotechnology*, pages 197–238. Springer.



# LIST OF FIGURES

1.1	Size comparison for various objects, in logarithmic scale. . . . .	5
1.2	Examples of micro- and nano-objects produces with different fabrication methods. . . . .	7
1.3	Structures produced by electron beam lithography. The smaller ones were 500 nm wide and 50 nm tall [Zhu et al., 2015]. . . . .	8
1.4	Characterization of a nano-structure in the SEM. (a) Sample before starting the measurements. (b) Membrane damaged by the measuring probe [Abrahamians et al., 2014]. . . . .	8
1.5	Representation of the characterization/assembly workflow of micro and nano-structures in SEM. . . . .	10
1.6	Carl Zeiss Auriga 60 scanning electron microscope, used during this work, and its main components. . . . .	13
1.7	Interaction between the focused electron beam with the surface of a sample produces backscattered electrons and secondary electrons. . . . .	14
1.8	Image of the mineral skeleton of a Radiolarian protozoa, acquired with optical and scanning electron microscopes [Newbury et al., 2003]. . . . .	15
1.9	SEM images of a micro-gripper extremity. . . . .	16
1.10	Examples of commercially available nano-manipulators. . . . .	17
1.11	Comparison between position measurements given by the internal sensor and by an external laser vibrometer for a step in the desired reference position. . . . .	18
1.12	Piezoelectric nano-manipulators from the MINIMAN family. Multiple robots were used in [Fahlbusch et al., 1999] to increase the flexibility for this manipulation station. In addition, the MINIMAN-II robot is mobile and could move freely over the platform. . . . .	18
1.13	Manipulation of a CNT over a surface using a needle-type end-effector [Hertel et al., 1998]. . . . .	19
1.14	Cutting of a ultra thin (50 nm) polystyrene film using a sharp needle. [Meyer et al., 2008] . . . . .	20
1.15	Two AFM tips with different stiffness were used to hold and perform traction test on a nanoparticle chain aggregate [Rong et al., 2006]. . . . .	20
1.16	A passive gripper used to assemble 3D structures inside the SEM [Dechev et al., 2004]. . . . .	21
1.17	Thermo-electric micro-gripper. By heating different parts of each finger, open and close movements could be produced [Nordström Andersen et al., 2009]. . . . .	22

1.18	Piezoelectric actuated gripper. The arms are composed of dual bi-morph structures, giving the end effector 6 DoF [Ciubotariu, 2015]. . . . .	23
1.19	Electrostatic comb-drive actuated gripper, located at the extremity of the circuit board (lower left corner of the image) [Beyeler et al., 2007]. . . . .	23
1.20	6 DoF force sensor [Beyeler et al., 2009]. . . . .	24
1.21	Tuning fork and application in characterization inside a SEM. . . . .	25
1.22	Electric characterization surface for nano-objects. It is composed of two gold covered pads, separated by 40 nm. Objects were carefully placed over the gap, and tested for its electric properties. [Suga et al., 2009]. . . . .	25
1.23	Proposed schematics for the first nano-manipulation station inside a SEM [Hatamura et al., 1990]. . . . .	26
1.24	SEM nanorobotic station. (a) Scheme for the station, which included 1 moving stage, 2 manipulators and an optical microscope to give lateral vision over the system. (b) Actual implementation, where all the components should be arranged to fit the vacuum chamber tight space [Koyano et al., 1996]. . . . .	27
1.25	Robotic manipulator developed in [Yu et al., 1999], to test CNTs in a free space, without the substrate interference. . . . .	27
1.26	CNT nano-tweezer fabricated on an AFM tip. Fingers could be controlled by applying a small voltage [Akita et al., 2002]. . . . .	28
1.27	SEM robotic station composed of 4 independent manipulators, for a total of 16 DoF. [Fukuda et al., 2003]. . . . .	28
1.28	Basic CNT transistor, build manually by placing the nanowire over pre-patterned electrodes [Kim et al., 2003]. . . . .	29
1.29	3D photonic crystal, built by stacking multiple planar structures. Scale bar of 5 $\mu\text{m}$ [Aoki et al., 2008]. . . . .	29
1.30	Robotic probing station. Combining vision servoing, the testing probes are automatically positioned over the desired spots. Contact between probes and substrate were detected by image inspection [Gong et al., 2013]. . . . .	31
1.31	Automatic selection and isolation of single carbon nanotubes, signaled by the red arrow in the image. Needle tips were used to sewer undesired connections between two electrodes [Zhang et al., 2012]. . . . .	31
1.32	Virtual manipulator model and interaction between virtual and real components. [Abrahamians et al., 2014]. . . . .	32
1.33	Desing of a microscale nanoassembly system to be fully contained on a chip, for operation in small environments, such as the SEM [Gorman et al., 2007]. . . . .	33
2.1	Effect of a short mechanical impulse to the SEM electron optical column (500000x amplification). From [Vladar, 2003]. . . . .	38
2.2	Effect of induced EMI disturbances on images [Pluska et al., 2009]. . . . .	40
2.3	Drift quantification of optical encoders on long usage inside the vacuum chamber [Zhang et al., 2013a]. . . . .	42

2.4	Deflection (a) and first resonance frequency (b) as a function of temperature for mono (silicon nitride, Cantilever A) and bi-material (silicon nitride with gold coating of different thickness, Cantilevers B,C and D) samples. [Mertens et al., 2003].	43
2.5	Normalized resonance frequencies of the first five flexural modes (M1–M5) of (a) the uncoated and (b) the gold-coated cantilever as functions of temperature [Sandberg et al., 2005]. . . . .	44
2.6	Carl Zeiss SEM Auriga 60, from the EQUIPEX ROBOTEX project, where the experiments were performed. . . . .	47
2.7	(a) Scheme of the experimental setup proposed and (b) implementation inside the SEM. . . . .	47
2.8	Vibrometer PSD results, considering different reflection levels and analog output gains. . . . .	49
2.9	Acquired signals for different output analog gains, at a constant reflection level of 50%. . . . .	50
2.10	Silicon cantilevers in the sample holder. . . . .	50
2.11	Averaged power spectrum density of the silicon cantilevers, detailing the frequencies with larger amplitude. . . . .	52
2.12	Finite element analysis for the vibrometer’s support. . . . .	52
2.13	PSD around 700 (a) and 955 Hz (b) comparing the SEM in two conditions. It indicates that the SEM could be the possible origin for these disturbances. . . . .	53
2.14	PSD of Cantilever 1, detailed for its first mode (1169.8 Hz), comparing both test conditions. . . . .	54
2.15	Photo of the experimental setup for external acoustic excitation, with the SEM, the loudspeaker and signal generator. . . . .	55
2.16	Displacements measured on Cantilever 1 under the influence of an external noise source of different powers, generated by the loudspeaker. A sinusoidal wave with frequency matching the sample’s first mode is applied as the disturbance signal. The black dashed line indicates when the external excitation starts. . . . .	56
2.17	Summary of the most important measured sources of disturbance. . . . .	57
2.18	Diagram relating the different sources of disturbances and their influence over systems of various sizes. . . . .	58
3.1	SEM image of the micro-gripper FT-G30 and its main components. . . . .	59
3.2	Example of the gripper’s step response in air, for a 30 V input. . . . .	60
3.3	Micro-gripper actuated finger and comb-drive system representation, showing its main components. . . . .	60
3.4	Micro-gripper representation, indicating that the laser beam measurement is not performed at the finger’s tip and that variations on the laser incident point can occur.	61
3.5	Experimental data used for estimating the relation between measured and actual tip displacement. The zoom box illustrates the contact between fingers. . . . .	61

3.6	Difference between experimentally measured and theoretical displacements for the micro-gripper electrostatic actuator. . . . .	62
3.7	Variation of model parameters for different input voltages, in air. . . . .	64
3.8	Comparison between responses for large step inputs (ranging from 5 to 45 V) in frequency domain. Experimental data is shown in blue, and simulated response based on the second order model is shown in red. . . . .	65
3.9	Influence of electronic input disturbance on the system in air. . . . .	66
3.10	Step response for the micro-gripper in vacuum, for a 40 V step input. . . . .	67
3.11	Duffing equation frequency responses. (a) shows the bifurcations (blue and red dots) for a softening non-linearity ( $\beta < 0$ ). (b) shows experimental response for the micro-gripper compared to a linear simulated response. . . . .	67
3.12	Variation of model parameters for different input voltages, in vacuum. . . . .	69
3.13	Comparison between responses for large step inputs (ranging from 5 to 45 V) in frequency domain, considering the gripper in vacuum. Experimental data is shown in blue, and simulated response based on the second order model is shown in red. . . . .	70
3.14	Effects of electronic input noise on the system. . . . .	71
3.15	Response comparison for micro-gripper step in air (blue) and vacuum (red). . . . .	73
3.16	Stiffness comparison for gripper in different environments, together with its corresponding polynomial fit functions. . . . .	73
4.1	Summary on several published works considering nano-positioning control in air and vacuum, accordingly to the main strategy employed and year of publication. . . . .	76
4.2	General LFT representation, containing the nominal system $G_0$ , the uncertainty block $\Delta$ and the controller $K$ . During robustness analysis, the nominal plant and controller are considered as a single system $M$ . . . . .	82
4.3	Feedback configuration for the small gain theorem. . . . .	84
4.4	LFT representation for the augmented structured disturbance $\Delta_{aug}$ , applied in the case of robust performance analysis. . . . .	85
4.5	Basic structure for the $H_\infty$ problem, in the LFT representation. . . . .	86
4.6	Block diagram representing the augmented plant $P$ , obtained from a nominal system $G$ and the weight functions $W$ . This structure is applied in the framework of $H_\infty$ synthesis to obtain the controller $K$ minimizing a relation between inputs ( $r, d, n$ ) and outputs in $z$ . . . . .	86
4.7	Sketch of the noise effects on the observer error. From [Khalil et al., 2014]. . . . .	93
4.8	Singular value plot from disturbance input $d$ to tracking error $e$ . Two different controllers were compared: one obtained through $H_\infty$ optimization when only reference tracking characteristics were considered ( $W_1$ , in blue), and another considering reference tracking and disturbance effects on the system ( $W_1 T_f^{-1}$ and disturbance characteristics $W_{dist}$ , in red). . . . .	96
4.9	Resulting sensitivity function $S$ and control sensitivity function $KS$ for the obtained $H_\infty$ controller (green line), compared with the target function (blue line). . . . .	97

4.10	The block diagram for the ESO controller implementation. . . . .	100
4.11	Robust stability index for the controllers. The curves show minimum and maximum bounds for the true value $\mu_{\Delta}$ . . . . .	100
4.12	Robust performance index for the obtained controllers. The curves show minimum and maximum bounds for the true value $\mu_{\Delta}^{perf}$ . . . . .	101
4.13	Simulated response to unitary step reference change considering various plants within the parametric variation range. (a) and (b) show the responses for a unitary reference step. The dashed-dot lined indicate the settling time ( $t_{98\%}$ ). (c) and (d) indicate the respective control signals applied. . . . .	102
4.14	Closed-loop Bode diagram, from the input disturbance $d$ to the system output $y$ , considering the nominal plant response (blue continuous line) and the worst case result (red, dashed line) achievable within the defined parametric variation range. . . . .	103
4.15	Closed-loop Bode diagram, from measurement noise $n$ to control signal $u$ , considering the nominal plant response (blue continuous line) and the worst case result (red, dashed line) achievable within the defined parametric variation range. . . . .	104
4.16	Experimental setup for validation of closed-loop control strategies. . . . .	105
4.17	Experimental response to step reference change of different amplitudes (between 50 nanometers and 25 micrometers). The responses are normalized, to contrast differences due to parametric variations. . . . .	106
4.18	Experimental closed-loop response to a constant reference signal, and control signal $u$ for each controller. No additional external disturbance is added. . . . .	108
4.19	Experimental responses for external acoustic excitations, considering the two controllers. The disturbance signal frequency is 1080 Hz with an intensity of 70 dB. The controllers are disabled at the start, to better illustrate their efficacy. . . . .	109
4.20	Impact test example, showing the sphere and approximated drop height. . . . .	109
4.21	Experimental impact test response, when a half-sphere of mass 10.8 grams is dropped near the microscope to mimic an impulsive disturbance on the system. . . . .	110
5.1	CAD representation of a serial 6 DoF robot for SEM developed at the FEMTO-ST laboratory, showing how it is positioned inside the SEM chamber. . . . .	115
5.2	Nano-helix between pads, to facilitate manipulation tasks without damaging the sample. Fabricated and kindly offered by the Laboratory of Photonics and Nanostructures (LPN) in Marcoussis, France. . . . .	116
B.1	Two possible representations for the LFT framework. . . . .	147



# LIST OF TABLES

1.1	Summary of issues presented during nano-manipulation tasks inside the SEM. . .	34
2.1	The vibrometer offers several analog output gain options, with different operation ranges. . . . .	48
2.2	Measurement noise RMS value and standard deviation for different output analog gains and reflection levels, and maximal measurement resolution for each gain. . .	49
2.3	Nominal dimensions (length $l$ , width $w$ and thickness $t$ ) and first resonance mode measured at atmospheric pressure for the different silicon cantilevers. . . . .	51
3.1	Summary of the identified parameter for the micro-gripper in different working environments. . . . .	72
4.1	Nominal parameters used for the micro-gripper dynamics, considered for the ESO.	98
4.2	Measured average RMS disturbance for the micro-gripper's tip, for different constant input voltage values, considering four operation conditions. . . . .	107



# LIST OF DEFINITIONS

1	Definition: Infinity norm . . . . .	83
2	Definition: Structured singular value . . . . .	84



# I

## APPENDIX



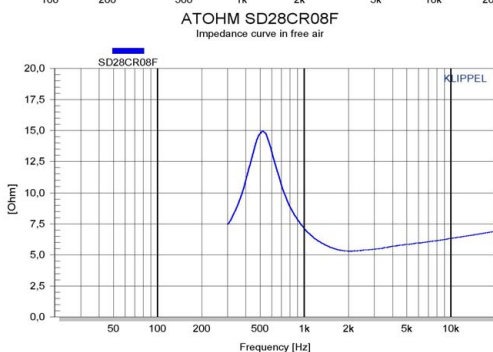
# ATOHM SD28CR08F DATASHEET

## ATOHM®

### CLASSIC SERIES SD28CR08F



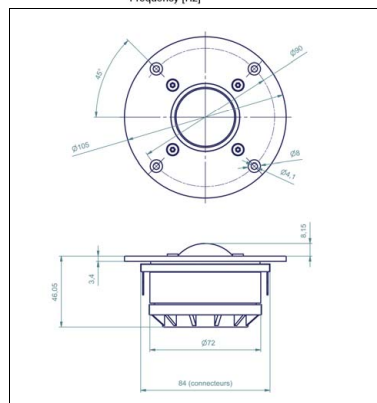
Le SD 28 CR08F est un tweeter hautes performances conçu pour couvrir une large bande de fréquence. Son dôme de 28mm en soie traitée est fixé à une bobine mobile support aluminium. L'entrefer est ferrofluidé afin d'augmenter la puissance admissible. Le noyau est doté d'une bague de cuivre dont l'avantage est de réduire sensiblement la distorsion par harmonique de rang 3. La face arrière du dôme est chargée par une cavité amortie permettant d'obtenir un excellent comportement aux fréquences les plus basses. La réponse en fréquence est caractérisée par une excellente linéarité conjuguée à une faible directivité et par une extension supérieure à 30kHz.



Puissance admissible (avec filtrage)	100 W(rms)
Puissance admissible en crête	300 W
Sensibilité	90 dB/2.83V/1M
Impédance nominale	8 ohms
Résistance au CC	5.8 ohms
Fréquence de résonance	660 Hz
QTS	-
QES	-
OMS	-
Cms	-
Mms	-
Vas	-
BL	-
Le	0.011mH
Surface émissive	6.6cm <sup>2</sup>
Diamètre bobine	28mm
Hauteur bobine	3.2mm
Hauteur entrefer	2.5mm
Densité de flux	11000 gauss
X-max linéaire	+/- 0.35mm
Excursion maximale en crête	-
Fréquence de coupure conseillée	1700 Hz/12dB

Paramètres faible amplitude obtenus avec une précision maximale par la méthode de mesure par analyseur Klippel et capteur micrométrique laser sur banc haute stabilité.

Conditions de mesure de la réponse en fréquence : bruit rose 2.83Vrms, distance 1m, support de 23°/150cm.



Notre souci de la performance nous conduit à faire évoluer fréquemment nos produits. Les présentes caractéristiques sont susceptibles d'être modifiées sans avertissement préalable.

ATOHM est une marque déposée de Welcolum Technology (France).  
WWW.ATOHM.COM tel : +33 3 81 47 91 01 fax : +33 3 81 47 90 53



# B

## THE LINEAR FRACTION TRANSFORMATION

A common framework for modeling and analysis of uncertainty in systems is the use of Linear Fraction Transformations (LFT), a notation that allows representing uncertainties and its effects on systems flexibly. Supposing a matrix  $P$ , complex, that can be partitioned as [Doyle et al., 1991]:

$$P = \begin{bmatrix} P_{11} & P_{12} \\ P_{21} & P_{22} \end{bmatrix} \in \mathbb{C} \quad (\text{B.1})$$

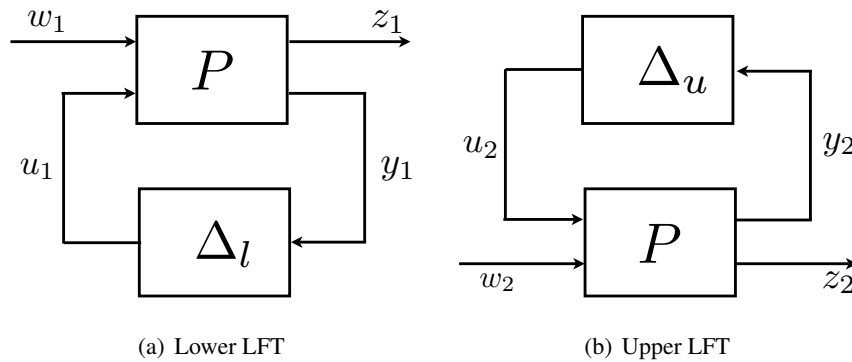


Figure B.1: Two possible representations for the LFT framework.

Let  $\Delta_u$  and  $\Delta_l$  be two other complex matrices of appropriate dimensions. Assuming the matrices are connected as shown in Figure B.1, the maps connecting its input  $w_i$  to the output  $z_i$  are given by:

$$\begin{bmatrix} z_1 \\ y_1 \end{bmatrix} = \begin{bmatrix} P_{11} & P_{12} \\ P_{21} & P_{22} \end{bmatrix} \begin{bmatrix} w_1 \\ u_1 \end{bmatrix}, \quad (\text{B.2})$$

$$u_1 = \Delta_l y_1$$

for the scheme on the left image and:

$$\begin{bmatrix} y_2 \\ z_2 \end{bmatrix} = \begin{bmatrix} P_{11} & P_{12} \\ P_{21} & P_{22} \end{bmatrix} \begin{bmatrix} u_2 \\ w_2 \end{bmatrix}, \quad (\text{B.3})$$

$$u_2 = \Delta_u y_2$$

for the scheme shown on the right image.

Considering the signals  $u_i$  and  $y_i$  as internal signals, the relation between input and output can be described by Equations B.4 and B.5:

$$F_l(P, \Delta_l) := P_{11} + P_{12}\Delta_l(I - P_{22}\Delta_l)^{-1}P_{21} \quad (\text{B.4})$$

$$F_u(P, \Delta_u) := P_{22} + P_{21}\Delta_u(I - P_{11}\Delta_u)^{-1}P_{12} \quad (\text{B.5})$$

where the  $F_l$  is the lower and  $F_u$  is the upper LFT. Those LFTs represent the transfer of signal  $w$  to  $z$ , for a system under effects of a perturbation proportional to  $y$ .

An interpretation of the LFT is that the system has a nominal mapping connecting  $w$  to  $z$  ( $P_{11}$  in the lower form and  $P_{22}$  in the upper form) while the other elements in  $P$  show the interaction of how perturbations affect this nominal map.

## NOISE IMPACT ON HIGH-GAIN OBSERVER

One of the limitations in the use of high-gain observers is that, as its structure approximates a differentiation, high-frequency measurement noises can lead to great deterioration in the signal/noise ratio. This demonstration was extracted from [Khalil et al., 2014].

Considering the system described in Equation C.1:

$$\begin{cases} \dot{x}_1 &= x_2 \\ \dot{x}_2 &= f(x, \Phi(\hat{x}, w), w, d) \\ y &= x_1 + n \end{cases} \quad (\text{C.1})$$

with  $w$  a vector of known external signals,  $d$  a vector of unknown external disturbances,  $\Phi$  a feedback control stabilizing the system around its origin,  $n$  the measurement noise and  $\hat{x}$  the estimated values of the real states  $x$ . The noise  $n$  and its derivatives are assumed to be bounded.

A high-gain observer for the system above will have the form:

$$\begin{cases} \dot{\hat{x}}_1 &= \hat{x}_2 + \frac{\alpha_1}{\varepsilon}(x_1 + n - \hat{x}_1) \\ \dot{\hat{x}}_2 &= \hat{f}(\hat{x}, \Phi(\hat{x}, w), w) + \frac{\alpha_2}{\varepsilon^2}(x_1 + n - \hat{x}_1) \end{cases} \quad (\text{C.2})$$

with  $\hat{f}(\cdot)$  the estimated value of the real system dynamics  $f(\cdot)$ ,  $\alpha_i > 0$  and  $0 < \varepsilon \ll 1$  the observer parameters.

Computing the estimation error  $\tilde{x}_i = x_i - \hat{x}_i$  considering the output with noise will result in:

$$\begin{cases} \dot{\tilde{x}}_1 &= -\frac{\alpha_1}{\varepsilon}\tilde{x}_1 + \tilde{x}_2 - \frac{\alpha_1}{\varepsilon}n \\ \dot{\tilde{x}}_2 &= -\frac{\alpha_2}{\varepsilon^2}\tilde{x}_1 + \delta(x, \tilde{x}, w, d) - \frac{\alpha_2}{\varepsilon^2}n \end{cases} \quad (\text{C.3})$$

with  $\delta(x, \tilde{x}, w, d) = f(x, \Phi(\hat{x}, w), w, d) - \hat{f}(\hat{x}, \Phi(\hat{x}, w), w)$ . Using the scaled estimation error transformation  $\zeta_1 = \frac{\tilde{x}_1}{\varepsilon}$ ,  $\zeta_2 = \tilde{x}_2$  allows to obtain the singularly perturbed equation C.4

$$\begin{cases} \varepsilon\dot{\zeta}_1 &= -\alpha_1\zeta_1 + \zeta_2 - \frac{\alpha_1}{\varepsilon}n \\ \dot{\zeta}_2 &= -\alpha_2\zeta_1 + \varepsilon\delta(x, \tilde{x}, w, d) - \frac{\alpha_2}{\varepsilon}n \end{cases} \quad (\text{C.4})$$

In this case, the estimation error in closed loop satisfies an inequality of the form:

$$\|x(t) - \hat{x}(t)\| \leq c_1\varepsilon + c_2\frac{\mu}{\varepsilon}, \quad \forall t \geq T \quad (\text{C.5})$$

with  $\mu = \sup |n|$ . The noise amplitude imposes a limit on the practical value of  $\varepsilon$ , limiting the speed for observer convergence.





## Abstract:

This work studies the nano-positioning problem inside the scanning electron microscope (SEM). To acquire fast and accurate positional information, a dedicated setup was implemented consisting of a vibrometer placed inside the SEM. This approach differs from methods based on image processing, as it allows to capture real-time data on the dynamic behavior of structures. In a first study, the mechanical disturbances acting inside the microscope's vacuum chamber were characterized and its sources were identified. This demonstrated how external mechanical vibrations and acoustic noises can largely influence the components inside the SEM through mechanical coupling, limiting the effective positioning precision of manipulators. Next, a commercial micro-gripper was studied, both in air and in vacuum, and the differences between its response were highlighted. This allowed to obtain two dynamic models for this end-effector, one for each environment. Two control laws were proposed ( $H_\infty$  control and Extended State Observer based control) for the system, to obtain a real-time, precise positioning in the vacuum environment and to attenuate the effects of the external mechanical disturbances. Results were demonstrated through simulation and experimental validation.

**Keywords:** Nano-manipulation and characterization, scanning electron microscope (SEM), robust position control, micro-gripper, disturbance characterization in SEM,  $H_\infty$  control, extended state observer.

## Résumé :

Cette thèse étudie le problème de nano-positionnement à l'intérieur d'un microscope électronique à balayage (MEB). Pour obtenir des informations de position avec rapidité et précision, une installation dédiée composée d'un vibromètre placé à l'intérieur du MEB a été mise en œuvre. Cette approche diffère de méthodes basées sur le traitement d'images, car elle permet de saisir des données en temps réel sur le comportement dynamique des structures étudiées. Dans une première étude, les perturbations mécaniques agissant à l'intérieur de la chambre à vide du microscope ont été caractérisées et leurs sources ont été identifiées. Cela a démontré comment les vibrations mécaniques externes et les bruits acoustiques peuvent influencer largement sur les composants à l'intérieur du MEB par couplage mécanique, limitant ainsi la précision des manipulateurs. Dans un deuxième temps, une micro-pince du commerce a été étudiée. Une différence entre ses comportements dans l'air et dans le vide a été mise en évidence, ce qui a permis d'obtenir deux modèles dynamiques pour cet organe terminal, un pour chaque environnement. Deux lois de commande ont été proposées (commande  $H_\infty$  et commande basée sur un observateur d'état étendu), afin d'obtenir en temps réel un positionnement précis dans le vide, et d'atténuer les effets des perturbations mécaniques externes. Les résultats ont été validés en simulation et expérimentalement.

**Mots-clés :** Nano-manipulation et caractérisation, microscope électronique à balayage (MEB), commande robuste de position, micro-pince, caractérisation des perturbations dans le MEB, commande  $H_\infty$ , observateur d'état étendu.

The logo for SPIM (École doctorale SPIM) features a stylized 'S' followed by the letters 'PIM' in a large, white, sans-serif font. A yellow horizontal bar is positioned to the left of the 'S'.

■ École doctorale SPIM 16 route de Gray F - 25030 Besançon cedex

■ tél. +33 (0)3 81 66 66 02 ■ [ed-spim@univ-fcomte.fr](mailto:ed-spim@univ-fcomte.fr) ■ [www.ed-spim.univ-fcomte.fr](http://www.ed-spim.univ-fcomte.fr)

The logo for the University of Franche-Comté (UNIVERSITÉ DE FRANCHE-COMTÉ) features a stylized 'U' and 'FC' in a bold, black, sans-serif font. A yellow vertical bar is positioned to the left of the 'U'. Below the 'U' and 'FC' are the words 'UNIVERSITÉ' and 'DE FRANCHE-COMTÉ' in a smaller, black, sans-serif font.